

Superconducting Detectors and Massive Gauge Bosons in Superconductivity

Thesis submitted for the degree of
Doctor of Philosophy
at the University of Leicester

by

Daniel Brandt
Space Research Centre
Department of Physics and Astronomy
University of Leicester

1st October 2008

Superconducting Detectors and Massive Gauge Bosons in Superconductivity

Daniel Brandt

Abstract

This thesis is concerned with the fundamental physics of the superconducting-to-normal transition (sn-transition), particularly the mechanisms which give rise to massive gauge bosons and applications of the superconducting-to-normal transition, particularly in the form of superconducting radiation detectors. The basics of three of the most common types of superconducting particle detectors are discussed in Chapter 2: Superconducting Tunnel Junctions (STJs), Transition Edge Sensors (TESs), and Metallic Magnetic Calorimeters (MMCs). The chapter continues with an investigation of the phenomenon of TES excess noise, a white noise source of uncertain origin apparently intrinsic to the device [1]. The current theories of Phase Slip Shot Noise (PSSN) and percolation noise are discussed and the quantitative analytical model proposed by Fraser [2] is extended to include the magnetic field dependence of the noise spectral current density. An analytical expression for the dependence of the percolation noise spectral current density on experimental parameters is derived.

In Chapter 3 the author addresses the question of whether quantum mechanical fluctuations of the vacuum energy can influence the sn-transition. The existing theory is refined by developing a treatment of the system using superconductor-specific electrodynamics. A mathematical model of the relevant vacuum interactions is derived and a quantitative estimate of the magnitude of the coupling is presented.

In superconductors photons have a non-zero rest mass arising from the Higgs mechanism. Chapter 4 discusses the optical properties of a hypothetical transparent superconductor and finds practical applications. In Chapter 5 it is found that the Higgs mechanism applies to any gauge field generated by the superconducting electrons, including their gravitational field and a theory of massive gravity is developed. The massive gravitational field is propagated by non-zero rest mass gravitons, and the theory predicts the sum of gravitomagnetic flux and magnetic flux through a superconducting ring to be quantised. Some of the implications and possible experiments are explored.

Declaration

I hereby declare that no part of this thesis has previously been submitted to this or any other university as part of the requirement for a higher degree. The work described herein was conducted solely by the undersigned except for those colleagues and other workers acknowledged in the text.

Daniel Brandt
December 5, 2008

IV

for my parents

with gratitude and love

Acknowledgements

I would like to acknowledge the contributions of a number of people who have made my work both easier and more enjoyable by investing their time (and patience) in helping me out: My supervisor George Fraser whose advise has been invaluable, along with his willingness to let me continue on various tangents, which have come to make up the bulk of this thesis. Tim Stevenson, Derek Raine, Chris Binns, and Richard Willingale who helped me turn those tangents into something worthwhile. Nigel Bannister, who has provided a lot of professional advice and common sense. Robert Limpenny, Chris Bicknel, Duncan Ross, David Bassford and Tony Crawford, without whose practical expertise none of my experimental work would have been possible. Richard Ambrosi, whose advice was very welcome, even if it wasn't taken. EADS Astrium, for providing the funding for my studentship. Michelle and Charly, for providing sanity in the office and for securing a steady succrose supply. And finally Laura, who has had to put up with me during those last few weeks of writing up.

Publications and Intellectual Property

Chapter 3 Sections 3.2.1 to 3.5

D. Brandt, G.W. Fraser, D.J. Raine, C. Binns. **Superconducting Detectors and the Casimir Effect**, *Journal of Low Temperature Physics*, Vol.151, p.25-31

Chapter 5:

D. Brandt, D.J. Raine, G.W. Fraser, **Massive spin-1 gravity and the gravitational flux quantum**, *Physics Letters A*, Vol.372, Issue 14

Chapter 4

At the time of writing patent protection is being sought for the Heavy Photon Optics technology outlined in chapter 4. An application for preservation of date of precedence has been filed, and the patent priority filing number is GB0806470.1

List of Figures

1.1	A disc magnet floating above a nitrogen cooled sample of Yttrium Barium Copper Oxide (YBCO). Image taken from Wikimedia [3]	5
1.2	Discontinuity in specific heat at sn-transition temperature (lambda-anomaly). The dotted lines are extrapolation of the respective superconducting and normal state heat capacities and are merely provided as a guide to the eye. Sketch according to [4].	9
1.3	Variation of macroscopic wave function $ \Psi $ with temperature T according to equation (1.2). The density of superconducting electrons is given by $ \Psi^2 $	11
1.4	Temperature variation of a) critical field according to equation (1.3) and b) penetration depth in aluminium ($T_c = 1.2K$ [5]) according to equation (1.5).	14
1.5	As the temperature decreases the minimum energy configuration of the system changes from $\phi = 0$ to $ \phi > 0$. Generally ϕ is a complex number, with the modulus of ϕ determining the number density of superconducting electrons and the argument of ϕ determining the phase of the macroscopic wave function. In the diagram above positive and negative ϕ are in anti phase.	16
2.1	Basic working principle of an STJ: an incoming photon is absorbed in the top electrode and breaks a cooper pair, creating two quasi particles. Due to the bias voltage across the potential barrier these quasi particles can now tunnel across the barrier into the bottom electrode where they can be counted. The number of quasi particle charges created depends linearly on the energy of the incoming photon. Diagram after Polushkin [6].	24
2.2	Experimental resistance vs. temperature curve of a TiAu bilayer TES in the sn-transition region. Data taken from Takei [7]	26

2.3	Sketch of a basic TES setup. Photons are stopped by the absorber and the thermal energy diffuses from the absorber into the TES. The TES resistance increases as a consequence of the change in temperature, which decays exponentially back to its equilibrium state as thermal energy diffuses through the weak thermal link G and returns the TES and absorber to their equilibrium temperature T_0	27
2.4	Example setup for a Metallic Magnetic Calorimeter (MMC)	29
2.5	Noise spectral current density in a TES with normal state resistance $R_n = 100m\Omega$. The solid line is the total noise observed, made up from the quadrature sum of an analytical fit to experimental excess noise according to equation (2.9)(dashed black line) and Johnson noise according to equation (2.5) (dashed gray line).	34
2.6	Shape of the percolation transition for finite and infinite networks	46
2.7	Predictions of the Fraser-PSSN model (eq. (2.11)) for the devices reported by Fraser [2] for a TiAu bilayer TES with ($I = 70.5\mu A; V = 0.55\mu V; \sqrt{\xi l} = 22nm; A = 0.125 \times 10^{-6}m^2$) and a MoCu bilayer TES with ($I = 20\mu A; V = 0.11\mu V; \sqrt{\xi l} = 39nm; A = 0.16 \times 10^{-6}m^2$), both at $T = 63mK$. The empirical excess noise (eq. (2.9)) has also been plotted for comparison.	49
2.8	Noise spectral current density as a function of TES resistivity as predicted by the percolation noise model, compared to the empirical noise spectral current density (eq.(2.9)).	50
2.9	Comparison between the predicted noise spectral current densities as a function of magnetic field for percolation noise (black line) and phase slip shot noise (blue line) as a function of magnetic field. In order for the predictions of the PSSN model to hold the field must be strong (i.e. all vortices in the TES due to the external field). The PSSN model has been plotted using the operating parameters for the TiAu TES used for figure 2.7. Percolation model constants of proportionality $A = 4.42 \times 10^{-12}, k = 50m^3$ were obtained by best fit to the empirical expression (eq.(2.9)).	51
2.10	Position and width of percolation transition depending on TES aspect ratio. Variations in transition behavior are small compared to variations in aspect ratio $R_A = \frac{height}{width}$. It can be seen that the critical fraction ρ_{cs} increases slowly with increasing aspect ratio R_A . The graphs were generated using the author's own recursive numerical simulation.	52
2.11	Zebra stripe geometry to suppress TES excess noise, a) illustration b) SEM image of actual device [8].	54

2.12 Illustration of a) the geometry of the TES as used by Takei et al. [7] when reporting a threshold current below which excess noise does not occur and b) microscope image of the same device (courtesy of Takei [7]) 57

3.1 Basic Casimir cavity. The dependence of the energy density on the discrete ZPE spectrum in between the plates causes them to attract. Image taken from [9] 65

3.2 Illustration of five-layer cavity layout for detection of vacuum energy change as proposed by Bimonte et al. [10]. In the initial version of the experiment proposed, the width of the superconducting film was $10nm$, the width of the dielectric spacer was $8nm$ and the thickness of the normal metal boundaries is irrelevant [10]. 69

3.3 Basic CorTES geometry[11]: An AlOx barrier separates the apex-electrode-film from the TES film, creating a Casimir cavity as discussed in the text. 72

3.4 Magnitude of photon group velocity vs. photon wavelength on the surface of an aluminium film with $\lambda_{crit} \approx 100nm$, according to equation (3.14). Note that for $\lambda_{vac} > \lambda_{crit}$ the value of v_g will be complex. The critical wavelength λ_{crit} has been determined from the London penetration depth of aluminium $\lambda_L = 16nm$ 78

3.5 Characteristic decay depth vs. wavelength for HPO element with critical wavelength $500nm$ 81

3.6 a) The relative changes to the Casimir force due to transverse mode (red) and longitudinal mode (black) contributions, as a function of cavity width b) The Casimir force as predicted by Maxwellian (dashed line) and Proca (solid line) electromagnetism (according to eqns.(3.28)-(3.29b)), as a function of cavity width. Both plots assume a photon mass of $1.4 \times 10^{-34}kg$, corresponding to superconducting aluminium (eqn.(3.11)) and a boundary thickness of $10\mu m$ 85

3.7 Symmetry structure of the cavity with superconducting boundaries (not to scale). . . . 90

3.8 Dielectric function of the vacuum due to heavy photon effects according to eq.(3.40) for the case of aluminium boundaries ($\lambda_L = 16nm$)and zero distance to the boundary surface. 95

3.9 Dimensionless dielectric function $\epsilon_{1,2}$ of gold as a function of imaginary frequency ξ . The solid black line represents the predictions of the Drude model (eq. (3.41)), while the dashed gray line has been recovered from experimental data provided in Palik [12]. 97

3.10	Relative error $\Delta F/F_0$ (left) and absolute error $\Delta F = F_L - F_0$ (right) of our implementation of Lifshitz theory for the case $\epsilon_3 = 0, \epsilon_{1,2} \rightarrow \infty$	98
3.11	The phase velocity v_p (left) and group velocity v_g (right) of Aluminium ($\lambda_{crit} \approx 100nm$) as a function of wavelength. The graphs show the real (black) and imaginary (red) components of the respective complex velocities. Note that v_p, v_g are either purely imaginary or purely real over the entire real wavelength axis.	100
3.12	Illustration of the variation of the real part of the phase velocity with cavity position (not to scale). The cavity boundaries are located at the left and right hand extremities of the plot.	101
3.13	Dimensionless geometric compensation factor $\Gamma^{1/8}$ (left) and cavity width reduction $2\Delta z$ (right) for aluminium as functions of wavelength. The dashed red line marks the transition from subcritical to supercritical regime.	104
3.14	Effective dielectric function $\epsilon_{1,2}(\xi)$ of superconducting Al cavity boundaries (solid black line) vs. imaginary frequency magnitude ξ . The predictions of the Drude model for Al boundaries are given for comparison (dashed gray line). The graph is divided into the region of supercritical modes (left of blue line) and sub critical modes (right of blue line).	105
3.15	Casimir force in an Al cavity with superconducting boundaries. The upper boundary of the shaded region is obtained from the normal Drude model for $\epsilon_{1,2}$, while the lower boundary is obtained from the finite step model.	107
3.16	Relative change in Casimir force in an Al cavity with superconducting boundaries compared to the normal state boundary Casimir force. The upper boundary of the shaded region is obtained from the normal Drude model for $\epsilon_{1,2}$, while the lower boundary is obtained from the finite step model.	108
3.17	Variation of Casimir force with London penetration depth λ_L for a $40nm$ cavity with Al boundaries as predicted by Lifshitz theory. The black line represents the total-isolation limit, the blue line represents the zero-isolation limit and the constant green line is the prediction of Lifshitz theory for the case of normal state boundaries.	109
3.18	Relative variation of Casimir force with cavity width for a Al boundary cavity filled with a perfectly transparent superconductor.	111

- 3.19 Variation of the Casimir force according to the total-isolation limit model with decay constant β , assuming a minimum stand-off distance Δz_{min} below which isolation breaks down. The dashed line at $F_{SC}/F_{normal} = 1$ is provided as a guide to the eye. 115
- 3.20 Relative variation of the Casimir force with London penetration depth λ_L for a cavity with Al boundaries as ratio of superconducting boundary force F_{sc} to normal state boundary force F_{normal} for a cavity of width 40 nm. The predictions of F_{SC} sharply reduce to those of conventional Lifshitz theory for large $\lambda_{crit} > 40nm$ since modes with wavelengths $\lambda \approx \lambda_{crit}$ are excluded from the cavity (we recall $\lambda_{crit} = 2\pi\lambda_L$). 115
- 4.1 Refractive index of prism glass (F2 Schott Glass as offered by CVI Laser [13]) and a HPO element made of indium tin oxide with $\lambda_{crit} = 667nm$ near the critical wavelength are plotted as a function of vacuum wavelength of the incident radiation 125
- 4.2 Group velocity v_g (left) and group dispersion (right) as functions of normalized wavelength λ/λ_{crit} for a hypothetical HPO element. 127
- 4.3 Variation of the normal incidence reflectivity of a HPO element with incident wavelength given as a fraction of the critical wavelength. 129
- 4.4 Reflectance from thin films: Light transmitted into the film at angle δ has a chance of leaving the film at the angle of reflection δ after multiple internal reflections. 130
- 4.5 Examples of thin film interference on a soap bubble (left, image by Aberdeen University) and an oil slick (right, image by Georgia State University) 132
- 4.6 Variation of carrier density with temperature T and external magnetic field H for a superconductor of critical temperature $T_c = 1.5K$ and critical field $H_c = 101G$ and electron number density $n_e = 3 \times 10^{21}cm^{-3}$ 135
- 4.7 Left: Variation of the London penetration depth $\lambda_L (= \lambda_{crit}/2\pi)$ with temperature T and external field H . Right: Variation of phase refractive index n_p with Temperature T and external field H . Both graphs are plotted for a superconductor with superconducting electron number density $n_s^0 = 3 \times 10^{21}cm^{-3}$ at $T = 0K$ 137
- 4.8 A prism with apex angle σ , with light incident at minimum deviation δ . a) The minimum deviation angle is the angle of incidence which causes light to travel parallel to the prism base. b) illustration of the working principle of a dispersion prism. Note: In order to achieve the best energy resolution the entire prism has to be illuminated. Image courtesy of Georgia State University [14] 140

- 4.9 Comparing the interference pattern of a conventional etalon (dashed line) and a HPO etalon (solid line) with critical wavelength $\lambda_{crit} = 431nm$. An external reflector of reflectivity $R_I = 30\%$ is applied to both etalons which have a thickness of $0.5\mu m$. The wide band and narrow band responses are plotted in figures a) and b) respectively. It can be seen from a) that far from λ_{crit} the peak fwhm resolution of the HPO etalon approaches that of the conventional etalon. 142
- 4.10 Illustration of the optical routing principle: Only the elements set to $\lambda_{crit} = \lambda_{signal}$ are reflective. All other elements allow the signal to pass unhindered. 145
- 4.11 Transmission coefficient of a HPO etalon as a function of wavelength. This etalon is used as a logic gate. The transmission coefficient varies with applied signal strength and transmission functions are plotted for signal strengths of $6mW/m^2$ (grey dashed line), $12mW/m^2$ (blue dashed line) and "no signal" (black solid line). 147
- 5.1 a) Argand diagram and b) Point on the complex plain undergoing U(1) rotation 152

Contents

Abstract	II
Declaration	III
Dedication	IV
Acknowledgements	V
Publications	VI
List of figures	VII
1 Introduction	3
1.1 Introduction to Superconductivity	4
1.1.1 A Brief History of Superconductivity	4
1.1.2 Basic Properties of Superconductors	8
1.2 Thesis Organization	18
2 Superconducting Particle Detectors	21
2.1 Types of Superconducting Detectors	23
2.1.1 Superconducting Tunnel Junctions	23

2.1.2	Transition Edge Sensors	25
2.1.3	Metallic Magnetic Calorimeters	27
2.2	Transition Edge Sensor Classical Noise Sources	29
2.2.1	Aspects of Transition Edge Sensor Noise and Operation	29
2.3	Transition Edge Sensor Excess Noise	33
2.3.1	Mathematical form of excess noise	35
2.3.2	Phase Slip Shot Noise	35
2.3.3	Percolation Noise	39
2.3.4	Comparison of Noise Theories with Experimental Data	47
2.3.5	Conclusion: A Combined Excess Noise Theory	58
3	Superconducting Phase Transition and the Quantum Mechanical Vacuum	61
3.1	Introduction to the Physics of the Quantum Electrodynamical Vacuum	62
3.2	The Casimir Effect and the Energy Balance of the Superconducting Casimir Cavity	64
3.2.1	Thermodynamics of the Superconducting State and the Casimir Effect	66
3.3	Conclusions Regarding the Superconducting Phase Transition and the Quantum Vacuum	70
3.4	Implications for Practical Detector Operation	71
3.5	The Superconducting Transition and Massive Electromagnetism	73
3.5.1	Longitudinal Photons	75
3.5.2	Massive Photon Velocity, Frequency and Momentum	76
3.5.3	Above the Critical Wavelength: Non-Propagating Low Frequency Components	80
3.5.4	Proca vs. Maxwellian Treatment	82
3.5.5	The Massive Casimir Effect	83

3.5.6	Applicability of Massive Electromagnetism and the Barton and Dombey Solutions to the Casimir Effect	86
3.5.7	Cavity Types	90
3.6	The Casimir Effect for Cavities with Superconducting Boundaries	91
3.6.1	Lifshitz Theory	92
3.6.2	Dielectric Functions and the Refractive Index	93
3.6.3	Dielectric Function of the Vacuum	93
3.6.4	Dielectric Function of Real Material Boundaries	94
3.6.5	Implementation of Lifshitz Theory	96
3.6.6	Effective Dielectric Function of the Cavity Volume	99
3.6.7	Supercritical Modes	100
3.6.8	Effective Width of the Cavity	102
3.6.9	Effective Dielectric Function of the Cavity Boundaries	104
3.6.10	The Magnitude of the Casimir Effect in Superconducting Cavities	104
3.6.11	Conclusions regarding the Casimir Effect in Cavities with Superconducting Boundaries	117
4	Heavy Photon Optics	121
4.1	Optical Parameters of HPO Elements	122
4.1.1	Phase Velocity, Phase Refractive Index and Phase Dispersion	123
4.1.2	Group Velocity, Group Refractive Index and Group Dispersion	126
4.1.3	Reflection and Reflectance of HPO Elements	128
4.2	Optical Properties of a Thin Film Heavy Photon Optics Element	131
4.2.1	Thin Film Reflectance and Interference	131

<i>CONTENTS</i>	1
4.2.2 Superconducting Parameters and the Critical Wavelength	133
4.2.3 Transparent Superconducting Materials: Towards Practical Heavy Photon Optics	137
4.3 Potential Applications for HPO Technology	140
4.3.1 Ultrahigh Resolving Power Dispersion Prisms	140
4.3.2 Interferometers and Etalons	141
4.3.3 Optical Routers and Quantum Non-Demolition Routing	143
4.3.4 Universal Optical Logic Gates and Optical Logic Chips	144
5 Massive Gauge Bosons in Quantum Coherent Matter	149
5.1 U(1) Phase Rotational Symmetry and Local Electromagnetic Gauge Invariance	150
5.1.1 The Relativistic Photon Field	153
5.2 Massive Gauge Bosons From Broken U(1) Symmetry	153
5.2.1 The Gravitoelectromagnetic Equations and Gravitoelectromagnetic Gauge Invariance	154
5.2.2 Massive Spin-1 Gravitons by GEM Gauge Invariance Breaking	157
5.2.3 Derivation of the Photonic Mass	158
5.2.4 Experimental Evidence for Massive Gravitons	159
5.2.5 Massive Gauge Bosons: Conclusions	160
5.3 Quantised Gravity and the Consequences	161
5.3.1 Quantisation of Gravitational Flux	161
5.3.2 Gravity Induced Currents in Multiply Connected Superconductors	163
5.4 Massive Gravity and Astrophysics - Neutron Star Cores and Gravitational Collapse .	164
6 Summary and Conclusions	167

6.1 Closing Remarks 170

Chapter 1

Introduction

This work covers what, at first glance, may appear to be a confusingly wide spread of topics. They range from terrestrial applications of superconductivity in the form of spectrometer technology to theoretical astrophysics when discussing neutron star cores, from refining operation of experimental devices (transition edge sensor excess noise) to the almost purely theoretical (massive gauge bosons). Even the practical applications of superconductivity discussed range from the well studied experimental (superconducting tunnel junctions) to completely new technologies (heavy photon optics).

However, one basic unifying concept exists for the plethora of topics - all of them depend on superconductivity as the central principle. Superconductivity, and the physics of transitions between the normal and superconducting states, is then the central topic of this thesis.

A complete introduction to the topic of superconductivity is well beyond the scope of this work, and the interested reader is referred to Tilley[4] for a thorough discussion of the basic principles. Nevertheless, the following section gives a short overview of some of the basic concepts of superconductivity. In the literature different symbols may be used for standard parameters, and by including a quick introduction at this point the symbols used in the following chapters are established.

Following this introduction to superconductivity, section 1.2 outlines the organization of this thesis and provides a draft outline of the arguments and conclusions developed in its course. This overview is intended to provide the motivation for the work undertaken in the following chapters.

1.1 Introduction to Superconductivity

Certainly the most prominent image associated with superconductivity is that of a disc magnet floating above a piece of high temperature superconductor (fig.1.1). This is just one of the many surprising effects that superconductivity is capable of producing, but it is by far the most visual one. Still, this experiment does not explain what a superconductor actually is.

From an experimentalist point of view a superconductor is any piece of material in which the electric resistivity ρ drops to zero discontinuously at a critical temperature T_c . Unlike so many other real world effects where a parameter of interest appears to vanish the resistivity in a superconducting sample is not *practically* zero or *almost* zero. It is actually, exactly, zero. A current in a superconducting loop of wire can persist forever.

In addition to having zero resistivity, a superconductor will exclude magnetic fields from its interior, producing the floating-disc effect in figure 1.1. This is known as the Meissner effect, or more accurately the Meissner-Ochsenfeld effect [15]. Together with zero electrical resistivity, magnetic flux exclusion is one of the two most widely known symptoms of superconductivity.

The Meissner effect highlights the difference between a *superconductor* and a *perfect conductor*. A perfect conductor will obey all classical physics while having a resistivity $\rho = 0$. A perfect conductor will “freeze-in” any magnetic field present in its interior at the time when perfect conductivity is established, while a superconductor will expel it. This is the first hint that something far more fundamental than just a transition to zero resistivity is happening inside a superconductor. It is the author’s hope that, at the end of this work and after having considered the many modifications and alterations required to classical physics in the presence of superconductivity, the attribute of zero electrical resistance will appear as an almost trivial side effect of something far more interesting.

1.1.1 A Brief History of Superconductivity

It has long been known that the resistivity of virtually all conductors reduces with decreasing temperature of the conductor. In 1911 liquid Helium had just become available as a refrigerant and when the Dutch physicist Heike Kammerlingh Onnes investigated the conductivity of solid Mercury he observed that the resistivity dropped to zero discontinuously at 4.2K [16]. This discovery was the beginning of the field of superconductivity.

In 1913 the heavy metal lead(Pb) was found to be superconducting and Kammerlingh Onnes received the Nobel prize in physics the same year for his work on the subject. Still, the physical basis for the

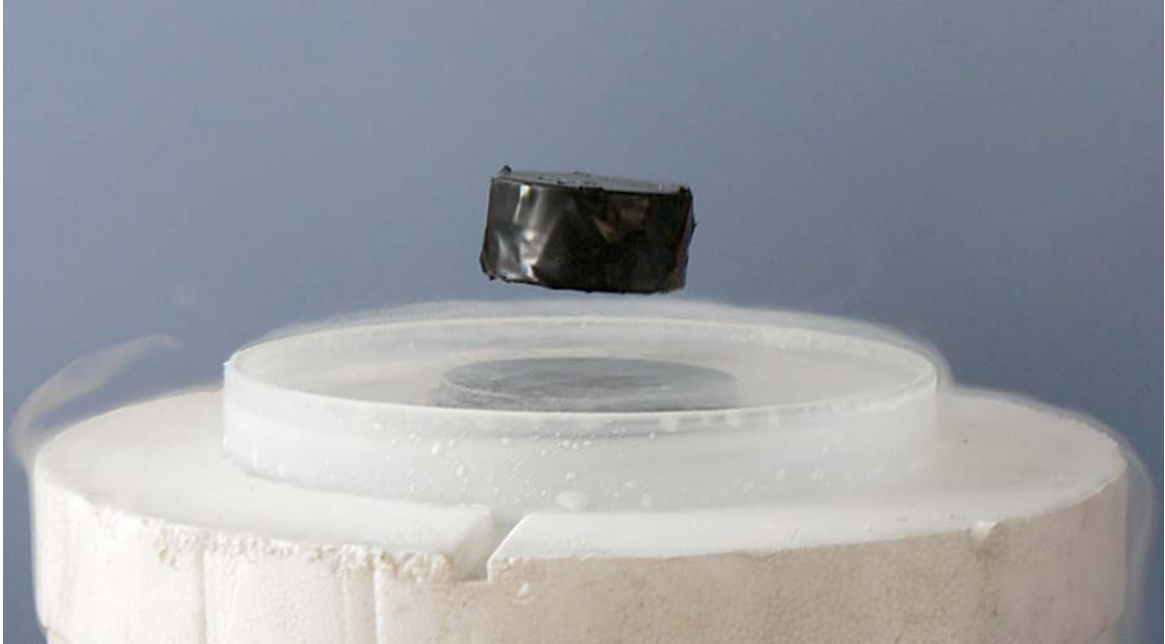


Figure 1.1: A disc magnet floating above a nitrogen cooled sample of Yttrium Barium Copper Oxide (YBCO). Image taken from Wikimedia [3]

effect was a mystery.

The first significant progress on the theoretical side of the field was made when in 1933 Walter Meissner and Robert Ochsenfeld showed that a superconductor expels any external magnetic field from its interior [15]. It was of tremendous importance, since the fact that also magnetic fields present at the time of the superconducting-to-normal transition (sn-transition) are excluded demonstrates that the superconducting state is a true thermal equilibrium state. In this way, Meissner and Ochsenfeld made superconductivity accessible to the theory of equilibrium thermodynamics.

A true understanding of the physical mechanism underlying superconductivity remained elusive until more than two decades after the publication of the Meissner-Ochsenfeld effect. The first significant breakthrough was achieved when the theoretical physicist Lev Davidovich Landau, who had previously worked on the mathematics and general physics of phase transitions, worked together with Vitaly Lazarevich Ginzburg to produce a phenomenological theory of superconductivity known as Ginzburg-Landau theory (GL-theory), which was first published in 1950 [17].

Besides successfully predicting a number of experimental results near the critical temperature, a very important feature of GL-theory was the introduction of a Schrodinger-like wave equation Ψ . From his earlier work, Landau knew that phase transitions were almost always transitions from an ordered to a disordered state. An example would be the melting of a solid crystal: The ordered crystal lattice is replaced by the disordered state of freely moving, uncorrelated atoms or molecules.

In order to be able to perform quantitative work on the basis of these assumptions Ginzburg and Landau introduced the GL-order parameter ϕ . The nature of the order parameter introduced for the sn-transition was unclear, but its relative magnitude was measured by the expectation value of the GL-wave function $\phi \propto \Psi^2$.

Building on GL-theory, Alexei Alexeyevich Abrikosov showed that two different types of superconductors should exist [18]: Those observed by Kammerlingh Onnes and discussed by Meissner and Ochsenfeld, which expel magnetic fields completely from their interior up to a critical field strength above which they revert to the normal state and those which, above a first critical field, would admit some magnetic flux to their interior and then smoothly make the transition back to the normal state with increasing magnetic field. The former class of superconductor was labeled type I, while the latter was labeled type II. In 2003 Ginzburg and Abrikosov shared a Nobel Prize for their combined works.

Yet another vital discovery was made in 1950, one which would lay the foundation for an actual understanding of the physical source of superconductivity, rather than "just" provide a phenomenological framework. Since the initial discovery in 1911 a whole host of materials had been shown to be superconducting at sufficiently low temperature. Maxwell and Reynolds showed [19][20] that the critical temperature varies with the isotopic masses of the constituent elements. This was taken as an indicator that interactions of the conduction electrons with the material's ion lattice might be the source of superconductivity, and led directly to the consideration of electron-phonon interactions in the context of superconductivity. Phonons are quantised vibrations of a material's ion lattice.

The approach of trying to use electron-phonon interactions as a source for superconductivity was finally successful in 1956 when Leon Nathan Cooper [21] showed that electron-phonon interactions lead to an attraction between electrons which, for sufficiently cold electron systems, leads to pairing of spin-antiparallel electrons. These electron Cooper pairs have zero net spin and as such cease to be leptons but become bosons. In consequence they are no longer subject to the Pauli Exclusion Principle (PEP) and all electrons inside the cold volume condense into the same quantum state. In this way the nature of the GL order parameter ϕ and wave function Ψ was discovered: Ψ is the macroscopic wave function of the electrons in the condensed quantum state and the order parameter $\phi \propto \Psi^2$ is the number density of electrons in the superconducting state. All this was expressed in the microscopic theory of superconductivity by Bardeen, Cooper and Schrieffer [22], today known as BCS theory. It was later shown that near T_c the GL equations are a rigorous consequence of BCS theory [4].

One might think that with the advent of BCS theory the mystery of superconductivity was basically solved, but far from it. A multitude of unexpected effects was yet to be discovered and quantified.

Magnetic fields create gradients in the superconducting order parameter, and the order parameter phase changes across electronically weak links (such as point contacts) between superconductors. These weak link effects are known as the Josephson effects, named after Brian David Josephson who predicted their existence in 1962 [23]. Since then, Josephson effects have led to the creation of Superconducting Quantum Interference Devices (SQUIDS), which are the most sensitive magnetic field sensors available today. They are routinely used in research and development, in small-field Magnetic Resonance Imaging (MRI) and Magnetoencephalography (MEG). A MEG allows for the contact-free measurement of a patient's brain activity. Furthermore, SQUIDS are becoming more and more common in industrial applications, and scanning SQUID microscopes are used by the oil industry for prospecting tasks. A good overview of the potential applications of SQUIDS is given by Clarke [24].

Besides the Josephson effect, even the fundamental physics of superconductivity itself was still only poorly understood. It was thought that the intrinsic maximum temperature at which superconductivity could occur was set by BCS theory to be approximately 25 – 30K [25]. This meant that helium would be required as a refrigerant, keeping the cost of operating superconducting equipment too high for bulk industrial exploitation and limiting superconductors to a few specialist research labs and applications. Against this background Johannes Bednorz and Karl Mueller presented in 1986 a superconducting cuprate ceramic compound with a critical temperature of 35K [26]. The compound presented by Mueller and Bednorz was Lanthanum-Barium-Copper-Oxide and the first of the high temperature (high- T_c) superconductors. BCS theory does not apply to this compound and the mechanism for superconductivity in cuprate ceramics is poorly understood even today.

The discovery of high- T_c superconductivity spurred a flurry of research into the subject of finding what is to this day the holy grail of the field: A room temperature superconductor. While no such compound has been found, a different extremely important temperature level has been reached. In 1987 Maw-Kuen Wu at the University of Alabama and Paul Chu at the University of Houston developed, together with their students, the compound Yttrium Barium Copper Oxide (YBCO) [27], which had a critical temperature $T_c \approx 93\text{K}$. This was the first superconductor with a critical temperature above the boiling point of liquid nitrogen (77K), thereby making superconductivity accessible without expensive and sophisticated cryogenic equipment and cooling affordable enough for industry to start taking an interest.

In 1987 the originators of the field of high- T_c superconductivity received a very prompt Nobel prize for their work. To date the record critical temperature, achieved under laboratory conditions under standard pressure, is still held by a cuprate ceramic, with $T_c \approx 138\text{K}$. High- T_c superconductivity will not be considered any further during this thesis for two reasons: The high transition temperature implies a large energy gap Δ_g between the superconducting and normal states which makes

high- T_c compounds unsuitable for the detectors considered in chapter 2, and the absence of a good microscopic quantum mechanical theory means that the applicability of the heavy photon theories developed in chapters 3 to 5 is questionable for high- T_c compounds. However, in the authors opinion an introduction to superconductivity would be incomplete without mention of these interesting materials.

The research following the 1957 breakthroughs was not limited to practical applications of superconductivity. Superconductors themselves proved to be a rich source of fundamental physics. In modern theoretical physics, zero resistance and exclusion of the magnetic fields are just symptoms of something deeper: Modifications to the fundamental form of electromagnetism, changing Maxwell's equations in the presence of superconductors. And, it seems, even new gravitational effects can be observed in the superconducting state [28]. These changes to what we consider fundamental and unchangeable physical principles are explored in more detail in chapters 3, 4 and 5, along with some of their consequences.

1.1.2 Basic Properties of Superconductors

In this section the basic properties of superconductors are established, along with some of the mathematical background required to make meaningful qualitative and quantitative assessments of problems involving superconductors. The only types of superconductors considered will be low temperature (low- T_c) superconductors. While of great scientific and industrial interest, high- T_c systems are poorly understood and, as already mentioned in the introduction, the underlying theory (as far as it is known) makes them unsuitable or just plain difficult to deal with in the context of the ideas and devices considered in the course of this work.

1.1.2.1 Zero resistivity, the Order Parameter and Critical Temperature

The property that has given superconductivity its name is that of zero electrical resistance. According to Gallop [29], of the 75 metals (single element and alloy) tested before 1991 the resistivity of 28 will drop to zero discontinuously below a critical temperature T_c . Below T_c dissipationless supercurrents will flow without any applied voltage, up to a total critical magnitude I_c .

The specific heat of any material that can be made to go superconducting has a discontinuous jump at T_c , called the lambda anomaly due to its distinct shape (figure 1.2).

The sn-transition has zero latent heat in the absence of an external magnetic field. Thus, with no external field applied, the sn-transition is a true second order transition. Second order transitions

Specific Heat vs Temperature

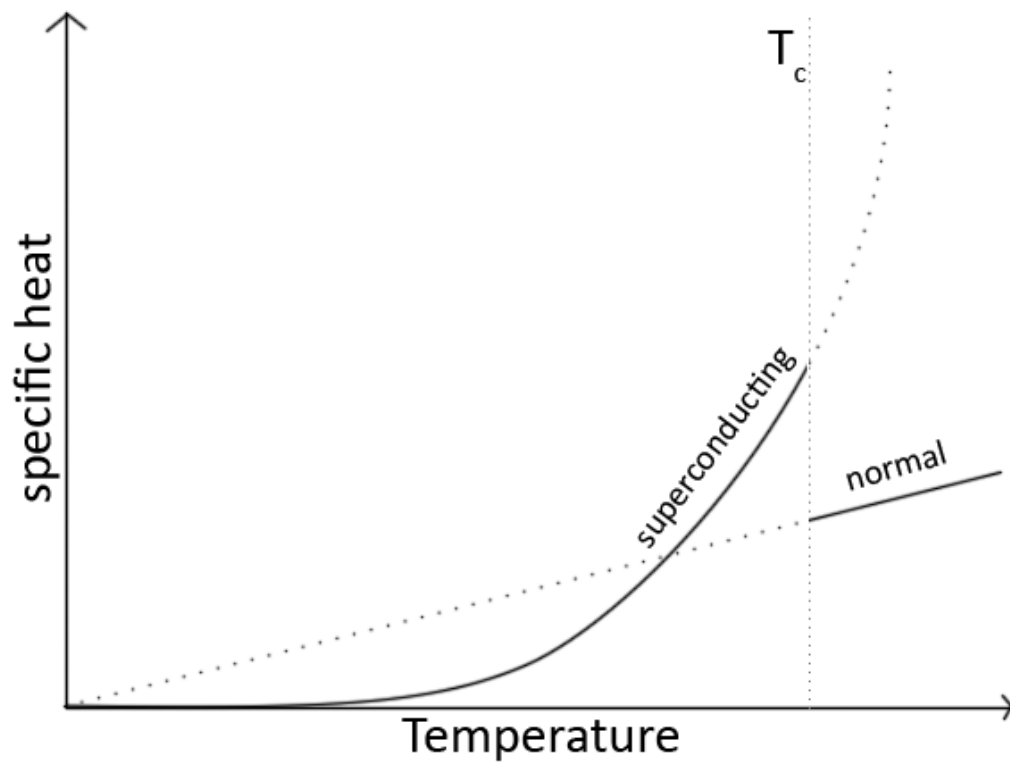


Figure 1.2: Discontinuity in specific heat at sn-transition temperature (lambda-anomaly). The dotted lines are extrapolation of the respective superconducting and normal state heat capacities and are merely provided as a guide to the eye. Sketch according to [4].

are those with no latent heat and no mixed phase associated with it: The entire volume changes phase at the same time. In the case of an external magnetic field, the field expanding into a material going from the superconducting into the normal state will absorb thermodynamic heat and thus add a non-zero latent heat to the transition. Consequently, a mixed phase may exist in the presence of an ambient magnetic field. This effect will become important for the discussion of the percolation noise in transition edge sensors in section 2.3.3.

In 1934 Hendrik Brugt Gerhard Casimir and Cornelis Jacobus Gorter were investigating the current carrying characteristics of superconductors and found that the behavior of a superconductor could be described by two separate electron populations, one in the normal state and one in the superconducting state, interpenetrating each other freely. This model is known today as the Gorter-Casimir two fluid model. According to the two fluid model, the fraction x of electrons in the superconducting state varies with temperature T and critical temperature T_c of the superconductor and is given by [29]:

$$x(T) = 1 - \left(\frac{T}{T_c}\right)^4 \quad (1.1)$$

The fact that this result holds today is remarkable, since the two fluid model was developed in 1934, before either GL-theory or BCS-theory had managed to shed any light on the fundamental physics behind superconductivity, and Gorter and Casimir had no concept at all about the nature of the superconducting state their equation was describing.

Trying to find a better way to describe the sn-transition than the dimensionless fraction x we turn to GL-theory. This theory assumes that superconducting electrons are governed by a Schroedinger-like macroscopic wave function Ψ and that the density of superconducting electrons can be calculated as $|\Psi|^2$. From equation (1.1) at $T = 0$ all the electrons in the sample are in the superconducting state, yielding $|\Psi_0| = x(0)^{1/2}$. Thus we have found the temperature dependence of the macroscopic wave function governing the superconducting electrons for the spatially homogeneous steady state:

$$\Psi(T) = \Psi(0) \left(1 - \left(\frac{T}{T_c}\right)^4\right)^{1/2} \quad (1.2)$$

The variation of the wave function $|\Psi| > 0$ with temperature T has been plotted in figure 1.3.

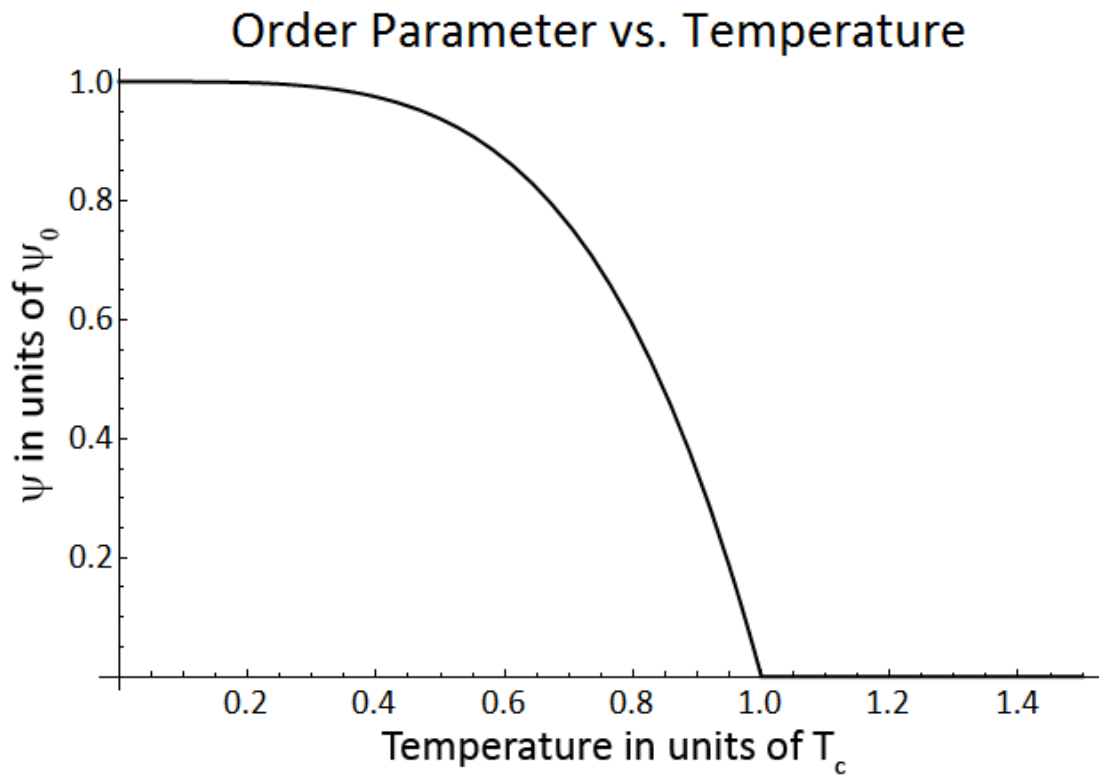


Figure 1.3: Variation of macroscopic wave function $|\Psi|$ with temperature T according to equation (1.2). The density of superconducting electrons is given by $|\Psi^2|$.

1.1.2.2 Magnetic Properties of Superconductors

When in 1933 Walter Meissner and Robert Ochsenfeld investigated the magnetisation of a superconducting sample they made two very important discoveries [15]:

1. When a magnetic field is applied to a superconductor the induced supercurrents create an equal and opposite induced field, causing $\vec{B} = 0$ inside the superconductor.
2. Even an applied field present at the time of cooling across sn-transition is expelled.

The Meissner effect demonstrates that superconductivity can be treated as a true thermodynamic equilibrium state: Below T_c it is energetically favorable for the material to make the transition into the superconducting state, doing work to expel the present magnetic field from the interior of the bulk. It is indeed possible to draw a phase diagram for a potentially superconducting material onto the $H - T$ plane, and mapping a coordinate space for which the material is superconducting (essentially the area under the graph of figure 1.4a). Thus the superconducting state is a thermodynamic state of specific energy $\Delta_g(T)$ below the normal state. The exclusion of magnetic flux is equivalent to the material becoming a perfect diamagnet (magnetic susceptibility $\chi = -1$) below T_c .

The Meissner-Ochsenfeld effect was the first significant progress towards a quantitative theory of superconductivity. While the Meissner effect in itself offered no new insights into the actual nature of the underlying processes it demonstrated that the sn-transition obeys equilibrium thermodynamics. As such it opened the door to theories of phase transition, such as Ginzburg-Landau theory (described in section 1.1.2.4) which greatly added to our understanding. Despite the fact that today the sn-transition is fairly well understood (for classical low- T_c superconductors) and known to be a quantum mechanical process, thermodynamics remains an important theoretical tool since it offers an algebraically tractable alternative to the difficult full quantum mechanical treatment. Therefore an understanding of the magnetic properties of the superconducting state is extremely important if one is to understand superconductivity.

Before discussing the magnetic properties of a superconductor mathematically it is important to establish some of the symbols and naming conventions that sometimes cause confusion in this context. Maxwell's equations define two magnetic vectors, \vec{B} and \vec{H} . The vector \vec{H} is known in the literature as the "magnetic field strength" or "magnetic field intensity", while \vec{B} is generally referred to as the "magnetic induction" or, casually, as the "magnetic field". Inside any sample magnetization currents and spin alignment will influence \vec{B} but not \vec{H} . Throughout this work "magnetic field" will refer to \vec{B} while "applied field" or "magnetic field intensity" will refer to \vec{H} .

Expelling the magnetic field from the interior of the bulk requires an amount of work $W_{expel} = \frac{1}{2}\chi H^2$. When $W_{expel} > \Delta_g(T)N(k_B T)$ it becomes favourable for the material to revert to its normal state. Here, $N(k_B T)$ is the density of states at energy $k_B T$. The thermodynamics of the superconducting equilibrium state are discussed in more detail in section 1.1.2.3.

The critical field \vec{H}_c can be shown to vary with temperature as [4]:

$$H_c = H_c^0 \left(1 - \frac{T^2}{T_c^2}\right) \quad (1.3)$$

where superscript 0 denotes the critical field at zero temperature. This convention will be kept throughout the work presented: When applied to the magnetic field a superscript 0 indicates zero temperature, while applied to the temperature a superscript 0 indicates zero applied field.

The magnetic field does not drop to zero discontinuously at the boundary of the superconducting sample. Instead, the induced surface currents force it to decay exponentially over a characteristic distance known as the London penetration depth λ_L [4], resulting in the expression:

$$B(x) = B(0) \exp(-x/\lambda_L) \quad (1.4)$$

where $B(0)$ is the magnetic field at the surface of the superconductor and x is the distance from the surface.

The penetration depth λ_L is typically of order 10 – 50 nm for a low- T_c superconductor and can be calculated from the material parameters and fundamental constants [4]. It scales as $\lambda_L \propto 1/\sqrt{n_s}$ where n_s is the number density of superconducting electrons, so that equation (1.1) can be used to obtain the temperature variation of λ_L :

$$\lambda_L(T) = \lambda_L(0) \left(1 - \left(\frac{T}{T_c}\right)^4\right)^{-1/2} \quad (1.5)$$

The temperature variations of the penetration depth λ_L and the critical field H_c are plotted in figure 1.4.

The second major macroscopic magnetic effect observed is the fact that any rotating superconductor generates a magnetic field. This is known as the London Moment, and the field generated at the cross section of the axis of rotation R with the surface of a superconductor symmetrical about R can be found to be [30]:

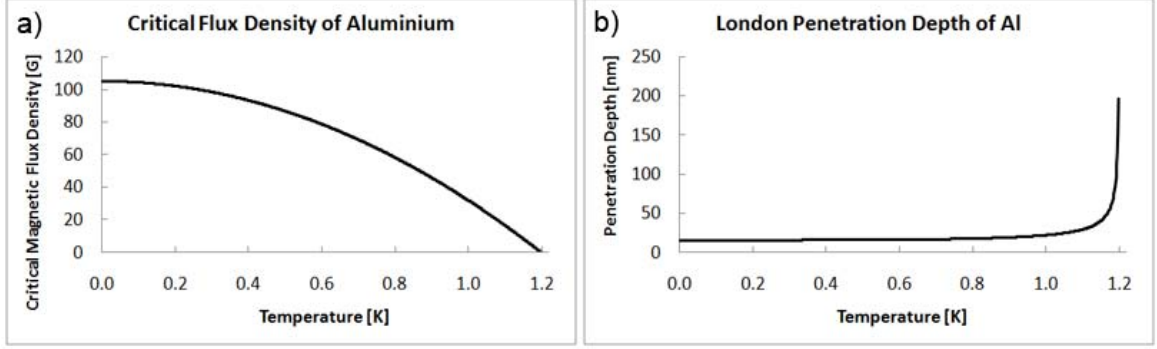


Figure 1.4: Temperature variation of a) critical field according to equation (1.3) and b) penetration depth in aluminium ($T_c = 1.2K$ [5]) according to equation (1.5).

$$\vec{B}_L = -2c \frac{m^*}{e^*} \vec{\omega} \quad (1.6)$$

where m^* and e^* are the effective mass and charge respectively of superconducting electron pairs (Cooper pairs, see sec.1.1.2.5) and $\vec{\omega}$ is the angular momentum vector.

1.1.2.3 Basic Equilibrium Thermodynamics and the Superconducting Energy Gap

This section contains a brief introduction on how to use thermodynamic equalities to derive parameters of the superconducting state. It will demonstrate how magnetic field exclusion and the existence of a critical field can be used to calculate the value of the energy difference between the normal and superconducting states, known as the condensate energy ϵ_{cond} , a result that will be important for sections 2.3.3.2 and 3.2.1 in order to discuss percolation noise in transition edge sensors and the influence of the quantum vacuum on the sn-transition, respectively.

The Gibbs free energy G of a system is a thermodynamic equality expressing the total amount of thermodynamically available energy ("free energy") of a system as a function of its thermodynamic parameters and its general differential form is given by [4]:

$$dG = dU - SdT - \vec{M} \cdot d\vec{H} \quad (1.7)$$

where U is the thermal energy of the system, S is the entropy of the system, \vec{M} is the magnetisation and \vec{H} is the magnetic field.

It is possible to calculate the change in Gibbs free energy of a superconducting system G_s when a magnetic field \vec{H} is introduced by integrating the last term on the right hand side of eq.(1.7). To-

tal magnetic field exclusion, also known as perfect diamagnetism, means that the superconducting volume is magnetised with susceptibility $\chi = -1$, yielding [4]:

$$G_s(H) = G_s(0) - \int_0^H \vec{M} \cdot d\vec{H} = G_s(0) + \frac{1}{2}\mu_0 H^2 \quad (1.8)$$

where G_s is the Gibbs free energy of the sample in the superconducting state, \vec{H} is the applied external field and \vec{M} is the magnetisation. The integral $\int_0^H \vec{M} \cdot d\vec{H}$ determines the amount of work done excluding the field.

We assume that the magnetic susceptibility of the normal state is negligible ($G_n(H) = G_n(0)$). If the external field H reaches the critical field H_c superconductivity breaks down. At the critical field the Gibbs free energy of the normal and superconducting states is equal ($G_n(H) = G_s(H)$) allowing us to write:

$$G_n(H = 0) - G_s(H = 0) = \frac{1}{2}\mu_0 H_c^2 \quad (1.9)$$

The left hand side of equation (1.9) is the difference in energy between the superconducting and normal state of any type I superconductor. This energy difference between the normal and superconducting states is the condensate energy ϵ_{cond} :

$$\epsilon_{cond} = \frac{1}{2}\mu_0 H_c^2 \quad (1.10)$$

The condensate energy is ϵ_{cond} is usually of order of a few tens of Joules per unit volume [31].

The microscopic quantity corresponding to the condensate energy ϵ_{cond} is the superconducting energy gap Δ_g . The energy gap Δ_g is the energy difference between the normal fermionic state and the superconducting state for an individual electron.

The magnitude of Δ_g is approximately proportional to the critical temperature T_c [4] and is generally small: For Aluminium ($T_c = 1.2K$) the energy gap $\Delta_g = 180\mu eV$ [5].

Equation (1.8) yields the Gibbs free energy of the system per unit volume. Consequently, in the above derivation all energies are specific energies per unit volume.

1.1.2.4 Ginzburg-Landau Theory and Coherence Length

At its core, GL-theory is a theory of second order phase transitions from an ordered to an disordered state [17]. An order parameter ϕ is at a maximum for $T = 0K$ and is smoothly reduced to zero as $T \rightarrow T_c$. One of the major achievements of GL-theory was to correctly identify the order parameter as the number density of electrons in the superconducting state so that $\phi \propto \Psi^2$.

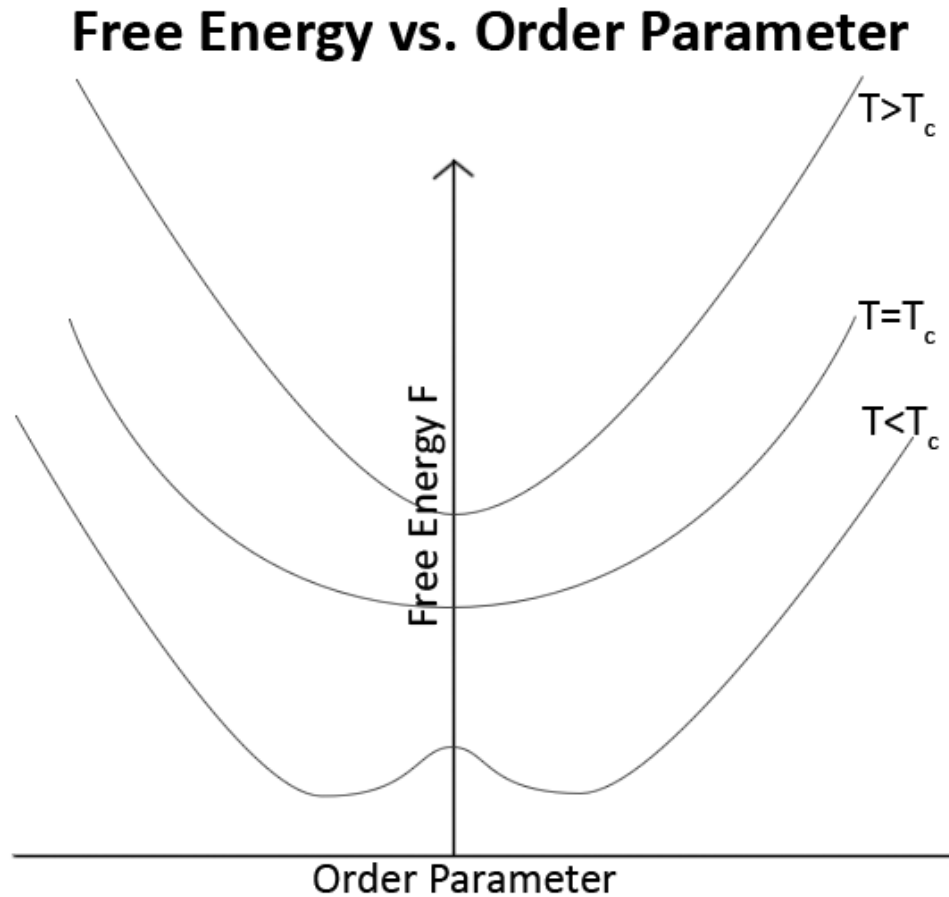


Figure 1.5: As the temperature decreases the minimum energy configuration of the system changes from $\phi = 0$ to $|\phi| > 0$. Generally ϕ is a complex number, with the modulus of ϕ determining the number density of superconducting electrons and the argument of ϕ determining the phase of the macroscopic wave function. In the diagram above positive and negative ϕ are in anti phase.

The two core assumptions of GL-theory were that

1. where ϕ is small the Helmholtz free energy F of the system can be expanded as a power series in ϕ and
2. The coefficients in the power series can themselves be expanded as a power series in $T - T_c$

When the system is in the normal state the only minimum in the Helmholtz free energy F can be found at $\phi = 0$, i.e. the fraction of electrons in the superconducting state is zero. As the system is cooled down this minimum becomes more and more shallow until it is turned into a local maximum, causing the system to adopt a state with $\phi \neq 0$, as illustrated in figure 1.5.

Just below the transition temperature superconducting films can still exhibit resistivity due to vari-

ous magnetic phenomena, such as flux flow or vortex flow resistivity (section 2.3) and consequently it can sometimes be difficult to determine the temperature at which the actual transition to the superconducting state occurs. It is possible to define the point of transition rigorously from the superconducting to the normal state from figure 1.5. The transition occurs when the minimum of the free energy F occurs for an order parameter $|\phi| > 0$.

Taking into account the kinetic energy of the superconducting electrons and various quantum mechanical boundary conditions the Helmholtz free energy per unit volume (specific free energy) f can be calculated by power series methods [4]:

$$f(\vec{r}) = f_n + \alpha(T)|\Psi(\vec{r})|^2 + \frac{1}{2}\beta|\Psi(\vec{r})|^4 + \frac{\hbar^2}{2m}|\nabla\Psi(\vec{r})|^2 \quad (1.11)$$

where α and β are coefficients of the power series expansion of Ψ . For the full derivation of equation (1.11) the reader is referred to Tilley and Tilley [4]. We introduce eq.(1.11) at this point to illustrate the reason for the existence of a superconducting coherence length.

Close inspection of (1.11) shows that variations of the order parameter in space cannot be infinitely sharp: The gradient term in (1.11) introduces an energy cost for variations in the order parameter that increases with increasing spatial derivative. This can be shown [4] to result in the second characteristic distance for superconductors (in addition to the London penetration length λ_L), the coherence length $\xi(T)$. The magnitude of the coherence length $\xi(T)$ indicates the minimum distance over which the superconducting order parameter ϕ will vary. This parameter will be important for the discussion of transition edge sensor noise dynamics (section 2.3).

Despite the fact that GL-theory is "only" a phenomenological theory it has been extremely successful in predicting experimental results, and it can be shown [4] that near the critical temperature of a superconductor GL-theory is a rigorous consequence of the microscopic BCS theory. Since GL-theory is mathematically far more tractable than BCS theory it is still in common use.

1.1.2.5 Cooper Pairs and Microscopic Theory

In 1950 H. Froelich proposed that interactions between electrons and phonons (quantized vibrations of the ion lattice) might actually lead to a nett attractive force between electrons at sufficiently low temperatures [32]. This pairing force would depend on the isotopic masses of the ions making up the material and might be partly responsible for superconductivity. In 1956 Cooper managed to solve the Schroedinger equation describing electrons interacting via the phonon exchange mechanism proposed by Froehlich and came to the conclusion that the attractive force did indeed exist and could

overcome Coulomb repulsion at roughly the right temperatures in order to be connected to superconductivity [21]. Hence superconducting electron pairs are known as Cooper pairs. In order for pairing to occur, two spin-antiparallel electrons with approximately antiparallel momentum vectors of equal magnitude are required. The bound pair has resultant spin zero, and as such is no longer governed by the Pauli exclusion principle. While the normal state electrons in a material are supported against collapse into a single quantum state, any number of Cooper pairs can occupy the same quantum state (i.e. have identical quantum numbers). The binding energy of Cooper pairs is $2\Delta_g$, i.e. the energy required to return both paired electrons to a normal state energy level.

The final break through for a true understanding of the superconducting state however was made by Bardeen, Cooper and Schrieffer when they showed that phonon coupling had to be considered between all the available electrons, causing them to condense into a single quantum state described by the macroscopic wave function of GL theory.

1.2 Thesis Organization

Following this quick introduction to superconductivity, this section is provided as an outline of the work which is presented herein. It is believed that the reader will find the considerations and derivations presented easier to follow if he is equipped with a clear idea of where they are going to lead and how they will tie into the rest of the thesis.

We begin by considering the most popular forms of superconducting radiation detectors in chapter 2. It is demonstrated how most superconducting detectors rely on the properties of the sn-transition to achieve their remarkable working characteristics. In the course of this consideration we take a closer look at the "excess noise" phenomenon encountered in Transition Edge Sensors (TESs) and perform a thorough investigation of the mechanisms responsible for it.

This consideration of excess noise illustrates the susceptibility of the sn-transition to small magnitude fields and energy variations, such as the movement of a single magnetic flux quantum across a thin superconducting film (section 2.3.2). This prompts us to consider quantum mechanical vacuum fluctuations in our search for possible mechanisms which may influence the physics of the sn-transition (chapter 3). During the investigation of the coupling mechanisms between the quantum vacuum and the superconducting-to-normal transition we find that current theory evaluating the influence of vacuum fluctuations on superconductors uses an inappropriate theory of electromagnetism. In section 3.2 a possible coupling mechanism between superconducting detector performance and the quantum vacuum is discussed. In section 3.4 the approximate magnitude of the change in STJ energy resolution as a result of vacuum fluctuations is found.

While it has not been possible to link vacuum fluctuations directly to excess noise, our investigation into the theory of electromagnetism suitable for analysing the behavior of photons near to (or inside) a superconductor leads directly to the consideration of non-zero rest mass photons in chapter 3. We find in chapter 4 that the equations which govern such massive electromagnetism allow for the creation of a new kind of optics technology, which we call "Heavy Photon Optics". The possible implications and practical applications of this technology are discussed, along with the equations required for a quantitative evaluation of the performance of Heavy Photon Optics devices.

The manifold applications of Heavy Photon Optics prompt a more thorough investigation of the mechanism that allows the gauge bosons of the electromagnetic field (i.e. photons) to acquire a rest mass. This investigation then leads to a derivation of a similar mechanism for the hypothetical gauge field of gravity in chapter 5, and yields a theory predicting the existence of non-zero rest mass spin-1 gravitons. The resulting theory also predicts the flux of the frame dragging field to be quantised and derives a quantitative expression for the gravitoelectromagnetic flux quantum. Chapter 5 concludes with speculations as to the applicability of massive spin-1 gravity to neutron stars and the consequences.

Finally, Chapter 6 will provide a summary of conclusions for the work performed herein.

At times the order in which some of the topics are presented may appear odd. It might have been more logical to first perform a systematic analysis of the Higgs mechanism in superconductors, followed by a discussion of the optical and electrodynamic properties of any medium in which non-zero rest mass electromagnetism exists. From this basis heavy photon optical elements and the Casimir effect could have been discussed, with an excursus into detector technology at the end. However, the order in which the work is presented is the order in which it has been performed. It is believed that the way in which the analysis of one topic seamlessly lead to research into another has an additional and worthwhile story to tell, about the way that research into superconducting devices and superconductivity has an incredible potential for creating links back and forth between what are traditionally considered deeply theoretical topics, such as quantum electrodynamics and the Higgs mechanism, and practical applications such as superconducting particle detectors and the (at this point speculative) heavy photon optical elements developed in Chapter 4.

Chapter 2

Superconducting Particle Detectors

Our investigation of superconductivity begins with a look at the superconducting particle and radiation detector technologies available today. Cryogenic photon and particle detector technologies can provide energy resolutions far superior to those afforded by semiconductor based systems. Ground based astronomy using arrays of superconducting tunnel junctions is providing ultrahigh energy resolution imaging spectroscopy [33] and transition edge sensors are used in a bid to detect the Weakly Interacting Massive Particles (WIMPS) which are a possible candidate for the nature of dark matter [34]. Thus transition edge sensors may provide a window onto a physical phenomenon that was hitherto entirely undetectable. Furthermore, the field of superconducting detectors is a suitable entry point into the topic of the superconducting-to-normal transition since between them the plethora of available detectors exploit all the fundamental characteristics of the sn-transition.

When making and operating superconducting detectors of any kind the constraints on the operating temperature and the magnetic environment are formidable, and even today, almost 100 years after the advent of superconductivity, producing a working detector is not a trivial task. Often operating temperatures significantly below $1K$ are required and shielding of any magnetic fields above tens of nT may be necessary [5] [6]. If an array of superconducting detectors is to be made, for example to produce a camera, even more problems arise. Many types of superconducting detectors are not easily multiplexed, requiring an enormous number of wires for even moderate imaging resolutions, and often precise (of order $\pm 10^{-5}T$ [5]) control of the applied magnetic field is required. The challenge to provide sufficiently accurate control over the magnetic field is further enhanced if a detector array providing imaging or spatially distributed read-out capacity is required, since the correct field has to be provided for each individual pixel.

Against the background of progressively cheaper semiconductor imaging devices, such as Comple-

mentary Metal Oxide Semiconductor (CMOS) or Charge Coupled Device (CCD) cameras, the question is what possible advantages superconducting detectors could bring that would outweigh the difficulties involved in fabricating, cooling and operating them. The answer is to be found in the very mechanisms fundamental to superconductivity. In one way or another all superconducting detectors exploit the very small energy gap Δ_g between the normal and superconducting states which is coupled to massive changes in electromagnetic properties (transition to zero resistance and total field exclusion). As such, the usefulness of superconducting detectors is almost a direct consequence of the low temperatures at which superconductivity occurs. If superconductivity occurred at higher temperatures this would imply a larger energy gap between the superconducting and normal states, in order to prevent thermal excitation of electrons across the gap.

The small energy gap between the superconducting and normal states means that even tiny variations in particle energy can be detected (resolving powers in excess of $R = 2000$ are available at photon energies of $2.5eV$ [35]), allowing for the fabrication of spectrometers which are of unprecedented energy resolution and sensitive to even a single photon. Such photon counting ultra high resolution spectrometers have a huge range of potential applications, from the purely scientific to the applied medical or industrial. Superconducting detectors are baselined for the Narrow Field Imager (NFI) on the X-ray Evolving Universe Spectroscopy mission (XEUS)[36] and the ultrahigh resolution read-out of biomedical research assays is set to revolutionize the biomedical engineering industry [37].

Two principal categories of superconducting spectrometers exist which are divided by their fundamental method of detecting and measuring energy deposited in the detector:

1. Particle counting detectors such as Superconducting Tunnel Junctions (STJs) exploit the low superconducting-normal energy gap (Δ_g of order meV) by counting the large number of electrons lifted from the superconducting into the normal state when a quantum of energy is deposited in the detector. The superconducting energy gap Δ_g is approximately 1000 times smaller than the semiconductor energy gap (which is of order eV) [5] and consequently 1000 times as many particle excitations occur as would be the case in a semiconducting detector. This means that the superior statistics of the STJ yield a much better full-width half-maximum (fwhm) energy resolution (about 30 times higher than semiconductor based energy resolutions [5]).
2. Equilibrium calorimeters such as Transition Edge Sensors (TESs) and Metallic Magnetic Calorimeters (MMCs) make use of the rapid change of electromagnetic parameters (resistivity and magnetic susceptibility) with changes in temperature of a sample material [1] [38]. In the case of TESs this is the rapid change of resistivity with temperature in the region of the sn-transition,

while in the case of MMCs it is the change in magnetisation with temperature of a metallic sample. Even the energy deposited by a single photon will cause a sufficiently large response to allow for much better fwhm energy resolution than any semiconductor based detector.

Strictly speaking an MMC is not an inherently superconducting detector. The magnetic sample is in the normal state. The superconducting component of an MMC is the SQUID magnetic field sensor, able to detect minute changes in sample magnetisation.

During the following discussion of basic superconducting detector types we will come across the concept of "excess noise" in TESs, a type of white noise originating inside TES type detectors which is little understood. The wish to improve the energy resolution of TES type devices, and some curiosity to find an explanation for an insufficiently explained phenomenon (independently of possible applications), leads to an in-depth investigation of the excess noise phenomenon (section 2.3). In the course of this investigation we develop some physical and mathematical concepts that can be of help in the analysis of excess noise experimental data and motivate a more in-depth look at the fundamental physics of the sn-transition. In this way a very practical interest (suppression of excess noise) will lead us to investigate the much more fundamental concepts of modifications to the vacuum energy, non-zero rest mass photons and massive spin-1 gravity, discussed in chapters 3 to 5.

2.1 Types of Superconducting Detectors

2.1.1 Superconducting Tunnel Junctions

Superconducting Tunnel Junctions (STJs) are particle counting detectors making direct use of the small superconducting-normal energy gap Δ_g [5]. They consist of two superconducting films (thickness \approx tens - hundreds of nm) separated by a thin (\approx 1nm) insulating barrier. A small bias voltage (\approx 100 – 500 μ V) is applied across the barrier. A photon absorbed in the cathode will excite a number of Cooper pairs across the energy gap Δ_g into their normal electron states. These normal electrons are known as quasiparticles since, if the device is in the superconducting state, they can only exist by absorbing energy from an external source. As soon as the quasiparticles lose their excitation energy to their surroundings they will decay back into the Cooper pair state. The quasiparticles created by a photon absorption event have sufficient energy to tunnel across the barrier into the anode. The resulting tunneling current can be measured and by integrating it the total tunneling charge can be calculated. In this way it is possible to determine the number of quasiparticles created in the photon absorption event. If we assume that all the photon energy is used to create quasiparticles the photon energy and number of quasiparticles n can be related by $n = E_{ph}/2\Delta_g$. The basic working principle

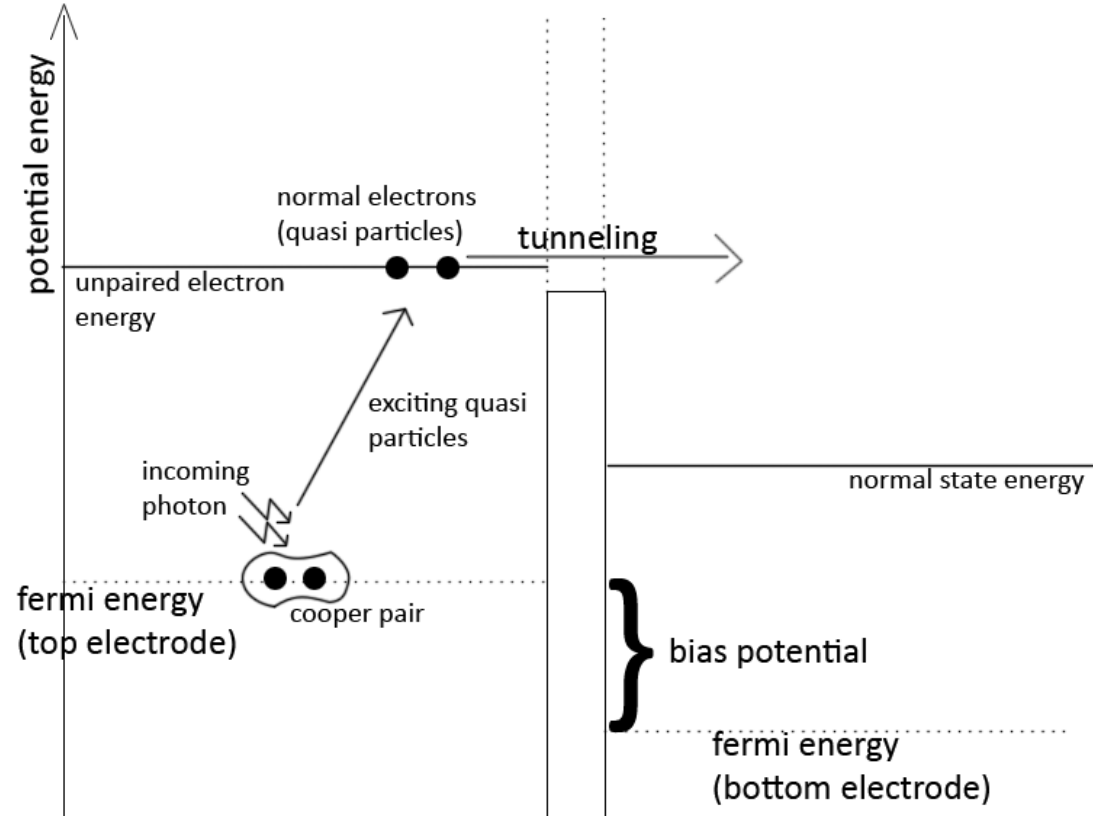


Figure 2.1: Basic working principle of an STJ: an incoming photon is absorbed in the top electrode and breaks a Cooper pair, creating two quasi particles. Due to the bias voltage across the potential barrier these quasi particles can now tunnel across the barrier into the bottom electrode where they can be counted. The number of quasi particle charges created depends linearly on the energy of the incoming photon. Diagram after Polushkin [6].

of an STJ is illustrated in figure 2.1. However, figure 2.1 is simplified significantly and only serves to illustrate the basic working principle of a STJ. In a real device quasi particles or holes may back-tunnel across the barrier, and contribute a number of times to the statistical processes governing STJ energy resolution [5].

As such, the basic working principle of an STJ is similar to that of Si-based photo diodes: The incoming photon excites a number of particles proportional to its energy, and by integrating the resulting current the number of excited particles, and consequently the absorbed photon energy, are inferred. However, in semiconducting devices the excitation process is that of normal state electrons across the semiconductor bandgap, which is typically of the order of a few eV [6]. By contrast, the superconducting-normal energy gap Δ_g is of order meV , resulting in ≈ 1000 times more excitation events inside a superconductor.

Since the excitation and decay of excited particles is a statistical process an intrinsic statistical limit exists for the best energy resolution that can be achieved with a particle counting detector. The intrinsic statistical energy resolution of a particle counting spectrometer is given by [5]:

$$\Delta E = 2.355\sqrt{1.7F\Delta_g E_{ph}} \quad (2.1)$$

where the Fano factor $F < 1$ (typically ≈ 0.2 [5]) results from the fact that particle excitation is not a purely statistical process but governed by physical restrictions and interactions and the factor of 2.355 results from the conversion from Root Mean Square (RMS) energy resolution to fwhm resolution. The factor of 1.7 has been introduced since the average energy necessary to create a quasi particle is about 15% smaller than $2\Delta_g$ [5]. From equation (2.1) the intrinsic best energy resolution scales as $\Delta E \propto \sqrt{\Delta_g}$. Since the energy gap for the sn-transition is three to four orders of magnitude smaller than that for the Si bandgap [5], the intrinsic statistical resolution limit of an STJ is about 30 – 100 times better than that for any semiconducting detector.

2.1.2 Transition Edge Sensors

Much research is currently dedicated to investigating thermal equilibrium calorimeters based on Transition Edge Sensors (TESs). Ideal thermal equilibrium calorimeters consist of a thermometer perfectly coupled to an absorber of heat capacity C and a heat reservoir at temperature T_0 coupled by a weak link of thermal conductivity G to the absorber. Any event depositing an amount of energy ΔE in the absorber automatically raises the absorber temperature by an amount ΔT . The temperature in the absorber then decays exponentially back to its equilibrium value of T_0 with a time constant $\tau = \frac{C}{G}$. By detecting this temperature pulse it is possible to accurately determine the amount of energy deposited by the event.

The role of a TES is that of a high sensitivity thermometer. In reality the sn-transition is not infinitely sharp but spans a region of typically $5 - 10mK$ width [7] and a TES consists of a thin film whose temperature is balanced inside this transition region. In this way even minuscule variations in temperature will result in large changes in device resistivity which can be read out by a Superconducting Quantum Interference Device (SQUID). The steep gradient of the resistance vs. temperature curve (figure 2.2) allows for the accurate determination of small temperature changes in the absorber while the greatly diminished heat capacity at low temperature increases the temperature change per unit energy deposited and allows for fast response times while helping to limit thermal fluctuation noise through the link with the heat bath[39]. A basic sketch of a TES working set-up is provided in figure 2.3.

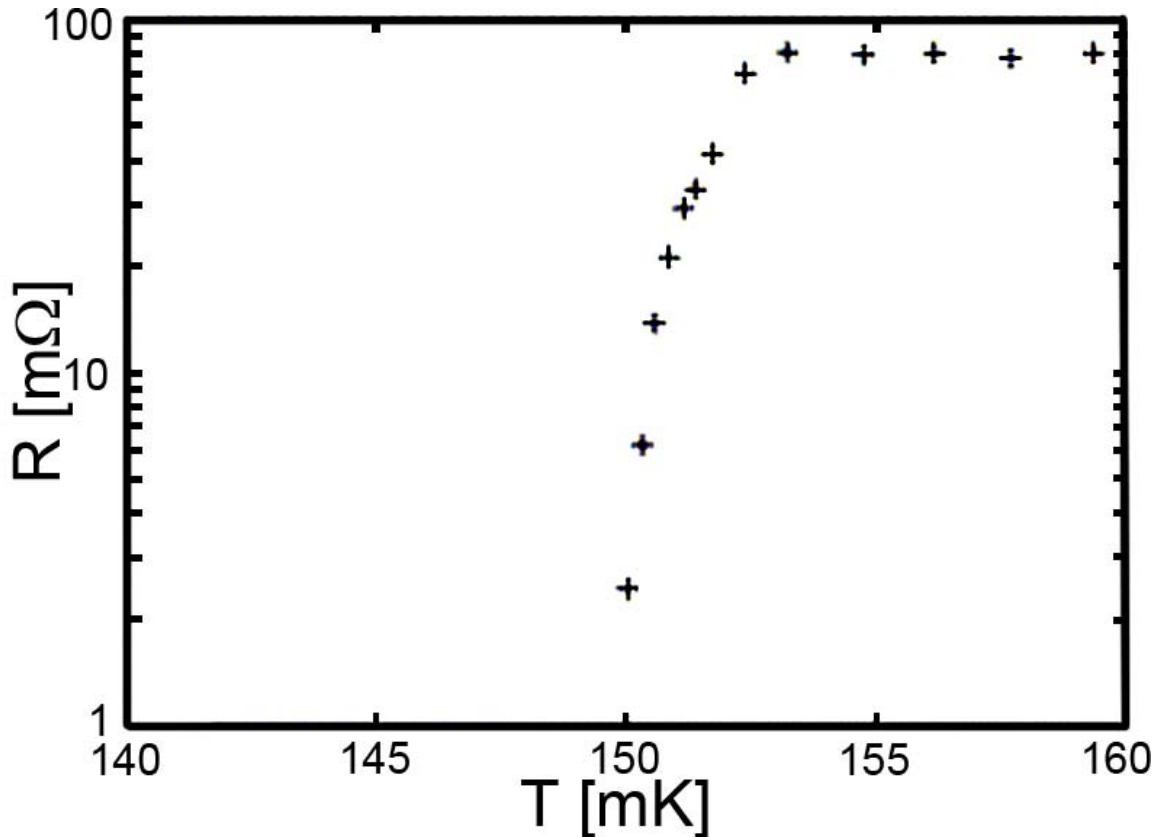


Figure 2.2: Experimental resistance vs. temperature curve of a TiAu bilayer TES in the sn-transition region. Data taken from Takei [7]

One advantage of TES based equilibrium calorimeters is the possibility to operate them in negative feedback mode: Since the ohmic resistance of the TES is not zero, any applied constant bias voltage will give rise to a bias current causing ohmic heating. The equilibrium temperature T_0 is determined by the ohmic heating from the bias voltage. If the TES resistance increases as a result of an increased temperature, the bias current is reduced and ohmic heating is lessened, causing the temperature to decay with the feedback time constant $\tau_f < \tau$. The possibility to use negative voltage feedback to return the TES to its equilibrium temperature T_0 is one of the reasons that the TES time response is much faster than that of a Metallic Magnetic Calorimeter (section 2.1.3).

In contrast to calorimeters, particle counting detectors such as Si-based semiconductor detectors or even STJs have an intrinsic energy resolution limit determined by the statistics of the particle creation process. There are no possibilities to improve the detector resolution beyond this value. For example, the limiting resolution for an Si semiconductor detector is $118eV @ 6keV$ [39]. Thermal equilibrium calorimeters have, at least theoretically, no such intrinsic limit [39]. Their energy resolution is generally limited by imperfections in thermal coupling or various forms of statistical thermodynamic noise which depends on the design details of the system [40] and can be improved by engineering efforts.

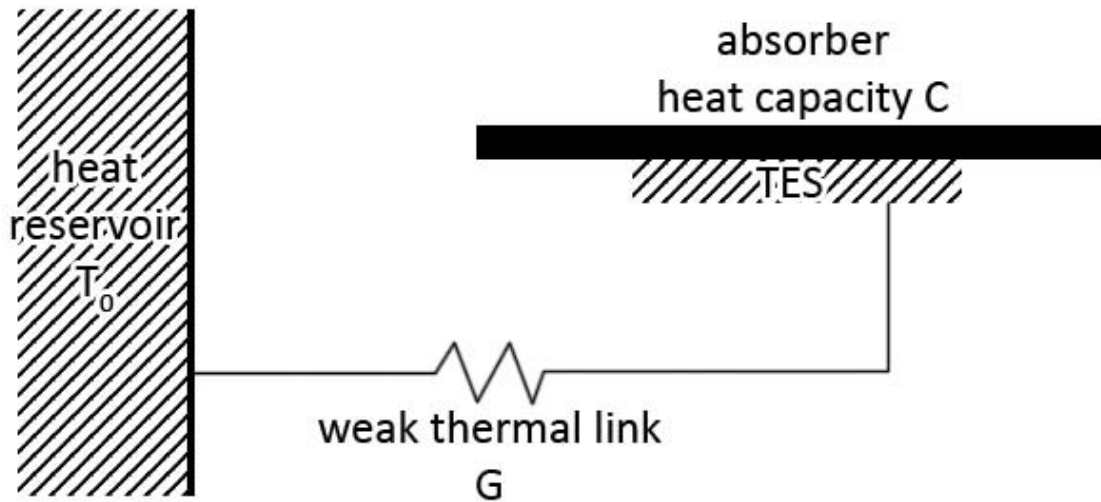


Figure 2.3: Sketch of a basic TES setup. Photons are stopped by the absorber and the thermal energy diffuses from the absorber into the TES. The TES resistance increases as a consequence of the change in temperature, which decays exponentially back to its equilibrium state as thermal energy diffuses through the weak thermal link G and returns the TES and absorber to their equilibrium temperature T_0 .

In 2004 Hoevers et al. [35] report the energy resolution of their TiAu bilayer TES as $2.5eV @ 5.9keV$.

2.1.3 Metallic Magnetic Calorimeters

The basic working principle of Metallic Magnetic Calorimeters (MMCs) is similar to that of TESs: incoming particles deposit their energy in an absorber. The deposited energy then diffuses into the sensor material through a strong thermal link. The sensor material in turn is coupled, via a weak thermal link, to a heat reservoir, returning it to a specified equilibrium temperature after a setup specific relaxation time, with the detector acting as a sensitive thermometer. Thus a MMC, just like a TES, is an equilibrium calorimeter and as such not limited by particle counting statistics in the way that an STJ or semiconductor detector are limited (see section 2.1.1). The difference between a TES and a MMC is that, while the TES measures the detector material's temperature by measuring variations in the sensors resistance, the MMC measures the absorber's temperature by measuring variations in the sensors magnetisation.

The change in magnetic moment δm of a system absorbing an amount of energy δE can be calculated if its volume V , temperature sensitivity of magnetisation $\partial M / \partial T$ and heat capacity C are known [38]:

$$\delta m = V \frac{\partial M}{\partial T} \frac{\delta E}{C} \quad (2.2)$$

Upon investigating the sensitivity of the magnetization M to changes in the temperature T one finds that the most sensitive materials are actually dielectric substrates supporting a population of paramagnetic ions. However, these materials yield extremely long time constants τ (of order minutes) when evaluating the exponential magnetisation decay back to the equilibrium value [38]. When a metallic substrate is used in place of a dielectric substrate, a superior response time is achieved at the price of reduced energy resolution [38].

The change in magnetic moment δm is due to re-alignment of N electron spins of magnetic moment $\mu_e = e\hbar/(2m_e) \approx 6 \times 10^{-5} eV/T$. The energy associated with this re-orientation is calculated as the interaction energy of the electron magnetic moment $N\mu_e$ with a background magnetic field B . The energy resolution can then be estimated as:

$$\Delta E \approx gN\mu_e B \quad (2.3)$$

where $g \approx 2.002$ is the Lande g-factor, also called the gyromagnetic ratio, which arises from quantum electrodynamics (QED) [5].

The change in magnetic moment δm can be detected using a SQUID magnetometer. According to Enss et al. [1] a SQUID can be used to detect changes in magnetic moment as small as that resulting from the reorientation of 3000 electron spins. Such high-sensitivity systems have been used to create MMC calorimeters with energy resolutions of $\approx 4meV$ in a background field of $5mT$ [41] at time constants of $\approx 1s$.

In a simple MMC setup the magnetic sensor material is located inside a SQUID loop . The entire setup has to be subject to an external magnetic field. A simple MMC setup is illustrated in figure 2.4.

According to Fleischmann et al. [42] MMCs have been shown to reach fwhm energy resolutions of $\Delta E = 3.4eV@6.5keV$. As such MMCs are serious competition for TES based calorimeters when it comes to the highest photon counting x-ray energy resolutions available. While MMCs are of great interest to particle physics and astronomy they are not considered any further in this work and are included merely for sake of completeness.

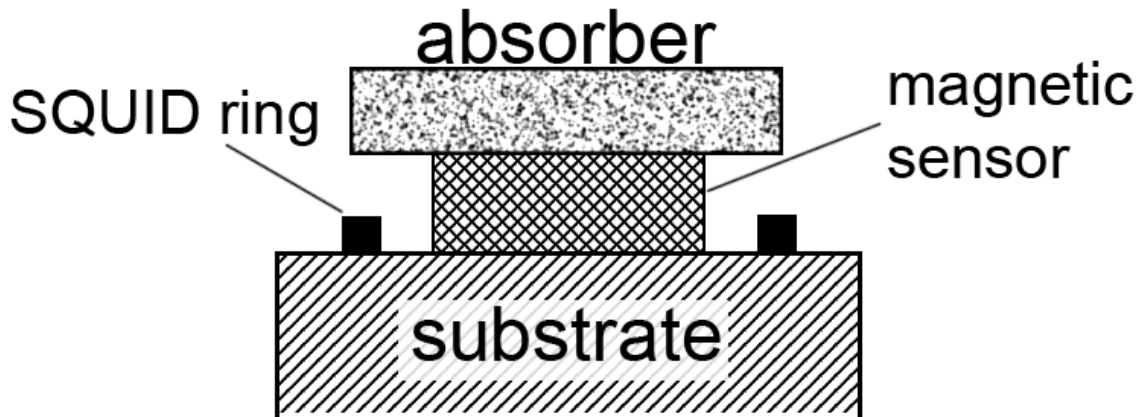


Figure 2.4: Example setup for a Metallic Magnetic Calorimeter (MMC)

2.2 Transition Edge Sensor Classical Noise Sources

To date, TESs have been unable to reach their predicted energy resolution (discussed in section 2.2.1, below) due to a phenomenon known as excess noise, a white current noise originating inside the device [1]. Before a sensible and detailed investigation of the TES excess noise phenomenon is possible, it is necessary to understand the basic operating principles of such devices, and the identified noise sources present. This section aims to give a quick overview of the most important types of noise relevant to TES operation.

2.2.1 Aspects of Transition Edge Sensor Noise and Operation

As discussed in section 2.1.2 no intrinsic statistical limits exist for the energy resolution of equilibrium calorimeters. Instead, the resolution is limited by statistical fluctuations and random thermal excitations and the resulting phonon noise in the calorimeter components.

A thermal equilibrium calorimeter consists of a thermometer perfectly coupled to an absorber of heat capacity C which in turn is coupled, through a weak link of thermal conductivity G , to a heat reservoir at the equilibrium temperature. Thermal fluctuations across the weak thermal link G introduce noise into the system and are well understood. They can be mathematically expressed as average energy fluctuations of magnitude [6][39]

$$\langle \Delta E^2 \rangle = k_B T^2 C \quad (2.4)$$

It can be shown that (theoretically) thermal fluctuation noise does not impose an intrinsic resolution

limit onto the calorimeter [39]. Taking the Fourier transform of the combined signal and noise and separating it into discrete frequency intervals (“bins”) of fixed width Δf we find that in the frequency domain the signal-to-noise ratio is constant with frequency (both thermal fluctuation noise and signal fall as $1/f$). Thus, each frequency bin provides an estimate for a signal with constant uncertainty (due to constant signal-to-noise ratio), and the knowledge of the signal can be improved to arbitrary statistical accuracy by sampling a sufficiently large number of bins [43]. If thermal fluctuation noise were the only noise source in an otherwise perfect system, calorimeter resolution would be limited only by our ability to sample arbitrarily high frequencies.

However, the ability to eliminate thermal fluctuation noise by high frequency sampling relies on the availability of the high frequency data. In any practical system the maximum-frequency bins available are generally determined by limitations in the read-out electronics as well as imperfections in the high frequency response of the system. Any effect that increases signal rise time will decrease the magnitude of high frequency components in the Fourier decomposition of the signal, causing the signal to fall faster than $1/f$ in frequency space. Possible reasons for increased signal rise times are imperfect coupling between absorber and thermometer or finite thermalisation times of the energy deposited. The thermalisation time is effectively the time it takes for the energy deposited in the absorber to relax from a set of excited phonons and electrons into thermal energy and raise the temperature of the device. Any such reduction in the high frequency part of the power spectrum of the signal causes the signal-to-noise ratio to rise rapidly with frequency, making the statistical sampling described above inefficient. In this case it is no longer possible to determine the signal to arbitrary precision. The maximum precision is then determined by the position and gradient of the high frequency roll-off at which the signal drops faster than $1/f$. Practical TES energy resolutions are discussed below, along with the relevant quantitative equations (eq.(2.7) and (2.8)).

The most important type of noise limiting calorimeter resolution is Johnson-Nyquist noise, commonly referred to as Johnson noise, which is caused by statistical deviations of particle energies from their expectation energy due to thermodynamic fluctuation/excitation effects. It occurs in any electronic component with non-zero resistance and its current spectral density i_J is of the form [44]

$$i_J = \sqrt{\frac{4k_B T}{R}} \quad (2.5)$$

where R is the ohmic resistance of the component and all other symbols have their usual meaning.

Since Johnson noise is white in the frequency domain (i.e. it is constant over all frequency space) it causes the signal-to-noise ratio to drop with frequency as $1/f$. In a standard calorimetric system the dominant sources of Johnson-Nyquist noise will be the thermometer and the load resistor.

The most significant noise source apart from Johnson noise and thermal fluctuation noise is amplifier noise, which will not be covered here since it is irrelevant to an understanding of fundamental TES

physics, or the physics of the sn-transition. The problem of amplifier noise is discussed in the relevant literature [1] [6].

In order to facilitate evaluation and comparison of calorimetre performance it is accepted standard to use the dimensionless local sensitivity α defined as [6]

$$\alpha \equiv \frac{d \log R}{d \log T} = \frac{T}{R} \frac{dR}{dT} \quad (2.6)$$

Using 2.6 and assuming Poisson statistics for the phonon noise in the absorber [6] the energy resolution of an equilibrium calorimeter subject to Johnson noise and thermodynamic fluctuation noise can be expressed as [39]

$$\Delta E = 5\alpha^{-\frac{1}{2}} \sqrt{k_B T_0^2 C_0} \quad (2.7)$$

Here C_0 is the heat capacity of the TES at the equilibrium temperature. It is necessary to introduce this constant explicitly since at the transition C is a strong function of temperature. The parameter α is called the *local* sensitivity since it varies strongly with position in temperature-magnetic field space.

The Space Research Organization of the Netherlands (SRON) is working on making a TES array and the values they report for their array pixel design are [35]: heat capacity $C_0 = 0.33 pJ/K$, equilibrium temperature $T_0 \approx 100 mK$ and local sensitivity $\alpha \approx 15 @ 5.9 keV$. Thus equation (2.7) yields $\Delta E \approx 1.72 eV @ 5.9 keV$ as the estimated energy resolution. Since the parameter α varies strongly with temperature, the actual value of α depends on the signal energy and alpha is reduced for higher energies.

The energy resolution $\Delta E \approx 1.72 eV @ 5.9 keV$ of the SRON array pixel as estimated by equation (2.7) is $\approx 0.8 eV$ better than the experimental energy resolution of $\approx 2.5 eV @ 5.9 keV$ reported for this design by the same group [35]. The reason for this is the presence of an unexplained constant voltage noise source in the device. Introducing M as the ratio of this excess noise to Johnson noise the energy resolution can be estimated as [35]:

$$\Delta E = 2.35 \sqrt{k_B T_0^2 C_0} \times [32(1 + M^2)/\alpha^2]^{1/4} \quad (2.8)$$

For $M = 2$ (reasonable estimate at $R = 0.2 R_n$, [35]) the estimated energy resolution then becomes $\Delta E \approx 2.9 eV @ 5.9 keV$, which is much closer to the value reported. Thus energy resolution has been decreased by more than 40% due to the presence of excess noise. This example illustrates the im-

portance of an understanding of the mechanism behind excess noise if TES calorimeters are to reach their full potential.

In calorimeter design the main challenge is to optimize the two parameters of energy resolution and count rate. It is important to choose the right thermometer for the intended application, since often increases in count rate require decreases in energy resolution and vice versa. The combination of the comparatively high count rate and energy resolution offered by a TES gives it an edge over semiconductor calorimeters in many applications where the stringent cryogenic cooling capabilities for such a device can be met [1]. However, the operation of the device on the superconducting-normal phase boundary opens the door to a whole host of new noise sources connected to the magnetic properties of the superconducting state (such as voltage shot noise due to magnetic vortex motion, section 2.3.2), as well as noise phenomena related to the phase transitions (such as percolation noise, section 2.3.3). In order to be able to understand the significance of these additional noise sources, an understanding of some of the fundamental processes and read out mechanisms of TESs is required.

A TES exploits the low heat capacity (of order pJ/K [35]) of materials at low-temperature and the rapid change of resistance with temperature within the superconducting-to-normal (sn)-transition (typically $\alpha \approx 10 - 30$ for x-ray energies). The film is biased on the sn-transition of the material, resulting in large changes in resistance for low event energies (single x-ray photon absorption event energies of a few keV). In the presence of normal bias currents TES transition widths are usually of order a few mK [40]. The local sensitivity α of a TES can be up to two orders of magnitude above that of cryogenic semiconductor thermometers [40]. The first demonstration of a sn-transition thermometer by Andrews et al. [45] in 1941 was as a bolometer measuring infrared signal power. Their device was a fine tantalum wire at its transition temperature of $T_c = 3.2K$ rather than a thin film, but the principle was the same. To date TESs have been used successfully across almost the entire electromagnetic spectrum, from infrared to gamma rays, in calorimeter mode (measuring energy deposited) as well as bolometre mode (measuring signal power) [40].

In a practical TES the signal is usually generated by an event (like photon or particle absorption) in a normal metal absorber film in direct contact with the TES. The absorbers can be used to tailor the device transition temperature by the proximity effect, as well as to improve the photon absorption efficiency [6][40]. Generally normal-state absorbers are used since the heat exchange mechanisms of a normal metal allow for faster thermalisation times. After the heat deposited by the event has generated a local hot spot in the absorber it diffuses through the absorber and into the TES by three main mechanisms [6]:

1. electron-electron interactions
2. electron-phonon interactions

3. phonon-phonon interactions

All three interaction rates are strongly temperature dependent, with *electron – electron* interactions dominant at sub-K temperatures [6], to the degree that thermalisation can be considered to be independent of lattice interactions. The TES measures temperatures by measuring electron temperature and is therefore most suitable for operation in the $T < 500\text{mK}$ regime.

One of the main barriers to the proliferation of TES technology was the difficulty of impedance-matching a TES to a suitable amplifier, a problem which was overcome with the increasing availability of SQUIDs as amplifiers [40]. The basics of SQUID theory and amplification are beyond the scope of this text but are discussed in great detail in [29]. The possibility to use SQUIDS as read out amplifiers for TESs gives them a major advantage over STJs, since it is possible to multiplex SQUID input signals, allowing for a manageable number of amplifier chains and a manageable number of wires to room temperature even for large TES arrays [29]. By contrast, STJs generally require one amplifier per pixel, resulting in a large number of wires for arrays. Still, the production of TES arrays as ultra high resolution imaging spectrometers remains difficult, requiring the creation of a highly uniform array of TESs that can be operated from the same bias temperature and bias voltage.

The increasing demand for production of TESs with predictable response and noise characteristics has driven the scientific effort to accurately model TES response to a known input signal. Accurate theoretical modeling of TES response is a non-trivial task. The sensitivity α and heat capacity C_0 are strongly local in $H-T$ space, causing the energy response to vary significantly with bias temperature, ambient field, energy input, bias current and device resistance. A good introduction to an analytical model of TES response can be found in Enss et al. [1] and Polushkin et al. [6].

While the basic mechanisms behind the sn-transition are fairly well described by BCS theory, a number of transient effects occur near the actual transition region which are difficult to quantify. We will return to these in the following section when dealing with the *excess noise* phenomenon in TESs.

2.3 Transition Edge Sensor Excess Noise

Using practical TESs it has so far been impossible to reach the high resolving powers predicted by the theory outlined in section 2.2. The reason for this is a noise source of uncertain origin intrinsic to the device [1]. The noise appears to be white at frequencies above 100Hz and inversely proportional to the TES bias point resistance [2]. A number of different theories have been suggested in an attempt to explain the origin of excess noise [2][35][46] but so far no closed, self contained model has been produced which is in agreement with all of the experimental data available.

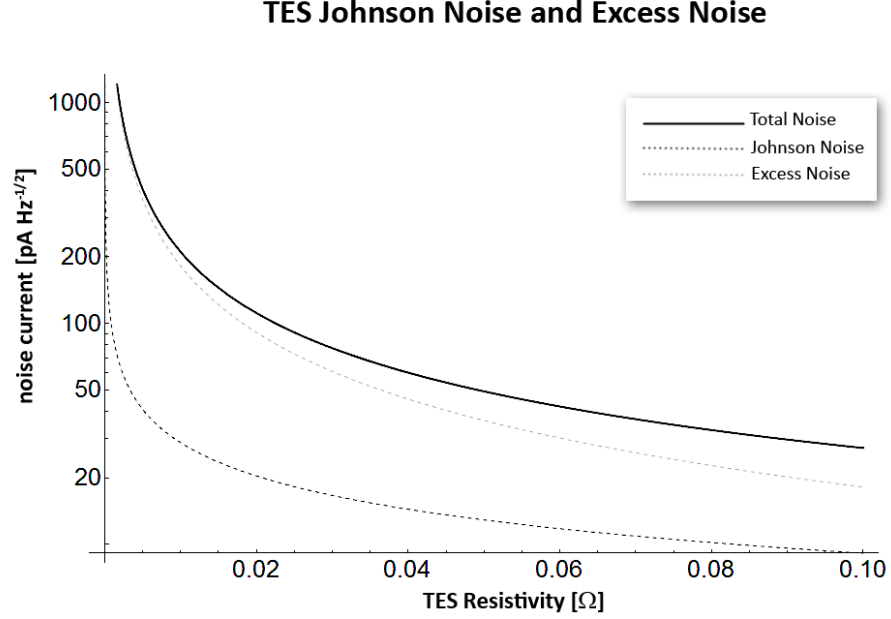


Figure 2.5: Noise spectral current density in a TES with normal state resistance $R_n = 100m\Omega$. The solid line is the total noise observed, made up from the quadrature sum of an analytical fit to experimental excess noise according to equation (2.9)(dashed black line) and Johnson noise according to equation (2.5) (dashed gray line).

In a modern TES system the most significant noise source predicted by theory is Johnson noise (discussed in section 2.2). However, experimenters report an excess noise current spectral density of a magnitude up to ≈ 5 times larger than the noise current expected from Johnson noise [7]. Using the expressions for Johnson noise current spectral density and empirical excess noise current spectral density (equations (2.5) and (2.9) respectively) the magnitudes of observed noise current, Johnson noise current and excess noise current have been plotted in figure 2.5.

We now begin a systematic investigation of the excess noise phenomenon, and two of the theories currently attempting to provide an explanation. Besides wanting to find ways of predicting - and suppressing - excess noise we are motivated simply by a wish to provide an unsolved question with an answer.

In this section we compare and contrast the competing theories of Phase Slip Shot Noise (PSSN) and Percolation Noise. We begin by recapitulating the mathematical expressions governing both theories as well as the functional form of the excess noise. The formalism for PSSN is extended to include the dependence of the excess noise current on the magnetic field. In the case of percolation noise a new set of semi-empirical equations is derived in order to provide a complete analytical framework within which to compare both theories.

2.3.1 Mathematical form of excess noise

A number of experimenters [2][7][35] have reported the excess noise phenomenon. Excess noise cannot be explained by the sum of Johnson noise, thermal fluctuation noise and read-out (amplifier) noise. Its two most dominant and most consistently reported features are its inverse proportionality to the TES bias point resistance, having led to the name " $\frac{1}{R}$ -noise" [7] and the fact that it appears to occur only above a given threshold bias current.

Mathematically, excess noise takes the form of a constant voltage noise source. It has been reported by Takei et al.[7] that in the case of their TiAu bilayer TES the curve of best fit to the experimentally observed excess noise voltage spectral density is given by:

$$v_e = 2\sqrt{4k_B T_c} \quad (2.9)$$

where for a typical setup Takei et al. [7] report $v_e \approx 2 - 5 \mu V Hz^{-\frac{1}{2}}$.

This result was obtained using a $500 \mu m$ square bridge-type TiAu bilayer TES, with operating temperatures between $63 mK$ and $77 mK$, and as such can only be regarded as a reliable quantitative representation of excess noise for exactly the conditions under which it was recorded, since it contains no information about how the excess noise depends on bias temperature, magnetic field or material parameters. As such, any excess noise model that is to be compared to this data has to be matched to the conditions under which the data was collected to which equation (2.9) is fitted [7] if a good agreement with the empirical expression (2.9) is to be reached.

2.3.2 Phase Slip Shot Noise

The theory of Phase Slip Shot Noise is based on the dynamics of vortices in thin film superconductors [2][47]. If magnetic flux penetrates a thin film superconductor at any one point, forcing it locally into the normal state, it creates a circular vortex. The total phase change in the superconducting order parameter along any closed curve containing the vortex must be $2\pi n$ due to the single valuedness of the superconducting order parameter, where n is the number of flux quanta penetrating the vortex [4]. In the literature n is often referred to as the vorticity and denoted q in order to differentiate it from the net number of flux quanta n penetrating the entire superconductor.

Any current flowing in the superconductor will exert a driving force on any vortices present, in a direction normal to the current flow [48]. If a current causes a vortex to move across the superconductor it causes the phase difference of the order parameter at two points along the direction of the supercurrent to change with time [4][47]. Any change of the phase difference with time causes a potential difference between the relevant points [4]. If vortex motion in the sample is random the

voltage signal from a series of vortex movements can appear as Phase Slip Shot Noise (PSSN) [2][47]. According to [4][47] vortex motion in a 2-dimensional superconductor gives rise to a white noise source with voltage spectral density:

$$v_{PSSN} = 2\varphi_0 V \left(\frac{\Delta\phi}{2\pi} \right) \quad (2.10)$$

where v_{PSSN} is the voltage spectral noise density, $\varphi_0 = h/2e$ is the magnetic flux quantum, $\Delta\phi$ is the phase change of the order parameter and V is the driving voltage.

Considering vortex dynamics in a thin film superconductor, Fraser[2] proposed the following expression for the noise spectral current density in terms of experimental variables:

$$i_n^2(V, I, T, A, R) = C \left(\frac{h^2}{e^2} \right) \frac{1}{k_B T} \xi_0 l \frac{VI}{R^2 A} \quad (2.11)$$

where i_n is the noise spectral current density, l is the electronic mean free path; ξ_0 is the Pippard coherence length, A is the area of film, R is the film resistance, V is the voltage across the film, I is the current through the film and $C = 21/2\pi^2$ is a constant of proportionality [2]. Since both the electronic mean free path l and the coherence length ξ_0 are limited by the device thickness d it is possible to approximate the normalized effective coherence length $\sqrt{\xi_0 l} \approx d$ [2].

The major deficiency of this model is that, although it is essentially a magnetic model, it makes no predictions about the dependence of i_n on the applied magnetic field. Since magnetic flux exclusion is not perfect in thin film superconductors [49] any applied magnetic field will cause the vortex density and behavior in the film to change.

The applicability of the PSSN model across the transition will be discussed in section 2.3.2.2 and a comparison with experimental data and with the percolation noise model (section 2.3.3) will be performed in section 2.3.4.

2.3.2.1 Magnetic Field Dependence of Phase Slip Shot Noise

At the time of writing, the quantitative expressions of the PSSN model do not contain any predictions as to the magnetic field dependence of the noise. In this section we derive, as an extension to the model according to equation (2.11), the magnetic field dependence of the PSSN-type noise in the strong field limit. We also show in section 2.3.4 that the PSSN model is in good agreement with experimental data available.

In the strong field limit, the vorticity of the sample is entirely due to the external magnetic field and the external magnetic field can be linked to the free vortex density [50]:

$$n^F = \frac{B}{\varphi_0} \quad (2.12)$$

where n^F is the free vortex number density. Any field for which (2.12) is a good approximation is considered strong. The index F of the free vortex number density n^F has been used as a superscript rather than a subscript for consistency with the literature [50].

An order of magnitude calculation performed by Fraser [2] predicts a reduction of excess noise with applied magnetic field in approximate agreement with experimental results obtained by Ullom [8].

According to Minnhagen [50], the onset of resistance in a thin film is entirely due to the energy dissipation due to vortex flux flow resistance R_{ff} and can be related to the normal state resistance R_N and free vortex density in the sample n^F by:

$$\frac{R_{ff}}{R_N} = 2\pi n^F \xi^2 \quad (2.13)$$

where ξ is the Ginzburg-Landau coherence length. The magnitude of ξ varies with the superconducting material, and for a pure superconductor at $T = 0$ it approximately equals the Pippard coherence length ξ_0 [4] (Example values of the Pippard coherence length are $\xi_{0,Al} \approx 1600nm$, $\xi_{0,Pb} \approx 83nm$ [14]).

Generally TESs tend to be "dirty" superconductors. A superconductor is considered dirty when the normal electron mean free path for elastic scattering l is much shorter than the GL coherence length ξ_0 [2]. The reason that TESs tend to be dirty superconductors is that the small film thickness has to be taken into account when determining the three dimensional average mean free path. Using the "dirty limit" relation for thin films [2] we obtain the temperature dependence of the coherence length:

$$\xi = 0.85 \left(\frac{\xi_0 l}{1-t} \right)^{\frac{1}{2}} \quad (2.14)$$

where ξ_0 is the Pippard coherence length, l is the electronic mean free path, t is the reduced temperature $\frac{T}{T_c}$.

Since we established that during the onset of resistance the film resistance is entirely due to flux flow resistance we can replace the resistivity R from expression (2.11) with the flux flow resistivity R_{ff} . By substituting from (2.12) to (2.14) into (2.11) we arrive at an extended PSSN model including the magnetic field dependence of the excess noise current in strong magnetic fields:

$$i_n = \sqrt{\frac{Ch^2}{2.89e^2} \frac{1}{k_B} \frac{VI}{A} \frac{1}{\xi_0 l} \frac{\varphi_0}{\pi B} \frac{1-T/T_c}{\sqrt{T}} \frac{1}{R_N}} \quad (2.15)$$

2.3.2.2 Validity of the PSSN model

All theories relevant to TES operation take into account effects which broaden the transition from a perfect step of zero width and finite height to a steep gradient of width *a few mK* (figure 2.2).

According to Fraser [2] the PSSN model is valid within the region of the Kosterlitz-Thouless-Berezinski (KTB) type transition. In this model the onset of resistance is explained by the spontaneous creation of vortex-antivortex pairs which unbind above the KTB transition temperature and are non-interacting. A detailed analysis of the dynamics of vortex-antivortex systems is performed by Minnhagen [50].

Since KTB theory assumes vortices to be weakly- or non-interacting these relations are valid only for relatively low vortex densities. The density of vortices in the TES increases with TES temperature. For large vortex densities the vortices form ordered structures, known as "Abrikosov lattices" [4]. If a sufficiently high driving current is applied this will lead to correlated vortex movement, starting in the form of plastic flow at relatively moderate driving currents and tending towards a single coherently moving vortex structure at the highest driving currents [51] [52]. We would expect the frequency of any noise generated by such a moving structure to be strongly related to the lattice constant of the structure, and therefore noise generated by moving coherent vortex structures would no longer be white. Consequently PSSN theory, which relies on random uncorrelated vortex motion to generate frequency independent (i.e. white) noise, is strictly valid only near the low temperature end of the sn-transition region, where n^F is small. Also, the assumption $R = R_{ff}$ is only strictly valid in the low temperature part of the transition [50].

2.3.2.3 Conclusions regarding the PSSN noise model

The functional form of Phase Slip Shot Noise (PSSN) has been investigated and the noise current equation (2.11) as proposed by Fraser [2] has been extended in order to include magnetic field effects.

The magnetic field dependence has been derived for strong magnetic fields, where strong fields are defined by the condition that virtually all free vortices in the TES are due to the applied field ($n^F = B/\varphi_0$). In absence of variations in TES temperature or driving voltage/current the excess noise current spectral density is found to scale as $i_n \propto \frac{1}{B}$ (eq. (2.15)). The suggestion that an increasing and constant magnetic field might actually suppress the noise current (as already suggested in [2]) may appear surprising. It is, however, merely a consequence of the increased flux flow resistance and the excess noise continuing to scale as $i_n \propto \frac{1}{R}$ where in the strong field case $R = R_{ff}$.

The mechanism used to include the field was the realisation that, at the low temperature end of the

sn-transition, the film resistance R can be replaced by the expression for the flux flow resistance R_{ff} which depends directly on the number density of free vortices n^F (eq. (2.12)). For dirty superconductors this changed the temperature dependence of the equation for the noise spectral current density since eq.(2.13) contains the Ginzburg-Landau coherence length as a parameter, which depends on the reduced temperature $t = T/T_c$ (eq. (2.14)).

While we used assumptions specific to the low temperature part of the transition (non-interacting vortices and $R = R_{ff}$) this does not impose any new restrictions on the regime of validity of the field-independent PSSN model (eq. (2.11)) since the assumptions used by Fraser [2] in the derivation of (2.11) already required the system to be in the low temperature part of the transition anyway. While current driven vortex motion still exists at higher vortex densities, vortex motion is correlated rather than random, and plastic flow effects need to be considered while the stationary vortex lattice has to be treated as a glass phase [51] [52], making the PSSN model in its current form invalid in the mid- to high temperature parts of the transition where vortex densities are substantially increased. Since excess noise persists throughout the whole sn-transition the model either needs to be extended to deal with interacting vortices or other theories have to be considered, despite the fact that the PSSN model is shown in section 2.3.4 to be in very good agreement with experiment.

2.3.3 Percolation Noise

Since our investigation of excess noise in the previous section found a theory that is only strictly valid in part of the sn-transition, investigation of an alternative theory is necessary in order to find a complete model of the sources of excess noise in TESs. In order to find a noise theory that may be applicable to the entirety of the sn-transition we consider an alternative to KTB theory for describing the sn-transition. While KTB theory is a convenient tool for getting a mathematical grip on the sn-transition it is only valid in the low temperature part of the transition and as such all conclusions derived from it are also restricted to the low temperature part of the transition.

Looking for a different mathematical model of the sn-transition, we consider percolation theory. In physics and material science percolation is often used to describe a variety of phase transitions. As such, percolation theory appears an obvious candidate in the search for a theory describing the sn-transition, which after all is a perfect second order phase transition [4], as was established in section 1.1.

The theory of percolation noise is based on the noise behavior of random resistor-superconductor networks. The entire system is modeled as a grid of domains of area (*coherence length*)². Any domain can either be in the normal or superconducting state. A comprehensive introduction to

percolation noise can be found in [46]. Mathematically, percolation noise is described by percolation theory, which is the mathematical field dealing with the behavior of randomly connected grids of vertices. The particular model used to describe percolation noise is called *site percolation*. In site percolation each site in the grid can either be *active* or *inactive*. Two sites are *connected* if it is possible to move from one site to the other while traversing only *active* sites. The set of an active site and all active sites *connected* to it is called a *cluster*.

The average cluster size depends on the fraction of sites in the active state. In the case of infinite networks the average cluster size goes to infinity discontinuously as the active fraction reaches a critical value ρ_c . Systems with $\rho > \rho_c$ are called *supercritical*. Systems with $\rho < \rho_c$ are called *subcritical*. In the case of two dimensional site percolation ρ_c can be determined numerically to be 0.593 [53].

Percolation noise assumes that in the sn-transition region the fluctuation of superconducting domains allows superconducting channels to form and collapse spontaneously, giving rise to strong fluctuations in the system's resistivity and was first proposed as a source of excess noise by Lindemann [46]. To date, no analytical expression is available describing the dependence of percolation noise on experimental parameters. In this section, we derive an approximate expression in order to facilitate comparison of the theory with experiment.

2.3.3.1 Temperature Dependence

Trying to find a set of analytical expressions governing the percolation behavior of superconducting domains during the sn-transition we start from the basic expressions given by Kiss and Svedlindh [54] for the behavior of resistivity and noise in random resistor-superconductor networks:

$$R_{rs} \propto (\rho_r - \rho'_{cr})^s \quad (2.16)$$

$$i_n^2 \propto R_{rs}^{-l_{rs}} \quad (2.17)$$

for supercritical networks (i.e. $\rho_r > \rho'_{cr}$). Here R_{rs} is the network resistivity, ρ_r is the density of normal state sites, ρ'_{cr} is the conjugate critical fraction defined as $\rho'_{cr} = 1 - \rho_{cs}$, ρ_{cs} is the critical fraction of superconducting domains (≈ 0.593), i_n is the current noise power spectrum of the network and l_{rs} and s are geometrical scaling constants from Kiss and Svedlindh [54]. By substituting (2.16) into (2.17) it is possible to obtain an expression for i_n in terms of ρ_r . From equation (1.1) we know:

$$n_s^0(T) = n_s^0(0) \left[\frac{T_c^0 - T}{T_c^0} \right]^4 \quad (2.18)$$

where n_s^0 is the density of superconducting electrons and T_c^0 is the Ginzburg-Landau transition temperature, keeping to the convention that superscript 0 indicates zero applied field.

If we assume $n_s^0 \propto \rho_s$ (the fraction of superconducting domains ρ_s scales linearly with the number of superconducting electrons n_s^0) and that $\rho_r = 1 - \rho_s$ (i.e. all sites that are not superconducting are in the normal state) it is possible to obtain an expression for the noise current spectral density in terms of temperature. We begin by substituting (2.16) into (2.17), using $\rho'_{cr} = 1 - \rho_{cs}$:

$$i_n^2 \propto (\rho_{cs} - \rho_s)^{-l_{rs}s} \quad (2.19)$$

We now substitute $\rho_s \propto n_s^0(T)$ into equation (2.19), using (2.18) to obtain an expression for $n_s^0(T)$:

$$i_n^2 = A^2 \left(\rho_{cs} - kn_s^0(0) \left[\frac{T_c^0 - T}{T_c^0} \right]^4 \right)^{-l_{rs}s} \quad (2.20)$$

where A and k are constants of proportionality. To the best of the author's knowledge this is the first analytical expression derived for the dependence of percolation noise on experimental parameters (i.e. maximum superconducting electron density $n_s^0(0)$, critical temperature T_c and temperature T). In order to use the percolation model to make quantitative predictions of the spectral noise current density, the constants of proportionality have to be determined by experiment. A numerical fit to of equation (2.9) to the empirical excess noise expression (2.9) is discussed in section 2.3.4.1.

2.3.3.2 Magnetic Field Dependence

For us to obtain a complete expression for the dependence of percolation noise on experimental parameters we still require the magnetic field dependence of the noise. In order to derive the magnetic field dependence of the noise current i_n it is necessary to derive the magnetic field dependence of the fraction of domains in the superconducting state $\rho_s(B)$. It would be tempting to just use the relation between the critical temperature and magnetic field $T_c = T_c^0 \sqrt{(1 - H/Hc)}$ (from eq. (1.3)) in order to introduce a magnetic field dependence into eq. (2.20). However, it is not immediately obvious that this is a valid substitution. An applied magnetic field will reduce the total number of superconducting electrons [4] but it has not been established whether an increasing magnetic field decreases the number of superconducting domains with constant carrier concentration or whether it reduces the density of carriers within a constant number of domains (or any combination of the two).

In order for the substitution $T_c = T_c^0 \sqrt{(1 - H/Hc)}$ to be valid the fraction of domains in the superconducting state ρ_s has to be proportional to $(1 - H/Hc)^{-2}$ which transforms into $1/\sqrt{(1 - H/Hc)}$ when introduced into the square brackets on the right hand side of equation (2.20).

As discussed in section 1.1.2 superconductivity is a true thermodynamic equilibrium state. As such it is possible to apply thermodynamic equalities in order to predict the properties of the sn-phase transition and we can use conservation of energy to predict the evolution of ρ_s with changes in B . We require an expression for the energy of the system as a function of the fraction of superconducting domains ρ_s . The Gibbs free energy G (eq. (1.7)) can be used to express the total energy of the system of normal and superconducting domains. If we assume that any external magnetic field is applied slowly enough that any phase transitions are adiabatic (i.e. nett energy change of the complete system is zero) the Gibbs free energy G can be used to obtain the change in ρ_s . We know from section 1.1.2.3 that the Gibbs free energies per unit volume of the superconducting state G_s and the normal state G_n as a function of applied field H can be expressed as [4]:

$$G_s(H) = G_s(0) + \frac{1}{2}\mu_0 H^2 \quad (2.21)$$

$$G_n(H) = G_n(0) \quad (2.22)$$

where a negligible magnetic susceptibility has been assumed for the material in its normal state.

At the critical field H_c , the Gibbs free energies of the normal and superconducting states have to be equal. Equating (2.21) and (2.22) and re-arranging we arrive at:

$$G_n(0) - G_s(0) = \frac{1}{2}\mu_0 H_c^2 \quad (2.23)$$

where $G_S(H)$ is the Gibbs free energy of a superconductor in field H , $G_n(H)$ is the Gibbs free energy of the same material in the normal state in field H and H_c is the critical field of the superconducting material. This equation has already been discussed (eq.(1.9)) and is restated here for the readers convenience. It is not strictly correct for a thin superconducting film (as is used in a TES) since any thin film superconductor admits some part of the external field. However, in the context of percolation theory it is still valid for any single *domain*, since each domain is either in the superconducting state (and perfectly excluding flux) or in the normal state (admitting flux). Thus the following arguments based on the energy balance of superconducting domains inside a non-zero external field and inside the superconducting transition region are still valid.

In zero external field the sn-transition is entirely second order, meaning that no latent heat is associated with it. In the presence of a non-zero external field the latent heat of the transition is non-zero, requiring energy to be stored in the superconducting domains. Assuming that the total energy in the sample stays constant with increasing field, conservation of energy will require some of the superconducting domains to be driven normal while a fraction f_s remain superconducting. Writing the energy balance equation for before and after introduction of a field H :

$$G_s(0) = f_s G_s(H) + (1 - f_s) G_n(H) \quad (2.24)$$

where f_s is the fraction (by volume) of the material still superconducting after introduction of the field H . Despite the fact that for the purposes of superconducting domain formation a TES can be considered two dimensional it still has a real physical volume, and it is this volume for which the Gibbs free energy is calculated. Since the thickness of the film is constant and the material state does not vary across the TES cross section, the fraction of the volume in the superconducting state relates linearly to the fraction of domains in the superconducting state, i.e. $f_s \propto \rho_s$. Substituting (2.21)-(2.23) into (2.24) we obtain:

$$f_s = \frac{H_c^2 - H^2}{H_c^2} = (1 - H/H_c)^2 \quad (2.25)$$

Thus the fraction of superconducting domains does indeed scale as $\rho_s \propto (1 - H/H_c)^2$, as required. We can now employ the relation $T_c = T_c^0 \sqrt{(1 - H/H_c)}$ as discussed at the beginning of this section. In order to conserve energy some of the superconducting domains revert to the normal state as the applied field is increased, allowing the field to penetrate the TES in order to obey conservation of energy. We can now introduce a magnetic field dependence into (2.20) by using the $T_c = T_c^0 \sqrt{(1 - H/H_c)}$ relation. Rearranging $\frac{T_c^0 - T}{T_c^0}$ to $1 - \frac{T}{T_c}$ we then obtain:

$$i_n = A \left(\rho_{cs} - kn_s^0(0) \left[1 - \frac{T}{T_c^0 \sqrt{(1 - H/H_c)}} \right]^4 \right)^{-l_{rs}s/2} \quad (2.26)$$

$$R_{rs} = B \left(\rho_{cs} - kn_s^0(0) \left[1 - \frac{T}{T_c^0 \sqrt{(1 - H/H_c)}} \right]^4 \right)^s \quad (2.27)$$

where A, B are constants of proportionality.

The values for the "new" noise exponents (so labeled to distinguish them from the noise exponents used for random resistor-superconductor networks before the publication of Kiss and Svedlinh [54]) l_{rs} and s are given in table 2.1.

Thus we have derived a complete analytical model of the dependence of percolation noise on experimental parameters, which can be compared with both experimental data and the predictions of the PSSN model discussed in section 2.3.2, above.

2.3.3.3 Numerical Simulation of Finite Site Percolation Networks

While the behaviour of an infinite percolation network is reasonably well understood it is extremely difficult to find an analytical description of the behaviour of a finite network. Investigating the relevant literature for such a description one quickly ends up in the (to physicists) quite unusual field

dimensionality	s	l_{rs}	$\lambda_{rs} = 2/s$
2D	1.297 ± 0.07	0.86 ± 0.02	1.54 ± 0.09
3D	0.73 ± 0.011	0.9 ± 0.32	2.74 ± 0.04

Table 2.1: New noise exponents for random resistor-superconductor networks according to [54] for 2-dimensional and 3-dimensional systems. Since TESs are thin films the 2D exponents apply.

of experimental mathematics: A simulation of a site percolation network was implemented by the author in order to determine the shape of the finite-network transition. In order to find the probability P that a sample spanning superconducting cluster exists for a network of $n \times n$ sites at a given fraction of domains ρ_s in the superconducting state, a random distribution of active and inactive sites of the $n \times n$ network is generated N times. The number of times N_s that a sample spanning cluster is detected is recorded, and the probability of a sample spanning cluster existing is calculated as $P = N_s/N$.

The actual simulation was written in Java. For each run a $n \times n$ grid of inactive sites is created and the standard Java random number class (`java.util.Random`) is used to decide randomly for each site whether to set it to *active* (with a probability of ρ_s that the site is set to *active*). Then a recursive algorithm is employed to search for sample spanning clusters. The program returns *true* if a sample spanning cluster is found. After the run the program displays the grid generated and highlights the path found in order to allow verification of the result. Alternatively the program can be instructed to run the simulation N times and return the percentage of runs that have yielded a sample spanning cluster. The data for figures 2.6 and 2.10 has been generated using this program.

The recursive algorithm is implemented using a strongly object-oriented programming approach. It searches for a cluster of active sites connecting two opposite boundaries of the network, which we label A and B . Each site is represented by a java object and has a member function of prototype "`boolean site.span(void)`" which will return true if the site is part of a cluster connected to side B . When "`.span()`" is called the site checks whether it is adjacent to side B . If this is the case "`.span()`" returns "`true`". Otherwise the site calls "`.span()`" of all its nearest neighbour sites and returns "`true`" if at least one of its own "`.span()`" calls returns "`true`". The search for a sample spanning cluster is initiated by calling `.span()` for all active sites adjacent to side A . This method is inefficient in terms of computation time and memory usage but it is reliable and comparatively easy to implement.

One of the most important results obtained with this simulation is that the percolation transition has a finite width for finite networks, with a critical fraction $\rho_{cs,finite} > \rho_{cs,\infty}$ where the critical fraction has been defined as the fraction of active sites ρ_s above which the probability of a sample spanning cluster is 100%.

2.3.3.4 Region of Applicability for Percolation Noise

Just as with the Phase Slip Shot Noise model discussed in section 2.3.2 it is necessary to examine the assumptions made during the derivation of the expressions governing percolation noise, in order to establish the regime of the model's applicability.

Percolation theory in its purest form describes the behavior of infinite networks. Since TESs are of finite size (of order $500\mu m \times 500\mu m$) we start by analysing the difference between percolation transitions in finite and infinite networks. In an infinite network the percolation transition is the change in average cluster size from some finite value for subcritical systems to infinity for supercritical systems. In the case of finite networks it is the change of the probability of the existence of a cluster in contact with opposite ends of the sample from 0 for subcritical systems to 1 for supercritical systems.

In order to fully explore the behavior of finite site percolation networks the simulation described in section 2.3.3.3 was used. However, since it is difficult to limit the depth of the recursion responsible for checking for sample spanning clusters and still be sure to find all existing connections, limitations in object stack and memory sizes limit the simulation to a maximum system size of 200×200 site systems. The algorithm is discussed in more detail in section 2.3.3.3.

As illustrated in figure 2.6, the change from the subcritical to the supercritical state is discontinuous for infinite networks, with $\rho_{cs} \approx 0.59$. The data for a finite network was generated using the numerical simulation programme described above for a 150 domain side length square network. The graph shown is the average of 500 runs of the simulation. Upon inspection the graph is found to be of a geometric shape very similar to the *resistivity vs. temperature* graph of the sn-transition, which seems a very promising indicator for the validity of the percolation model.

The percolation equations and noise exponents obtained from Kiss and Svedlindh [54] are strictly valid only for subcritical systems ($\rho_s < \rho_{cs}$). We assume that a finite system can be considered as approximately subcritical as long as the probability of a sample spanning cluster is < 1 . If the probability of a sample spanning cluster existing is 1 the steady state resistivity of the random resistor-superconductor network is zero, no percolation noise exists (for non-zero driving currents flux flow resistivity and thus PSSN may exist). For extremely subcritical systems ($\rho_s \ll \rho_{cs}$) the resistivity is non-zero but depends on density and position of the superconducting domains, thus some form of percolation noise may still exist despite the fact that no spontaneous formation of sample spanning superconducting channels occurs. From figure 2.6 we see that the fraction of domains in the superconducting state ρ_s has to fall below $\approx 62\%$ for the system to be subcritical. Thus for a finite system $\rho_{cs,finite} > \rho_{cs,\infty}$ using the definition that the probability for a sample spanning cluster has to be

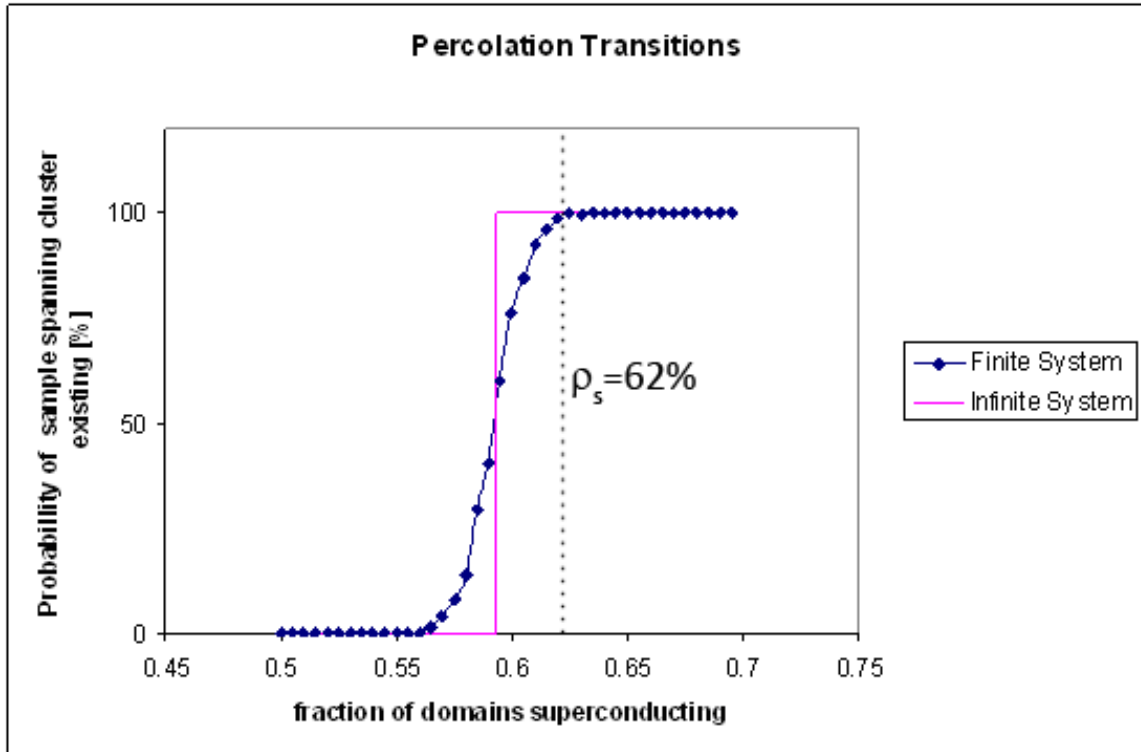


Figure 2.6: Shape of the percolation transition for finite and infinite networks

100% for $\rho_s \geq \rho_{cs}$. Percolation noise only occurs when the probability of a sample spanning cluster existing is $< 100\%$. Thus, while percolation theory itself remains valid, it predicts no percolation noise for the low temperature part of the sn-transition.

2.3.3.5 Conclusions Regarding the Percolation Noise Model

Prompted by a wish to find a theory describing excess noise which is valid throughout the entire sn-transition we have considered the theory of percolation noise as proposed by Lindemann [46]. To date the only quantitative evaluation of this theory has been by numerical simulation [46], an approach which makes the inclusion of spatially non-local effects, like the influence of the applied magnetic field and vector potential, difficult.

The author has derived an analytical expression, showing the predicted dependencies of the percolation noise current on temperature and external field in the sample volume. The derivations were based on the expressions describing random resistor-superconductor networks as introduced by [54]. In order to establish the approximate region of applicability of percolation noise a numerical simulation program developed by the author was employed to investigate the change in behavior for systems when changing from infinite to finite size regimes.

The result of these investigations is a complete set of analytical expressions describing percolation excess noise in transition edge sensors, taking into account temperature and external magnetic fields. No material parameters have been taken into account in the derivation of those expressions. As such they have to be considered approximations, since material differences in the coherence length will change the domain size and as such the resolution (i.e. the number of domains per unit area) of the percolation network, yielding percolation transitions of varying widths depending on the TES material. Also, it seems likely that changes in the coherence length (which depends on the temperature T) over the width of the transition will cause significant changes in the network percolation behaviour. The constant of proportionality k effectively maps the fraction of superconducting domains onto the number of superconducting electrons. Thus changes in the coherence length (and consequently domain size) with temperature will effectively turn the constant k into function of temperature $k(T)$.

And while the model derived, despite all its limitations, will be shown in section 2.3.4 to be in reasonable agreement with the experimental data available, we have yet again ended up with a model that, while in all other respects perfectly suitable to describe excess noise, is not applicable throughout the entirety of the transition. Percolation Noise appears only in the medium to high temperature part of the transition (see section 2.3.3.4 where the site percolation network formed by the superconducting domains is sub-critical. In fact, qualitatively it appears that the temperature region over which percolation noise is not valid is approximately the region of validity of PSSN (section 2.3.2.2), a result which will prompt us to propose a combined noise model in section 2.3.5.

2.3.4 Comparison of Noise Theories with Experimental Data

In this section we compare the predictions of PSSN and percolation noise with experimental results, trying to identify any shortcomings in the existing theories. The comparison with experimental data will serve to give us confidence in both theories, and the fact that both theories will be shown to be in approximate agreement with the data available at the time of writing will serve to encourage us in the development of the combined noise theory which will be outlined in section 2.3.5. In fact, the level of quantitative agreement displayed by the PSSN model is very much better than the predictions of our analytical percolation model. However, while phase slip shot noise in superconducting films has been studied in great detail since about 1980 [47], the topic of percolation noise in a thin superconducting film balanced inside its transition region is very much new and the equations presented here are the first attempt at a quantitative description of percolation noise in a TES. We believe that future refinements may serve to either improve the predictions of percolation theory to the point where their agreement with experimental data is of a level comparable to that of the PSSN predictions or disprove the percolation noise model altogether.

2.3.4.1 Excess Noise vs. Device Resistance

Several experimenters [7][55][56] report a linear scaling of excess noise with inverse bias point resistance ($i_n \propto 1/R_{TES}$). This agrees with the PSSN model (equation (2.11)) as derived by Fraser [2]. The prediction of the PSSN model are plotted in figure 2.7. The predictions according to the PSSN model for the TiAu TES as plotted in figure 2.7 are in extremely close agreement with the empirical expression (2.9), increasing our confidence in the theory. The predictions for the MoCu TES are of the right magnitude and functional form but not of the same high level of quantitative agreement with the empirical expression (2.9). This discrepancy can be explained by the fact that expression (2.9) according to Takei et al. [7] has been obtained by finding the best fit to experimental data gathered from TiAu devices which have different characteristic microscopic features (like, for example, the coherence length ξ and mean free path l) compared with MoCu devices. These different features are not accounted for in the experimental fit (eq. (2.9)), reducing the level of quantitative agreement of the fit with theoretical models applied to different devices. The parameters used to create the predictions in figure 2.7 are not arbitrarily chosen, but are the operating parameters used by Fraser [2] for his devices.

Attempting a similar comparison for the percolation noise model created in section 2.3.3 is much more difficult. In order to attempt a quantitative comparison of the percolation noise spectral current density predicted by eq. (2.26) with the empirical excess noise according to eq.(2.9) it is first necessary to obtain a reasonable estimate for the constants of proportionality A, k . A first order estimate of A and k has been achieved using Wolfram Research's *Mathematica* in order to perform a best fit of eq. (2.20) to eq. (2.9) using the conjugate gradient method, yielding $A = 4.42 \times 10^{-11} pAHz^{-1/2}$, $k = 50m^3$. As can be seen from figure 2.8, the quantitative agreement of the percolation model with the empirical noise is much less convincing than is the case with the PSSN model. Even the functional form does not agree exactly. This may be due to the fact that the current implementation of the percolation noise model assumes a perfectly linear relationship between the fraction of superconducting domains and the density of superconducting electrons $\rho_s \propto n_s$. In a real system, any significant change in n_s will lead to changes in the microscopic parameters, like the coherence length ξ . Since the basis for the percolation noise model is a site percolation network with domain size *coherence length*² it is likely that the total number of domains (and therefore the percolation behaviour of the system) changes significantly with n_s . As such, in order to achieve a good quality fit the temperature evolution of ξ will have to be taken into account, replacing the constant k with a function of temperature $k(T)$ as discussed in section 2.3.3.5. Implementing such variations of ξ into the model is not a trivial task, since variations in the total number of domains of the finite percolation network may change the critical fraction of superconducting domains ρ_{cs} . If the number of domains changes significantly, it may even lead to breakdown of the large system condition discussed below (see sec-

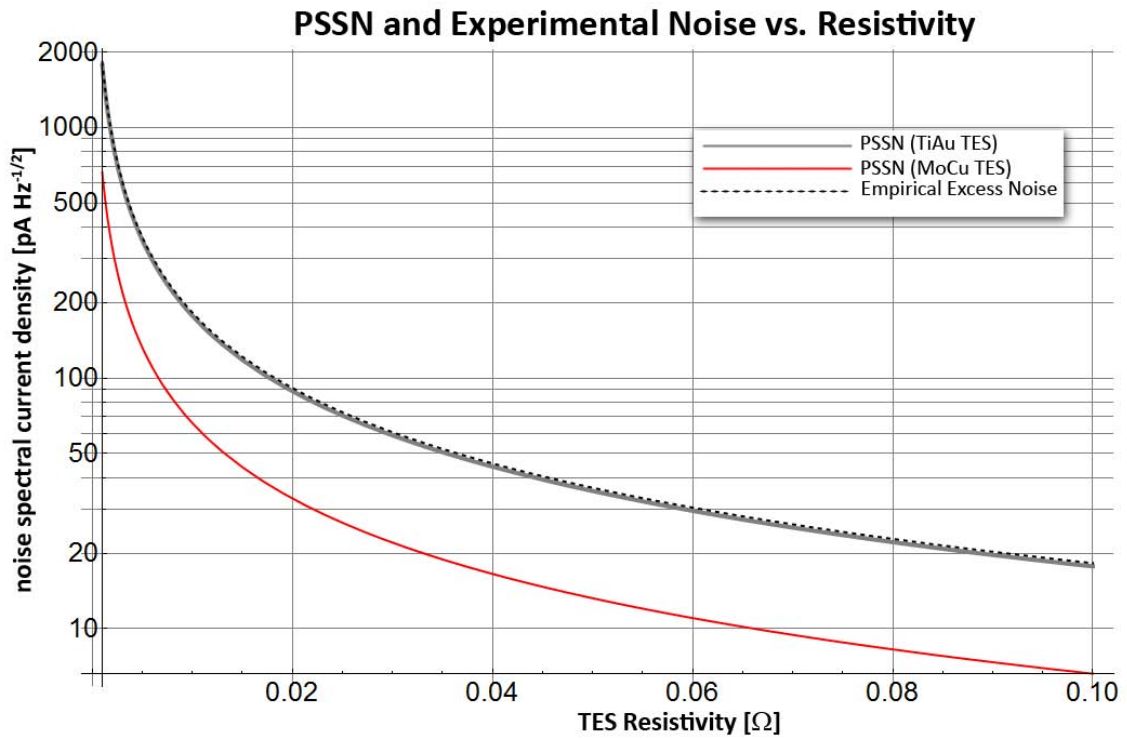


Figure 2.7: Predictions of the Fraser-PSSN model (eq. (2.11)) for the devices reported by Fraser [2] for a TiAu bilayer TES with ($I = 70.5\mu A$; $V = 0.55\mu V$; $\sqrt{\xi l} = 22nm$; $A = 0.125 \times 10^{-6}m^2$) and a MoCu bilayer TES with ($I = 20\mu A$; $V = 0.11\mu V$; $\sqrt{\xi l} = 39nm$; $A = 0.16 \times 10^{-6}m^2$), both at $T = 63mK$. The empirical excess noise (eq. (2.9)) has also been plotted for comparison.

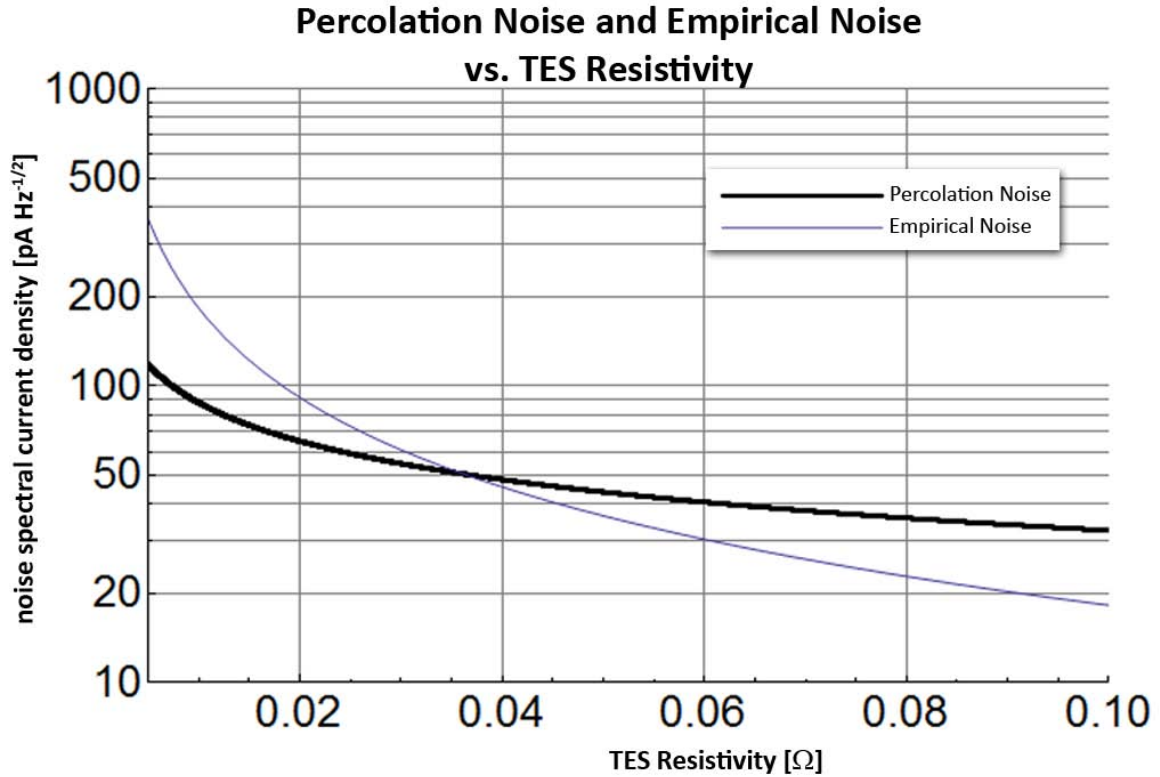


Figure 2.8: Noise spectral current density as a function of TES resistivity as predicted by the percolation noise model, compared to the empirical noise spectral current density (eq.(2.9)).

tion 2.3.4.3). Still, we believe that in the face of the rather simple approximations made in assuming $k = \text{constant}$ the qualitative agreement of the percolation noise model with the empirical expression is good enough to warrant continued interest in this model. Rather than being an exact model of TES percolation noise, the expressions developed in 2.3.3 are a first order analytical tool which can be used to investigate experimental results for indicators of the presence or absence of percolation noise.

2.3.4.2 Excess Noise vs. Magnetic Field

Very little data is available at time of writing regarding the magnetic field dependence of the noise. Ullom et al. [8] present a change in excess noise-to-Johnson noise ratio with magnetic field. It appears that the excess noise spectral current density scales approximately linearly with $1/B$, in good agreement with percolation noise and PSSN. In fact, the predictions of both models agree remarkably well when considering strong magnetic field effects (figure 2.9).

The Ullom data has been obtained using MoCu devices at different fields (of order mG) and at constant bias point resistance, implying variable (and unknown) bias point temperatures. This makes

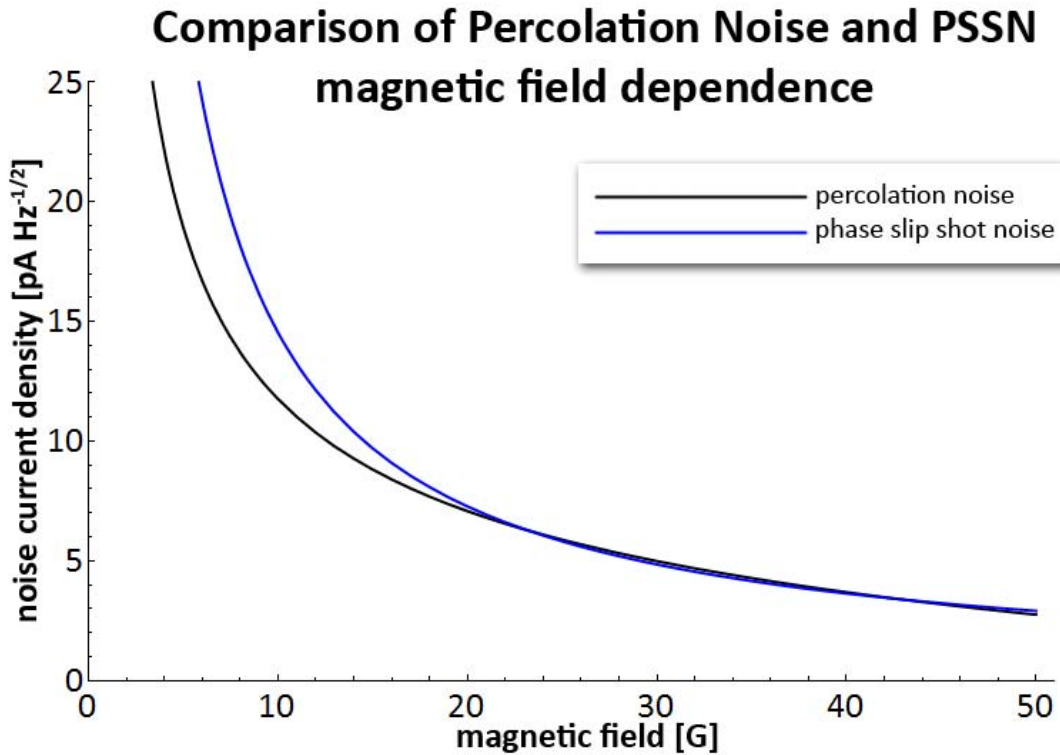


Figure 2.9: Comparison between the predicted noise spectral current densities as a function of magnetic field for percolation noise (black line) and phase slip shot noise (blue line) as a function of magnetic field. In order for the predictions of the PSSN model to hold the field must be strong (i.e. all vortices in the TES due to the external field). The PSSN model has been plotted using the operating parameters for the TiAu TES used for figure 2.7. Percolation model constants of proportionality $A = 4.42 \times 10^{-12}$, $k = 50m^3$ were obtained by best fit to the empirical expression (eq.(2.9)).

the Ullom data unsuitable for direct quantitative comparison with our excess noise models, since both models depend on bias point temperature. Furthermore, the constants of proportionality for the percolation noise model have been obtained by fitting it to noise data from a TiAu TES. Still, the agreement of the approximate $1/B$ dependence between both models and the experimental data reported [8] give us a degree of confidence in the models derived.

2.3.4.3 Excess Noise vs. Device Geometry

The equations derived above (sections 2.3.3.1 and 2.3.3.2) for dealing with percolation noise do not seem to indicate any dependence on device geometry. Intuitively, the noise level should depend strongly on the TES aspect ratio (length-to-width ratio). Assuming the bias current to be flowing along the length of the device, it seems reasonable to assume that a short, wide device allows random

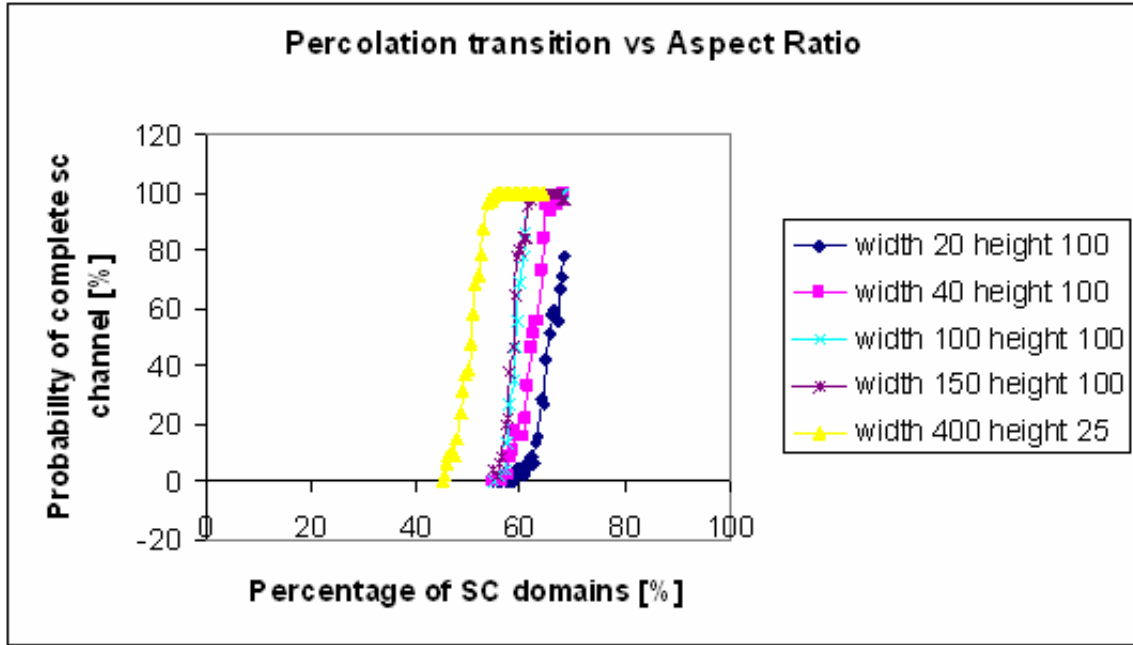


Figure 2.10: Position and width of percolation transition depending on TES aspect ratio. Variations in transition behavior are small compared to variations in aspect ratio $R_A = \frac{\text{height}}{\text{width}}$. It can be seen that the critical fraction ρ_{cs} increases slowly with increasing aspect ratio R_A . The graphs were generated using the author's own recursive numerical simulation.

superconducting bridge connections to occur more frequently than a long narrow device. However, numerical simulations show (figure 2.10) that even for relatively small TESs (smallest relevant dimension tens of coherence lengths) with strongly varying aspect ratios the shift in critical fraction ρ_{cs} at which the transition occurs is comparatively small and the width of the transition is almost unaltered (figure 2.10). From figure 2.10 it appears that the transition temperature can be influenced by device geometry if at least one dimension of the film approaches magnitude $\leq \text{tens of } \xi_0$.

For large networks there is no dependence on aspect ratio at all. The large system condition can qualitatively be expressed as: *If the smallest relevant dimension d in a percolation system is large enough for a square system of side length d to behave as a quasi-infinite system, the system can be considered large. A system behaves as a quasi-infinite system when its critical fraction ρ_{cs} is close to the infinite network critical fraction $\rho_{cs,\infty} \approx 0.59$.*

If the large system condition is fulfilled the whole system can be considered quasi-infinite and the transition will occur at the critical value for infinite networks. The exact network size required for the onset of large system behaviour in site percolation networks is unknown (even an exact expression for the infinite network threshold of a site percolation system has not yet been found [53]). However, using the data from Fraser [2] the effective coherence length of a TiAu bilayer TES may be of order

22nm yielding $\approx (20,000 \text{ domains})^2$. Systems with smallest relevant dimension 100 domains already have transitions almost independent of aspect ratio (figure 2.10). Thus we assume TESs can safely be considered large. Percolation Noise predicts no dependence of the noise on macroscopic device geometry if the large system condition is fulfilled. This is usually the case for TESs which consist of $\approx 20,000 \text{ domains}^2$. However, if the smallest effective dimension of a TES is reduced to $\approx \text{hundreds of nm} = \text{tens of coherence lengths}$ device aspect ratios begin to have an effect (figure 2.10).

By contrast, from equation (2.11) PSSN predicts a $1/\sqrt{A}$ dependence of the noise current on device area A .

No dependence of excess noise on macroscopic device geometry has been reported by experimenters. This agrees with percolation theory in the large system limit (see above), while it appears to be a problem for Phase Slip Shot Noise. However, the dependence of the noise current on device area A is weak to begin with, and variations in other parameters may have obscured the dependence. Added to this, most experimenters appear to keep to similar device sizes. As such it is possible that the $1/\sqrt{A}$ dependence of the noise current will remain undetected until an effort is made to look for it specifically. To the best of the author's knowledge, no dedicated effort to detect this $1/\sqrt{A}$ dependency has yet been made.

It is known that the level of excess noise can be lowered by depositing normal-metal "zebra stripe" patterns on top of the device [46]. A detailed description of this effect can be found in [55]. These patterns consist of a series of thin stripes protruding from one side of the TES towards the opposite side while not quite reaching across. Zebra stripes start on alternating sides of the film and are normal to the direction of the bias current. The proximity effect drives the portion of the TES covered by the zebra stripes normal, forcing the supercurrent to meander across the film in a zig-zag path. The technique is found to be most effective for dense systems of stripes [8] and the geometry is illustrated, along with an image of an actual device, in figure 2.11. As the number density of stripes decreases, so does the level of noise reduction. Since most experimenters only run their experiment with two different density settings (i.e. dense stripes and rare stripes), it is not known whether this decrease in noise suppression with stripe number density is continuous or step-shaped. The same effect can also be observed for dense stripes perpendicular to the bias current reaching across the entire superconducting film ("dense full perpendicular") while no effect can be observed for dense stripes parallel to the direction of the bias current ("dense full parallel")[8].

Percolation theory explains the noise suppression effect of the zebra stripes by pointing out that the super current meandering around a long zig-zag path is now effectively traversing a long, thin TES (i.e. large aspect ratio), making randomly occurring clusters spanning the entire length of the device less likely. While usually a TES qualifies as a large network and is as such independent of aspect ratio,

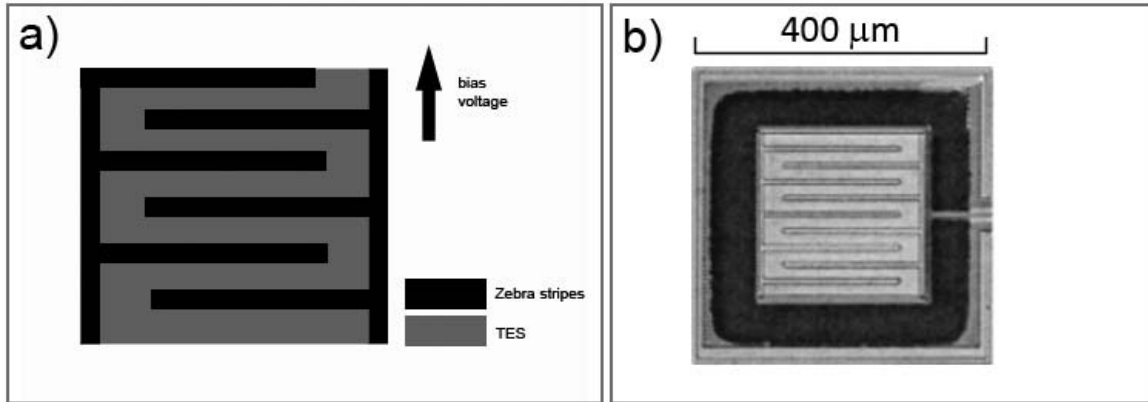


Figure 2.11: Zebra stripe geometry to suppress TES excess noise, a) illustration b) SEM image of actual device [8].

the introduction of the zebra stripes in figure 2.11 has separated the TES into 10 parallel units, interspersed with 10 normal material stripes of approximately the same width. Thus the smallest relevant dimension has been reduced from $\approx 20,000$ to ≈ 100 , which is sufficient for the large system condition to break down (figure 2.10 shows variations in ρ_{cs} for systems with smallest relevant dimension ≈ 100 domains). Break down of the large system condition and introduction of aspect ratio as a relevant parameter also explains why rare perpendicular stripes have little noise suppression effect since they are presumably insufficient to cause break down of the large system condition. However, according to this theory, dense full perpendicular stripes should turn the TES into a series of short, wide systems while causing break down of the large system condition, increasing the noise current significantly. This is not in agreement with experiment. Also, dense full parallel stripes should have a noise suppressing effect, although the absence of this could be explained by the relatively lower aspect ratio compared to the single long meandering path in the case of zebra stripes.

In the case of PSSN, no difference exists between dense full perpendicular and zebra stripes: In both cases the noise suppression arises from the fact that vortices can get pinned or absorbed under the normal-metal stripes. The phase slip per vortex depends on the total fraction of film width traveled [2][47]. Since in the presence of dense perpendicular stripes the vortices are traveling a smaller fraction of the film before becoming pinned, the noise contribution per vortex is decreased. This also explains why dense full parallel stripes have no effect: Although vortices now travel only a fraction of the film width before their motion is stopped in a parallel stripe, every space between stripes has to be considered as a separate system, and a vortex traversing the complete distance between stripes yields the full phase slip of 2π instead of just a fraction thereof. The main problem for PSSN is the $1/\sqrt{A}$ dependence of (2.11). According to this, any deposition of normal material onto the TES resulting in a reduction of the effective superconducting area should result in a measurable reduction in excess noise, independently of geometry. This does not agree with experiment [8]. Also,

evenly distributed normal material islands deposited onto the TES, for example, should absorb and pin vortices in much the same way as stripes, and the total reduction in superconducting area should also contribute to reducing the amount of excess noise. Experimentally Ullom et al. [8] find almost no difference between the noise levels in the normal (i.e. no normal material deposited onto the TES) and "dense island" geometries. However, it is possible that some superconducting electron pairs have moved into the deposited structure (due to the proximity effect, citeBrammertz), effectively lowering the Cooper pair density in the sample and thus increasing the vortex density [50]. A meaningful analysis of this effect is not possible without a prior detailed investigation of the relevant interaction between superconducting and normal state materials in contact, taking into account the fact that the superconducting volume is far greater than the normal metal volume.

In conclusion, it would appear that both models are in reasonably close agreement with experimental data on noise-geometry interactions. While PSSN predicts the hitherto unobserved dependence of noise current on the inverse square root of the film area, percolation noise has trouble explaining the suppression effects of some types of microscopic substructures deposited onto the film. This is particularly troubling for the percolation noise model since its ability to explain the noise suppression effect introduced by zebra stripes was the reason for its creation in the first place [46].

2.3.4.4 Excess Noise vs. Bias Current

The PSSN equation (2.11) contains a direct dependence on bias power $I_{bias}V_{bias}$. According to the data taken by Takei et al. [7] the bias power is approximately constant over the regime of bias currents of interest (Figure 4 in Takei et al.[7]), which makes a direct detection of this effect difficult. The analytical expression for percolation noise eq.(2.26) derived above currently contains no term expressing its dependence on bias current or voltage.

According to Voss et al. [47] the experimental noise voltage power spectrum v_n in a thin superconducting film of Aluminium or Tin itself is consistent with Johnson noise for zero bias current. Excess noise then manifests as a peak in the noise vs. temperature curve that becomes more pronounced for increasing bias currents and is located in the temperature region where sn-transition occurs. The peak increases in magnitude with increasing bias current. Thus, excess noise is purely a feature of the sn-transition. It does not occur in superconductors operated far from their transition temperature. Since both percolation theory and PSSN are features of the transition this is in agreement with both theories.

Takei et al. [7] report an absence of excess noise for small bias currents ($< 10\mu A$), consistent with the absence of excess noise in Al films at zero bias current reported by Voss et al. [47]. Excess noise then increases steeply with bias current. It appears that a threshold current exists, below which no

excess noise is observed. Percolation noise is currently unable to explain the existence of a threshold current. This appears to be a major shortfall in percolation noise theory.

Kim et al.[57] have proposed that vortex motion should be inhibited by vortices being pinned at impurities and imperfections in the superconductor. The potential energy of a vortex located at an imperfection would be reduced by $\Delta E = \epsilon l_p$, where ϵ is the pinning energy per unit length and l_p is the total length over which the vortex flux line is pinned. The pinning force can then be calculated as:

$$F_p = \frac{\epsilon l_p}{\delta} \quad (2.28)$$

where δ is the distance the vortex has to be moved in order to be unpinned. We can estimate δ as the coherence length $\delta \approx \xi$. The pinning energy per unit length ϵ is given by [58]:

$$\epsilon = \frac{\phi_0^2}{64\pi^2 \lambda_L^2} \quad (2.29)$$

Where $\phi_0 = h/2e$ is the magnetic flux quantum. In the presence of a non-zero bias current density J the pinned vortices are subject to a driving force given by [58]:

$$F_d = J\phi_0 l \quad (2.30)$$

where l is the total length of the vortex line subject to the bias current density J .

2.3.4.5 Quantitative Estimate of Pinning Force and Driving Current

In order to mathematically test the assumption that vortex unpinning is responsible for the sudden onset of excess noise above a threshold current I_t we will numerically evaluate the expressions for the driving force F_d and pinning force F_p . For the unpinning hypothesis to be correct, their ratio $F_d/F_p \approx 1$ at the threshold current. We use the TES described by Takei et al.[7] as an example. The device is a $500\mu\text{m}$ square bridge type TiAu bilayer system with the Au absorber deposited as a $300\mu\text{m}$ square on top of the Ti layer (figure 2.12). The device has a zero field transition temperature T_c of 151mK . At 151mK gold is not superconducting. However, according to van Son et al. [59] Cooper pairs will leak from the 40nm thick superconducting Ti layer into the Au layer, up to a depth of $\approx 100\text{nm}$, a phenomenon known as the proximity effect. This has the effect of increasing the thickness of the superconducting layer from 40nm to 140nm while at the same time decreasing the

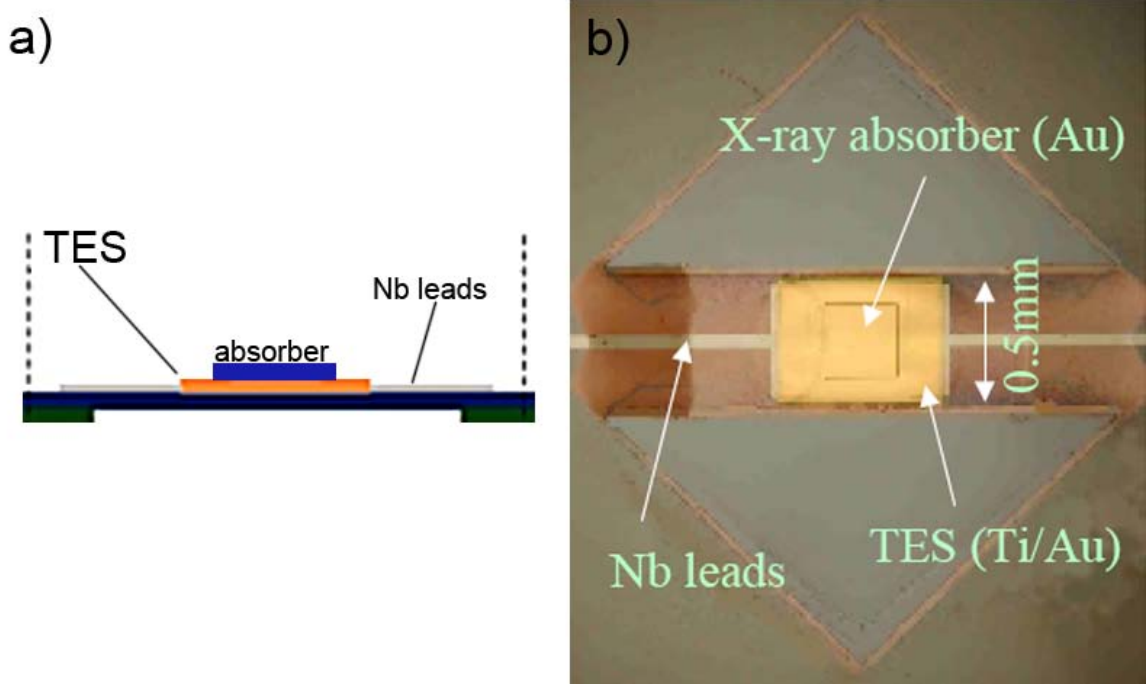


Figure 2.12: Illustration of a) the geometry of the TES as used by Takei et al. [7] when reporting a threshold current below which excess noise does not occur and b) microscope image of the same device (courtesy of Takei [7])

average density of Cooper pairs. For ease of calculation we assume the number density of paired electrons to be constant throughout the superconducting volume and to drop to zero discontinuously at a depth of 100nm inside the gold. In order to determine the driving force F_d and pinning force F_p quantitatively from equations (2.28), (2.29) and (2.30) we require the threshold current density J_t , the London penetration depth inside the TES λ_L and the effective coherence length ξ .

Assuming the current density to be approximately constant throughout the entire superconducting region, we have to find the superconducting cross sectional area in order to determine the threshold current density J_t from the threshold current $I_t = 10\mu\text{A}$ as reported by [7]:

$$J_t = \frac{I_t}{t_{TES}w_{TES} + t_{absorber}w_{absorber}} \quad (2.31)$$

Here $t_{TES} = 40\text{nm}$ and $t_{absorber} = 100\text{nm}$ are the thicknesses of the superconducting cross sections of the Ti layer and superconducting Au absorber layer respectively, $w_{TES} = 500\mu\text{m}$ is the width of the bilayer and $w_{absorber} = 300\mu\text{m}$ is the width of the Au absorber. This yields $J_t = 200\text{kA}/\text{m}^2$.

The London penetration depth of Titanium can be determined from the electron number density n_e in Titanium as $\lambda_L = \sqrt{m_e/e^2\mu_0 n_e}$ [60]. From the atomic mass of Titanium $m_{Ti} = 47.88u$ and density $\rho_{Ti} = 4500\text{kg}/\text{m}^3$ we find the number density of Titanium atoms. Assuming Titanium to be divalent

we obtain $n_e = 1.1 \times 10^{29} m^{-3}$, yielding $\lambda_L = 22.3 nm$. However, since $\lambda_L \propto \sqrt{n_e}$ we have to take into account the fact that superconducting electrons are shared with the Au absorber:

$$\lambda_{L,eff} = \sqrt{\frac{V_{Ti}}{V_{Ti} + V_{scAU}}} \lambda_{L,Ti} \approx 1.38 \lambda_{L,Ti} \quad (2.32)$$

where we have calculate $V_{Ti} = 40 nm \times (500 \mu m)^2$ and $V_{scAU} = 100 nm \times (300 \mu m)^2$ (since the penetration depth of the cooper pairs into the Au layer is about $100 nm$ [59]).

Since the vortex is assumed to penetrate the entire superconducting region its length is given by:

$$l = t_{bilayer} + t_{absorber} \approx 240 nm \quad (2.33)$$

The only missing parameter is the effective coherence length ξ which can be found from Fraser [2] who reports $\xi \approx 22 nm$ for a TiAu bilayer TES. We now have all the relevant parameters required in order to evaluate F_d, F_p if we assume that the vortex is pinned over its entire length (i.e. $l_p = l$). Using the parameters discussed above we find

$$F_p/F_d = 0.87 \quad (2.34)$$

at the threshold current $I_t = 10 \mu A$ ($J_t = 200 k A m^{-2}$). This seems to suggest that vortex unpinning is of approximately the right order of magnitude to be responsible for the excess noise threshold current reported [7][47].

2.3.5 Conclusion: A Combined Excess Noise Theory

We have so far discussed both Phase Slip Shot Noise (PSSN) and percolation noise as competing candidate theories for the origin of the excess noise phenomenon. The PSSN model has been shown in section 2.3.4.1 to be in extremely good agreement with the experimental fit provided by Takei [7] (equation (2.9)), but so far the $1/\sqrt{A}$ dependence predicted by PSSN has not been reported by experimenters. The predictions of the percolation noise model, on the other hand, only agree to within about an order of magnitude with the experimental data, a shortcoming that can be accounted for by the approximations made in deriving it. Percolation noise is made attractive because it readily and intuitively explains the noise suppression effect that zebra stripe geometries have on TESs. However, the level of agreement of the current form of the percolation noise model with equation (2.9) is very much lower than the agreement provided by the PSSN model, and currently two constants of proportionality A, k contained in the model (equations (2.20) and (2.26)) have to be determined by a numerical fit to experimental data. No physical derivation of those constants is available.

The applicability of both theories is restricted to a subset of the sn-transition while experimenters report excess noise throughout the whole of the sn-transition [2][7][35]. The theory of PSSN is strictly valid only in the low temperature part of the transition, where vortex densities are low and vortices are non-interacting. While vortices themselves exist throughout the entirety of the transition, high vortex densities lead to non-negligible interaction between vortices. Since non-interacting vortices are one of the basic assumptions of the PSSN model [2], the model is no longer applicable. Percolation theory on the other hand remains valid throughout the entire transition but predicts zero noise level for low temperatures where the probability of a sample spanning superconducting cluster existing is 100%. Thus, as a description of the excess noise phenomenon both theories are necessarily incomplete.

Note that the existence of a sample spanning superconducting cluster does not signify that the sn-transition is complete and electric currents experience zero resistivity. The remaining normal state domains admit magnetic flux lines to penetrate the superconductor, and the resulting magnetic vortices cause flux flow resistance as discussed in section 2.3.2.

As discussed above, the validity of the PSSN model is restricted to the low temperature part of the sn-transition where KTB-theory applies and vortex densities are low 2.3.2. Percolation theory on the other hand predicts noise near the central-to-high temperature part of the sn-transition (section 2.3.3.4) where the fraction of superconducting domains falls below the critical fraction ρ_{cs} . It appears plausible that the excess noise observed during the transition is separated into two discrete regimes, PSSN and Percolation Noise. Provided that the sn-transition can be modelled as a percolation transition, both percolation noise and PSSN have to occur as a consequence of the physics of the sn-transition. Since the predictions of both theories are similar, a transition from the PSSN regime to the percolation regime would be very difficult to detect.

It is important to note that both percolation noise and PSSN are necessary attributes of the sn-transition. At low temperatures vortex motion will induce a voltage shot noise [47], while superconducting electrons will form into domains of approximate dimension ξ , resulting in the formation of a random superconductor-resistor network, as described by Kiss and Svedlindh [54]. As such we believe that any complete noise model of the sn-transition must incorporate aspects of both phase slip shot noise as well as percolation noise, with PSSN dominant in the low- T part of the transition and percolation noise dominant in the high- T part of the transition. Any model describing voltage noise inside a thin superconducting film (i.e. a TES) will have to be reconcilable with the predictions of PSSN and percolation noise.

While the quantitative PSSN model as described by Fraser [2] and discussed in section 2.3.2 has reached very good quantitative agreement with experimental data (see section 2.3.4) due to the high

level of maturity of vortex dynamics theory, the percolation noise model still contains two free parameters, A and k . We attribute discrepancy in this model quality to the fact that the percolation behaviour of thin superconducting films and TESs is almost unstudied, with only a few exceptions [46].

A change in spectral noise density with bias current has been reported [47] and seems to indicate the existence of at least two different noise processes. Provided that a good quantitative expression for the parameter k in the percolation model can be developed, a speculative combined noise model might be able to account for most, and possibly all, of the features of excess noise observed to date.

An alternative interpretation, relying on the extremely good quantitative agreement of the PSSN model with the experimental noise expression (2.9) over the entire width of the resistive transition (figure 2.7), is that some form of PSSN remains valid even at high resistivities. In this case the scaling of the voltage noise caused by vortex movement remains approximately the same as vortices begin to interact. The main difference in this model is the correlation of vortex motion which increases with increasing bias current [51][52]. We would expect the noise spectral density to change from being constant over all frequency space to having a pronounced peak related to the Abrikosov lattice constant, since the rate r at which lattice points of a two dimensional lattice moving at constant velocity v cross a boundary which runs perpendicular to the direction of lattice motion is given by lrv where l is the length of the boundary and n is the linear density of lattice rows.

It appears clear that more experimental data is required in order to determine the actual noise mechanism over the entire transition with much certainty. Especially an effort to detect the $1/\sqrt{A}$ dependence predicted by the PSSN model would be informative. However, we believe that the work presented in this chapter presents a good outline of the experimental parameters relevant to an investigation of the excess noise phenomenon. Section 2.3.4 provides a guide as to which observations might be necessary to either reinforce or reject the popular theories of percolation noise and phase slip shot noise.

Chapter 3

Superconducting Phase Transition and the Quantum Mechanical Vacuum

Up to this point all the work described in this thesis has been of a practical nature in that it was directly applicable to experimental device physics; We have tried to develop an understanding of superconductors in order to be able to analyse the device physics of superconducting detectors, namely TESs. We discussed the physics of magnetic flux trapping, vortex motion and the sn-transition in order to gain insight into the excess noise processes of TESs and methods for excess noise suppression. So what motivates this excursion into theoretical physics?

In section 2.3 we have discussed the phenomenon of transition edge sensor excess noise, and between them the different models discussed appear capable of explaining most of the features of excess noise (section 2.3.5). However, chapter 2 has demonstrated the sensitivity of the sn-transition on which STJs and TESs rely to a diverse range of unexpected effects, such as the voltage shot noise resulting from the motion of individual flux quanta. It is this sensitivity to electromagnetic interactions that has prompted us to take a closer look at the interactions of vacuum fluctuations with the sn-transition. We cannot help but wonder whether the intrinsically noisy field of the quantum electrodynamic (QED) vacuum might influence the performance of sensitive superconducting devices.

It is well known that the quantum mechanical vacuum is not a state of zero energy. The easiest route to this conclusion is via the Heisenberg uncertainty principle, which forbids us from ever knowing the exact energy content of any given volume of space, thus not allowing this energy to be fixed to zero. In fact, it can be shown that the vacuum energy of a given volume fluctuates continuously. If a mechanism existed by which this vacuum energy can couple into the sn-transition then vacuum fluctuations might contribute to the excess noise phenomenon. In this chapter we will demonstrate

that certain macroscopic manifestations of vacuum energy fluctuations can have measurable macroscopic effects on the sn-transition. We use equilibrium thermodynamics to evaluate the change to the condensate energy resulting from changes in the binding energy of parallel plate cavity systems, an idea which was first introduced by Bimonte et al.[10].

In the course of this chapter it will be necessary to consider electrodynamics in the framework of non-zero photon rest mass electromagnetism. The theoretical frame work of non-zero photon rest mass electromagnetism is a consequence of the breaking of electromagnetic U(1) phase rotational symmetry in superconductors. Investigation of this traditionally almost purely theoretical branch of physics still allows for some predictions regarding changes in the performance of superconducting detectors, such as STJs and some kinds of TESs (section 3.4). Furthermore, the physics of massive photons will be exploited in chapter 4 for the theoretical development of a completely new technology for the creation of active optical elements, which in turn motivates the investigation of the Higgs mechanism responsible for the symmetry breaking and leads directly to the development of the theory of massive spin-1 gravitational bosons developed in chapter 5.

3.1 Introduction to the Physics of the Quantum Electrodynamic Vacuum

In order to arrive at a quantum mechanical description of electromagnetic fields we require a quantum mechanical description of field-like systems which is known as Quantum Field Theory (QFT). In 1926 Max Born and Werner Heisenberg developed QFT using canonical quantisation of the degrees of freedom of a field-like system. From QFT, quantum electrodynamics (QED) was developed, which allows a quantum mechanical description of electromagnetic fields. Such a quantum mechanical description of electromagnetic fields consistent with Maxwellian electromagnetism was perceived as an important step towards the unification of quantum mechanics and relativity since relativity itself had resulted from observations of Maxwellian electromagnetism. Today QED is often referred to as "the best theory of physics" or "the jewel of science" since it is the most accurately tested theory in existence; Experiments agree with theoretical predictions to an accuracy of 1 part in 10^{12} [61] and are limited by experimental error, not by theoretical inaccuracies.

This remarkable theory produces one very counter intuitive result: The vacuum is not a state of zero energy. It is possible to arrive at this result (and indeed determine the predicted energy density of the vacuum) without recourse to the uncertainty principle but merely by the mathematical necessities of QED. The theory of QED is based on the fact that it can be shown [62] that Maxwellian electromagnetic fields are mathematically equivalent to harmonic oscillators. A volume of space containing n

photons of frequency ω is then equivalent to a quantum mechanical harmonic oscillator of state n and fundamental frequency ω . It is a standard result of quantum mechanics [63] that the quantised energy levels E_n of a harmonic oscillator in state n can be written as $E_n = (\frac{1}{2} + n)\hbar\omega$. Thus, the energy of the harmonic oscillator describing the photon field of frequency ω in the presence of $n = 0$ photons is still $E_0 = \frac{1}{2}\hbar\omega$. We have found the expectation value of the vacuum energy $\langle E_v \rangle = E_0$ of the electromagnetic field of photon frequency ω , often referred to as the zero point energy (ZPE) or Vacuum Expectation Value (VEV) of the field. The harmonic oscillator corresponding to the photon field of frequency ω is called the ω field mode.

The zero point energy discussed above has a number of observable physical manifestations. In 1947 Hans Bethe [64] managed to explain a non-degeneracy in the energy levels of the hydrogen $2S_{1/2}$ and $2P_{1/2}$ states previously measured by Lamb et al. [65]. This is a result of $n = 0$ quanta of different frequencies ω being absorbed and re-radiated by the hydrogen atom. The effect is today known as "Lamb Shift". The $n = 0$ photons are the "virtual photons" of the zero point field.

A further ZPE effect is the Hawking radiation emitted by black holes. According to the work by Hawking [66] ZPE fluctuations can create virtual particle-antiparticle pairs near the event horizon of a black hole: One member of the pair falls into the black hole while the other one escapes. The potential energy lost by the particle falling into the black hole serves to make the escaping particle from a virtual particle into a real particle. In order to preserve energy conservation the particle falling into the black hole must be treated as having negative energy, thus reducing the mass of the black hole and making it appear to an external observer that the black hole has just emitted a single particle. It can be shown [66] that the spectrum of photons emitted in this way is exactly the black body spectrum. However, currently there is no way of verifying, experimentally or observationally, the existence of Hawking radiation.

As an extension to Hawking radiation, Unruh [67] showed in 1976 that any non-geodetic detector (i.e. any detector not free falling) should register a black body temperature in the vacuum proportional to its level of acceleration. This effect is detectable in principle by electromagnetic pulse acceleration of an electron: The interaction of a violently accelerated electron with this Unruh-Davies radiation has been observed by Chen et al. [68].

Finally, the only known macroscopic manifestation of ZPE is the Casimir effect. This effect and its influence on the energy balance of the sn-transition will be discussed during the following sections.

3.2 The Casimir Effect and the Energy Balance of the Superconducting Casimir Cavity

Still with an application to superconducting detector performance in mind, we require a way to couple the vacuum energy to the physics of the superconducting-to-normal transition. A survey of the available literature reveals that a mechanism for a coupling between the sn-transition and the QED vacuum does indeed exist via the Casimir effect [10]. We begin by introducing the Casimir effect and consider the superconductivity specific effects in the following subsection (section 3.2.1).

The Casimir effect is a direct manifestation of gradients in the vacuum energy density. The ZPE density can in principle be calculated by integrating the ZPE of a harmonic oscillator of frequency ω over all frequency space $E_{ZPE} = \int_0^\infty \frac{1}{2} \hbar \omega d\omega$. By itself this integral will diverge, yielding $E_{ZPE} = \infty$. It is possible to limit this energy density by introducing ultraviolet cut-offs as described in [62] but they seem to be motivated by a wish to make the relevant mathematics more algebraically tractable rather than by any real scientifically compelling reason. However, since the vacuum energy density is uniform everywhere it can only be detected by its gradients. This is analogous to being on a high plateau. Even though the observer is many kilometers above the true ground level he has no way of detecting this altitude directly if he cannot see the edges of the plateau. Only changes in altitude are detectable. The Casimir effect arises from an experimental set-up that creates a detectable gradient in the ZPE.

The Casimir effect was predicted by H.B. Casimir and D. Polder [69] and has since been experimentally verified to an accuracy of better than 1% [70]. The Casimir Effect describes the existence of an attractive force exerted between any two or more separate macroscopic or microscopic objects separated by sufficiently small distances (usually of order $< \mu m$). The most common example is that of the attractive force between two perfectly reflecting parallel uncharged metal plates (figure 3.1), known as parallel plane geometry case. The attractive force is inversely proportional to the fourth power of the plate separation and at a separation $a = 10nm$ it is equivalent to ≈ 1 atmosphere of pressure.

The Casimir force F_c arises directly from the mathematical form of the vacuum energy density. The expectation value of the total zero point energy E_{ZPE} inside the cavity formed by the plates is found from the integral over the zero point energies of all allowed modes ω . If we assume that the field modes do not penetrate the cavity walls, the cavity effectively forms an infinite potential well, and the continuous spectrum of allowed modes becomes quantised, turning into a discrete spectrum. The ZPE in the cavity E_c is then the sum of the energies of all allowed modes in the quantised spectrum:

$$E_c = \sum_n (2) \frac{1}{2} \hbar \omega_n \quad (3.1)$$

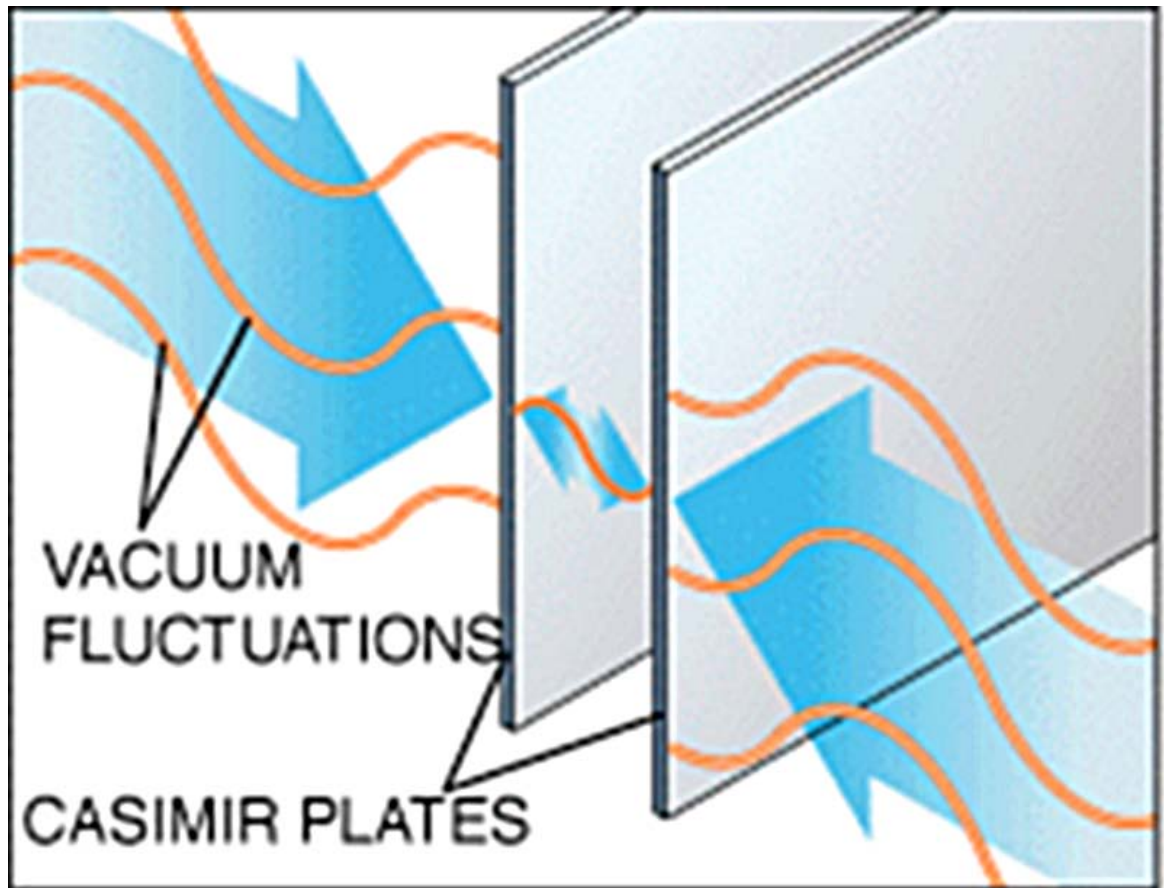


Figure 3.1: Basic Casimir cavity. The dependence of the energy density on the discrete ZPE spectrum in between the plates causes them to attract. Image taken from [9]

where the sum is over all allowed modes n and the factor of(2) arises because two polarization states exist for every allowed mode, each with their separate zero point energy [62].

Considering a perfectly reflecting cavity with plate separation a , the boundary conditions (amplitude of wave on impenetrable barrier equals zero [63]) dictate that the tangential components of the electric field have to vanish on the plate surfaces. This basically reduces the problem of finding the allowed modes to the 3-dimensional infinite square well problem, for a well of length, height and width equal to plate separation, plate height and plate width respectively. In a cavity of plate separation a and plate height and width b the allowed modes are then given by:

$$\omega_{lmn} = \pi c \left(\frac{l^2}{b^2} + \frac{m^2}{b^2} + \frac{n^2}{a^2} \right)^{1/2} \quad (3.2)$$

where l, m, n are the allowed mode quantum numbers. Thus, the total number of allowed modes and the total energy in the cavity reduce with reducing plate separation. The total energy over all allowed modes as a function of plate separation $E(a) = \sum_{lmn} (2) \frac{1}{2} \hbar \omega_{lmn}$ is infinite in the absence of any cut-offs. However, the potential energy $U(a) = E(a) - E(\infty)$ of the plates can be shown to be finite [62]. In this case the potential energy is defined as the energy change when one of the boundaries is removed to infinity, and is caused essentially by the exclusion of long wavelength modes from the cavity.

By taking the derivative of U w.r.t. plate separation it is possible to calculate the force exerted on the plates as the gradient of the potential energy [62]. For the case of perfectly reflecting boundaries with $a \ll b$ an analytical solution exists, and is given by [62]:

$$F_C(a) = \frac{\partial U(a)}{\partial a} = -\frac{\pi^2 \hbar c}{240a^4} A \quad (3.3)$$

with

$$U(a) = \frac{\pi^2 \hbar c}{720a^3} A \quad (3.4)$$

where A is the area of the parallel plates.

For a full derivation and detailed discussion of the Casimir effect the reader is referred to the book by P. Milonni [62]. In the following section we turn to the connection between the Casimir effect and the sn-transition.

3.2.1 Thermodynamics of the Superconducting State and the Casimir Effect

A mechanism for coupling between the sn-transition and the Casimir effect has been suggested by Bimonte et al. [10]. It is based on the influence the sn-transition of the boundaries of a Casimir cavity has on the binding energy of the system, and how this binding energy enters the energy balance of the sn-transition. The basic principle of the effect will be outlined in this section.

As was discussed in the previous section, the exclusion of long wavelength vacuum modes from the parallel plane cavity creates an attraction between the cavity boundaries. This attraction contributes to the total energy of the system in the form of the potential binding energy $U_{bind}(a) = E(a) - E(\infty)$, binding the plates together. The Gibbs free energy equation (eq. (1.8)) then becomes:

$$G_s(H) = G_n(0) + \frac{1}{2}\mu_0 H^2 + u_{bind}(a) \quad (3.5)$$

where $u_{bind}(a)$ is the binding energy per unit volume $U_{bind}(a)/V$ where V is the total volume of the boundary material.

All quantitative expressions so far presented in this chapter have assumed perfectly reflective cavity boundaries. In any real set up the strength of the Casimir force depends crucially on the reflectivity of the boundaries, where higher reflectivity yields a higher binding energy [62]. It has been shown experimentally [71] that the reflectivity and transmissivity of a film change when it undergoes sn-transition and consequently the Casimir binding energy U_{bind} of the cavity system is changed when the cavity boundaries undergo sn-transition. We recall our assumption from section 1.1.2.3 that the magnetic susceptibility in the normal state $\chi \approx 0$ allowing us to write $G_n(H) = G_n(0)$. Finding the difference between superconducting and normal state Gibbs free energies analogous to eq.(1.9) we now have to include the term for the difference between normal state and superconducting state binding energies Δu_{bind} . Expression (1.9) then becomes:

$$G_n(0) - G_s(0) = \frac{1}{2}\mu_0 H_c^2 - \Delta u_{bind} \quad (3.6)$$

where we have used a negative sign for the change in binding energy Δu_{bind} in order to stress that the change will be negative, since the superconducting material is more reflective and thus yields a higher binding energy than the normal state material [10].

Since the difference between the normal state energy G_n and the superconducting state energy G_s is the condensate energy $G_n - G_s = \epsilon_{cond}$ we can rearrange eq.(3.6) to yield:

$$\frac{1}{2}\mu_0 H_c^2 = \epsilon_{cond} + \Delta u_{bind} \quad (3.7)$$

Thus, the change in binding energy will cause a change in the critical field H_c . And since, according to microscopic theory, the critical temperature T_c of the superconducting system depends linearly on the square of the critical field $T_c \propto H_c^2$ [4], we conclude that T_c is also changed. Considering the choice of sign for Δu_{bind} , which was made on the basis of our assumption that the superconducting system is bound more strongly than the normal state system, both critical field and critical temperature of a superconducting film will be increased, compared to a free film, if the film is the boundary

of a Casimir cavity. The reason we expect a stronger Casimir effect (= stronger binding) for the superconducting state is that, experimentally, the average reflectivity of a material in the superconducting state is increased compared to its normal state reflectivity [71].

Bimonte et al. [10] use Lifshitz theory to evaluate the approximate change in Casimir force between superconducting boundaries, taking into account the change in reflectivity reported by Glover [71]. Lifshitz theory provides the mathematical basis for evaluating the Casimir force in the presence of imperfectly reflecting boundaries and a cavity volume with a dielectric function different from unity (i.e. filled with a dielectric spacer, rather than vacuum). Lifshitz theory is discussed in detail by Milonni [62]. Using Lifshitz theory to find the change in specific binding energy Δu_{bind} , Bimonte et al.[10] determine the approximate change in critical field to be:

$$\frac{\delta H_c}{H_c} \approx \frac{\Delta U_{bind}(T)}{2\epsilon_{cond}(T)} \quad (3.8)$$

The relative change in binding energy predicted for a cavity system undergoing sn-transition is minute, of order 1 part in 10^8 [10]. Despite the small magnitude of the change predicted, Bimonte et al. [10] have proposed an experiment to measure this change in binding energy by detecting changes in the critical field H_c of the superconductor. The key to the detectability of the field shift is in the ratio on the right hand side of expression (3.8): The magnitude of the relative critical field change depends on the ratio of the change in specific binding energy Δu_{bind} to the condensate energy ϵ_{cond} , where ϵ_{cond} is known to be small (sub-meV per electron) [4]. Thus, the largest relative changes in critical field $\delta H_c/H_c$ result from materials with low condensate energies $\epsilon_{cond}(T)$ (i.e. materials with low critical temperatures). The critical field of beryllium is just $H_c \approx 107\mu T$ [72], yielding an estimated condensate energy of $\epsilon_{cond}(0) = 1/2\mu_0 H_c^2 = 4.6 \times 10^{-3} Jm^{-3}$. For a cavity with unit area parallel plane boundaries of thickness $t = 50nm$ the total zero temperature condensate energy is then $\epsilon_{cond}(0) \times 2t \times 1m^2 = 4.6 \times 10^{-10} J$. The total binding energy U_{bind}^{normal} for two boundaries of unit area and separation $10nm$ according to equation (3.4) is $U_{bind}^{normal} = 2.7 \times 10^{-3} J$. Thus, even for a change in binding energy U_{bind}^{normal} of 1 part in 10^8 we find the relative change in critical field according to equation (3.8) to be $\frac{U_{bind}^{normal}/10^8}{\epsilon_{cond}(0)} \approx 6\%$.

For their attempt to detect the influence of the Casimir effect on the sn-transition Bimonte et al.[10] originally proposed a double cavity layout as illustrated in figure 3.2. The sample film (centre) is sandwiched between two insulating layers. The setup is capped at top and bottom by a high-reflectivity metal layer. It is well known that the Casimir effect in real-material cavities(i.e. non-perfect reflectivity) depends strongly on the reflectivity of the cavity boundaries [62]. Since the reflectivity of the central sample film will change as it undergoes sn-transition [71] the Casimir attraction between the sample film and the two capping layers respectively will change, altering the binding

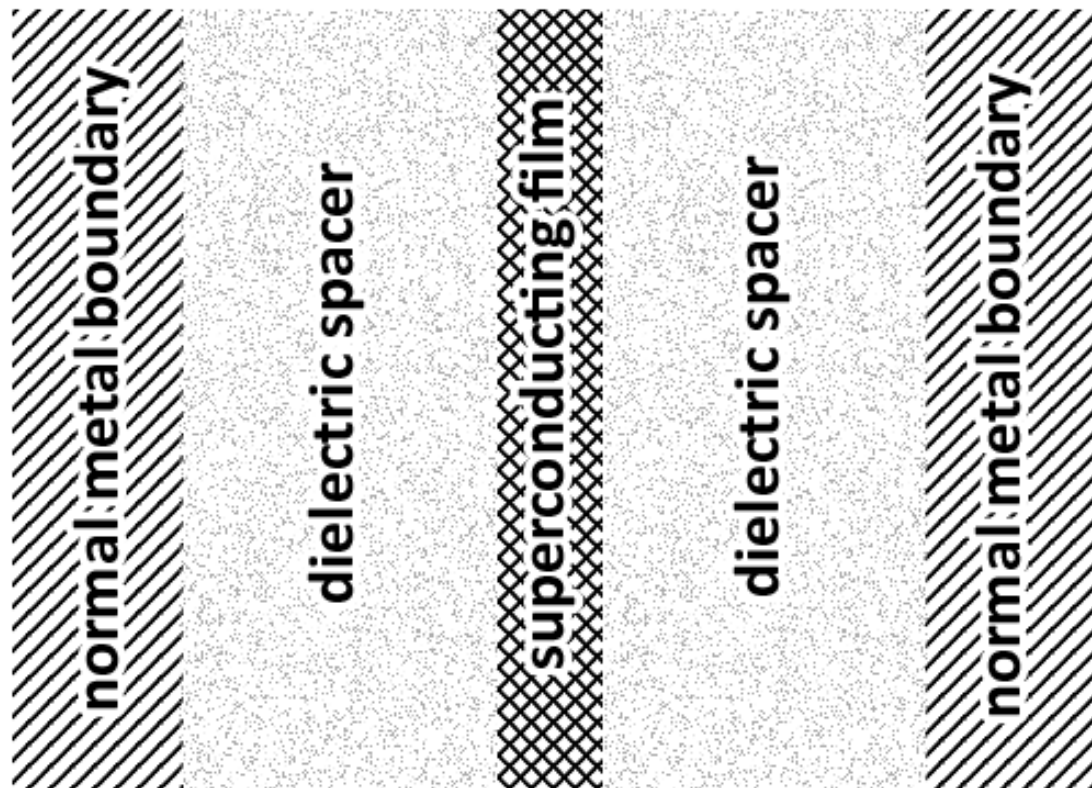


Figure 3.2: Illustration of five-layer cavity layout for detection of vacuum energy change as proposed by Bimonte et al. [10]. In the initial version of the experiment proposed, the width of the superconducting film was $10nm$, the width of the dielectric spacer was $8nm$ and the thickness of the normal metal boundaries is irrelevant [10].

energy of the system according to eq.(3.6). In this way the single superconducting film is part of two Casimir cavities at the same time, effectively doubling the effect. Since the idea was first published in 2006, the proposed experiment has been build and refined a number of times [73] [74].

3.3 Conclusions Regarding the Superconducting Phase Transition and the Quantum Vacuum

The discussion up to this point has basically been a summary outlining the theory currently available for describing the interaction between the sn-transition and the QED vacuum. The purpose of this section is to summarize the key concepts of this interaction before we begin a more rigorous discussion of the interactions between superconductivity and the quantum vacuum.

We have established that quantum mechanical vacuum energy as predicted by QED does indeed have the ability to influence the sn-transition, provided that the superconducting material forms part of a Casimir cavity. The Casimir attraction between the boundaries of the cavity is increased in the superconducting state [10] due to the increased reflectivity of the boundary compared to the normal state [71]. The binding energy of the system introduces a new term into the Gibbs free energy equations for the normal and superconducting state material which does not cancel when calculating the condensate energy $\epsilon_{cond} = G_n - G_s$ (eq. (3.6)) resulting in an increase in critical magnetic field \vec{H}_c (eq. (3.7)), and consequently in critical temperature T_c .

The change in critical field \vec{H}_c has been predicted by Bimonte et al. [10] and should be measurable in principle. Experiments are underway to try and confirm those predictions [10]. The experimental setup described above (figure 3.2) is expected to yield a variation in critical field of as much as 6% for beryllium ($H_c \approx 107\mu T$) [10]. This would constitute the first direct measurement of zero point *energy* of a system rather than the Casimir force which just results from ZPE gradients. It would also show that the ZPE field obeys equilibrium thermodynamics, a discovery that might be of similar importance to the field of QED vacuum physics as was the Meissner effect for superconductivity, since it might allow, in some cases, the reduction of complicated quantum field equalities to thermodynamic energy balance equations (like e.g. Gibbs free energy, eq. (1.7)). This alone should be enough reason to motivate a continued interest in the interactions between vacuum energy and the sn-transition, quite independently of the original intention of finding a mechanism that might link vacuum fluctuations to superconducting detector performance.

3.4 Implications for Practical Detector Operation

The Casimir effect and the strength of its coupling as predicted by Bimonte et al. [10] have been discussed in sections 3.2 and 3.3. We found that, for variations in binding energy of order 1 part in 10^8 , the critical field H_c of a superconducting cavity boundary can be altered by as much as 6% in the case of a Be film. Since the critical temperature T_c and superconducting energy gap Δ_g scale linearly with H_c^2 (using $\Delta_g \propto \epsilon_{cond}$ [4]) this corresponds to a change of as much as 10% in T_c and Δ_g .

After establishing that the Casimir effect does indeed have an influence on the sn-transition which is of an order of magnitude that is detectable in principle, the question that needs to be addressed is whether any implications for practical detector operation exist.

In the case of STJ based detectors the full width-half maximum (FWHM) energy resolution ΔE_{FWHM} is proportional to the square root of the superconducting energy gap Δ_g [6] (see section 2.1.1). Correcting for the influence of the Casimir energy on the sn-transition using the change in condensate energy resulting from the system binding energy (eq.(3.7)) we obtain

$$\Delta E_{FWHM} \propto \sqrt{\zeta \Delta_g} \quad (3.9)$$

where we have defined the relative change ζ in the energy gap Δ_g so that the effective energy gap inside the cavity Δ_{eff} is given by $\Delta_{eff} = \zeta \Delta_g$. The correction factor $\zeta = \delta H_c^2 / H_c^2$. We effectively introduce an additional factor into equation (2.1) to yield:

$$\Delta E = 2.355 \sqrt{1.7F\zeta \Delta_g E_{ph}} \quad (3.10)$$

Despite the relatively weak (square root) dependence of ΔE on ζ the effect may yet be measurable. A change in Δ_g of 10% (as predicted by Bimonte [10], see section 3.3) corresponds to a change in STJ energy resolution of $\approx 5\%$. However, we do expect the real modifications to the energy resolution of an STJ to be smaller than half the values predicted by Bimonte et al. [10] since the values derived in the original paper [10] were for a double cavity as illustrated in figure 3.2. Thus, coupling with the QED vacuum may introduce a change to STJ energy resolution on the percent level. Such a contribution would be extremely difficult to detect, since it would require fabrication of a series of devices with varying cavity properties and otherwise identical performance.

In the case of TESs, it is more difficult to see the relevance of the Casimir effect since, in its most basic form, a TES is a single superconducting film on a dielectric substrate. The Corbino Disc TES (CorTES) as discussed by Luukanen *et al.* [11] consists essentially of a circular TES with one superconducting

Corbino Disc TES (CorTES) Geometry

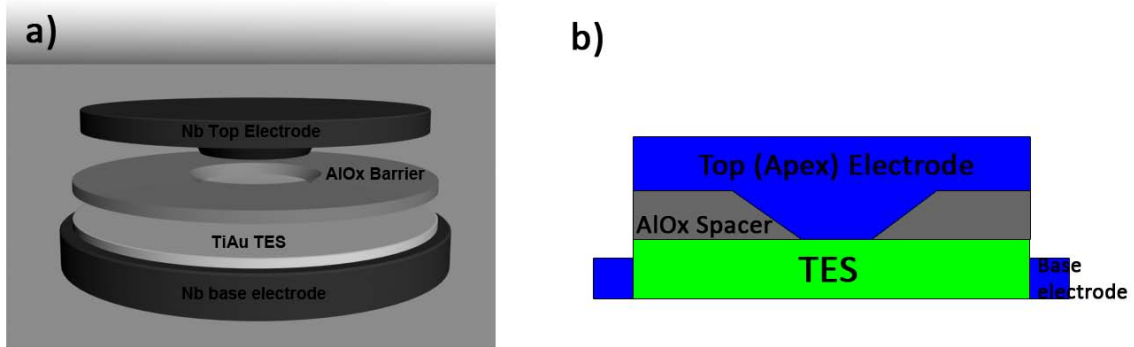


Figure 3.3: Basic CorTES geometry[11]: An AlOx barrier separates the apex-electrode-film from the TES film, creating a Casimir cavity as discussed in the text.

electrode at the centre (apex electrode) and an annular geometry electrode around the circumference. In this set-up, there is no current parallel to the film edge and edge effects are effectively eliminated. The current flows radially outwards from the apex electrode, with the direction of current flow normal to any circle drawn around the centre of the apex electrode. Since the circumference of any such circle increases with increasing radius, the current density decreases with increasing radius. A CorTES is usually biased at a current that will cause the device to exceed the critical current density for small radii (i.e. close to the apex electrode) [11]. In this way a circular fraction of the CorTES close to the centre of the device will be in the normal state, while the ring shaped region around it will be in the superconducting state. The position of this phase boundary controls the resistivity of the CorTES. In this way, energy deposited in the CorTES is detected by changes in the radius of the circular phase boundary rather than by the transition of the entire device (see section 2.1.2).

The CorTES geometry requires a dielectric spacer, between the TES and the top electrode, effectively creating a Casimir cavity (fig. 3.3).

In the case of the CorTES the position of the phase boundary depends on the critical current density of the device. Since the change in condensate energy Δu_{bind} introduced by the Casimir effect will vary with separation between cavity walls the response of the CorTES will be influenced especially in the region between the apex electrode and the outside perimeter of the sloping part in the top electrode. Thus the Casimir effect will indeed influence the response of a CorTES by introducing a non-linearity into the phase boundary position vs. temperature curve of the device.

Another effect exists which is relevant to both STJs and TESs despite their very different basic working principles. Vortex dynamics are of significance for both STJ and TES based detectors. In the case of STJs movement of vortices trapped during cool down increases detector leakage current and re-

duces the quality of the IV-curve [5]. In the case of TESs phase slip shot noise due to vortex motion is a possible explanation for excess detector noise (section 2.3). We recall from the discussion of TES excess noise that vortex motion is inhibited by vortex pinning (sections 2.3.4.4 and 2.3.4.5). It can be shown [57] that the amount of work required to remove a vortex from a pinning site scales linearly with H_c^2 . Since it has been established in the course of this chapter that the Casimir effect may influence the magnitude of the critical field H_c it may well be relevant for vortex dynamics in CorTES devices.

In conclusion, we have demonstrated a mechanism by which the Casimir effect can influence the sn-transition of an STJ or CorTES. Increases in superconducting energy gap Δ_g may influence STJ energy resolution and changed vortex dynamics may be relevant for both TESs and STJs.

In this way our discussion has led us to the point where it appears that superconducting detectors may be used to probe the fundamental physics of the quantum vacuum. Thus a completely new field of physics, which was hitherto almost entirely theoretical, becomes available for experimentation.

3.5 The Superconducting Transition and Massive Electromagnetism

In the previous section we have established the basic principle by which the zero point energy of a system may couple into the sn-transition. We have outlined the method by which Bimonte et al. [10] arrive at a first order quantitative estimate for the influence of the Casimir effect on the sn-transition, and that this influence is detectable in principle. In fact, it appears that even implications for practical detector operation may exist (section 3.4). However, all previous calculations have assumed that the only relevant coupling mechanism between the Casimir effect and the sn-transition is the change in reflectivity of the superconducting boundaries according to Lifshitz theory as outlined by Bimonte et al. [10] and experimentally reported by Glover [71]. This is because Bimonte et al. [10] assume in their calculations that the boundary reflectivity is the only parameter relevant to the Casimir effect that is changed during the sn-transition, naturally assuming that the fundamental form of electromagnetism is unchanged, and that therefore Maxwell's equations (or their quantum field equivalent) hold. This is not correct. Inside a superconductor the fundamental form of Maxwell's equations is changed [30]. Photons inside the superconducting region can no longer be treated as massless particles, requiring modifications to Maxwell's equation [60]. The reasons for this, and the modifications required, will be outlined in this section. The aim of this section is to demonstrate that in dealing with superconducting cavity boundaries the existing theories and models are unsuitable, and that analysis of the data predicted and obtained by Bimonte et al. [10] [74] requires a new model for the Casimir force.

The rest mass of the photon is an area of active research, an overview of which can be found in Tu [75], including a number of experiments which have placed progressively smaller limits on the magnitude of the photon rest mass. Currently the experimentally verified upper limit of the photon rest mass is $m_\gamma \leq 10^{-52} \text{kg}$, while ultimately cosmological arguments and the uncertainty principle fix the smallest possible upper limit at $m_\gamma \leq 10^{-69} \text{kg}$.

Inside a superconductor photons acquire non-zero rest mass via the Higgs mechanism [60]. This is a complex mechanism based on the breaking (or more precisely 'hiding') of certain gauge symmetries and will be discussed in more detail in Chapter 5. Using the mechanism described by Aitchison and Hey [60], it is possible to show that the photon rest mass m_γ inside a superconductor is given by:

$$m_\gamma = \frac{\hbar}{\lambda_L c} \quad (3.11)$$

where λ_L is the London penetration depth in the superconductor and all other symbols have their usual meaning. For example, inside Niobium ($\lambda_L = 39 \text{nm}$) we find $m_\gamma \approx 10^{-35} \text{kg}$, far greater than the vacuum value for the photon rest mass ($\leq 10^{-52} \text{kg}$).

The scientific field of non-zero rest mass photons, called massive electromagnetism (massive-em), is well studied and a good overview is given by Tu [75]. However, it is usually considered in the context of determining the effects of a universal non-zero vacuum rest mass of the photon, rather than in the context of superconductivity. Massive-em is governed by the Proca equations, which transform smoothly into Maxwell's equations as the photon rest mass m_γ approaches zero. In vector form and SI units the Proca equations are given by [75]:

$$\nabla \cdot \vec{E} = \frac{\rho}{\epsilon_0} - \frac{\phi}{\lambda_L^2} \quad (3.12a)$$

$$\nabla \times \vec{E} = -\frac{\partial \vec{B}}{\partial t} \quad (3.12b)$$

$$\nabla \cdot \vec{B} = 0 \quad (3.12c)$$

$$\nabla \times \vec{B} = \mu_0 \vec{J} + \mu_0 \epsilon_0 \frac{\partial \vec{E}}{\partial t} - \frac{\vec{A}}{\lambda_L^2} \quad (3.12d)$$

where ϕ and \vec{A} are the scalar- and vector potentials of the electromagnetic field and all other symbols have their usual meaning. The electric field \vec{E} and magnetic field \vec{B} are defined in terms of the scalar- and vector potential in the following way:

$$\vec{E} = -\frac{1}{c} \frac{\partial \vec{A}}{\partial t} - \nabla \phi \quad (3.13a)$$

$$\vec{B} = \nabla \times \vec{A} \quad (3.13b)$$

In order to solve any problem in electromagnetism inside a superconductor it is necessary to solve the Proca equations (3.12a)-(3.12d).

Describing electromagnetic interactions in terms of the scalar and vector potentials (ϕ, \vec{A}) is not a method specific to superconductivity or massive-em. Some otherwise mathematically difficult problems in electromagnetism can be simplified considerably by expressing the problem in terms of the potentials (ϕ, \vec{A}) rather than in terms of the fields (\vec{E}, \vec{B}) . This is because the potentials themselves are usually not observable. Consequently it is possible to change the potential under consideration to whatever potential is best suited for solving the problem provided that the derivatives outlined in eqs.(3.13a),(3.13b) remain unchanged. Those kind of potential changes are known as "gauge transformations" and will be discussed in more detail in Chapter 5 (particularly section 5.1).

When considering superconductors, great care must be taken in the application of such gauge transformations. Inside a superconductor, the potentials (ϕ, \vec{A}) are not arbitrary, forbidding the use of gauge transformations for many (but not all) applications. This is actually the reason for the non-zero photon rest mass and will be discussed in more detail in Chapter 5.

It is easy to see that the Proca equations transform back into the Maxwell equations as $\lambda_L \rightarrow \infty$ (equivalent to $m_\gamma \rightarrow 0$). Many of the surprising characteristics of superconductors are linked to non-zero photon rest mass. The magnetic London moment (section 1.1.2.2) can be shown to be a direct consequence of the change from Maxwellian to massive electromagnetism [30], and the Meissner effect magnetic field exclusion can be shown to be of the decay type required by a massive vector field [60]. In fact, a closer look at the topic in Chapter 5 will show that the exponential decay of a vector field inside the superconductor and a non-zero rest mass of the field's gauge bosons are one and the same thing. All those relations between massive-em and basic superconducting effects serve to further motivate us in our investigation of massive electromagnetism, and the search for a theory describing the influence of a Casimir cavity on the sn-transition of the boundary materials.

3.5.1 Longitudinal Photons

Before beginning with a quantitative discussion of the changes that need to be made to the Casimir force in the presence of superconducting boundaries it is necessary to consider one of the funda-

mental changes to the basis of the theory resulting from the introduction of a non-zero photon rest mass. The Casimir force is calculated by computing the changes to the zero point spectrum of allowed modes inside the cavity (section 3.2). The discrete cavity spectrum is created by reflection of the photon vacuum modes from the cavity boundaries and a finite cavity width, essentially forming a square well. In any real material where reflectivity is not perfect it is then necessary to consider the two different polarisation states of an electromagnetic wave (Transverse-Electric(TE) modes and Transverse-Magnetic(TM) modes)separately.

Massive-em, however, introduces a third possible polarisation. The Proca equations (3.12a)-(3.12d) allow for longitudinally polarized photons [75]. If we assume that the photons are traveling in the z -direction, perpendicular to the boundaries of a parallel plane Casimir cavity, then longitudinal polarisations are those with the z component of the vector potential \vec{A} non-zero, i.e. $A_z \neq 0$. Therefore longitudinal polarisations will be referred to as A_z modes. Longitudinal modes are non-propagating in Maxwellian electromagnetism, but they do contribute to the ZPE spectrum in the presence of massive-em.

Any photon can have a polarization which is an arbitrary superposition of TM , TE and A_z modes. However, these can all be accounted for by considering the separate polarization components, so that e.g. circular polarization states don't have to be considered explicitly.

The separate contributions to the Casimir force F due to the different polarisations will be indicated by a superscript according to the relevant modes, i.e. the Casimir force due to the longitudinal modes will be written as F^{A_z} .

3.5.2 Massive Photon Velocity, Frequency and Momentum

In order to be able to discuss the interactions of non-zero rest mass photons with the cavity boundaries it is necessary to establish the kinetic parameters of a massive photon in relation to its Maxwellian kinetic parameters. In this section we discuss how a photon's velocity, frequency and momentum are changed when it enters a region of massive-em.

The optical properties of non-zero rest mass photons ("heavy photons") will be discussed in detail in chapter 4. This section will merely give a concise summary of the controlling parameters in order to allow discussion of the Casimir effect in cavities with superconducting boundaries.

Inside a region of Proca electromagnetism, electromagnetic wave fronts travel with the group velocity v_g , while changes in the phase of the electromagnetic wave propagate at the phase velocity v_p . The group velocity v_g and phase velocity v_p respectively can be derived from the Klein-Gordon

equation [75] and are given by:

$$v_g = c \left(1 - \frac{\lambda_{vac}^2}{4\pi^2 \lambda_L^2} \right)^{1/2} \quad (3.14)$$

$$v_p = c \left(1 - \frac{\lambda_{vac}^2}{4\pi^2 \lambda_L^2} \right)^{-1/2} \quad (3.15)$$

where λ_{vac} is the vacuum wavelength of the photon, λ_L is the local London penetration depth and all other symbols have their usual meaning. The heavy photon velocities will be discussed in more detail in section 4.1.

Upon inspection of eqs. (3.14) and (3.15) we notice that the group velocity $v_g \rightarrow 0$ and the phase velocity $v_p \rightarrow \infty$ if $\lambda_{vac} \rightarrow 2\pi\lambda_L$. This leads us to introduce the critical wavelength λ_{crit} as an important parameter for the determination of photon kinetic properties in regions governed by Proca electromagnetism. The critical wavelength λ_{crit} is defined in terms of the London penetration depth λ_L . It is given by:

$$\lambda_{crit} = 2\pi\lambda_L \quad (3.16)$$

In section 3.5.3 we will take a closer look at what happens as λ_{vac} exceeds the critical wavelength λ_{crit} . For now, it is sufficient to realize that the speed of propagation of a wavefront v_g approaches zero as the vacuum wavelength λ_{vac} approaches the critical value λ_{crit} (fig. 3.5.2). The microscopic dependencies of λ_L (and consequently of λ_{crit}) are introduced in section 3.5.6.2 and discussed in detail in section 4.2.2.

A further important parameter required is the complex refractive index η . Throughout this entire chapter we will be dealing with problems of phase change of a vacuum mode across the Casimir cavity, and the relevant complex phase refractive index η_p can be calculated as:

$$\begin{aligned} \eta_p &= c/v_p \\ &= \left(1 - \frac{\lambda_{vac}^2}{4\pi^2 \lambda_L^2} \right)^{1/2} \end{aligned} \quad (3.17)$$

In general, the complex refractive index η_p can be written as the sum of a real part n_p and an imaginary part ik , i.e. $\eta_p = n_p + ik_p$. The real part n_p describes the free propagation/oscillation behavior of the electromagnetic wave while ik_p governs absorption effects [76]. If at anytime in the following discussion we quote the phase refractive index as n_p rather than η_p this is because we have assumed zero absorption.

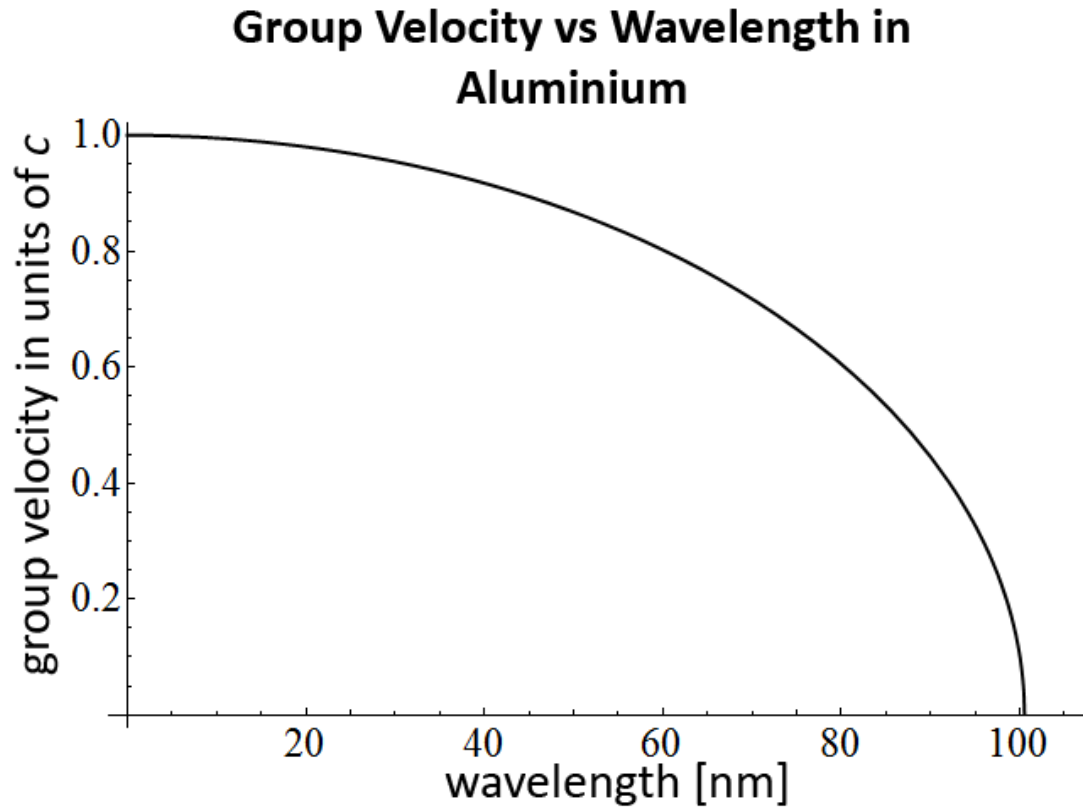


Figure 3.4: Magnitude of photon group velocity vs. photon wavelength on the surface of an aluminium film with $\lambda_{crit} \approx 100nm$, according to equation (3.14). Note that for $\lambda_{vac} > \lambda_{crit}$ the value of v_g will be complex. The critical wavelength λ_{crit} has been determined from the London penetration depth of aluminium $\lambda_L = 16nm$.

The next question to answer is that of variation of frequency. We recall that the breaking of U(1) phase rotational symmetry is what gives rise to the photon rest mass. We assume that the photon does not exchange energy with the symmetry breaking field (i.e. the Cooper pair wave function). It is not at all obvious whether the photon frequency will remain constant when it moves from the vacuum into the region of broken symmetry. In the Maxwellian case a photon's energy can be calculated from its frequency f as $E_{ph} = hf$. Some of the photon energy is now stored in its rest mass instead of electromagnetic oscillations.

We will now show that this change in energy combined with the change in speed of propagation means that the photon frequency remains constant as a photon moves between regions of Maxwellian and Proca electromagnetism respectively.

The total energy E of a non-zero rest mass relativistic particle is given by:

$$E^2 = c^2 p^2 + m^2 c^4 \quad (3.18)$$

where p is the particle's relativistic momentum and m is the rest mass.

Assuming that no energy is exchanged between the Cooper pair field and the photon, we can equate the energy E of the massive photon to its Maxwellian vacuum energy E_0 . Expressing the photon momentum in terms of the photon rest mass m_γ , photon velocity v_g and the relativistic gamma factor $\gamma = \frac{1}{\sqrt{1 - \frac{v_g^2}{c^2}}}$ we obtain:

$$E_0^2 = c^2 m^2 (\gamma^2 v_g^2 + c^2) \quad (3.19)$$

After expressing γ in terms of v_g and c and substituting (3.14) for every instance of v_g we obtain:

$$E_0^2 = m_\gamma^2 c^4 \left[\frac{\left(-\frac{\lambda^2 c^2}{4\pi \lambda_L^2} \right)}{1 - \left(-\frac{\lambda^2 c^2}{4\pi \lambda_L^2} \right)} + 1 \right] \quad (3.20)$$

After substituting $\frac{c}{f} = \lambda$ and some re-arranging we obtain:

$$f = \frac{E_0}{2\pi m_\gamma \lambda_L c} \quad (3.21)$$

which, after substituting $E_0 = hf_0$ and $m_\gamma = \hbar/\lambda_L c$ (from eq. (3.11)) yields $f = f_0$. Thus the frequency of a photon entering the region of broken symmetry is unaltered.

This is a very important result, since it implies that the energy E of a photon of frequency f can be calculated as $E = hf$, independently of photon mass. It can be shown [62] that the spectral energy density $dE = (1/2 + n)\hbar d\omega$ is the only possible Lorentz-invariant spectral energy density. Therefore any prediction of a change in spectral energy density would violate relativity since it would imply an absolute rest frame and thus indicate a flaw in our theory.

The remaining parameter that could potentially be changed is the photon momentum. We know that photon velocity is decreased for a massive photon (eq. (3.14)). Looking to the no-energy-exchange assumption we also know that the total relativistic mass of the photon has to be unchanged. The combination of reduced velocity and constant relativistic mass invariably leads to a decrease of relativistic momentum as the photon enters the symmetry breaking region. This implies an exchange of momentum with the symmetry breaking field due to conservation of momentum. Exchange of momentum is not a problem for the no-energy-exchange assumption as long as the total inertial mass of the particles associated with the symmetry breaking wave function (i.e. the sum of the mass of all superconducting electrons) is significantly larger than the relativistic inertial mass of the incident photon, similar to a rubber ball bouncing off the floor which exchanges momentum with the Earth, while the amount of energy exchanged is negligible. In the future, unless stated differently, λ will refer to the vacuum wavelength of any photon under consideration.

3.5.3 Above the Critical Wavelength: Non-Propagating Low Frequency Components

Up to this point the discussion of the massive-photon velocity of propagation (i.e. the group velocity) has been limited to the case of $\lambda \leq \lambda_{crit}$ and no attempt was made to interpret the meaning of the complex group velocity which occurs for $\lambda > \lambda_{crit}$. In order to understand what happens as λ reaches and exceeds λ_{crit} it is necessary to recall the mathematical expressions governing plane wave propagation.

In mathematical terms, $\lambda > \lambda_{crit}$ requires the wave velocity to be complex. However, the interpretation of a complex velocity is not always obvious. In order to yield the physical interpretation of the phenomena at $\lambda > \lambda_{crit}$ it is necessary to consider the strict mathematical implications of a complex velocity.

Consider a plane wave of amplitude a and angular frequency ω . For the purpose of this discussion, only the mathematical form of a plane wave is of interest, independently of the physical system under consideration. The aim is an understanding of the meaning of a complex speed of propagation.

It is possible to express a plane wave as an exponential of the form $u(t) = e^{i\omega t}$. The angular frequency ω can be replaced by $\omega = 2\pi \frac{v_g}{\lambda_{local}}$ where we have used the subscript "local" to indicate that the relevant wavelength is that inside the host medium, as opposed to the vacuum wavelength. The plane wave equation then becomes:

$$u(t) = ae^{i(2\pi \frac{v_g}{\lambda_{local}})t} \quad (3.22)$$

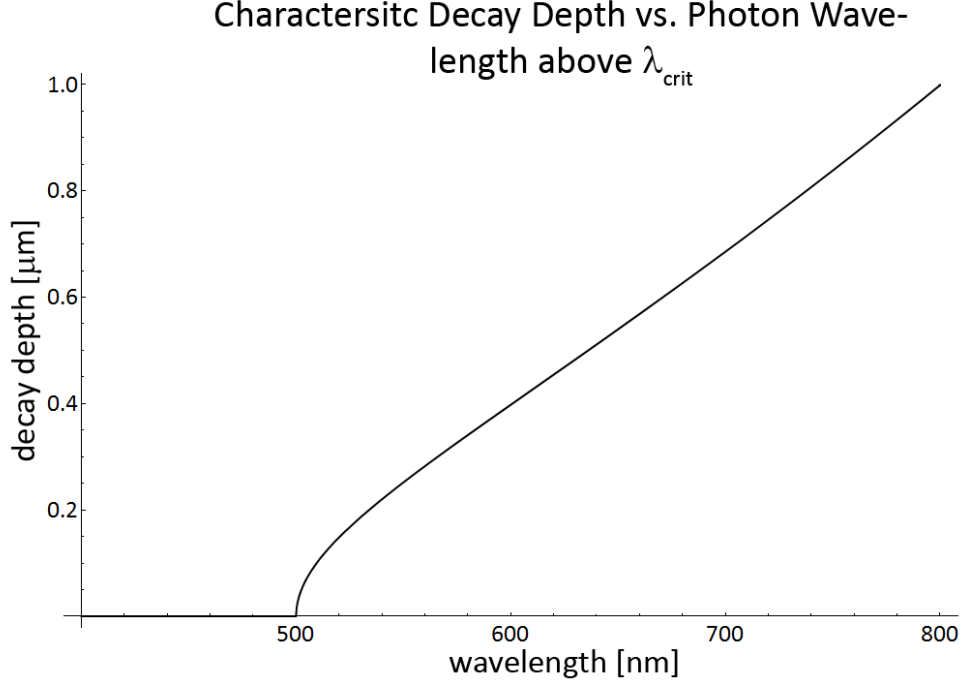


Figure 3.5: Characteristic decay depth vs. wavelength for HPO element with critical wavelength $500nm$.

For $\lambda > \lambda_{crit}$ the expressions for both phase and group velocity (3.14)(3.15) become complex. We Re-express the velocity v_g in (3.22) by a sum of the real and imaginary velocity components v_r, iv_i respectively, with $v_r, v_i \in real$. The resulting sum $v_g = v_r + iv_i$ in the exponential of eq.(3.22) allows for the separation into the product of two separate exponential functions:

$$u(t) = ae^{i(2\pi \frac{v_r}{\lambda_{local}})t} \exp^{-(2\pi \frac{v_i}{\lambda_{local}})t} \quad (3.23)$$

The second exponential on the r.h.s. of eq.(3.23) is non-oscillating and decays with characteristic time t_d calculated as $t_d = \frac{\lambda_{local}}{2\pi v_i}$. From this the characteristic decay depth d can be calculated as $d = t_d \times v_i$ (fig. 3.5), i.e. the amplitude of the wave is attenuated by factor e^{-1} over a distance d . By evaluating eqs. (3.14),(3.15) it can be seen that, for $\lambda > \lambda_{crit}$, the real part of the group- and phase velocity is zero.

Considering figure 3.5, it can be seen that sufficiently thick HPO films may be used as transmission filters, preventing EM-radiation with $\lambda \geq \lambda_{crit}$ from passing the element. From the above discussion it becomes apparent that the separation of wavelengths into those with $\lambda < \lambda_{crit}$ and those with $\lambda > \lambda_{crit}$ is quite a significant one. During the remainder of this work we will distinguish between them as subcritical ($\lambda < \lambda_{crit}$) and supercritical ($\lambda > \lambda_{crit}$) wavelengths, respectively.

3.5.4 Proca vs. Maxwellian Treatment

It is common in the field of superconductivity to treat problems in electromagnetism within the frame of Maxwell's equations. This yields a correct result in almost all instances. In fact, we will show in the following subsection 3.5.4.1 that the dispersion relations (3.14),(3.15) can also be found from the Maxwellian treatment. So why have we decided to use the more complicated Proca equations?

As indicated in the introductory part of section 3.5, the non-zero photon rest mass in the Proca equations originates from the broken phase rotational symmetry. In order to protect the phase of the Cooper pair condensate from changes introduced by Maxwellian gauge transformations, it is necessary to introduce additional terms linear in the vector potential \vec{A} when calculating current densities or magnetic fields [29] using Maxwell's equations. For example, the current density

$$J = \frac{e\hbar}{m}|\psi|^2\nabla S \rightarrow \frac{e\hbar}{m}|\psi|^2\nabla S - \frac{2e^2}{m}|\psi|^2\vec{A}. \quad (3.24)$$

Without these additional phase-preserving terms it is often impossible to arrive at the correct results. For example, phase preserving terms are required in order to predict magnetic flux quantisation through a superconducting ring, or to predict the transition to perfect diamagnetism. Without the phase preserving terms, Maxwell's equations will predict a magnetic field present at the time of the sn-transition to persist in the superconducting state and be "frozen into" the superconductor.

It is not always easy to tell which problems require phase preserving terms and which don't. When using the Proca equations instead of Maxwell's equations, these phase preservations are taken care of automatically by the photon mass terms. For example, we can arrive at both the exponential decay of static magnetic fields (i.e. the Meissner effect) and the magnetic London moment simply by taking the curl of both sides of equation (3.12d) and solving the resulting differential equation.

The Proca equations (3.12a)-(3.12d) are essentially a generalization of Maxwell's equations to an arbitrary photon mass $m_\gamma \propto 1/\lambda_L$. Maxwell's equations are the special case with $m_\gamma = 0$. Consequently, the Proca are valid everywhere where $1/\lambda_L$ is non-negligible. As $\lambda_L \rightarrow \infty$ they transform smoothly back into Maxwell's equations as the strength of the symmetry breaking is reduced to zero and massless electromagnetism restored.

3.5.4.1 Deriving HPO Dispersion from Maxwell's Equations

In ITO the low energy edge of the transparent window is set by the plasma frequency ω_p of the free electron gas and contributions of the bound electron system are negligible [77]. For this case the group refractive index η_g as a function of incidence angular frequency ω can be calculated as [76]:

$$\eta_g^2(\omega) = 1 + \frac{nq^2/\epsilon_0 m}{-\omega^2 + i\gamma\omega} \quad (3.25)$$

where γ is the characteristic scattering time and $\omega_p = nq^2/\epsilon_0 m$ is the plasma frequency of a free charge cloud with carrier mass m , carrier charge q and carrier density n . In a superconductor the charge carriers are Cooper pairs with $q = 2q_e; m = 2m_e, n = n_s/2$, where q_e, m_e and n_s are the electronic charge, electronic mass and superconducting electron density, respectively. Furthermore, superconducting electrons do not scatter, so $\gamma \rightarrow \infty$ and the imaginary component of (3.25) goes to zero.

We can write $\omega = 2\pi f$, where f is the frequency in Hertz, and use $f = c/\lambda$ to write:

$$\eta^2(\omega) = 1 + \frac{n_s q_e^2 \mu_0}{m_e} \frac{\lambda^2}{4\pi^2} \quad (3.26)$$

where we have used $1/c^2 = \mu_0 \epsilon_0$. As will be discussed in more detail in section 4.2.2, the first fraction on the rhs of eq.(3.26) is the squared London penetration depth λ_L^2 , yielding:

$$\eta^2(f) = 1 + \frac{\lambda^2}{4\pi^2 \lambda_L^2} \quad (3.27)$$

The above equation (3.27) is identical to the dispersion relation (3.14). Consequently, most of the heavy photon effects discussed in this thesis can also be derived from Maxwell's equations. This result gives us a degree of confidence in our predictions.

We will continue to use the Proca treatment for two reasons: It saves us having to worry about phase preservations and yields superconductivity specific results like the Meissner effect and magnetic London moment directly, and it will aid our understanding of the behaviour of massive gauge bosons when we extend the discussion to massive gravitons in Chapter 5.

3.5.5 The Massive Casimir Effect

After having discussed the basics of massive electromagnetism we return to the problem that prompted this discussion in the first place: An evaluation of the Casimir effect in the presence of one or more superconducting boundaries. The obvious way forward is to attempt an evaluation of the Casimir effect for Proca electromagnetism (massive-em). Barton and Dombey [78] have derived a complete set of corrections expressing the difference between the massive-em and Maxwellian-em Casimir force, and a short summary can be found in Tu [75]. However, at the end of this section we will realize that

the massive-em solutions are unsuitable for most, if not all, practical cavity systems. Nevertheless, it is instructive to evaluate the massive Casimir effect and compare it to the Maxwellian Casimir effect, since the correct solutions will rely on a mixed state of Proca and Maxwellian electromagnetism, and we may obtain an estimate for the order of magnitude we expect of any massive-em corrections to the Casimir effect. An attempt at a solution suitable for practical cavity systems is made in section 3.6.

Barton and Dombey [78] suggest that two principal approaches exist for the evaluation of the massive Casimir effect in a parallel plane geometry: One can evaluate how either the vacuum expectation value of the electromagnetic stress tensor or the energy in the discrete spectrum of allowed ZPE modes vary with plate separation.

Using the latter approach Barton and Dombey [78] find that massive-em corrections to the Casimir force F consist of two principal components:

1. kinematic corrections $\Delta F^{[TE, TM]}$ to the Casimir effect due to non-zero rest mass TE and TM modes
2. the contributions F^{A_z} by $A_z \neq 0$ modes (longitudinal photons) which are zero in the Maxwellian case

Explicitly the massive Casimir force can be expressed as the sum of the power series of the contributions by the [TE, TM] modes and the contributions by the A_z modes [78]:

$$F^{m_\gamma \neq 0} = F^{[TE, TM]} + F^{A_z} \quad (3.28)$$

In natural units we find:

$$F^{[TE, TM]} = -\frac{1}{a^4} \frac{\pi^2}{240} + \frac{1}{a^4} \left\{ \frac{1}{12} \lambda^2 - \frac{1}{\pi^2} \lambda^4 \log\left(\frac{1}{\lambda}\right) + \frac{1}{\pi^2} \lambda^4 \left(\frac{1}{4} - \log(\pi)\right) + \dots \right\} \quad (3.29a)$$

$$F^{A_z} = \frac{1}{a^4} \frac{1}{2\pi^2} \left\{ -\lambda^4 \log\left(\frac{N}{2a}\right) \right\} \quad (3.29b)$$

where the dimensionless parameter λ equals $\frac{m_\gamma a}{2}$ in natural units ($\lambda = \frac{a}{\pi \lambda_L}$ in SI inside a superconductor [60]), m_γ is the photon mass, a is the plate separation and N is the thickness of the plates, required because longitudinal modes are penetrating even in ideal media (perfect dielectric or perfect conductor) [78]. The first term in expression (3.29a) is the Maxwellian electromagnetism Casimir force, and the following power series terms are the corrections $\Delta F^{[TE, TM]}$.

In order to convert the above equations (3.28)-(3.29b) from natural units into SI units they have to be prefixed by a factor $\hbar c$. Note that in the coordinate system used to derive equations 3.29a-3.29b

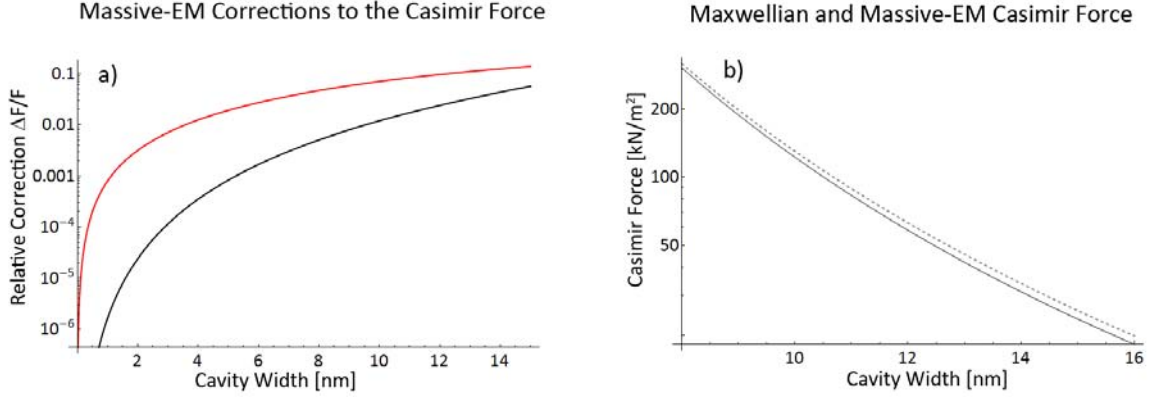


Figure 3.6: a) The relative changes to the Casimir force due to transverse mode (red) and longitudinal mode (black) contributions, as a function of cavity width b) The Casimir force as predicted by Maxwellian (dashed line) and Proca (solid line) electromagnetism (according to eqns.(3.28)-(3.29b)), as a function of cavity width. Both plots assume a photon mass of $1.4 \times 10^{-34} kg$, corresponding to superconducting aluminium (eqn.(3.11)) and a boundary thickness of $10 \mu m$.

a negative magnitude indicates an attractive force. Positive terms in equations 3.29a-3.29b diminish the Casimir attraction while negative terms increase it. According to Barton and Dombey [78], when evaluating the above equations explicitly one finds that for any practical system the kinetic corrections to the transverse modes (eq. 3.29a) are dominant compared to the longitudinal mode contributions F^{Az} . Since the leading correction to the transverse modes (i.e. the $\frac{1}{12}\lambda^2$ term) is positive the magnitude of the Casimir attraction is then diminished in the case of massive electromagnetism. This is intuitively correct since an increased rest mass leads to smaller vacuum fluctuations [62].

However, the derivation of equations (3.28)-(3.29b) as presented by Barton and Dombey [78] is only strictly valid for the case where $a/\lambda_L < 1$ ($m_\gamma a < 1$ in natural units [78]). Generally this is an acceptable assumption since the upper limit on the photon vacuum rest mass of $10^{-52} kg$ implies an associated characteristic length scale of $\lambda_L \approx 3.5 \times 10^9 m$, far larger than any separation a over which calculating the Casimir force would yield a result significantly different from zero. At this point we encounter the first problem with applying the equations (3.28)-(3.29b) to superconducting materials. Inside a superconductor we expect a photon rest mass of order $m_\gamma \approx 10^{-35} kg$ (eq.(3.11)), approximately 17 orders of magnitude greater than the experimental upper limit for the vacuum value of m_γ , with the increased photon mass resulting from a London penetration depth $\lambda_L \approx 10s$ of nm . Care has to be taken to ensure that the plate separation a in the setup under consideration yields $a/\lambda_L < 1$. The magnitude of the finite mass corrections has been plotted in figure 3.6, along with the total magnitudes of the Proca and Maxwellian Casimir force, assuming a London penetration depth of $\lambda_L \approx 16nm$, corresponding to Aluminium. Consequently, the equations (3.29a),(3.29b) are applicable only for plate separations $a < 16nm$.

With equations (3.29a) and (3.29b) we have a complete set of expressions for the massive Casimir force in a parallel plane geometry cavity. However, on closer examination of the original problem, which was to determine the magnitude of the Casimir force in a cavity with superconducting boundaries in order to determine the influence of vacuum fluctuations on the sn-transition, we find the massive Casimir effect as outlined by Barton and Dombey [78] to be unsuitable. The reason for this is that the massive Casimir effect assumes a globally constant photon mass. In a superconducting cavity the photon mass is large ($m_\gamma \approx 10^{-35}kg$) inside the superconducting boundaries and takes its vacuum value ($m_\gamma < 10^{-52}kg$ [75]) far from the boundary. In order to accurately determine the boundary conditions when trying to evaluate the spectrum of allowed modes in the cavity from which the Casimir effect is derived (see section 3.2) we have to establish how the photon mass varies with increasing distance from the superconducting boundary.

3.5.6 Applicability of Massive Electromagnetism and the Barton and Dombey Solutions to the Casimir Effect

In section 3.5 we have introduced the Proca equations for massive electromagnetism, which govern the propagation of electromagnetic field modes inside a superconductor. We have then gone on to discuss the results obtained by Barton and Dombey [78] for the Casimir effect in the Proca framework. We have however not considered the possibility that Proca electromagnetism might not be applicable over the entire energy range of vacuum modes, or throughout the entire cavity space.

In this section we will establish that, while the Proca equations are indeed valid over the entire energy range of vacuum modes, the photon mass varies over the cavity volume. Indeed, it will be found that for the major part of the cavity volume photons can be considered as massless and Maxwellian electromagnetism can be used. These results will prompt us to attempt an implementation of a varying-photon mass electromagnetism in section 3.6.

3.5.6.1 Cooper Pair - Vacuum Mode Interactions

It is well known that the energy gap Δ_g between the normal and superconducting state is very small, of order $\leq 1meV$, and that photons may break such cooper pairs. As such, any photon of energy $E_{ph} \geq 2\Delta_g$ can excite two electrons across the energy gap, breaking a cooper pair. Does this mean that Proca electromagnetism is valid only for vacuum modes n with $E_0(\omega) = 1/2\hbar\omega^2 < 2\Delta_g$?

As was discussed in section 3.1, the vacuum mode $E_0(\omega)$ is the lowest possible energy state of the electromagnetic field mode of frequency ω , i.e. the $n = 0$ state. Like with any other quantum me-

chanical system, energy can only be extracted from the ω -field mode by transition to a lower quantum mechanical state $n' < n$. However, since the field mode is in its ground state, no energy can be extracted from it.

Breaking a Cooper pair requires energy $2\Delta_g$. Since no energy can be extracted from a field mode in its ground state (= vacuum state), vacuum modes cannot break Cooper pairs. Consequently, the Proca equations and all derived dispersion equations remain valid over all vacuum modes $0 < \omega < \infty$.

3.5.6.2 Symmetry Structure of the Casimir Cavity with Superconducting Boundaries

In order to find a quantitative expression for the change in Casimir binding energy of a system undergoing a transition it is necessary to calculate the change in the discrete spectrum of allowed modes in the system. In this section we will attempt to settle the question of the boundary conditions and the type of electromagnetism (Proca or Maxwellian) applicable to the problem.

In the previous sections, we have introduced massive electromagnetism and the concept of non-zero rest mass photons inside superconductors (sec.3.5). We briefly discussed the massive Casimir effect and presented the equations derived by Barton and Dombey [78] to predict the Casimir force in the presence of a global non-zero photon rest mass m_γ . It is tempting to infer that the suitable equations for describing the Casimir effect between superconducting boundaries are the Proca equations (3.12a)-(3.12d), and that the equations derived presented in section 3.5.5 are suitable for predicting the Casimir effect for cavities with superconducting boundaries. On closer inspection we find that assuming global massive electromagnetism is not a suitable solution to the problem. For one, the ground state of the quantum vacuum outside the cavity far away from the boundaries is that of the massless Maxwellian vector field. Similarly, if the boundaries are separated far enough that the electronic wave functions on both sides of the cavity are independent, then normal Maxwellian electromagnetism will apply at the centre of the cavity.

As has been pointed out in section 3.5, the non-zero photon rest mass inside a superconductor arises because the phase of the electronic wave function is no longer arbitrary and U(1) phase rotational symmetry is lost. In order to form an accurate picture of the effect of superconducting boundaries on the form of electromagnetism inside the cavity we have to rigorously analyse the symmetry structure of the cavity, determining the dependence of photon mass on position inside the cavity. The photon rest mass will only be non-zero in regions of broken U(1) symmetry and the magnitude of the rest mass will depend on the strength of the symmetry breaking.

The symmetry breaking is caused by the macroscopic wave function of the Cooper pair condensate [60], and the strength of the symmetry breaking as well as the photon mass can be calculated directly

from the local density of Cooper pairs via the London penetration depth λ_L [60].

We will now consider the electromagnetic symmetry structure near the surface S of the superconducting boundary. We chose S parallel to the x, y -plane with $z = 0$. Inside the boundary (i.e. for z negative) the macroscopic wave function Ψ describes the state of the superconducting electron pairs (Cooper pairs, see section 1.1.2.4). The number density of Cooper pairs n_c is given by $n_c = \Psi^2$. Quantum mechanics requires that the macroscopic wave function Ψ and its first derivatives $\nabla\Psi$ and $\frac{\partial\Psi}{\partial t}$ must be continuous functions of (t, z) [63]. Thus, the wave function Ψ cannot drop to zero discontinuously at the film's surface. Two possible classes of solutions to the Schroedinger equation present themselves: Either we require $\Psi \rightarrow 0$ as $z \rightarrow 0$ which corresponds to the infinite square well solutions of the Schroedinger equation [63] or we require Ψ to decay exponentially with z for $z > 0$, corresponding to the finite square well solutions of the Schroedinger equation [63].

It is a well known fact that Cooper pairs can tunnel from one superconducting film to another through a thin dielectric barrier [4]. This seems to suggest that the correct class of solutions for Cooper pair wave functions inside a superconductor are the finite square well solutions, since the infinite square well solutions would imply that no communication between wave functions of particles in different wells (i.e. in different superconductors) is possible. Furthermore, if the dielectric barrier is thin enough a weak supercurrent can flow from one film to the other. This weak-link supercurrent and a number of similar effects are collectively called the Josephson Effect, and they arise due to the two films' order parameters overlapping in the barrier [4]. Thus, it appears that the correct class of solutions are indeed the finite square well solutions.

Returning to the problem of evaluating the electromagnetic symmetry structure near the surface S and assuming the solutions of Ψ to correspond to finite square well solutions of the Schroedinger equation, the wave function penetrating into the vacuum has to be of the form [63]:

$$\Psi = \Psi_0 e^{-\beta z} \quad (3.30)$$

with

$$\beta = \left(\frac{2m_c}{\hbar^2} |E| \right)^{-\frac{1}{2}} \quad (3.31)$$

where $m_c = 2m_e$ is the mass of the superconducting electron pairs (Cooper pairs), m_e is the electronic mass, $|E|$ is the depth of the potential well, $z > 0$ is the distance from the boundary and Ψ_0 is the value of Ψ on the surface of the superconducting boundary.

The depth of the potential well for Cooper pairs penetrating the vacuum/dielectric region is of order $|E| = 10eV$ [4], yielding the characteristic decay constant $\beta \approx 2.3 \times 10^{10} \text{m}^{-1}$. Since the supercon-

ducting electron density scales as Ψ^2 we find that it decays to zero within approximately 0.1nm of the surface of a conventional superconductor. Using the expression for the London penetration depth λ_L in terms of Ψ [4] we obtain:

$$\lambda_L = \sqrt{\frac{m_c}{e^2 \mu_0 \Psi^2}} \quad (3.32)$$

where m_c is the cooper pair mass and e is the electronic charge.

From substituting (3.32) into (3.11) we obtain $m_\gamma \propto \Psi$. Recalling $\lambda_{crit} = 2\pi\lambda_L$ we can now write variations in the photonic mass m_γ and critical wavelength λ_{crit} in terms of the exponential decay of Ψ :

$$m_\gamma = m_{\gamma,0} e^{-z\beta} \quad (3.33a)$$

$$\lambda_{crit}(z) = \lambda_{crit,0} e^{z\beta} \quad (3.33b)$$

where $m_{\gamma,0}$ is the photonic mass inside the boundary, λ_{crit} is the corresponding critical wavelength inside the boundary, z is the distance from the boundary and we have assumed that the separation between boundaries $z \gg \beta$ so that only one of the sc-boundaries contributes to the photon mass. The case of overlapping wave functions is significantly more complicated since Josephson effects and magnetic flux quantisation in the cavity would have to be considered.

Thus, the photonic mass is non-zero in a thin sheath near the surface of the superconducting boundary and decays exponentially with distance from the boundary, on length scales of order 1Å. Since the mass of photons inside this sheath is increased from their vacuum value they are traveling more slowly than their vacuum velocity, effectively decreasing their wavelength. Consequently, the thin superconducting layer has an effect similar to extending the distance between cavity walls. Photon velocity and the allowed modes will be discussed in more detail in the following section.

In a cavity of width 100 nm with two superconducting boundaries each having a massive electromagnetism layer of thickness $\approx 1\text{\AA}$ this corresponds to 1 part in 500 of the cavity volume (fig. 3.7). Since it was shown by [10] that changes of 1 part in 10^8 of the cavity energy can lead to measurable changes in the superconducting critical field (sec. 3.2.1) this thin region of massive electromagnetism may well be relevant to practical cryogenic systems.

In conclusion, we have demonstrated that neither the conventional form of the Casimir effect, as derived from the Maxwell equations [62], nor the massive Casimir effect, as derived from the Proca equations [78] are suitable to describe the Casimir effect in a cavity with superconducting boundaries. The conventional Casimir effect is unable to deal with the thin, highly refractive massive-em layer

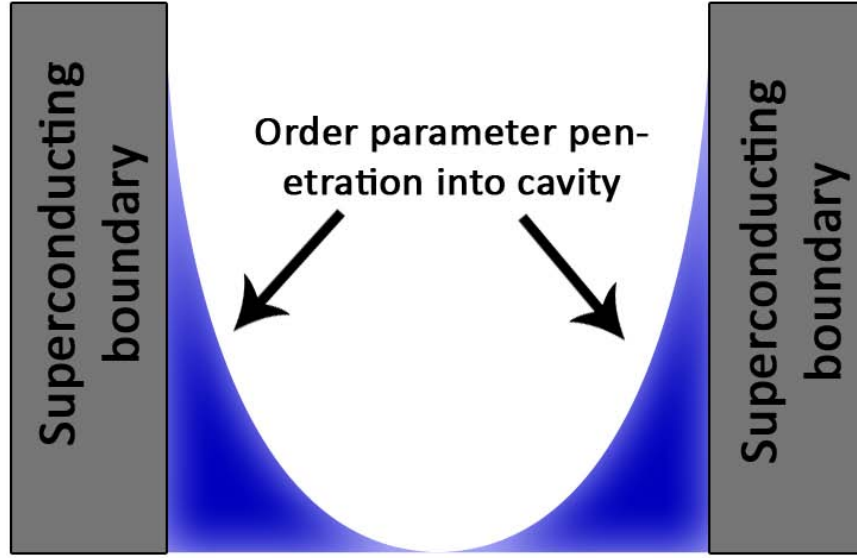


Figure 3.7: Symmetry structure of the cavity with superconducting boundaries (not to scale).

near the boundary surface which results from Cooper pair tunneling, while the massive Casimir effect erroneously assumes a photon mass constant throughout the cavity. In the context of the experiments presented by Bimonte et al. [10] [73] [74] this failure of both the conventional as well as the massive Casimir effect equations to correctly implement the physics of the superconducting cavity is quite a significant result since it indicates that no good quantitative framework exists in which to evaluate data obtained by Bimonte's experiment.

3.5.7 Cavity Types

Based on the exponential decay of the photon mass (and consequently of the critical wavelength λ_{crit}) as outlined in section 3.5.6.2 we can now identify three different types of parallel plane cavities with superconducting boundaries.

1. Cavities with superconducting boundary separation $s \leq (2\beta)^{-1}$. There is strong overlap between Cooper pair wave functions from opposite cavity boundaries, and the photon mass m_γ is approximately constant throughout the cavity. In this case the expressions for the massive Casimir effect as derived by Barton and Dombey [78] and as discussed in section 3.5.5 apply. Since in section 3.5.6.2 we have estimated $\beta \approx 10^{10}m$ this condition only holds for cavities with sub-Å separation, or for those with the cavity volume material selected specifically to reduce β .

2. Cavities with superconducting boundary separation a in the range $\lambda_{crit,0} \geq a > (2\beta)^{-1}$, where $\lambda_{crit,0}$ is the critical wavelength at the boundary surface. In these cavities no significant overlap of Cooper pair wave functions from opposite boundaries occurs, and electromagnetism can be considered Maxwellian throughout most of the cavity. Photon velocity is reduced by massive photon effects near the boundaries, decreasing the effective wavelength of photons with wavelengths $\lambda_{vac} \approx \lambda_{crit}$ near the boundary. A detailed numerical solution for this cavity type is provided in section 3.6.
3. Cavities with superconducting boundary separation $a > \lambda_{crit,0} > (2\beta)^{-1}$. In these types of cavity, waves with supercritical wavelengths $\lambda_{vac} > \lambda_{crit}$ can propagate freely near the centre. However, there will be a critical distance z_{crit} from the cavity boundary at which the exponentially decaying critical wavelength λ_{crit} matches λ_{vac} , i.e. $\lambda_{vac} = \lambda_{crit,0} e^{z_{crit}\beta}$. For $z < z_{crit}$ photons of wavelength λ will decay exponentially. We recall that from section 3.5.3 that η_p is entirely imaginary for supercritical modes, i.e. $\eta_p = 1/v_g = ik$. Taking into account the varying photon mass with distance from the boundary, it is extremely difficult to find analytical solutions for the wave function of the supercritical modes, since they would require the solution of the Proca equations in the presence of a finite-height, finite-width, non-square potential well with varying height and width. Nevertheless we will find a way of dealing with these modes in section 3.6.

The discussion of type 2 and 3 modes is entirely focused on transverse-polarization photons. Longitudinal photons only have to be considered for type 1 cavities, where there is significant Cooper pair wave function overlap. For all other cavities the Maxwellian-em center does not propagate longitudinal photons.

3.6 The Casimir Effect for Cavities with Superconducting Boundaries

In the previous section 3.5 we established that inside a superconductor Maxwellian electromagnetism is replaced by Proca electromagnetism in order to allow for non-zero rest mass photons. We discussed the Casimir effect for non-zero rest mass photons (section 3.5.5) and came to the conclusion that it is unsuitable for evaluating the Casimir effect in the presence of superconducting boundaries (section 3.5.6.2). While this result is in itself significant, we wish to at least estimate the magnitude of the Casimir effect in the presence of superconducting boundaries.

In the course of this section we will show how Lifshitz theory can be employed in order to achieve

an estimate of the order of magnitude of the corrections required to the Maxwellian-em Casimir effect. We begin by introducing the integrals which govern the magnitude of the Casimir effect in the presence of real material boundaries, rather than perfect reflectors. We then discuss the terms required in order to evaluate the equations presented and conclude with an evaluation of the Casimir effect for a cavity with superconducting aluminium boundaries. Finally, this evaluation will allow for an estimate of the order of magnitude corrections required to the estimate of the aluminium film critical temperature T_c and critical field H_c according to equation (3.8).

3.6.1 Lifshitz Theory

In section 3.2 we outlined how an expression for the Casimir effect can be obtained by considering a cavity with perfectly reflecting boundaries and calculating its vacuum energy as the sum of the zero point energies of all electromagnetic field modes permitted in the cavity. The allowed modes have been determined as being all those modes which can be made to go to zero at both cavity boundaries simultaneously, i.e. those modes with angular frequency ω satisfying $c/(2\omega) = \lambda/2 = a/n$, with $n \in \text{integer}$ and a the cavity width. As such we have effectively treated the Casimir cavity as an infinite square well of width a .

We now wish to consider cavities with real material boundaries. Since real materials are not perfect reflectors, the allowed modes of the cavity are now found by finding the solutions to Maxwell's equations inside the cavity and inside the cavity boundaries. Any real material reflector will allow incident electromagnetic radiation to penetrate into the reflector, with the intensity of the penetrating radiation decaying exponentially with a characteristic decay constant known as the skin depth [76]. Consequently, in going from perfect reflectors to real material boundaries we have transformed the problem of finding the allowed modes of the cavity from the infinite square well problem to the finite square well problem.

Finding all the allowed solutions to the finite square well problem is a mathematically involved process, and various approaches exist. A good introduction to the problem is given by Bransden and Joachain [63]. The full derivation of the Lifshitz theory describing the Casimir force for cavities with real material boundaries is given by Milonni [62].

The Casimir force for a cavity with real material boundaries according to Lifshitz theory can be written as [62]:

$$F_L(a) = -\frac{\hbar}{2\pi^2 c^3} \int_1^\infty \int_0^\infty p^2 \xi^3 \epsilon_3^{3/2} \left(\left[\frac{(\epsilon_3 s_1 + \epsilon_1 p)(\epsilon_3 s_2 + \epsilon_2 p)}{(\epsilon_3 s_1 - \epsilon_1 p)(\epsilon_3 s_2 - \epsilon_2 p)} e^{2\xi p \sqrt{\epsilon_3} d/c} - 1 \right]^{-1} + \left[\frac{(s_1 + p)(s_2 + p)}{(s_1 - p)(s_2 - p)} e^{2\xi p \sqrt{\epsilon_3} d/c} - 1 \right]^{-1} \right) d\xi dp \quad (3.34)$$

where

$$s_{1,2}^2 = p^2 - 1 + \frac{\epsilon_{1,2}}{\epsilon_3} \quad (3.35)$$

with a the boundary separation and ξ the magnitude of the imaginary frequency $i\xi$. The symbols $\epsilon_1, \epsilon_2, \epsilon_3$ are the dielectric functions of the first and second boundary and cavity spacer material respectively. The dielectric functions are discussed in detail in section 3.6.2.

The integral is over all imaginary frequencies $i\xi$ ($\xi \in real$) as a matter of mathematical convenience during the derivation. No physical interpretation of the nature of complex frequencies is required. Rather, an integral over all complex frequencies has been employed during the derivation to obtain results relevant to the real frequency allowed modes, by using complex calculus identities [62].

3.6.2 Dielectric Functions and the Refractive Index

In order to evaluate equation (3.34) explicitly we require expressions for the dielectric functions $\epsilon_{1,2,3}$ as functions of imaginary frequency magnitude ξ . In general, a material's dielectric function can be determined from its refractive index. We recall that the refractive index $\eta_p = n_p + ik_p$ (section 3.5.2). Then the dielectric function ϵ of the material is given by:

$$\begin{aligned} \epsilon &= \eta_p^2 \\ &= (n_p + ik_p)^2 \end{aligned} \quad (3.36)$$

In section 3.6.3 we will discuss how to find the effective dielectric function ϵ_3 of the vacuum near a superconducting boundary by employing Proca electromagnetism. Section 3.6.4 is dedicated to a discussion of the dielectric functions $\epsilon_{1,2}$ of the real material boundaries.

3.6.3 Dielectric Function of the Vacuum

We recall from section 3.5.2 that the complex phase refractive index η_p of a material can be obtained from the photon phase velocity v_p as $n_p + ik_p = c/v_p$ yielding

$$\epsilon(\omega) = \frac{c}{v_p(\omega)^2} \quad (3.37)$$

where $v_p(\omega)$ is the electromagnetic phase velocity according to equation (3.15), for an electromagnetic wave of wavelength $\lambda = 2\pi c/\omega$, and with ω the complex frequency of the electromagnetic wave. The critical wavelength λ_{crit} required to evaluate equation (3.15) decays exponentially away from the boundaries according to equation (3.33b). For type 2 and 3 cavities, the explicit form of the dielectric function of the vacuum as a function of wavelength λ and distance z from the nearest superconducting boundary is then given by

$$\epsilon_3(\omega, z) = 1 - \left(\frac{c^2}{\omega^2 \lambda_{crit}^2} e^{-2\beta z} \right) \quad (3.38)$$

Since the expression for the phase velocity v_p has been derived directly from the Klein-Gordon equation it can be extended to complex frequencies without any modifications. The reason is that the Klein-Gordon equation itself is defined over the entire complex plain. It is immaterial whether such an extension does have a physical interpretation in the context of the original derivation of $v_p(\omega)$. Re-writing equation (3.38) in terms of the imaginary frequency $i\xi$ we obtain

$$\epsilon_3(\xi, z) = 1 - \left(\frac{c^2}{(i\xi)^2 \lambda_{crit}^2} e^{-2\beta z} \right) \quad (3.39)$$

which can be simplified to

$$\epsilon_3(\xi, z) = 1 + \left(\frac{\xi_{crit}^2}{\xi^2} e^{-2\beta z} \right) \quad (3.40)$$

where we have introduced the critical frequency $\xi_{crit} = c/\lambda_{crit}$. Equation (3.40) can be found to be real over all imaginary frequencies $i\xi$.

3.6.4 Dielectric Function of Real Material Boundaries

For the real material boundaries we can approximate their dielectric function using Drude theory. In Drude theory the conduction electrons in a metal are essentially treated as a free electron gas, with characteristic plasma frequency ω_p and relaxation frequency γ [76]:

$$\epsilon_{1,2}(\omega) = 1 - \frac{\omega_p^2}{\omega^2 + \gamma^2} + i \frac{\omega_p^2 \gamma}{\omega^3 + \omega \gamma^2} \quad (3.41)$$

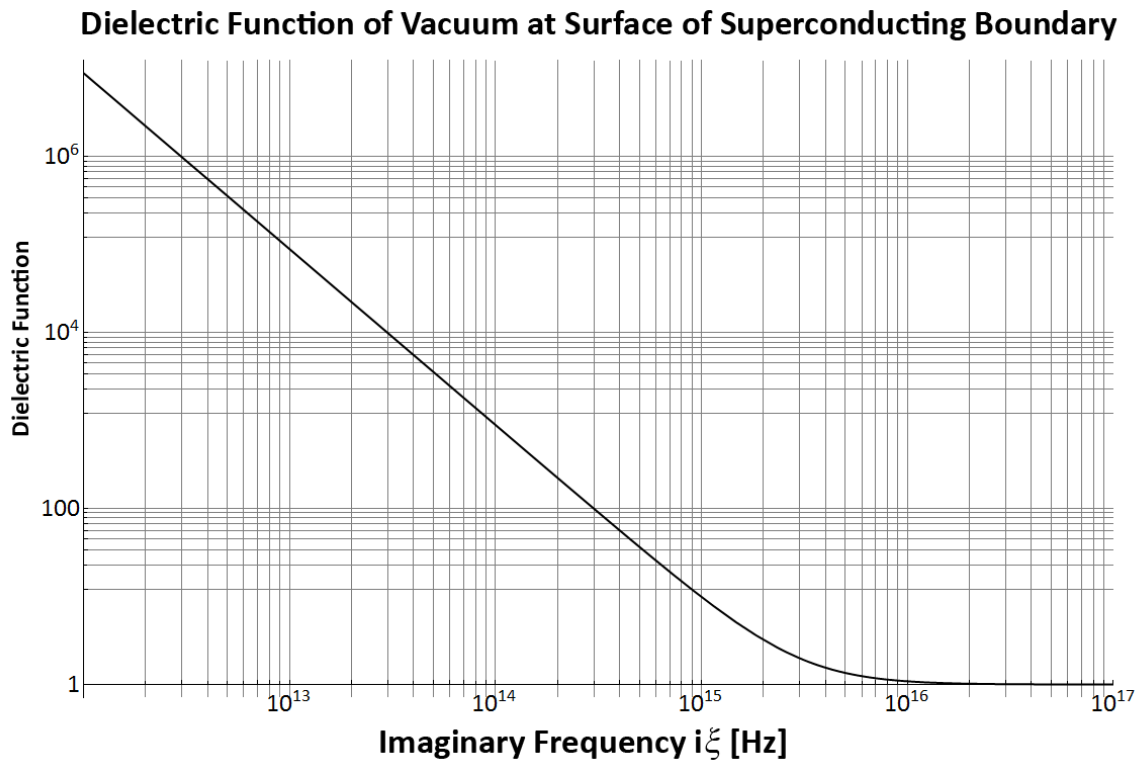


Figure 3.8: Dielectric function of the vacuum due to heavy photon effects according to eq.(3.40) for the case of aluminium boundaries ($\lambda_L = 16nm$) and zero distance to the boundary surface.

where ω is the complex angular frequency of the incident photons. The real and imaginary parts of eq.(3.41) are labeled $\epsilon'_{1,2}$ and $\epsilon''_{1,2}$, respectively.

Equation (3.41) can be used directly with the Lifshitz equation (3.34) where it will be integrated over all positive imaginary frequencies. However, in some situations such an approach may not be convenient. Drude theory is only an approximation, and especially towards the high-energy end of the optical spectrum it may differ from the real values. If experimental data describing the dielectric constant $\epsilon_{1,2}$ of the boundary material is available it may be desirable to replace the equation (3.41) with a fit to the experimental data. Since experimental data is in general only available over real frequencies, such a fit is not directly applicable for computing the Casimir force according to equation (3.34). In this case the real part of the dielectric constant for imaginary frequencies can be found from the imaginary part of the dielectric constant at real frequencies by employing the Kramers-Kronig relation [62]:

$$\epsilon_{1,2}(\xi) = 1 + \frac{2}{\pi} \int_0^{\infty} \omega \frac{\left(\frac{\omega_p^2 \gamma}{\omega^3 + \omega \gamma^2} \right)}{\omega^2 + \xi^2} d\omega \quad (3.42)$$

The expressions for the reflectivity of the boundaries discussed above are solely based on the normal state optical parameters of the materials, since a direct analytical combination of the material based optical effects and massive-em dispersion is impossible. As such, all estimates presented for the Casimir effect in a cavity with superconducting boundaries will only contain the corrections due to the effect of the broken symmetry inside the cavity volume. Corrections due to changes in boundary reflectivity have to be treated separately. Consequently, changes to the binding energy ΔU_{bind} predicted by our implementation of Lifshitz theory have to be added to the corrections predicted by Bimonte [10] due to the changes in boundary reflectivity reported by Glover [71].

A comparison between the predictions of equation (3.41) and experimental data obtained from Palik [12] shows a very good match between theory and experimental data, especially over the low frequency range (figure 3.9). The data plotted is for a gold film, with plasma frequency $\omega_p = 9eV/h$ and inverse relaxation time $\gamma = 0.045eV/h$. In the course of this chapter we will use the Drude models for Gold (Au), Aluminium (Al) and Beryllium (Be), which are summarized in table 3.6.4, below.

3.6.5 Implementation of Lifshitz Theory

Section 3.6.2 has established the correct functional form for the dielectric constants $\epsilon_{1,2,3}(i\xi)$ (equations (3.40),(3.41)) for using Lifshitz theory to calculate the Casimir force in parallel plane geometry cavities with normal state, real material boundaries. Integral (3.34) cannot be solved analytically.

Material	Plasma frequency $\omega_p[eV/h]$	Relaxation Frequency $\gamma[eV/h]$	Reference
Aluminium (Al)	12.7	0.155	Beaglehole [79]
Gold (Au)	8.5	0.045	Palik [12]
Beryllium (Be)	18.4	29.5	LaVilla [80]

Table 3.1: Experimental values for the plasma frequency ω_p and relaxation frequency γ in order to evaluate Drude theory according to equation (3.41). All values for the plasma frequency ω_p and relaxation frequency γ are given in units of eV/h . This convention is often used in the literature in order to facilitate comparison with photon energies.

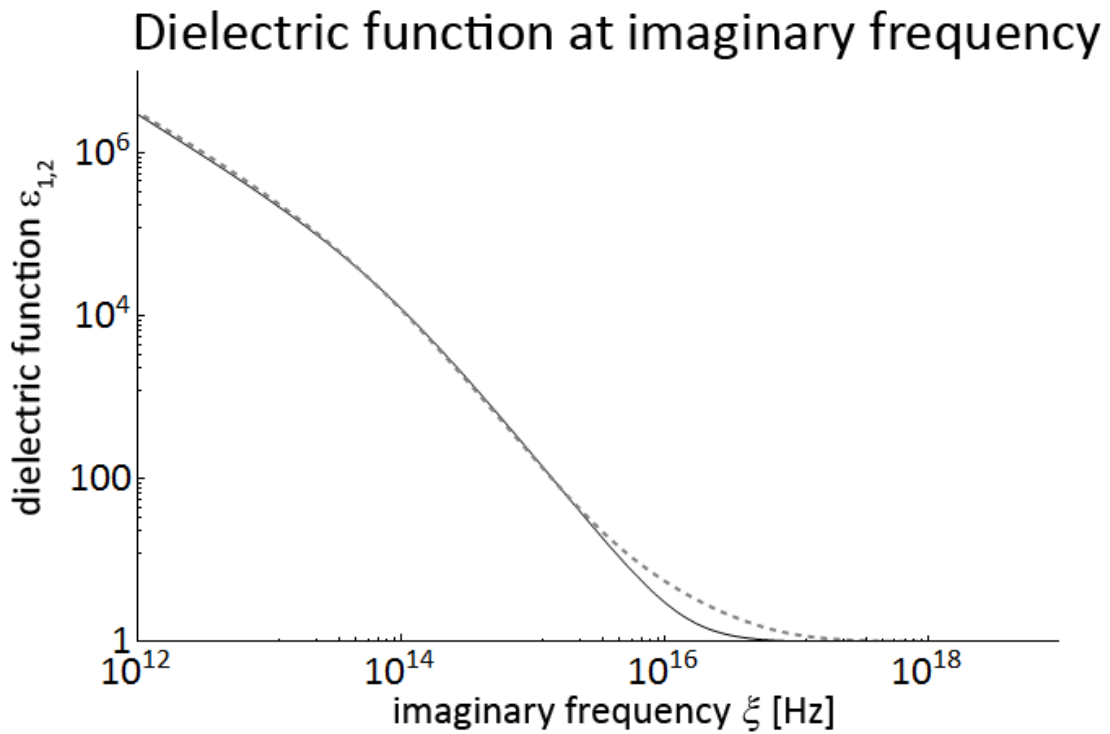


Figure 3.9: Dimensionless dielectric function $\epsilon_{1,2}$ of gold as a function of imaginary frequency ξ . The solid black line represents the predictions of the Drude model (eq. (3.41)), while the dashed gray line has been recovered from experimental data provided in Palik [12].

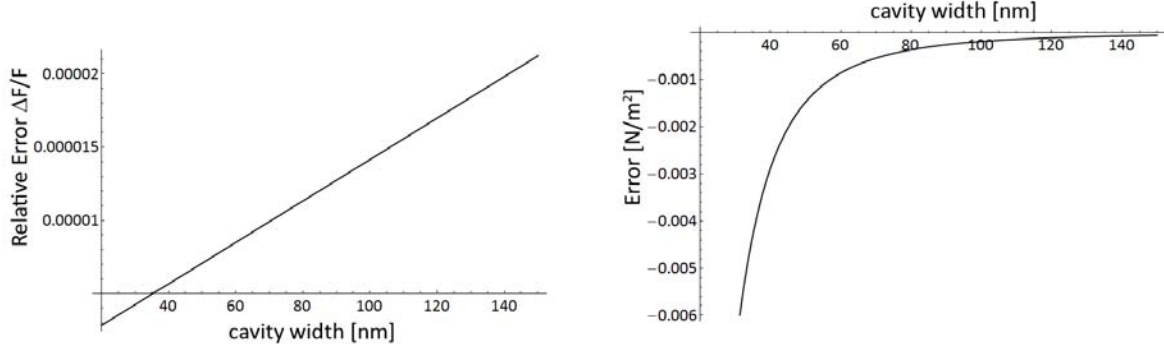


Figure 3.10: Relative error $\Delta F/F_0$ (left) and absolute error $\Delta F = F_L - F_0$ (right) of our implementation of Lifshitz theory for the case $\epsilon_3 = 0, \epsilon_{1,2} \rightarrow \infty$.

Instead, we are employing Wolfram Research's *Mathematica* to attempt a numerical evaluation.

In order to assess the results obtained by numerical evaluation of (3.34), we let $\epsilon_3 = 1$ which corresponds to the cavity volume being a vacuum. We also let $\epsilon_{1,2} \rightarrow \infty$ which corresponds to perfectly reflecting boundaries. In this way, if our implementation of Lifshitz theory is correct, we should recover the same force $F_L(a)$ as obtained from the analytical expression (3.3) for the Casimir force $F_0(a)$ of a cavity with perfectly reflecting boundaries separated by a vacuum. We use F_L to refer to the Casimir force according to Lifshitz theory, while F_0 refers to the analytical expression for the Casimir force for the case of perfectly reflecting boundaries. Evaluating expression (3.34) for the Lifshitz theory based force $F_L(a)$ we obtain the absolute error $\Delta F = F_L - F_0$ as well as the relative error $\Delta F/F_0$ as a function of cavity width a (figure 3.10). As can be seen from figure 3.10 the relative error remains below 1 part in 10^4 for small boundary separations (for large boundary separations F_L quickly goes to zero). We are satisfied with the precision of our evaluation and proceed.

In this section we will present methods for the quantitative evaluation of the Casimir effect in type 2 and type 3 cavities. We begin by considering wave propagation in the vacuum near superconducting boundaries in general. It seems logical that the treatment of type 2 cavities should be significantly easier than the treatment of type 3 cavities, since the spectrum of allowed modes in a type 2 cavity contains no supercritical modes. However, since Lifshitz theory obtains its results from integrating over ALL imaginary frequency modes, including imaginary supercritical modes (i.e. $i\lambda > i\lambda_{crit}$), both types of cavity require a valid description of supercritical modes to be implemented in their mathematical treatment.

3.6.6 Effective Dielectric Function of the Cavity Volume

The first step towards using Lifshitz theory according to eq. (3.34) to determine the Casimir force for a cavity with superconducting boundaries is to establish the dielectric functions $\epsilon_{1,2,3}$ required. As was already indicated in section 3.5.6.2, the increased refractive index as compared to its vacuum value (and, consequently, the increased dielectric function ϵ_3) of the cavity volume results in an increased phase change in a mode traversing the cavity. Thus it effectively increases the cavity width. We cannot simply use equation (3.40), since it varies with distance from the cavity boundaries z and imaginary frequency ξ . Lifshitz theory, however, requires an expression of ϵ_3 as a function of ξ only. It is possible to proceed by calculating the average dielectric function of the cavity. By integrating equation (3.40) we obtain:

$$\bar{\epsilon}_3(\xi) = \frac{\int_0^{a/2} 1 + \left(\frac{\xi_{crit}^2}{\xi^2} e^{-2\beta z} \right) dz}{a/2} \quad (3.43)$$

where we have assumed the cavity to be perfectly symmetric and obtained the average by integrating over the cavity half-width $a/2$. The average dielectric function $\bar{\epsilon}_3$ will yield the correct phase change for a mode traversing the cavity.

It is tempting to now use $\bar{\epsilon}_3(\xi)$ as the expression for the dielectric function $\epsilon_3(\xi)$ in equation (3.34) for the Casimir force and in this way implement the dielectric function of the vacuum and the change to the effective cavity width for the superconducting boundary cavity at the same time. This does not yield the correct result. The reason for this is that Lifshitz theory determines the allowed modes from the effective reflectivity of the cavity boundaries, and this effective reflectivity is calculated from the local differences in dielectric functions $\epsilon_{1,2}(\xi)$ and $\epsilon_3(\xi)$, respectively. Since the value for $\epsilon_3(\xi)$ (according to eqn.(3.40)) on the surface of the boundary (i.e. $z = 0$) is much larger than the average value $\bar{\epsilon}_3(\xi)$ such a treatment would yield significant errors in the estimate of the boundary reflectivities.

In order to obtain a correct estimate of the boundary reflectivity at frequency ξ , it is therefore necessary to use the local vacuum dielectric constant $\epsilon_3(\xi, z = 0)$ according to equation (3.40). This method yields two problems:

1. It does produce a wrong estimate of the effective cavity width, since the total phase change across the cavity has to be calculated according to eq.(3.43) rather than eq.(3.40)
2. It does not handle supercritical modes, which have a vanishing imaginary phase velocity near the boundary

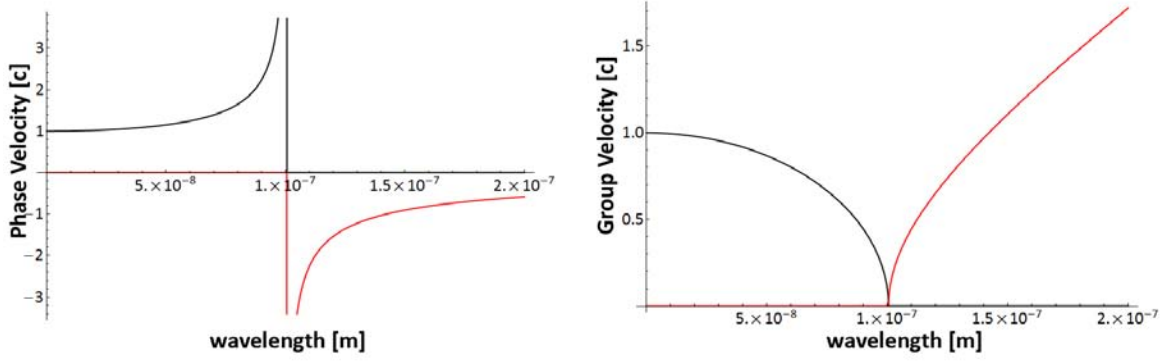


Figure 3.11: The phase velocity v_p (left) and group velocity v_g (right) of Aluminium ($\lambda_{crit} \approx 100nm$) as a function of wavelength. The graphs show the real (black) and imaginary (red) components of the respective complex velocities. Note that v_p, v_g are either purely imaginary or purely real over the entire real wavelength axis.

Problem one will be dealt with later, in section 3.6.8 while problem 2 will be addressed in section 3.6.7.

3.6.7 Supercritical Modes

In our search for an implementation of Lifshitz theory that can be used to calculate the Casimir force between parallel superconducting boundaries we now turn to the problem of supercritical modes, i.e. modes with $\lambda > \lambda_{crit}(z = 0)$. As was already outlined in section 3.5.7, these modes will be equal to the vacuum critical wavelength at a distance Δz from the boundaries, i.e. $\lambda = \lambda_{crit}(\Delta z)$ where the critical wavelength of the vacuum due to Cooper pair tunneling $\lambda_{crit}(\Delta z)$ is calculated according to eq.(3.33b). Since $\lambda > \lambda_{crit}(z)$ for $z < \Delta z$ the refractive index $n_p + ik_p$ is entirely imaginary in the supercritical region ($n = 0$) (figure 3.11). For a purely imaginary refractive index, dissipationless photon propagation is impossible and no zero-point modes exist.

The modes under consideration are subcritical for the fraction of the cavity volume with $z > \Delta z$. For each half-cavity with the boundary surface at $z = 0$ and positive- z pointing away from the boundary, the region $a/2 > z > \Delta z(\lambda)$ is the region in which modes of wavelength λ can propagate freely. Thus, the supercritical modes really see a cavity whose effective width is a function of wavelength. Modes of sufficiently long wavelength may never reach the material cavity boundaries in order to be reflected by them. Rather, the modes see a finite potential well of variable barrier height and width. The variation of the phase velocity, which is essentially identical to the depth of the potential well, is illustrated in figure 3.12. The plot is not to scale in order to allow for better visualization of the effective variations in the phase velocity, which are usually confined to an extremely thin layer near

Variation of phase velocity across cavity

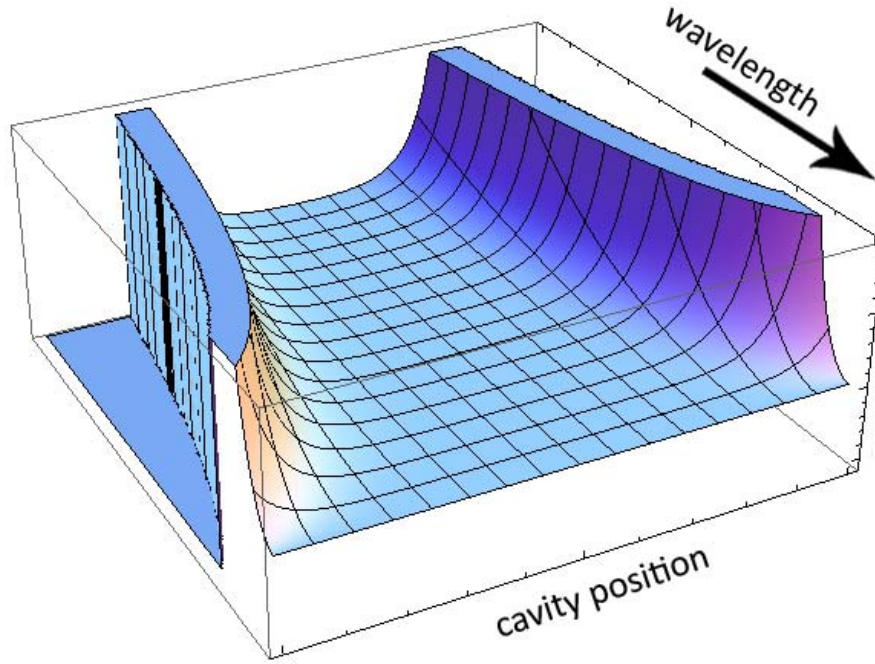


Figure 3.12: Illustration of the variation of the real part of the phase velocity with cavity position (not to scale). The cavity boundaries are located at the left and right hand extremities of the plot.

the boundary surface. The actual wave functions of the modes penetrating into the forbidden region would be extremely difficult to calculate. However, considering the nature of Lifshitz theory, we realize that the exact wave functions are not actually required. The only parameter of importance is the height of the barrier (i.e. the magnitude of the decay constant [63]) at the boundary, which in the context of Lifshitz theory is defined by the dielectric function. In this case the dielectric function of the vacuum has to be taken as $\epsilon_3(\xi, \Delta z)$ rather than $\epsilon_3(\xi, 0)$. The value of Δz may be computed from equation (3.33b), using $\lambda = \lambda_{crit}(\lambda_L, z)$ and solving for z :

$$\Delta z(\lambda, \lambda_L) = \begin{cases} \lg\left(\frac{\lambda}{2\pi\lambda_L}\right) / \beta & \text{if } \lambda \text{ is supercritical} \\ 0 & \text{if } \lambda \text{ is subcritical} \end{cases} \quad (3.44)$$

As mentioned above, the mode may not actually reach the material boundary of the cavity. The dielectric constant for the cavity volume $\epsilon_3(\xi, z)$ then has to be computed at $z = \Delta z$ from the boundary. Since Lifshitz theory is formulated as an integral over the imaginary frequencies $i\xi$ we replace the wavelength argument λ with the frequency argument c/ξ . We now have a complete expression for the effective dielectric constant $\epsilon_3(\xi, z)$ required for calculating the reflectivity of the boundaries with

dielectric constant $\epsilon_{1,2}(\xi)$:

$$\epsilon_3(\xi) = 1 + \left(\frac{c^2}{\xi^2 \lambda_{crit}^2} e^{-2\beta \Delta z(\xi, \lambda_L)} \right) \quad (3.45)$$

The above expression (3.45) is the final expression we will use for evaluating (3.34) in the case of the Casimir cavity with superconducting boundaries. The attentive reader will have realized, however, that expression (3.45) is only valid at the points where the relevant vacuum mode is reflected, rather than throughout the entire cavity. Therefore using eq.(3.45) to calculate the Casimir force according to Lifshitz theory (eq. (3.34)) we underestimate the phase change of the vacuum modes traversing the cavity by overestimating ϵ_3 . This problem will be addressed in the following section.

3.6.8 Effective Width of the Cavity

We will now deal with the problem of finding the correct effective cavity width a_{eff} . This problem consists of two parts: We have to implement the reduced width of the cavity in the case of supercritical modes, which cannot travel the entire width of the cavity (see section 3.6.7), and we have to find a way to allow for the errors in phase change for modes traversing the cavity introduced by assuming $\epsilon_3(\xi)$ to be constant throughout the entire cavity (rather than employ $\bar{\epsilon}_3(\xi)$).

The first part of the problem is easily solved. Supercritical modes approach the cavity boundaries to within $\Delta z(\xi)$ according to eq.(3.44). Thus, the cavity width a has to be replaced with the frequency dependent effective cavity width $a_{eff}(\xi)$:

$$a_{eff}(\xi) = \begin{cases} a & \text{if } c/\xi \text{ is subcritical} \\ a - 2\Delta z(\xi) & \text{if } c/\xi \text{ is supercritical} \end{cases} \quad (3.46)$$

where the factor of 2 has been introduced for supercritical modes since a layer of thickness $\Delta z(\xi)$ at each end of the cavity is inaccessible to supercritical modes.

The remaining part of the problem is that, by treating $\epsilon_3(\xi)$ as independent of z , we have not taken the phase propagation across the cavity into account properly. As was outlined in section 3.6.3 the dielectric function increases the effective cavity width by decreasing the effective wavelength. Since we are using the local dielectric function $\epsilon_3(\xi)$ according to equation (3.45) rather than the average dielectric function $\bar{\epsilon}_3(\xi)$ according to eq. (3.43) we are overestimating the effective dielectric constant significantly with respect to the effective wavelength of the mode ξ . However, we require $\epsilon_3(\xi)$ in order to properly calculate the reflective behaviour of the cavity boundaries.

We use a geometric solution. Since the effect of $\bar{\epsilon}_3(\xi)$ is to alter the phase change of the mode ξ traversing the cavity with respect to its vacuum value, we can also achieve the correct phase change by manipulating the effective cavity width $a_{eff}(\xi)$ instead. From Lifshitz theory the relative change Γ to the phase refractive index n_p scales linearly with the fourth root of the relative change to the effective cavity width a_{eff} . Since in the subcritical region the imaginary component of the refractive index $ik_p = 0$ we find $\epsilon_3 = n_p^2$ and we can write

$$\begin{aligned} F(a, \Gamma\epsilon_3) &= F(\Gamma^{1/8}a, \epsilon_3) \\ F(\Gamma^{-1/8}a, \Gamma\epsilon_3) &= F(a, \epsilon_3) \end{aligned} \quad (3.47)$$

This relation can be easily tested by evaluating Lifshitz theory according to eq.(3.34) with $\epsilon_{1,2} = \infty$ (perfectly reflecting boundaries) and substituting a_{eff} with $\Gamma \in Real \geq 1$ into eq.(3.34).

If we know the factor Γ by which we overestimate ϵ_3 we can make geometric corrections to a_{eff} in order to compensate for this. Since we know that the correct value for ϵ_3 with respect to calculating the phase change for a mode traversing the cavity is given by $\bar{\epsilon}_3(\xi)$ (eq.(3.43)) we can find Γ by dividing eq.(3.45) by (3.43). We obtain the equation for the compensation factor Γ :

$$\Gamma(\xi) = \left(\frac{\left(\int_{\Delta z(\xi)}^{a/2} 1 + \left(\frac{\xi_{crit}^2}{\xi^2} e^{-2\beta z} \right) dz \right) / (a/2 - \Delta z(\xi))}{1 + \left(\frac{\xi_{crit}^2}{\xi^2} e^{-2\beta \Delta z(\xi)} \right)} \right) \quad (3.48)$$

where the lower limit of the integral is given by Δz rather than 0 in order to take into account the cavity region in which the mode ξ is supercritical. The divisor $a/2$ in the numerator has been similarly modified to $a/2 - \Delta z(\xi)$ in order to allow for the correct average to be calculated.

Using the correction factor $\Gamma(\xi)$ from eq.(3.48) and the effective width a_{eff} calculated in eq.(3.46) we can now substitute the Γ -corrected effective width $\Gamma(\xi)^{-1/8}(a - 2\Delta z(\xi))$ for the width d when using the Lifshitz formula as outlined in equation (3.34). The geometric compensation factor $\Gamma(\xi)^{1/8}$ and the effective cavity width reduction $2\Delta z$ have been plotted in figure 3.13.

We now have a correct implementation of both the dielectric constant of the cavity volume ϵ_3 (eq.(3.45)) and the Γ -corrected effective cavity width $d = \Gamma(\xi)^{-1/8}a_{eff}(\xi)$ (eqs. (3.46) and (3.48)) for the cavity with superconducting boundaries. However, there is still a problem with the implementation of the dielectric function of the cavity boundaries $\epsilon_{1,2}$, which will be tackled in section 3.6.9, below.

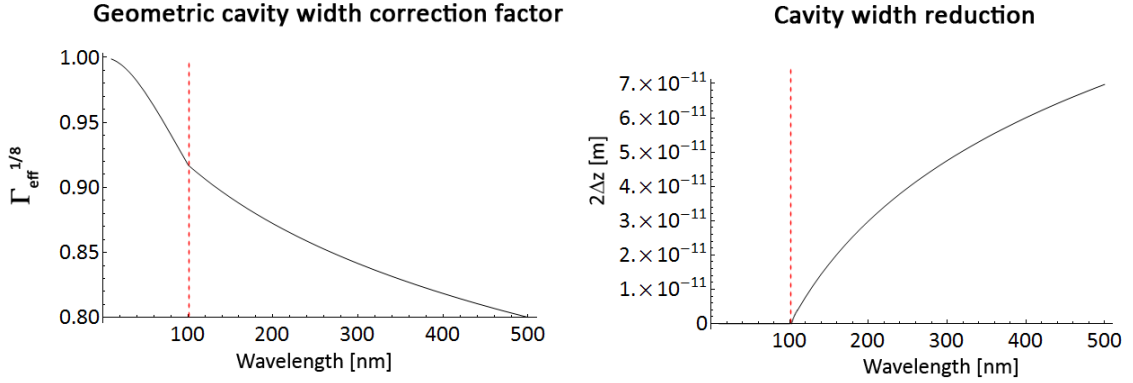


Figure 3.13: Dimensionless geometric compensation factor $\Gamma_{\text{eff}}^{-1/8}$ (left) and cavity width reduction $2\Delta z$ (right) for aluminium as functions of wavelength. The dashed red line marks the transition from subcritical to supercritical regime.

3.6.9 Effective Dielectric Function of the Cavity Boundaries

The dielectric function $\epsilon_{1,2}$ describes the reflectivity of the cavity boundaries as seen by the zero point modes. However, supercritical modes do not actually penetrate all the way to the cavity boundaries, but instead get reflected a distance Δz from the boundary surface. For these modes we require $\epsilon_{1,2}$ to be equal to the local dielectric function of the vacuum $\epsilon_3(\xi, \Delta z)$ according to equation (3.40), while subcritical modes require the Drude theory implementation of $\epsilon_{1,2}(\xi)$ according to eq.(3.41). The correct implementation of $\epsilon_{1,2}$ can then be written as:

$$\epsilon_{1,2}(\xi) = \begin{cases} 1 - \frac{\omega_p^2}{(i\xi)^2 + \gamma^2} + i \frac{\omega_p^2 \gamma}{(i\xi)^3 + (i\xi)\gamma^2} & \text{if } c/\xi \text{ is subcritical} \\ 1 + \left(\frac{c^2}{\xi^2 \lambda_{\text{crit}}^2} e^{-2\beta\Delta z(\xi, \lambda_L)} \right) & \text{if } c/\xi \text{ is supercritical} \end{cases} \quad (3.49)$$

Plotting the dielectric function $\epsilon_{1,2}(\xi)$ according to equation (3.49) versus the imaginary frequency magnitude ξ (figure 3.14) it is easy to spot the point on the frequency axis where the transition from supercritical modes to subcritical modes occurs. For the case of supercritical modes, the boundary dielectric function is given by the vacuum dielectric function (eq. (3.40)) while for subcritical modes it is given for Drude theory (eq. (3.41)).

3.6.10 The Magnitude of the Casimir Effect in Superconducting Cavities

Following the mathematical discussion of the previous sections 3.5.6.2 to 3.6.9 we are now finally in a position to quantitatively evaluate the Casimir effect for the cavity with superconducting boundaries.

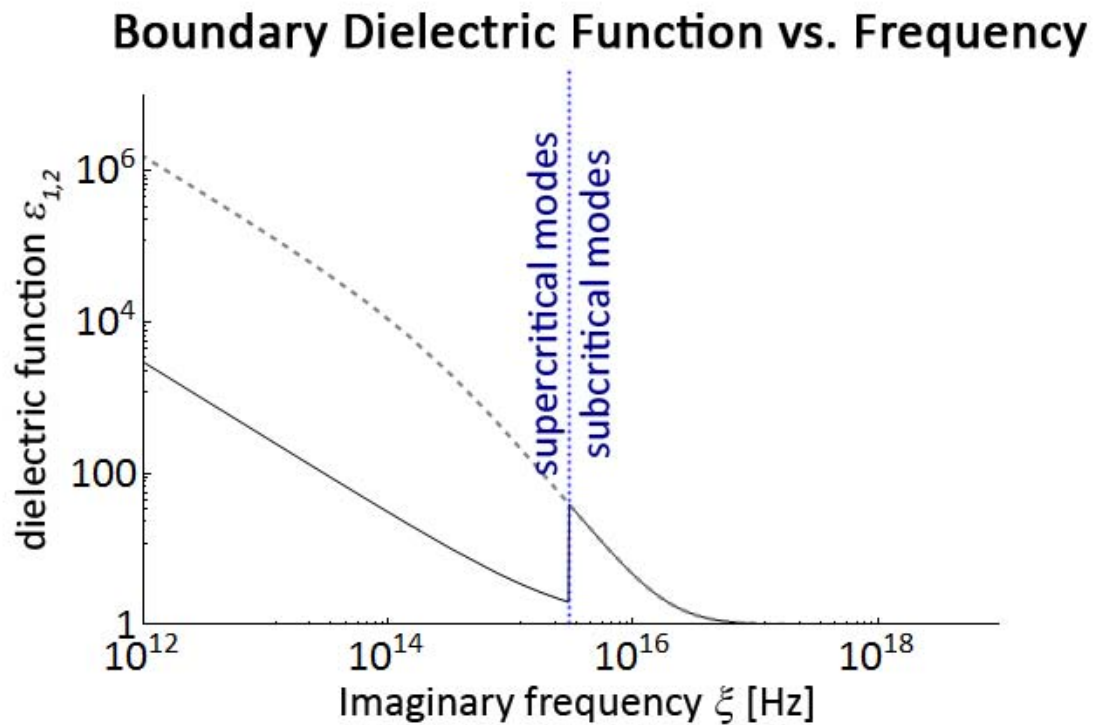


Figure 3.14: Effective dielectric function $\epsilon_{1,2}(\xi)$ of superconducting Al cavity boundaries (solid black line) vs. imaginary frequency magnitude ξ . The predictions of the Drude model for Al boundaries are given for comparison (dashed gray line). The graph is divided into the region of supercritical modes (left of blue line) and sub critical modes (right of blue line).

However, in order to correctly assess the reliability of the results we are about to present, one final problem has to be addressed: In the previous section 3.6.9 we have assumed that supercritical modes will not interact with the superconducting boundary at all, and that the only contribution to the boundary dielectric function relevant for determining the cavity modes is given by the local value of $\epsilon_{1,2}(\xi)$ at the standoff distance Δz . Effectively, we have treated the barrier width at Δz as infinite. We have established in section 3.5.6.2 that we are dealing with heavy photon layers of sub- \AA thickness inside the cavity. In section 3.5.3 we have established that decay depths are of order μm (figure 3.5). Consequently, a fraction of the supercritical modes will penetrate the heavy photon layer and interact with the boundary as well.

In the current implementation no supercritical mode will ever interact with the cavity boundaries, even if Δz approaches zero. Consider a supercritical mode with $\lambda = 1.1\lambda_{crit}$. In this case the standoff distance $\Delta z \approx 40pm$, which is of order of an atomic radius. The model developed in section 3.6.9 to describe the dielectric function of the superconducting boundaries $\epsilon_{1,2}(\xi)$ assumes that no interaction at all can occur between supercritical modes and the boundaries, no matter how small Δz becomes.

It seems physically dubious to specify the spatial position of the boundary to a precision better than an atomic radius. For $\Delta z < \lambda_{local}$ we expect some interaction between the supercritical mode and the boundary (see section 3.5.3). We speculate that effects like quantum uncertainty of the boundary position will turn the transient step between the supercritical and subcritical regions illustrated in figure 3.14 into a smoothly varying function. However, to precisely model the quantum level transition between a solid and the vacuum, along with all its optical implications, is beyond the scope of this work.

In order to arrive at a good estimate of the effect the sn-transition may have on the Casimir effect (and vice versa) we use two extreme approaches for estimating the dielectric function of the boundary. In this way we put an upper and a lower limit on the possible values the heavy photon Casimir effect may take.

The transient step approach discussed in section 3.6.9 will be used as one limit. This approach assumes perfect isolation of supercritical modes from the cavity boundaries. Any supercritical mode will have a dielectric function entirely due to the refractive index of the vacuum value (figure 3.14). The other limit will be obtained conversely by assuming no isolation of the supercritical modes and uses normal Drude theory according to equation (3.41) to determine the dielectric constant of the cavity boundaries. In future we will refer to these two limits for $\epsilon_{1,2}$ as the total-isolation model and the zero-isolation model respectively.

Plotting the magnitude of the Casimir effect it can be seen from figures 3.15 and 3.16 that the su-

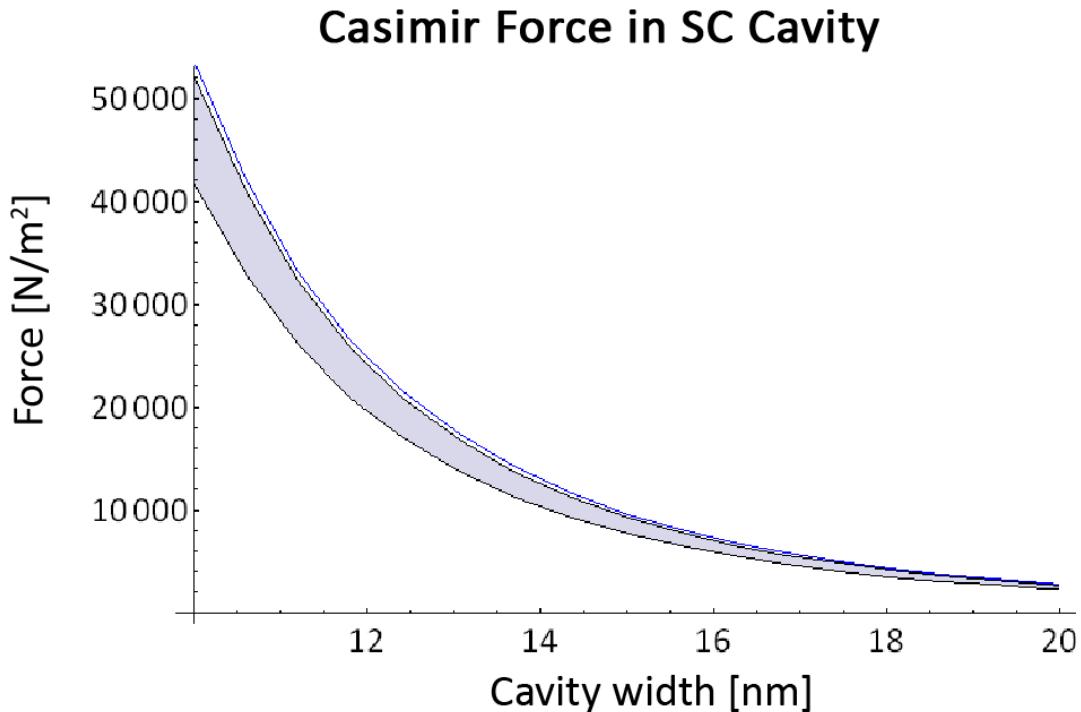


Figure 3.15: Casimir force in an Al cavity with superconducting boundaries. The upper boundary of the shaded region is obtained from the normal Drude model for $\epsilon_{1,2}$, while the lower boundary is obtained from the finite step model.

perconducting boundary Casimir effect is diminished compared to the normal state effect. This is in qualitative agreement with the predictions made by Barton and Dombey [78] who predict a diminished Casimir effect for the case of globally massive electromagnetism (section 3.5.5). The upper boundary of the relative change in Casimir cavity when the boundaries undergo sn-transition predicts changes of order *a few* %, which is consistent with the order of magnitude changes predicted by Barton and Dombey [78] for the globally massive case. This boundary is generated by considering our implementation of Lifshitz theory in the zero-isolation limit.

The magnitude of the predicted Casimir force varies with the critical wavelength $\lambda_{crit} = 2\pi\lambda_L$ on the surface of the superconducting boundary. As can be seen from figure 3.17 a cross over exists in the Casimir force between the total-isolation limit model and the zero-isolation limit model for $\epsilon_{1,2}$. Most significantly, for $\lambda_L > 32nm$ the zero-isolation model predicts a super conducting boundary Casimir force F_{SC} exceeding the Casimir force for normal state boundaries F_n , indicating an increase in binding energy.

Changes in the ambient magnetic field and temperature will lead to changes in the London penetration depth λ_L and consequently also in the critical wavelength λ_{crit} [4]. Thus, experiments with

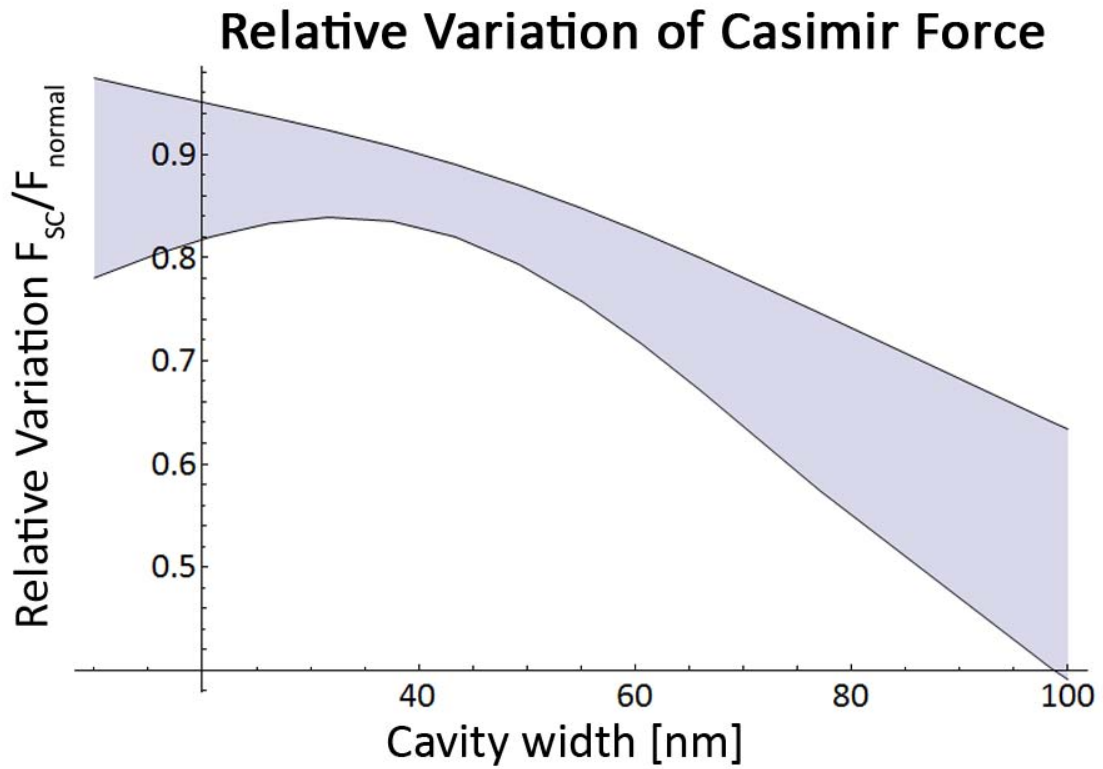


Figure 3.16: Relative change in Casimir force in an Al cavity with superconducting boundaries compared to the normal state boundary Casimir force. The upper boundary of the shaded region is obtained from the normal Drude model for $\epsilon_{1,2}$, while the lower boundary is obtained from the finite step model.

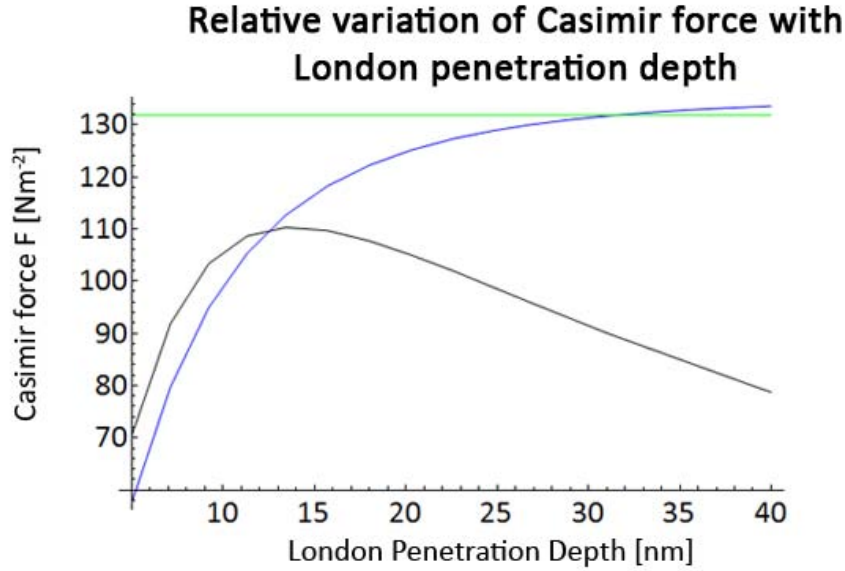


Figure 3.17: Variation of Casimir force with London penetration depth λ_L for a 40nm cavity with Al boundaries as predicted by Lifshitz theory. The black line represents the total-isolation limit, the blue line represents the zero-isolation limit and the constant green line is the prediction of Lifshitz theory for the case of normal state boundaries.

superconducting boundary Casimir cavities are much more susceptible to thermal and magnetic interference than their normal state counter parts. It also seems to imply that precision control over the local magnetic field might yield control over the Casimir attraction between superconducting plates. An experiment demonstrating such a modulation of the Casimir force could provide a good window on the physics of the massive-em vacuum. The dependence of λ_L , λ_{crit} on ambient temperature and magnetic field will be discussed in more detail in section 4.2.2.

3.6.10.1 Special Case: The Superconducting Cavity

Anticipating the discussion in Chapter 4 we now turn to the special case of a cavity filled with a superconducting material. Generally, we would of course expect a superconducting material to be entirely opaque, and consequently the system would not act as a Casimir cavity at all. However, in Chapter 4 our discussion of possible applications of the optical properties of superconductors prompts us to investigate the possibility of transparent superconducting materials, and a few good candidate materials are indeed identified (see section 4.2.3). In this case the density of superconducting carrier density Ψ^2 does not decay exponentially as described by equation (3.30) but rather stays constant everywhere so that the dielectric function of the cavity volume $\epsilon_3(\xi)$ is then given by

$$\epsilon(\xi, z) = 1 + \left(\frac{\xi_{crit}^2}{\xi^2} \right) \quad (3.50)$$

where we have used equation (3.40) with $z = 0$. If the boundaries are a material in the normal state, then the dielectric function of the boundaries $\epsilon_{1,2}(\xi)$ can be found from Drude theory (eq.(3.41)).

Most of the candidate materials for achieving transparent superconductors are wide-band gap oxides, and their optical behaviour is complicated even in the normal state. Rather than attempt to create a speculative model on how the change to Proca electromagnetism changes the optical behaviour of the transparent oxide we put an upper boundary on the effect by assuming the cavity volume to be perfectly transparent over all wavelengths with the only contributions to the dielectric function $\epsilon_3(\xi)$ arising from heavy photon effects according to equation (3.50)). This assumption leads to a good quality approximation of the Casimir effect since Indium Tin Oxide (ITO), which is currently the prime candidate for a transparent superconductor, has high (> 95%) transparency from near-IR to near-UV wavelengths [81]. The expected critical wavelength λ_{crit} of ITO will be shown to be of order $\lambda_{crit,ITO} \approx 500nm$ (section 4.2.3), so that most of the heavy photon effects will be concentrated in the transparent waveband of ITO. Since the error introduced by neglecting the optical response of ITO away from the transparent waveband is systematic, approximately the same errors should be introduced into the estimate of the superconducting and normal state Casimir effect, respectively. Consequently this approach is expected to yield a good estimate of the change in Casimir effect as the cavity undergoes sn-transition. A thorough introduction to the optical properties of transparent conducting oxides is given by Edwards et al. [77].

We can now evaluate the difference in Casimir force between an ITO filled cavity with ITO in its normal state and ITO in its superconducting state. We employ standard Lifshitz theory according to eq.(3.34) for the normal state, with the dielectric function of the boundaries $\epsilon_{1,2}(\xi)$ given by Drude theory (eq. (3.41)) and treating the cavity volume as perfectly transparent (i.e. $\epsilon_3 = 1$). For the superconducting state we replace the dielectric function of the cavity $\epsilon_3 \rightarrow \epsilon_3(\xi) = 1 + \left(\frac{\xi_{crit}^2}{\xi^2} \right)$ according to equation (3.50). The resulting difference between the normal state Casimir force F_n and superconducting state Casimir force F_{sc} has been plotted in figure 3.18. Significantly, we find that for small separations $F_{SC} > F_n$. Integrating F_{SC} we also find the cavity binding energy to be increased, resulting in an increase in superconducting transition temperature of the cavity material.

3.6.10.2 Cavity Binding Energies

Lifshitz theory directly yields the Casimir force between two parallel reflecting plates (section 3.6.1) from the dielectric functions of the reflectors and the dielectric function of the cavity volume, $\epsilon_{1,2}(\xi)$

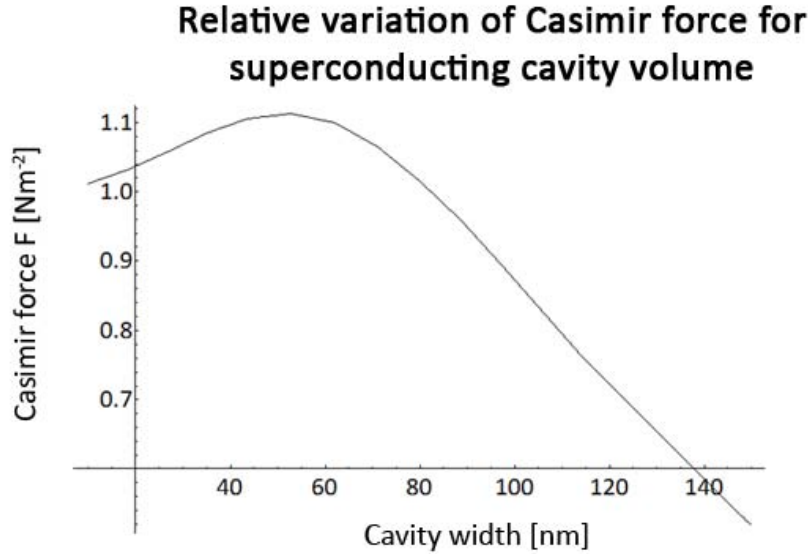


Figure 3.18: Relative variation of Casimir force with cavity width for a Al boundary cavity filled with a perfectly transparent superconductor.

and $\epsilon_3(\xi)$ respectively. Using the mathematical forms for $\epsilon_{1,2}(\xi)$, $\epsilon_3(\xi)$ and the corrections $\Gamma(\xi)^{1/8}$ discussed in sections 3.6.2 - 3.6.9 we can calculate the changes to the Casimir force for the case of superconducting boundaries by numerically integrating equation (3.34).

In order to achieve an estimate of the change to the superconducting critical field H_c (and consequently to the energy gap Δ_g) according to equation (3.8) we have to estimate the change to the Casimir potential energy $\Delta U_{bind}(a)$ (section 3.2). Since the Casimir force per unit area $F(a)$ was calculated from the potential energy $U(a)$ as $F(a) = \partial U(a)/\partial a$ (eq. (3.3)) we can conversely find the potential energy per unit area of superconducting boundary cavity $U_{SC}(a)$ by integrating the relevant Casimir force $F_{SC}(a)$ over a . This is necessary since, as opposed to the analytical solution for the perfectly reflecting cavity, Lifshitz theory does not provide a mechanism for directly calculating $U_{SC}(a)$. We then find the Casimir energy per unit area $U_{SC}(a)$ according to

$$U_{SC}(a) = \int_a^{\infty} F_{SC}(a) \quad (3.51)$$

where a is the cavity separation for which the potential energy per unit area U_{SC} is to be calculated and $F_{SC}(a)$ is the Casimir force per unit area according to the Lifshitz theory expression (3.34), using ϵ_3 according to equation (3.40), $\epsilon_{1,2}$ according to equation (3.49) and cavity width $d \rightarrow d_{eff} = a\Gamma^{-1/8}(\xi)$, with a the physical plate separation. The numerical integration of equation (3.34) in order to predict the Casimir force F_{SC} for the cavity with superconducting boundaries is already computationally intensive, and numerical integration of the obtained result F_{SC} is very time consuming.

	$\Delta U_{Lif,t}$	$\Delta U_{Lif,0}$	ΔU_{SC}
$\lambda_L = 16nm$ $a = 10nm$	$-32.8\mu Jm^{-2}$	$-5.7\mu Jm^{-2}$	$3.55\mu Jm^{-2}$
$\lambda_L = 51nm$ $a = 10nm$	$-88.6\mu Jm^{-2}$	$0.3\mu Jm^{-2}$	

Table 3.2: Variation of Casimir energy U per unit boundary area of the superconducting state cavity compared to normal state Casimir energy U_n computed as $(U - U_n)$ for a cavity with aluminium boundaries. Consequently a negative value indicates a decrease in binding energy, while a positive value indicates an increase. The subscripts Lif,t , $Lif,0$ and SC denote the results for the total-isolation limit, the zero-isolation limit and the special case of the transparent superconductor cavity respectively.

Using a 2.2Ghz dual core processor, the commercial numerical integration algorithms provided with *Mathematica* can take up to a couple of hours to compute a single data point. For this reason, only a few selected configurations have been computed. Some sample points are given in table 3.6.10.2, below. A full systematic exploration of the entire parameter space a, β, λ_L within a reasonable amount of time is beyond the computational resources available to the author.

In order to estimate the change we expect to the superconducting critical field H_c according to equation (3.8) we require an estimate of the condensate energy according to equation (1.10). Using the Aluminium critical field $H_c \approx 101G$ [31] we find the specific condensate energy for Al to be $\epsilon_{AL} \approx 40Jm^{-3}$. In order to quantitatively estimate the influence of the massive electromagnetism Casimir effect on the outcome of the experiments proposed by Bimonte et al. [10] [73] [74] we consider a Al film of thickness $D = 10nm$. We find the corresponding condensate energy per unit area $E = 4 \times 10^{-8}Jm^{-2}$.

We estimate the change to the critical field according to equation (3.8) as $\frac{\delta H_c}{H_c} \approx \frac{\Delta U_{bind}}{2(2E)}$ where we have introduced an additional factor of 2 in front of the condensate energy, since our calculations are for the case of a double cavity with superconducting boundaries, rather than for a single Al film as proposed in the latest version of Bimonte's experiment [74]. By using values for ΔU_{bind} according to table 3.6.10.2 we can estimate the changes in H_c .

Considering a cavity of width a with aluminium boundaries it can be seen from table 3.6.10.2 that our predictions for the change in Casimir energy $\Delta U(a)$ are far too large to be realistic. The entire range of values between the total-isolation and zero-isolation limits we obtained for $\Delta U(a)$ is several times larger than the condensate energy per unit area $E = 4 \times 10^{-7}Jm^{-2}$. Since the binding energy change ΔU is negative for the cavity with $a = 10nm$, $\lambda_L = 16nm$ the Aluminium boundaries of the cavity

would never go superconducting since their critical field would be depressed to $H_c = 0$. One possible reason for this problem is that we have assumed the bulk value of the London penetration depth λ_L . According to Nishio [82] the in-plane London penetration depth Λ_L for thin superconducting films can be calculated as

$$\Lambda_L = \frac{2\lambda_L^2}{d} \quad (3.52)$$

where $d < \lambda_L$ is the film thickness. For an Aluminium film with $d = 10nm$, $\lambda_L = 16nm$ we obtain $\Lambda_L = 51nm$. The estimated change in binding energy ΔU predicted for an Aluminium cavity with $d = 10nm$, $\Lambda = 51nm$ is given by row 2 in table 3.6.10.2. Using equation (3.8) to obtain the relative critical field shift $\delta H_c/H_c$ for the total isolation limit and the zero-isolation limit we find the total range of possible field shifts $\delta H_c/H_c \in [-1 < +0.1875]$ (-1 is the maximum possible negative shift since it indicates a critical field $H_c = 0$). While this is quite a large range, our predicted range of field shifts includes $\Delta U = 0$, indicating that it is reconcilable with conventional Lifshitz theory, even if no critical field shift δH_c is detected.

3.6.10.3 Convergence of the Model

So far our efforts to create a model of the superconducting boundary Casimir cavity appear quite successful. We have produced a mathematical description of it which can be implemented and evaluated by means of Lifshitz theory, and sign and magnitude of the corrections predicted agree approximately with the predictions made by Barton and Dombey [78] regarding the Casimir effect in the presence of globally massive electromagnetism (compare figures 3.15 and 3.6). Still, it is difficult to test our predictions directly, or to verify the correct operation of the numerical integration techniques applied, since these are the only tools available to achieve a result in the first place.

A good test for the quality of our model is to see if it converges with the predictions of conventional Lifshitz theory as the heavy photon effects are reduced. Our entire model is based on the interactions of the zero point modes with the thin heavy photon layer near the cavity boundary. If the decay constant $\beta \rightarrow \infty$ the width of this layer $\Delta z \rightarrow 0$. Thus, for the case of a large decay constant β or a small photon mass m_γ ($=$ large London penetration depth λ_L) the predictions by the model for the Casimir force in the cavity with superconducting boundaries have to reduce to those made by conventional Lifshitz theory. As can be seen from figure 3.19, as β increases the ratio of the superconducting state Casimir force F_{SC} to the normal state Casimir force F_n approaches $F_{sc}/F_n = 1$. This convergence gives us a good degree of confidence in the results obtained so far. However, convergence only occurs if we specify a minimum stand-off distance z_{min} , which is effectively the

precision limit to which the boundary position can be defined. If $\Delta z < z_{min}$ the zero-isolation limit applies, if $\Delta z > z_{min}$ the total isolation model applies. If no such minimum stand-off distance is defined, then supercritical modes will remain perfectly isolated from the boundaries for arbitrarily high values of β , and no convergence occurs. The minimum stand-off distance used to generate figure 3.19 is $z_{min} = 1pm$, one order of magnitude smaller than an atomic radius. Furthermore, it can be seen from figure 3.20 that for large λ_L the predictions made by our model for the Casimir cavity with superconducting boundaries reduce to those of conventional Lifshitz theory. Both figures are plotted for the total-isolation limit.

The extremely sharp transition which can be seen in figure 3.20 is a result of modes with wavelengths $\lambda \approx \lambda_{crit}$ being excluded from the cavity when $\lambda_{crit} = a$ (where a is the cavity width). This indicates that our model successfully accounts for the transition to Maxwellian behaviour for strongly subcritical modes (i.e. $\lambda \ll \lambda_{crit}$). In the full superconducting boundary implementation of the total-isolation limit our model succeeds in handling the very short wavelength modes as unperturbed vacuum modes and produces predictions in agreement with conventional Lifshitz theory. Since we have made no effort to artificially introduce such a transition to Maxwellian electromagnetism for strongly subcritical modes, this behaviour is very encouraging.

The convergence condition for a minimum stand-off distance z_{min} to exist serves to reinforce our opinion that some interaction between the boundaries and supercritical modes has to be taken into account. The convergence of our model's predictions with those of conventional Lifshitz theory both for large β and large λ_L increases our confidence in the model.

3.6.10.4 Remaining Issues and Next Steps

While the model presented in the above sections for determining the Casimir effect in a cavity with superconducting boundaries appears to yield physically reasonable results, it is a simplification of a real world system. In this section we will give a quick outline of the problems attached to a practical detection of the effect, as well as suggesting areas in which the theory requires refinement. At this point it is important to point out again that the corrections we calculated are entirely due to heavy photon effects inside the cavity. We have not considered any changes in boundary reflectivity itself, which were the basis for Bimonte's predictions [10]. A first step towards a better model might be to include the changes in boundary reflectivity reported by Glover [71] in our model. The experimental data reported by Glover [71] are entirely over the long wavelength regime. However, we believe that heavy photon effects might also have an effect on the boundary reflectivity for wavelengths with $\lambda \approx \lambda_{crit}$. Rather than just preventing supercritical modes from reaching the boundary (section 3.6.7) the diverging refractive index near λ_{crit} may also increase the reflectivity for subcriti-

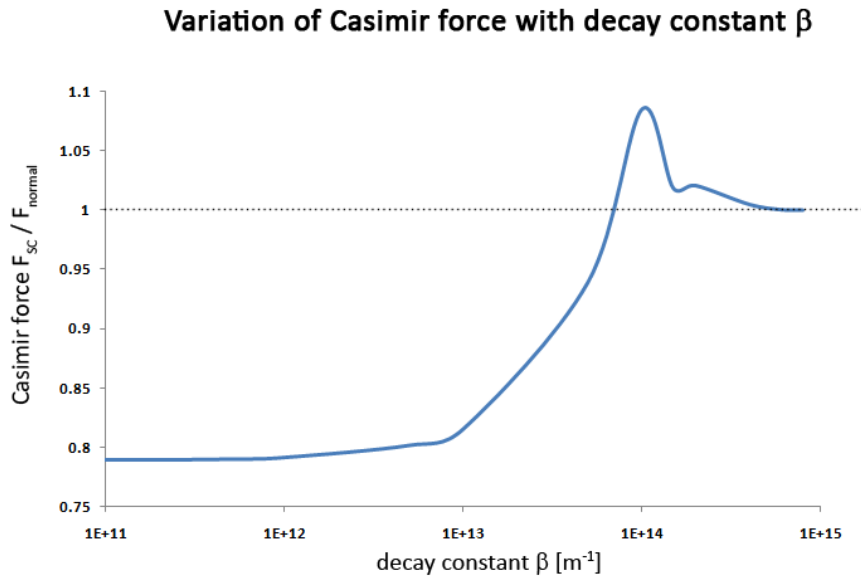


Figure 3.19: Variation of the Casimir force according to the total-isolation limit model with decay constant β , assuming a minimum stand-off distance Δz_{min} below which isolation breaks down. The dashed line at $F_{SC}/F_{normal} = 1$ is provided as a guide to the eye.

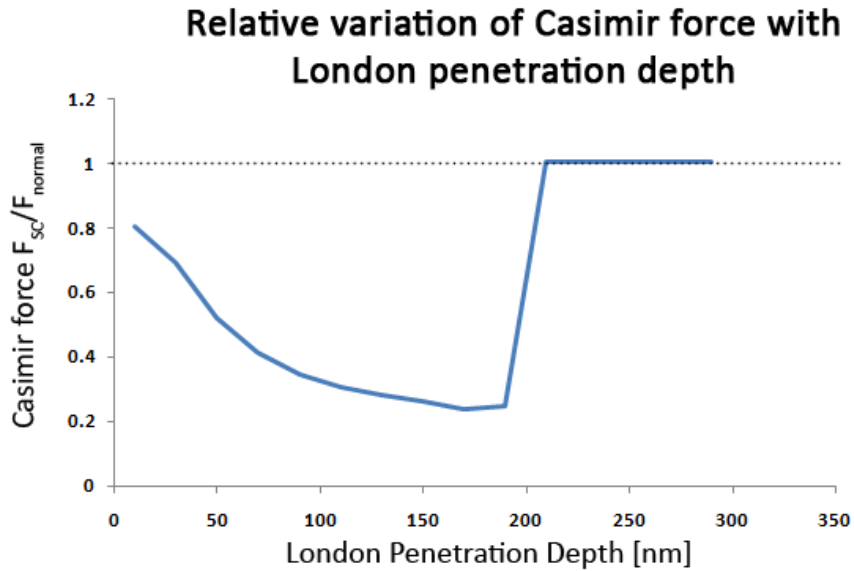


Figure 3.20: Relative variation of the Casimir force with London penetration depth λ_L for a cavity with Al boundaries as ratio of superconducting boundary force F_{sc} to normal state boundary force F_{normal} for a cavity of width 40 nm. The predictions of F_{SC} sharply reduce to those of conventional Lifshitz theory for large $\lambda_{crit} > 40\text{nm}$ since modes with wavelengths $\lambda \approx \lambda_{crit}$ are excluded from the cavity (we recall $\lambda_{crit} = 2\pi\lambda_L$).

cal wavelengths. However, a detailed mathematical description of this effect requires a theory of the influence a non-zero photon mass has on the radiation-matter interaction.

One of the main issues is that the tunneling of Cooper pairs into the cavity volume, which creates the thin layer of massive-em responsible for the changes in the Casimir effect in the first place, also results in a decrease in Cooper pair density inside the boundary. This decrease in Cooper pair density, in turn, reduces the London penetration depth λ_L , and consequently λ_{crit} . This "leaking" of Cooper pairs across an interface is described in most text books dealing with superconductivity or superconducting devices and is generally known as the proximity effect [4][29][31]. This reduction in λ_L near the boundary becomes more important as β decreases. Since the London penetration depth is generally sensitive to changes in ambient temperature and magnetic field, these dependencies (which will be discussed in more detail in chapter 4) also need to be taken into account. The magnetic field dependence of the London penetration depth λ_L is especially relevant since the method employed by Bimonte et al. [74] to detect the shift in condensate energy relies on measuring the critical temperature T_c of the superconducting Al boundary at increasing ambient magnetic field values H . It will become apparent in section 4.2.2 that an increased magnetic field H_c inside the cavity leads to a decrease in λ_L and consequently in λ_{crit} . Thus, a variation in ambient magnetic field may actually alter the magnitude of the change to the binding energy ΔU_{bind} significantly.

We have already seen in section 3.6.10.2 that the magnitude of the London penetration length λ_L has a strong influence on the magnitude of the change in binding energy ΔU . We have estimated the effective London penetration depth as the in-film penetration depth Λ according to equation (3.52). This still assumes that Λ is constant over all allowed modes. If Λ is anisotropic this is equivalent to assuming that the wave vectors of all allowed zero point modes are parallel to each other, a clearly erroneous assumption since the spectrum of wave vectors is quantized only in the z-direction, normal to the cavity boundaries [62]. In a precise implementation Λ then has to be replaced by a second rank tensor Λ_{ij} , so that the photon mass effectively becomes a function of the direction of the wave vector \vec{k} .

Another potential problem can be found in the derivation of Lifshitz theory. The derivation of Lifshitz theory for the Casimir attraction of the plates automatically cancels any contributions which are independent of boundary separation [62]. This is generally a very reasonable simplification, since any observable effects in the normal state cavity are caused by changes in boundary separation. However, if the magnitude of these separation-independent contributions changes with the sn-transition of the boundaries we could potentially have overlooked quite a significant contribution to the energy balance of the sn-transition.

Finally, the matter of the minimum stand-off distance z_{min} and the interaction strength of supercrit-

ical modes with the boundaries remains unresolved. It arises because Lifshitz theory only accepts a single boundary dielectric constant as an argument (section 3.6.1). In principle two possibilities exist to solve this problem. One can either re-derive Lifshitz theory from scratch, for a spatially varying dielectric function, or one can try to determine all the allowed modes by numerical solution of the Klein-Gordon equation inside the cavity. The former approach would require a significant mathematical research effort, and is beyond the expertise of the author, while the latter requires computational resources of a magnitude not available to the author at the time of writing, since a large number of modes would have to be determined.

3.6.11 Conclusions regarding the Casimir Effect in Cavities with Superconducting Boundaries

After all the mathematical effort of this Chapter we have now reached the end point of an investigation which began with the question of whether the performance of superconducting detectors may be influenced by quantum mechanical vacuum fluctuations. The question as to the existence and strength of such a coupling mechanism has already been partially answered in section 3.4: A coupling mechanism exists, and the coupling should be detectable in principle, but it is likely to be very small.

However, our wish to find a quantitative estimate of this coupling has led us to consider the field of non-zero photon rest mass electromagnetism and we now have a closed and self-consistent model of the Casimir effect for superconducting cavities. This is a significant result in itself, entirely independently of the question that motivated its derivation in the first place. To the best of the author's knowledge, this is the first systematic quantitative analysis of the massive-em vacuum energy of a Casimir cavity with superconducting boundaries. If the effect can be demonstrated experimentally whole new avenues of research become available. For example, experimental data about the variation of the superconducting Casimir force with the decay constant β could provide information about the magnitude of the minimum stand-off distance z_{min} (section 3.6.10), providing information about the transition between macroscopic systems (the boundary) and quantum mechanical systems (the precision to which the boundary width can be defined from the point of view of a zero point mode).

The results presented in section 3.6.10 for the change in cavity energy are particularly interesting in the light of the experiments currently carried out by Bimonte et al. [10]. As was discussed in section 3.2 Bimonte and his group proposed a mechanism by which a change in reflectivity of the cavity boundaries undergoing sn-transition might change the cavity binding energy, and in this way lead to an increase in the superconducting critical field H_c . The original experiment proposed by Bimonte has been refined a number of times [73] [74] but at time of writing no unambiguous result has been

obtained [74].

The heavy photon effects discussed in this chapter appear to reduce the Casimir binding energy of the cavity over almost the entire realistic parameter space (section 3.6.10). Thus, the changes due to massive photon effects oppose the changes introduced by an increased boundary reflectivity as assumed by Bimonte [10]. Independently of which effect is dominant, the overall measurable change to the superconducting energy gap Δ_g , and consequently to the critical field H_c and critical temperature T_c , is likely to be reduced compared to the change predicted by either the heavy photon effect or the increased boundary reflectivity mechanism individually. This could be part of the reason for the continued difficulties with detecting this change in condensate energy predicted by Bimonte et al. [10]. A better estimate is needed of the quantitative corrections required when calculating the Casimir binding energy of real world cavities if a meaningful quantitative description of the change in condensate energy of any cavity system is to be attempted (see section 3.6.10.4).

While no unambiguous proof of the critical field shift due to zero point modes has been obtained at this point, Bimonte et al have demonstrated the basic principle by applying a microwave and radio frequency (RF) radiation field to a Casimir cavity with one Al boundary and to a free Al film and measured the respective critical fields and transition temperatures [74]. This setup effectively demonstrates an amplified version of the zero-point field shift predicted. Since heavy photon effects are most significant near λ_{crit} (which is generally in the optical or UV band, see previous discussion), they would not have been detected in this demonstration-of-principle setup. As was established in section 3.6.10.2, for the case of thin films the London penetration depth for aluminium is in the interval $[16nm, 51nm]$ (eq.(3.52)), yielding a critical wavelength λ_{crit} in the interval $[100nm, 320nm]$, significantly shorter than the microwave and RF-wavelengths in Bimonte's test field [10].

As can be seen from the results presented in section 3.6.10, the dependencies of the Casimir effect on system parameters such as the London penetration length λ_L or the decay constant β are strongly non-linear. However, limited computational resources and the amount of time even a single evaluation of the Lifshitz theory for this complex system can take are currently preventing the author from fully exploring the entire parameter space.

Of particular interest in this regard appear systems where the Casimir cavity is filled with a transparent superconductor (section 3.6.10.1). In this case the Casimir attraction is increased by heavy photon effects. In principle, for this cavity type longitudinally polarized modes have to be taken into account according to equation (3.29b). However, these will also serve to increase the binding energy. Such a cavity might significantly increase the superconducting energy gap Δ_g , along with the critical temperature T_c and critical field H_c , of the transparent superconducting material. Periodic stacks alternating between a transparent superconducting material and a reflector could have significantly

increased critical temperatures.

Alas, a precise prediction of the binding energy in such a stack is a major theoretical and mathematical undertaking since, for the thin films and small gaps which yield the highest increase in binding energy, neighboring cavities are interacting. Still, despite such difficulties in making quantitative predictions about such heavy Casimir stacks, we cannot help but wonder whether a link exists between the ability of the Casimir effect to boost the critical temperature of a superconductor and high temperature superconductivity. After all, current high- T_c compounds essentially consist of thin (of order *tens of* Å) layers of copper oxide separated by equally thin layers of metal, effectively forming a stack of Casimir cavities. At this point any such connection is highly speculative, but the potential implications are significant enough that we still consider it an important point.

Chapter 4

Heavy Photon Optics

In chapter 3 our desire to understand the influence of the quantum vacuum on the operation of practical superconducting detectors lead us to investigate the nature of photon propagation in superconductors. In the course of this research we found it necessary to consider photons which had acquired a non-zero rest mass due to the Higgs mechanism (section 3.5), and we were forced to replace Maxwell's equations with the Proca equations when evaluating problems in electromagnetism (eqs. (3.12a)-(3.12d)). We also found that the velocity v of photons propagating inside a superconductor is smaller than the vacuum velocity of light c . In fact it appears that v depends strongly on the photon vacuum wavelength λ , an effect known as dispersion.

The dispersion D of a material is quantified as the derivative of the refractive index η w.r.t. photon wavelength λ . The magnitude of the dispersion is what governs the theoretical maximum spectral resolving power of dispersive optics of any kind. In the following sections we show that the dispersion D of superconducting materials can be expected to diverge near the critical wavelength λ_{crit} (eq. (3.16)). The material dependent critical wavelength $\lambda_{crit} = 2\pi\lambda_L$ is the wavelength at which the photon velocity goes to zero. We also show how this divergence of D can be exploited along with the high refractive index η in order to create a new kind of optical element of unprecedented power and flexibility.

This new kind of optical element relies on the non-zero photon rest mass as the basic concept. The fact that the photon rest mass is independent of photon frequency or wavelength (eq.(3.11)) while the photon energy is unchanged from its vacuum value (i.e. the spectral energy density is unchanged) leads to the variation of photon velocity with photon wavelength (eq.(3.14)). Based on the working principle we have decided to call this new kind of optics "Heavy Photon Optics" (HPO), referring to the non-zero photon rest mass as the key ingredient of the technology.

In this way we will have closed the loop, having digressed from the practical field of superconducting detectors into the theoretical field of vacuum fluctuations and the gauge symmetry structure of the vacuum, and having returned to the field of practical applications with the design for a new optics technology.

4.1 Optical Parameters of HPO Elements

In this section we begin our discussion of HPO technology by establishing the macroscopic optical parameters, such as refractive index η and Dispersion D , of HPO elements. In the introduction of this chapter the dispersion D was introduced as the wavelength derivative of the refractive index η , which itself depends on the electromagnetic wave velocity v . While as a casual definition for the purpose of qualitative discussions this may suffice, it is necessary to discriminate between the phase velocity v_p and group velocity v_g of the wave, and also between their respective refractive indices η_p, η_g and dispersions D_p, D_g . The quantitative expressions governing these optical parameters will be introduced in this section along with their dependencies on experimental parameters. The expressions describing the HPO refractive indices then allow for the determination of the optical characteristics of superconductor-vacuum boundaries, yielding quantitative expressions for the coefficients of reflection and refraction as functions of various experimental parameters. In this way we will have assembled the set of equations necessary to model the optical behavior of a perfect heavy photon optics element.

In the course of the entire discussion one key assumption is that electromagnetic radiation can propagate freely inside the superconductor. For most conventional superconducting materials like aluminium this is obviously untrue. However, it turns out that superconductor materials transparent to electromagnetic radiation do exist, and these will be discussed in more detail in section 4.2.3. The question which remains is whether these materials retain their optical transparency in the superconducting state. In this context of finding a suitable material from which to fashion practical HPO devices the various dependencies of the optical parameters discussed in this section are of great importance, since they are necessary to determine the required material parameters.

In general HPO devices are based on the fact that the phase refractive index η_p and phase dispersion D_p of a transparent superconductor diverge near a temperature dependent critical wavelength $\lambda_{crit}(T) = 2\pi\lambda_L(T)$ where $\lambda_L(0)$ is dependent on the superconductor material. The critical wavelength λ_{crit} introduced in equation (3.16) is actually $\lambda_{crit}(0)$, and the temperature dependence stems from the temperature dependence of the London penetration depth $\lambda_L(T)$ which is discussed in more detail in section 4.2.2. The zero temperature value of $\lambda_{crit}(T)$ is one of the most important

parameters which determines the potential applications of any candidate material.

Unless specifically stated otherwise, when considering the optical parameters of any HPO element we will assume that the only relevant optical mechanisms are those resulting from the non-zero photon rest mass. A full optical treatment considering the dielectric and metallic optical response in combination with the heavy photon response of real materials is beyond the scope of this work. While a real device may be subject to both HPO and conventional optical mechanisms, the conventional material response in the vicinity of the active wavebands considered here is so small that they can be safely neglected for the purpose of discussing the basic effect. Thus, despite those simplifications it is still possible to make meaningful predictions about practical devices, since dispersions in normal materials are shown in section 4.1.1 to be more than three orders of magnitude smaller than those of HPO devices near their critical wavebands. While the transparent superconducting material may contribute to the effective refractive index, any constant refractive index effects introduced by the substrate material do not fundamentally change any of the predictions regarding prism or etalon performance made in the following sections. Currently, the most promising candidate material for the creation of practical HPO devices is Indium Tin Oxide (ITO), which will be discussed in more detail in section 4.2.3. The critical wavelength of ITO will be shown to fall into the material's window of transparency, located in the optical band, where the material refractive index η is approximately constant at $n \approx 2$, and absorption effects in optimized films are small ($< 1\%$) [81]. As such the following discussion of potential practical devices does not require a complete combined theory taking into account both normal-material and HPO effects.

4.1.1 Phase Velocity, Phase Refractive Index and Phase Dispersion

The phase velocity v_p describes the speed at which changes of phase of a given frequency component of any wave propagate. Considering the plane wave equation $u = ae^{ip}$ the phase velocity is the speed with which changes in the phase p propagate.

The phase velocity of any photon of frequency ω and wave vector k is defined as:

$$v_p \equiv \frac{\omega}{k} \quad (4.1)$$

It is possible to find an expression for v_p as a function of λ from expression(4.1)[75], and consequently determine the refractive index $\eta_p = 1/v_p$. Since the HPO applications investigated in this chapter are all based around transmission optics the discussion will focus entirely on subcritical wavelengths, where the HPO induced extinction coefficient $k = 0$. This allows us to use $\eta_p = n_p = 1/v_p$ throughout the rest of this chapter. The resulting macroscopic optical parameters (phase velocity, phase refractive index and phase dispersion) can then be found to be:

$$v_p = c \left(1 - \frac{\lambda^2}{4\pi^2 \lambda_L^2} \right)^{-1/2} \quad (4.2a)$$

$$n_p = \left(1 - \frac{\lambda^2}{4\pi^2 \lambda_L^2} \right)^{1/2} \quad (4.2b)$$

$$D_p = -\frac{\lambda}{4\pi^2 \lambda_L^2} \left(1 - \frac{\lambda^2}{4\pi^2 \lambda_L^2} \right)^{-1/2} \quad (4.2c)$$

Any variation of v_p with λ will lead to variations of the phase refractive index n_p (eq.(4.2b)). The magnitude of the variation is quantified by the phase dispersion D_p (eq. (4.2c)). Since the angle of refraction of an electromagnetic wave depends on n_p , different frequency components of the wave will undergo a different angle of refraction when incident on the material, leading to the spatial separation of the spectral components of the incident light. Thus, phase dispersion is responsible for the prism effect, as discussed in section 4.3.1. Because of this, phase dispersion is also known as "chromatic dispersion".

It can be seen from equations (4.2a) to (4.2c) how the critical wavelength λ_{crit} arises from the heavy photon dispersion: as the ratio in the bracket approaches $\frac{\lambda^2}{4\pi^2 \lambda_L^2} = 1$, the bracket goes to zero and v_p and D_p diverge to infinity. Thus the waveband of interest when trying to exploit the diverging refractive index and dispersion of a HPO element is near the critical wavelength λ_{crit} given by:

$$\lambda_{crit} = 2\pi \lambda_L \quad (4.3)$$

Since $\lambda_{crit} \propto \lambda_L$ it can be varied by adjusting any parameters to which λ_L is susceptible (i.e. zero-temperature carrier concentration n_s^0 , magnetic field H and temperature T , see section 4.2.2).

Especially in older optics textbooks one often finds calculations referring to the refractive index of a material with little or no indication of whether the phase or group refractive index are required. When the refractive index of a material is quoted in relation with conventional optical elements such as prisms or lenses and no indication is given as to whether the phase or group refractive index is meant, it is usually safe to assume that the required parameter is the phase refractive index. A comparison between normal material refractive indices and a HPO element of critical wavelength $\lambda_{crit} \approx 662nm$ has been plotted in figure 4.1.

It can be seen from figure 4.1 that far from λ_{crit} the refractive index of an HPO element is a slowly varying, well behaved function of λ . However, as $\lambda \rightarrow \lambda_{crit}$ the function diverges because the ratio

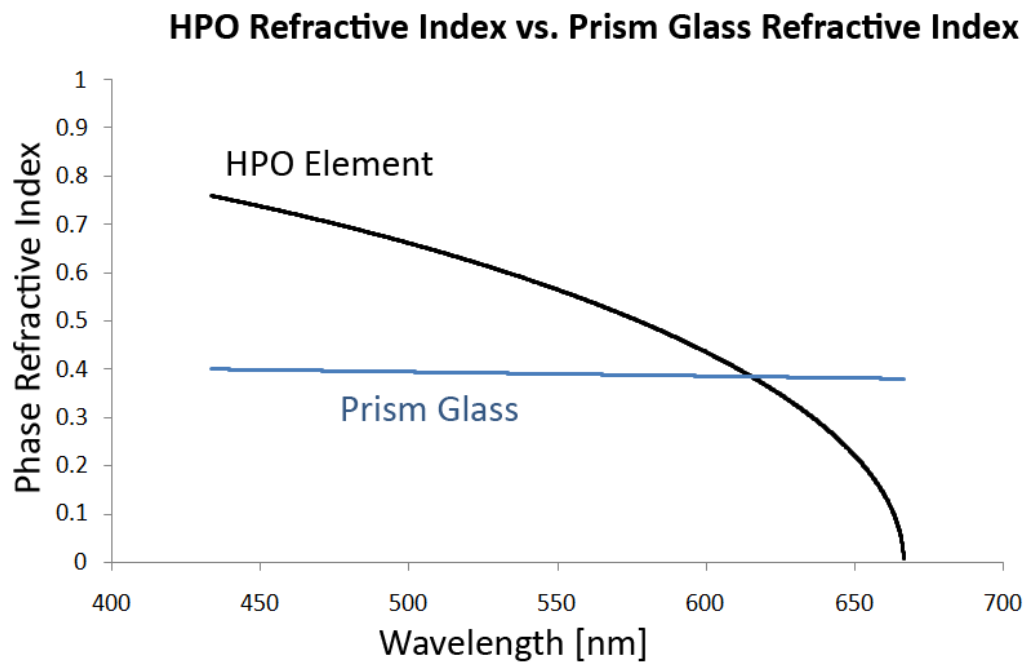


Figure 4.1: Refractive index of prism glass (F2 Schott Glass as offered by CVI Laser [13]) and a HPO element made of indium tin oxide with $\lambda_{crit} = 667nm$ near the critical wavelength are plotted as a function of vacuum wavelength of the incident radiation

$\frac{\lambda}{4\pi^2\lambda_L} \rightarrow 1$ and the sum inside the root on the right hand side of (4.2a) goes to zero. It is this divergence from which hypothetical HPO elements derive some extraordinary characteristics, allowing for ultra-high resolution dispersion prisms and etalons which will be discussed in section 4.3.

The fact that the phase velocity is slowly varying over the entire electromagnetic spectrum except for a narrow active waveband near the critical wavelength means that it is possible to employ HPO technology to create optics which have a strong influence on a selected waveband while allowing other radiation to pass. Wavelengths above λ_{crit} can be shown to decay exponentially inside a HPO element but their characteristic decay depths are sufficiently large to allow them to pass thin film HPO devices (section 3.5.3).

4.1.2 Group Velocity, Group Refractive Index and Group Dispersion

The group velocity v_g describes the velocity with which changes in the amplitude of the wave propagate. Again considering the plane wave equation $u = ae^{ip}$, we find the group velocity to be the speed with which changes in the amplitude parameter a propagate. Since the energy of any oscillation depends directly on the oscillation amplitude the group velocity is also the speed at which individual photons are transmitted, and the speed at which information and energy are conveyed.

Consider a pulse of electromagnetic radiation made up of many different frequency components (i.e. a non-monochromatic pulse). For the purpose of this discussion we assume the pulse is "white", i.e. the spectral energy density is constant over all wavelengths within the bandwidth of the pulse (the pulse cannot contain components of half-wavelength bigger than the pulse length). Any variations in v_g with λ will cause the different wavelength components of the pulse to travel at different velocities, causing the pulse shape to change. The pulse will begin to elongate, and the deformation of the pulse will increase with distance traveled. The strength of the effect is quantized by the group dispersion D_g . If $D_g < 0$ the high frequency components of any pulse will travel slower than the low frequency components. In this case any receiver will detect a pulse whose frequency is continuously rising with time, an effect called "up-chirping". Conversely, if $D_g > 0$ the frequency will decrease continuously while the pulse is received ("down-chirping"). The group dispersion inside a superconductor diverges to $+\infty$ at $\lambda = \lambda_{crit}$. Thus, electromagnetic signals inside a superconductor will be down-chirped.

Since the group velocity governs the time delay between sending and receiving a photon group, the dispersion D_g is sometimes referred to as "group delay dispersion parameter" in the literature.

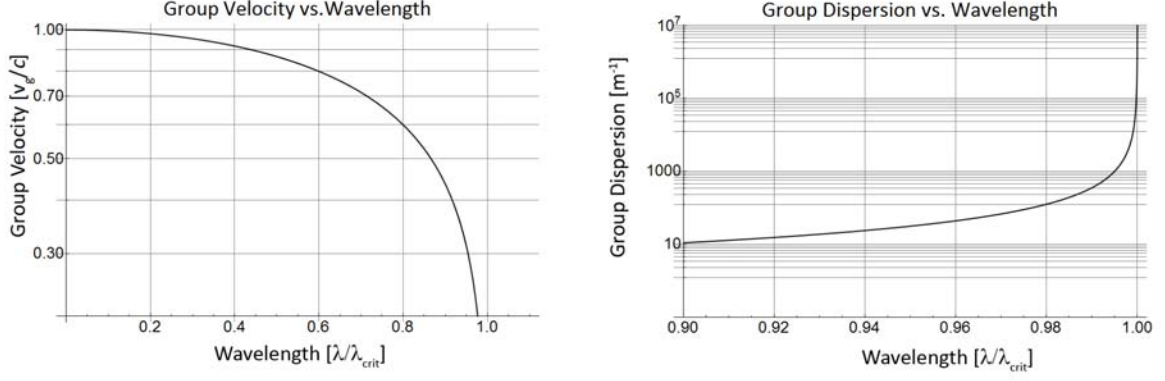


Figure 4.2: Group velocity v_g (left) and group dispersion (right) as functions of normalized wavelength λ/λ_{crit} for a hypothetical HPO element.

The group velocity of any photon of frequency ω and wave vector k is defined as:

$$v_g \equiv \frac{d\omega}{dk} \quad (4.4)$$

Again employing the Proca equations to find the photonic group velocity v_g inside any HPO element [75] we obtain the following expressions for the group velocity dependent optical parameters (Group refractive index n_g and group dispersion D_g):

$$v_g = c \left(1 - \frac{\lambda^2}{4\pi^2 \lambda_L^2} \right)^{1/2} \quad (4.5a)$$

$$n_g = \left(1 - \frac{\lambda^2}{4\pi^2 \lambda_L^2} \right)^{-1/2} \quad (4.5b)$$

$$D_g = \frac{\lambda}{4\pi^2 \lambda_L^2} \left(1 - \frac{\lambda^2}{4\pi^2 \lambda_L^2} \right)^{-3/2} \quad (4.5c)$$

The group velocity v_g and group dispersion D_g of a HPO element have been plotted in figure 4.2 as functions of normalized wavelength λ/λ_{crit} . Upon inspection of figure 4.2 we see that the group velocity $v_g \rightarrow 0$ as $\lambda \rightarrow \lambda_{crit}$. Since the group velocity v_g is actually the velocity of photon propagation this implies that photons are slowed down inside a HPO element, coming to a complete standstill at $\lambda = \lambda_{crit}$.

4.1.3 Reflection and Reflectance of HPO Elements

One of the controlling parameters for most types of potentially interesting HPO application is the behavior of light incident on the superconductor-normal (or superconductor-vacuum) boundary. Independently of the nature of the application, the light has to penetrate the boundary if HPO mechanisms are to be exploited, since the ultrahigh dispersion and refractive index specific to HPO elements require the light to be inside the region of massive-em.

At normal incidence, the fraction of light reflected can be calculated as:

$$R_I = \left[\frac{n_2 - n_1}{n_2 + n_1} \right]^2 \quad (4.6)$$

where R_I is the coefficient of reflection (fraction of incident energy reflected), also known as reflectivity. In the absence of absorption, conservation of energy dictates that the coefficient of reflection R_I and the coefficient of transmission T_I satisfy $R_I + T_I = 1$. The parameter n_1 is the refractive index of the medium on the incidence side of the boundary and n_2 is the refractive index of the medium on the transmission side of the boundary [76]. We have used the subscript I in order to prevent confusion of the transmission coefficient T_I with the temperature T .

Expression (4.6) is derived from Fresnel's equations [83] and valid at normal incidence. Considering the two refractive indices n_p, n_g available, we find the correct refractive index to use with equation (4.6) to be the phase refractive index n_p . The reason for this is that we are concerned with wave propagation rather than individual photons. For the same reason, whenever considering interference effects it is also the phase velocity v_p and its derived values η_p, D_p that have to be used.

Considering figure 4.3 we see that the total amount of light reflected at normal incidence from a vacuum-HPO element boundary depends strongly the correlation between wavelength of the incident light and the critical frequency of the HPO element. It can be seen from figure 4.3 that the reflectivity R_I is generally small (at the sub-percent level) far from the critical wavelength while it rises rapidly as $\lambda \rightarrow \lambda_{crit}$. The critical wavelength λ_{crit} depends linearly on the London penetration depth λ_L and consequently on the temperature, magnetic field and material parameters of the superconductor. The reflectivity R_I rises steeply near λ_{crit} , and approaches unity as $\lambda \rightarrow \lambda_{crit}$. Consequently, some kinds of HPO devices may encounter problems when it comes to actually injecting light into the device. Especially a prism which is to be operated at wavelengths λ very near λ_{crit} may suffer from the high reflectivity. For many thin film devices this problem can be eliminated by exploiting thin film interference effects. The thin film transmittance of HPO devices is discussed in section 4.1.3 and the reflectivity problem of a prism is addressed in section 4.3.1. The dependencies of λ_{crit} (and consequently of the refractive index n_g and reflectivity R_I) are discussed in section 4.2.2.

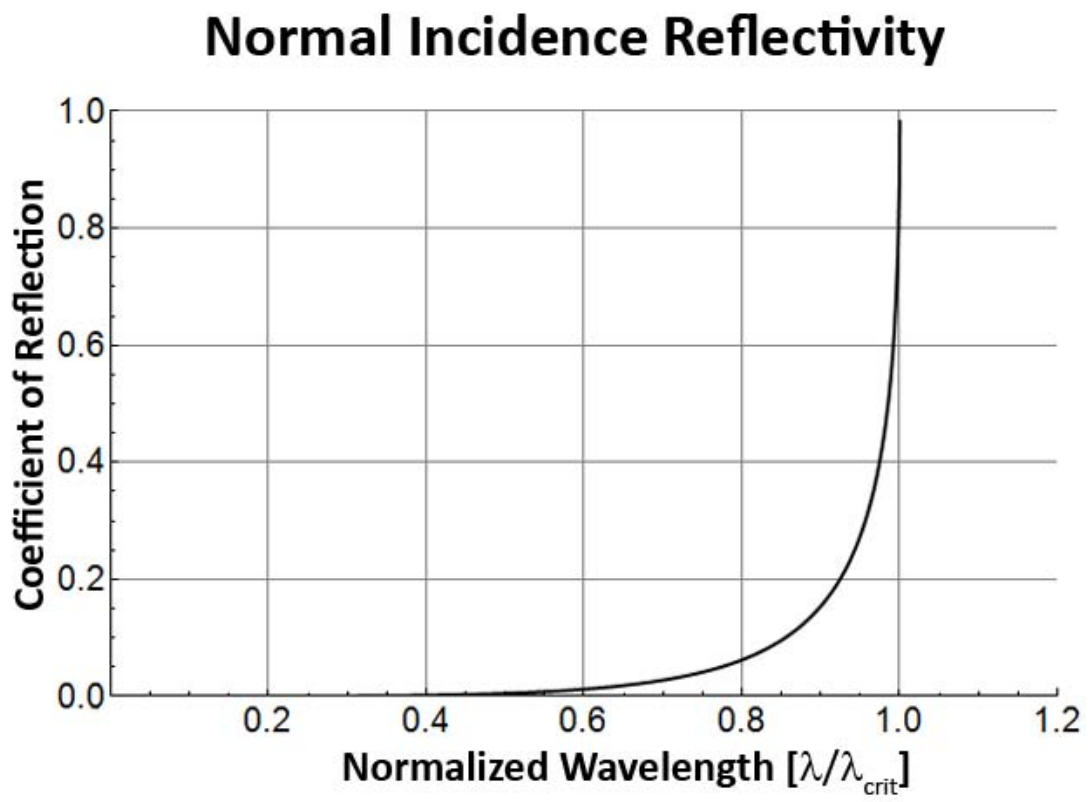


Figure 4.3: Variation of the normal incidence reflectivity of a HPO element with incident wavelength given as a fraction of the critical wavelength.

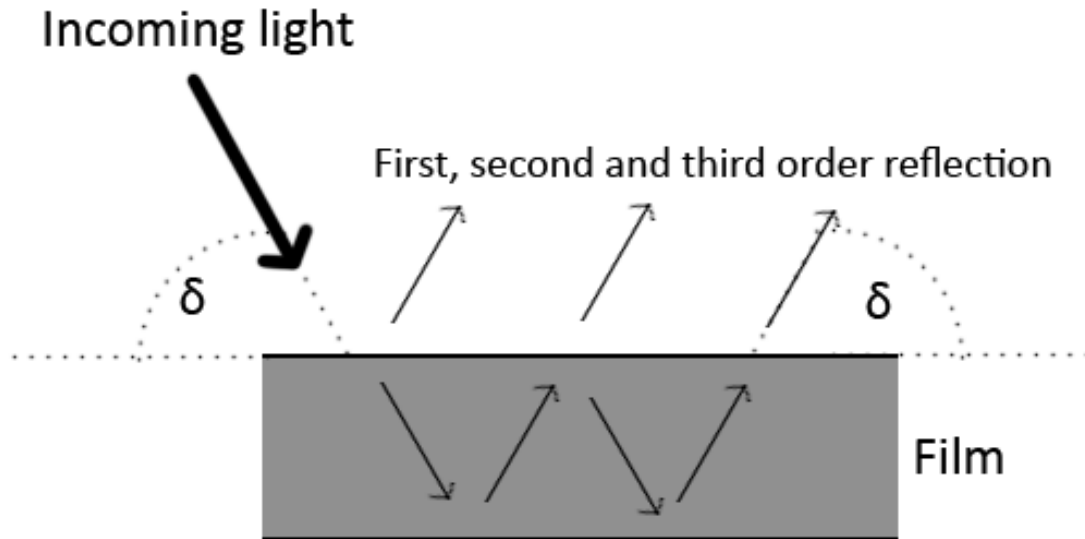


Figure 4.4: Reflectance from thin films: Light transmitted into the film at angle δ has a chance of leaving the film at the angle of reflection δ after multiple internal reflections.

One crucial aspect of the reflection behavior has so far been left unconsidered: The good candidate materials available for the creation of practical HPO elements require the HPO elements to be deposited as thin films rather than bulk devices. Reflection from thin films is of a different degree of complexity, even at normal incidence, and interference effects have to be considered.

In the thin film case light is reflected not only from the top surface of the film, but a fraction of R_I of the light transmitted through the top boundary will also be reflected from the bottom boundary, as illustrated in figure 4.4. By multiple internal reflections, and still assuming $R + T = 1$ (i.e. no absorption), the total fraction of reflected energy can be calculated by the converging series:

$$r = R_I + T_I^2 R_I + T_I^4 R_I^3 + T_I^6 R_I^5 + T_I^8 R_I^7 + \dots \quad (4.7)$$

where R_I and T_I are the coefficients of reflection and transmission respectively. The parameter r is called the "reflectance" of the film. From now on the term "reflectivity" will be used to refer to the fraction of light reflected from a single boundary only whereas "reflectance" will refer to the fraction of energy reflected from a thin film system.

The physics of thin film reflection is yet more complicated than indicated by the previous paragraph and equation (4.7). The first order reflected beam interferes with higher order reflected beams, causing the reflectance of the system to oscillate strongly with incident wavelength and physical film

parameters.

The reflectance interference pattern and its applications will be discussed in more detail in section 4.2. While the reflectance behavior at non-normal incidence is important to practical devices it is merely a question of using the full Fresnel treatment as outlined in Grant and Phillips [83] in place of equation (4.6). As such this problem is mostly an algebraic one and separate from the physics under consideration. Therefore non-normal incidence will not be considered in the following discussion, since it does not add to the scientific content discussed.

4.2 Optical Properties of a Thin Film Heavy Photon Optics Element

In the previous section the basic optical parameters of bulk HPO elements and their boundaries have been established. However, material constraints currently seem to limit HPO elements to thin film devices (see section 4.2.3). The aim of this section is to find quantitative expressions that will allow determination of the optical parameters of the system from information about the superconducting state of the system, taking into account thin film effects. As such, by the end of this section we will understand the theory of HPO devices well enough to draft some example applications and make quantitative estimates of their working parameters.

4.2.1 Thin Film Reflectance and Interference

Interference itself is not a HPO specific feature. However, it is of great importance when considering the transmission and reflection characteristics of any thin film device, and as such a working knowledge of thin film interference is important for a true understanding of the working mechanisms behind practical HPO devices.

In thin film optical devices interference is important, since, as illustrated in fig.4.4, any light entering the film will be reflected a number of times before being transmitted and the transmitted beam may interfere with itself [76]. The light may then be focused onto a screen, producing an interference pattern.

Such an interferometer is called a Fabry-Perot interferometer, or an etalon. Technically an etalon is a thin transparent film with partially reflective surfaces, while a cavity with reflecting walls is a Fabry-Perot interferometer, but the terms are often used interchangeably.

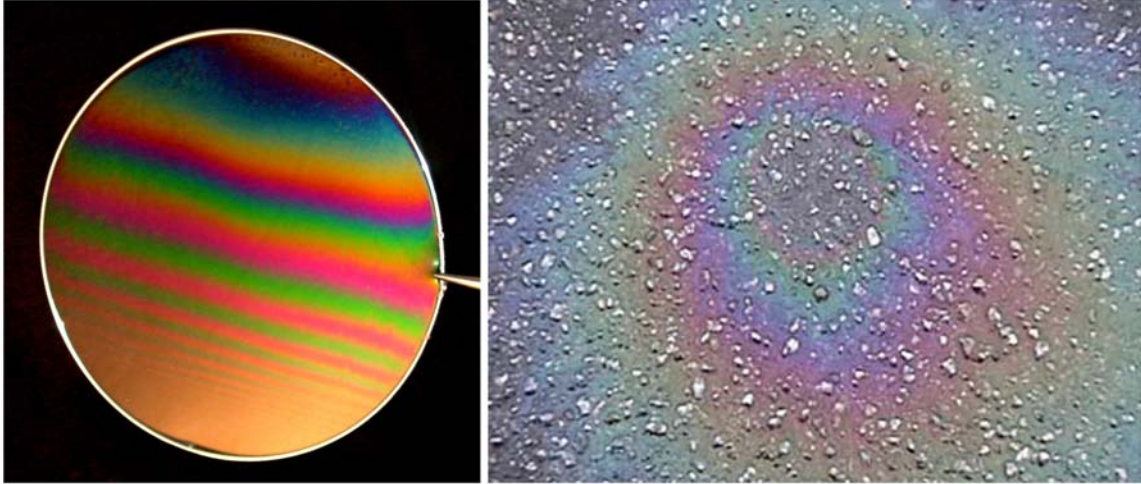


Figure 4.5: Examples of thin film interference on a soap bubble (left, image by Aberdeen University) and an oil slick (right, image by Georgia State University)

When observing an oil film or a soap bubble it is often possible to see a multitude of shimmering colours. These are produced by the interference of light that is reflected of the top and bottom boundary of the film, and the changing colours result from variations in film thickness (see figure 4.5). The basic working mechanism behind these colourful effects is thin film interference, identical to the interference occurring in an etalon: The reflected beam interferes with itself, and only those colours which have an interference maximum under the current viewing angle are seen by the observer.

Consider a thin film of reflectivity R_I and transmissivity T_I . The transmitted amplitude A_T of the electric field in the wave with incident amplitude A_{inc} can be calculated from the sum of the complex amplitudes of all transmitted rays (see figure 4.4). This can be written as a sum:

$$A_T = A_{inc} \sum_{m=0}^{\infty} R_I^m e^{im\delta} \quad (4.8)$$

where the series considers all the rays which have been reflected $2, 4, \dots, m$ times, i.e. $m \in \text{even}$ (since rays with $m \in \text{odd}$ are reflected by the film rather than transmitted) and δ is the phase change any ray undergoes as it traverses the etalon once.

Thus, by evaluating expression (4.8) an interference pattern can be constructed. It turns out that (4.8) is a geometric series and standard methods of series analysis show that it converges to [76]:

$$A_T = A_{inc} \frac{T_I}{1 - R_I \exp^{i\delta}} \quad (4.9)$$

We can evaluate the intensity transmitted I_T in terms of the incident intensity I_{inc} as [76]:

$$I_T = A_T^* A_T = I_{inc} \frac{T_I^2}{1 + R_I^2 - 2R_I \cos(\delta)} \quad (4.10)$$

where the phase shift δ when the beam traverses the etalon is calculated from its wave number k as $\delta = 2kl \cos(\theta)$. Here, l is the width of the etalon, θ the angle the incident light makes with the etalon and the wave number k can be calculated from the wave length of the incident light λ and the material refractive index n as $k = 2\pi n/\lambda$.

Thus the transmission function for light of wavelength λ incident on a HPO etalon of boundary separation l can be calculated as:

$$I_T = I_{inc} \frac{T_I(\lambda, \theta)^2}{1 + R_I(\lambda, \theta)^2 - 2R_I(\lambda, \theta)^2 \cos\left(\frac{4\pi n(\lambda)l \cos(\theta)}{\lambda}\right)} \quad (4.11)$$

where the refractive index n , coefficient of reflected intensity R_I and coefficient of transmitted intensity T_I are calculated according to sections 4.1.1 and 4.1.3 respectively. Assuming zero absorption, the reflected intensity I_R of the film can be calculated as $1 - I_T$. Equation (4.11) is actually valid for any etalon, whether HPO or conventional, but conventional material dispersion is small enough that n can be considered constant with λ for the purpose of calculating etalon transmission. The high reflectivity R_I of a HPO film near the critical wavelength λ_{crit} is not detrimental to thin film interferometer operation, as will be discussed in section 4.3.2.

A conventional etalon interference pattern and a HPO etalon interference pattern are plotted in figure 4.9 in section 4.3.2. It can be seen that near the active frequency the HPO based etalon produces peaks of superior full-width half-maximum resolution. This is a result of the extremely high refractive index of the HPO element near the critical wavelength as discussed in sections 4.1.1 and 4.1.2. The advantages and potential applications of HPO etalons will be discussed in more detail in section 4.3.2.

4.2.2 Superconducting Parameters and the Critical Wavelength

Two principal features make heavy photon optics such a desirable technology. These are

1. The diverging refractive index near a critical wavelength λ_{crit} .
2. The possibility to vary the refractive index, and by association the reflectivity and transmissivity, of an element by varying ambient temperature and magnetic fields.

In order to be able to exploit these features two questions have to be answered:

1. Is the stability of λ_{crit} against temperature and field variations good enough that the high refractive index for wavelengths very close to λ_{crit} can be exploited?
2. Is it possible to manufacture a HPO device that is sensitive enough to temperature and field variations that real-time control of the refractive index can be exploited?

For these questions to be answered an understanding of the microscopic parameters controlling λ_{crit} is required.

From eq.(4.2b) the parameter controlling the refractive index of a HPO element at any given wavelength is the critical wavelength λ_{crit} which is calculated from the London penetration depth λ_L as $\lambda_{crit} = 2\pi\lambda_L$. The microscopic dependence of λ_L on the superconducting carrier concentration has already been briefly discussed in section 3.5.6.2. It is possible to derive the expression for λ_L in terms of microscopic parameters from Maxwell's equations by considering a steady ($\partial/\partial t = 0$) current with homogeneous distribution of superconducting electrons ($\nabla\Psi_e = 0$) [60]. The resulting expression is:

$$\lambda_L = \sqrt{\frac{m_e}{2e^2\mu_0 n_s}} \quad (4.12)$$

where m_e is the electronic mass, n_s the density of superconducting electrons, and all other symbols have their usual meaning. Consequently the critical wavelength λ_{crit} can be found as:

$$\lambda_{crit} = 2\pi\sqrt{\frac{m_e}{2e^2\mu_0 n_s}} \quad (4.13)$$

Thus the variation of the refractive index n at any given wavelength λ with temperature T and applied magnetic field H ultimately depends on the variation of the superconducting carrier concentration n_s with T and H .

Equation (4.12) goes a long way towards answering our question about the variation of λ_L (and consequently λ_{crit}) with T and H , since the only free parameter in eq.(4.12) is the concentration of superconducting electrons n_s . The variation of n_s with T and H has been discussed in section 1.1.2. Remembering $\Psi_e^2 = n_s$ we use eqs. (1.1)(1.3) to find an expression for the variation of λ_L with T, H :

$$n_s = n_s^0 \left(1 - \frac{T}{T_c^0(1 - H/H_c)^{1/2}} \right)^4 \quad (4.14)$$

Variation of Carrier Concentration with T, H

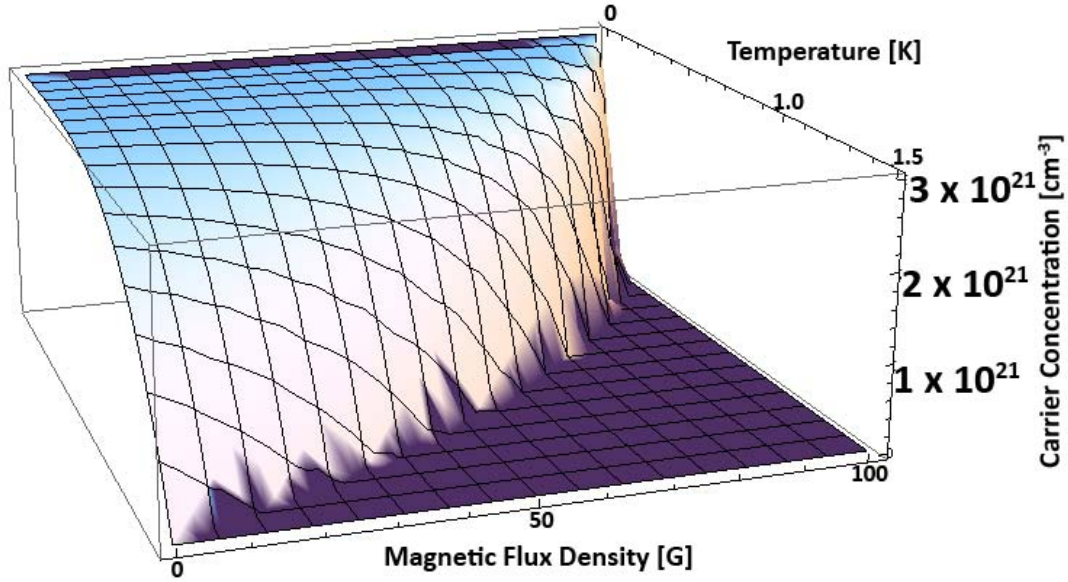


Figure 4.6: Variation of carrier density with temperature T and external magnetic field H for a superconductor of critical temperature $T_c = 1.5\text{K}$ and critical field $H_c = 101\text{G}$ and electron number density $n_e = 3 \times 10^{21}\text{cm}^{-3}$

where a superscript zero indicates the relevant quantity at zero T, H . The carrier density variation for a hypothetical HPO element (based on superconducting indium tin oxide as reported by Mori [84]) is plotted in figure 4.6.

Substituting eqs. (4.12)(4.14) into (4.2b) a full and closed expression for the T, H -variation of the phase refractive index n_p at wavelength λ of any HPO element can be determined:

$$n_p = \left(1 - \frac{\lambda^2 e^2 \mu_0 n_s^0 \left(1 - \frac{T}{T_c^0 (1 - H/H_c)^{1/2}} \right)^4}{4\pi^2 m_e} \right)^{1/2} \quad (4.15)$$

The analytical way to find the stability of the refractive index at a given wavelength would be to compute the relevant derivatives. Using the chain rule the derivative of the whole function may be found by the product of a number of rather simpler derivatives of the form $\frac{dn_p}{dT} = \frac{dn_p}{d\lambda_L} \frac{d\lambda_L}{dn_s} \frac{dn_s}{dT}$ (analogue for dn_p/dH).

When performing such an analysis it becomes clear that the temperature stability of n_p depends strongly on the temperature and magnetic field at which the superconductor operates, as can be seen from the varying slope of the $n_p(T, H)$ graph in figure 4.7. The following discussion assumes that operation is intended to be at $\lambda \approx \lambda_{crit}$, since this is where any HPO specific effects are strongest. Since $\lambda_{crit} = 2\pi\lambda_L$ it may be varied by using variations in T, H to achieve the carrier density n_s that will yield the desired λ_{crit} (eqs.(4.12)(4.14)). The temperature and field stability will increase the further away from the critical field and temperature the device can be operated in order to achieve the desired critical wavelength.

As an example, consider a HPO element made from a hypothetical transparent superconductor of critical temperature $T_c = 1.5K$ and zero temperature superconducting electron concentration $n_s^0 = 2 \times 10^{27} m^{-3}$ (based on superconducting indium tin oxide, discussed in section 4.2.3). If the HPO element is operated at $T = 0.1K$ the critical wavelength $\lambda_{crit} \approx 527nm$. At this temperature, the phase refractive index $n_p(525nm)$ ($2nm$ from λ_{crit}) will vary by less than 5 parts in 10^3 for a temperature change of $T(0.1K \rightarrow 0.2K)$, and by less than 7 parts in 10^6 for an external field change of $B(0G \rightarrow 1G)$. By contrast, operating the same HPO element at $\lambda_{crit} \approx 798nm$ ($T = 1.3K$) the variation of $n_p(796nm)$ (again $2nm$ from λ_{crit}) is about 785% for the a temperature variation $T(1.3K \rightarrow 1.4K)$ and a field change of $H(0G \rightarrow 1G)$ is going to yield a change in n_p of $\approx 136\%$. Thus, depending on the operating temperature, the relative sensitivity of the HPO device to variations in temperature varies by more than factor 10^5 . The variation of London penetration depth and phase refractive index $n_p(500nm)$ with T, H have been plotted in 4.7 for a hypothetical HPO element with $\lambda_{crit} = 500nm@T = 0K$.

Thus it is now possible to answer the questions posed at the beginning of this section: Can we create HPO elements of high stability against thermal and magnetic variation? And can we create elements whose stability is low enough that there optical characteristics can be varied in real time?

The answer is "yes" to both of these questions. As can be seen from figure 4.7, far from the T_c and H_c the slope of λ_{crit} and n_p with changes in temperature T and magnetic field H is small. Thus a high degree of stability can be achieved by designing HPO elements that are operated far from T_c . It can also be seen from figure 4.7 that the slope of both λ_{crit} and n_p with variations in T, H diverges near T_c, H_c , implying that the sensitivity to temperature and field variations can be increased arbitrarily by designing for combinations of superconducting materials and operating wavelengths close to T_c . Thus, HPO elements operated near their critical temperature T_c act as non-linear optically active materials, with high non-linearity.

Variation of Critical Wavelength and Phase Refractive Index

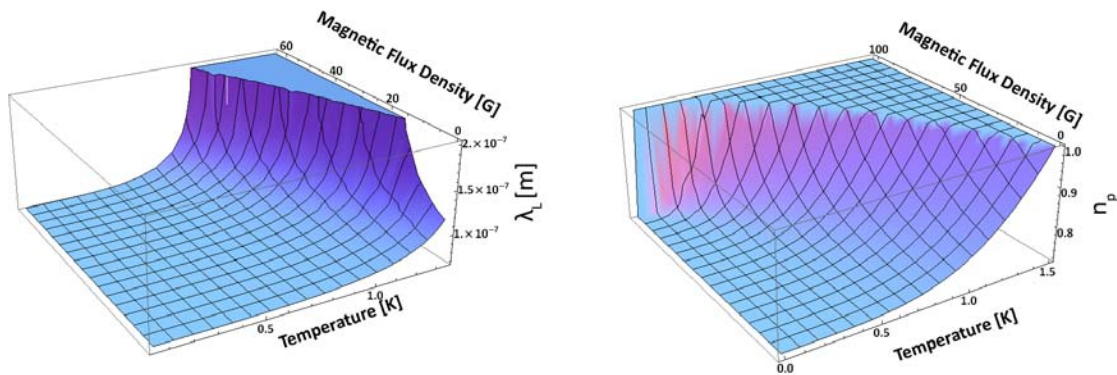


Figure 4.7: Left: Variation of the London penetration depth λ_L ($= \lambda_{crit}/2\pi$) with temperature T and external field H . Right: Variation of phase refractive index n_p with Temperature T and external field H . Both graphs are plotted for a superconductor with superconducting electron number density $n_s^0 = 3 \times 10^{21} \text{ cm}^{-3}$ at $T = 0 \text{ K}$.

4.2.3 Transparent Superconducting Materials: Towards Practical Heavy Photon Optics

In order to create any kind of practical HPO transmission optics or etalon/Fabry-Perot interferometer a superconducting compound is required which has good transparency at the wavelength of interest. Furthermore, the concentration of superconducting electrons must be of the correct magnitude that the critical wavelength can be made to fall into the transparent waveband of the superconductor. If the carrier concentration is too low the maximum critical wavelength attainable (λ_{crit} at $T = 0 \text{ K}$) will be so low as to be outside the transparent band. If, on the other hand, the carrier concentration is too high (a very unlikely case) the material will have to be operated so close to its critical temperature that thermal instabilities will make consistent operation impossible.

Essentially two different types of transparent conductors exist [81]: Either a succession of very thin metal layers, such as Ag, Au or Cu is separated by transparent films anti-reflecting the metal or a wide-bandgap oxide semiconductor is employed. In this section we will be concentrating on the latter type of material, since it yields better transmissivities coupled to comparatively high conductivities.

Of particular interest is Indium Tin Oxide (ITO) which combines good transparency in the optical and near-IR (300nm - $\approx 2 \mu\text{m}$) with a comparatively high carrier concentration ($\approx 10^{27} \text{ m}^{-3}$) [81].

It has been shown that thin ($\approx 20nm$) ITO films deposited onto glass or polyester substrates will go superconducting at temperatures of $\approx 1 - 3.5K$ [84], depending on substrate, deposition and annealing regime. Since the mechanisms for conduction and transparency are similar throughout the entire field of wide bandgap conducting oxide films, the superconductivity of ITO turns the entire range of wide bandgap conducting oxides into a set of likely candidates. An overview can be found in [85].

Using equation (4.12) it is possible to calculate the London penetration depth λ_L , and by extension the critical wavelength λ_{crit} (eq. (4.13)) from the carrier density of ITO. Assuming an ITO film with high but reasonable $n_s \approx 2 \times 10^{21} cm^{-3}$ [81] the zero-temperature λ_{crit} of ITO is found to be $\approx 550nm$. This is well within the transparent bandpass for an ITO film with carrier concentration $n_s < 3 \times 10^{21} cm^{-3}$ [81].

From the superconductivity of ITO reported by Mori [84], at least one transparent compound exists which can be made to go superconducting, along with a whole field of potential candidates. However, Mori [84] has not verified whether ITO retains its transparency in the superconducting state. While Cooper pair breaking was not an issue for our considerations when evaluating the massive-em Casimir effect since it is impossible to extract energy from a vacuum mode (section3.5.6), it seems reasonable to expect that real photons with energy $E_{ph} > 2\Delta_g$ will break Cooper pairs. Hence, HPO devices would be opaque to frequencies above the far infrared. This issue will be addressed in section 4.2.3.1, where we will find that some materials exist for which we may expect transparency to continue well into the optical spectrum.

4.2.3.1 Transparency of Superconducting Oxides to Optical Photons

It seems from the preceding discussion that wide bandgap superconducting oxides are a good candidate for a HPO element. This section attempts to establish whether such superconducting oxides can be expected to retain their transparency, focussing on ITO.

For light interacting with bulk matter two chief mechanisms for dissipative absorption exist [76]:

1. The electromagnetic radiation may excite the free electron plasma, which dissipates energy by oscillation.
2. A photon may excite an atom into a higher quantum state. The excited atom can be expected to transfer its excitation energy via collisions or lattice vibrations (i.e. phonons) to the bulk matter before a photon can be re-radiated.

We will first examine case 1. A cloud of free charge carriers with plasma frequency ω_p excited by radiation of frequency ω behaves as a forced harmonic oscillator, yielding a group refractive index η_g as discussed in section 3.5.4.1 and given by [76]:

$$n^2(\omega) = 1 + \frac{\omega_p^2}{-\omega^2 + i\gamma\omega} \quad (4.16)$$

Dissipation by the gas is governed by the imaginary component of (4.16) proportional to the inverse scattering time $1/\gamma$.

For normal materials, as ω approaches ω_p the imaginary part of equation (4.16) becomes dominant and the material is opaque. However, inside a superconductor two separate electron populations have to be considered. According to eq. (1.1) the fraction of electrons in the normal state is non-zero for a superconductor at non-zero temperature and according to the Gorter-Casimir two fluid model discussed in section 1.1 the normal state and superconducting electron populations interpenetrate each other freely. Consequently, inside a superconductor it is necessary to separately consider the two plasma frequencies ω_p^n and ω_p^s of the normal state electron cloud and the superconducting condensate respectively. Since superconducting electrons do not scatter, the superconducting scattering time $\gamma_s \rightarrow \infty$, and no dissipation occurs for $\omega \rightarrow \omega_p^s$. Provided that the number density of superconducting electrons is larger than the number density of normal electrons the relevant plasma frequencies are related by $\omega_p^s > \omega_p^n$, and dissipation by the normal state electron gas is small.

For conventional superconducting materials the transmissivity drops steeply as the photon energy E_{ph} approaches and exceeds the excitation energy of a Cooper pair $2\Delta_g$. This is because the incident photons will expend a fraction of their energy to break Cooper pairs. Since the superconducting energy gap Δ_g is small compared to the energy of an optical photon [5], the majority of the photon energy is given to the electron as kinetic energy. However, for the case of wide band gap oxides, a large band gap of order $E_g = 3.8\text{eV}$ prevents photons from directly exciting Cooper pairs (or, indeed, electrons). There are simply no allowed states at the accessible energies. A thorough introduction to the band structure of ITO can be found in [86]. The wide band gap is also the reason for the optical transparency, and the maximum transmitted photon energy is given by $E_{ph,max} = E_g$.

In summary, we believe that the same mechanism which provides optical transparency for ITO in the normal state also provides optical transparency for the superconducting medium. While the small amount of dissipation provided by excitation of the normal state electron plasma may serve to increase the temperature of an ITO element (and thereby reduce the superconducting carrier density), any such problems may be counter acted by thermally anchoring the ITO element and ensuring that the resulting equilibrium temperature provides the superconducting carrier concentration n_s which yields the required critical wavelength λ_{crit} according to eq.(4.13).

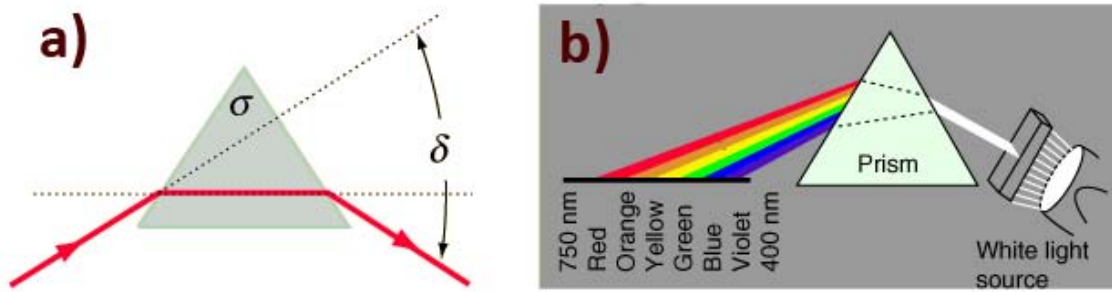


Figure 4.8: A prism with apex angle σ , with light incident at minimum deviation δ . a) The minimum deviation angle is the angle of incidence which causes light to travel parallel to the prism base. b) illustration of the working principle of a dispersion prism. Note: In order to achieve the best energy resolution the entire prism has to be illuminated. Image courtesy of Georgia State University [14]

4.3 Potential Applications for HPO Technology

4.3.1 Ultrahigh Resolving Power Dispersion Prisms

The most obvious application of heavy photon optics is for the creation of ultrahigh resolution dispersion prisms. In the course of this section we will outline how the divergence of the phase dispersion D_p can be exploited in order to create prism spectrometers with resolving powers exceeding those of conventional prisms of comparable size by three orders of magnitude.

The phase dispersion D_p of a prism is the controlling parameter for its spectral resolution. The simplest expression for the resolving power R of a prism, the Raleigh limit, is given by [87]:

$$R = BD_p = B \frac{\partial n_p}{\partial \lambda} \quad (4.17)$$

where B is the base width of the prism, and the entire prism is illuminated by a collimated beam. This expression is valid for the case where the angle of incidence of the light to be dispersed is that of minimum deviation δ (figure 4.8). For light incident at angle δ , the angle between incident and transmitted beam is at the absolute minimum.

Considering eq.(4.17) it can be seen that the resolution ratio $r = \frac{R_1}{R_2}$ of two prisms of identical geometry and respective resolving powers R_1 and R_2 only depends on the ratio of their respective phase dispersions.

The phase dispersion of a conventional dispersion prism based on F2 Schott Glass is quoted by CVI

Laser to be approximately $D_{p,prism} = -8.54 \times 10^4 m^{-1}$ [13]. Using eq.(4.2c) we find the magnitude of the phase dispersion of a HPO element $D_{p,HPO}$ with critical wavelength $\lambda_{crit} \approx 780nm$ to be $> 8 \times 10^7 m^{-1}$ within a $0.1nm$ band around λ_{crit} . This seems to imply that the resolving power of the HPO element described would exceed that of a typical conventional dispersion prism of identical size and geometry by a factor of $D_{p,HPO}/D_{p,prism} \approx 10^3$.

A problem with ultrahigh resolving power HPO dispersion prisms is the high reflectivity of the device. For the prism described in the previous paragraph the heavy photon phase refractive index at the wavelength of interest ($\lambda = 789.9nm$) is approximately $n_p \approx 0.016$ yielding a reflectivity R_I of $\approx 94\%$. However, for smaller resolutions the situation is improved significantly. A dispersion of 8×10^6 still yields a spectral resolution superior to that of a conventional prism by two orders of magnitude, while only requiring the relevant light to be within $\Delta\lambda = 1nm$ of the critical wavelength, yielding $n_p \approx 0.16$ and a reflection coefficient $R_I \approx 52\%$. As such there appears to be a trade-off between the resolving power and the efficiency and bandwidth of a HPO prism, and it may be possible to optimize a prism depending on the application. Also, if low dispersion-high refractive index antireflection coatings are introduced the problem may be mediated somewhat [76].

Still, it seems frustrating that the usefulness of such an elegant effect should be restricted by the reflectivity of the films surface. For this reason we will investigate thin film interference based devices next. These exploit the high reflectivity of the films surface rather than be limited by it.

4.3.2 Interferometers and Etalons

An interesting potential application for HPO technology is Interferometry. HPO based etalons and Fabry-Perot interferometers as outlined in section 4.2.1 exploit the diverging refractive index and diverging dispersion near λ_{crit} . A high gradient of the phase refractive index n_p results in a large change of phase shift δ with incident wavelength λ for a beam traversing the film. This can be seen by taking the derivative of the phase shift $\delta = 4\pi n(\lambda)l \cos(\theta)/\lambda$ from equation (4.11) w.r.t. λ and applying the chain rule to obtain $\frac{\partial\delta}{\partial\lambda} = \frac{\partial\delta}{\partial n} \frac{\partial n}{\partial\lambda}$. The combination of a high refractive index n and ultrahigh dispersion D means that HPO etalons yield higher, narrower transmission peaks over a small waveband, compared to conventional etalons.

The equations outlined in sections 4.1.1,4.2.1 and 4.2.2 have been used to create a simple analytical model for normal incidence etalon transmission of both conventional and HPO etalons. Equation (4.15) for the phase refractive index n_p as a function of experimental and material parameters T, T_c, H, H_c, n_s^0 has been substituted into equation (4.11) where the transmission coefficient T_I and reflection coefficient R_I have been calculated according to equation (4.6) using $T_I = 1 - R_I$, assuming

Etalon Transmission Functions

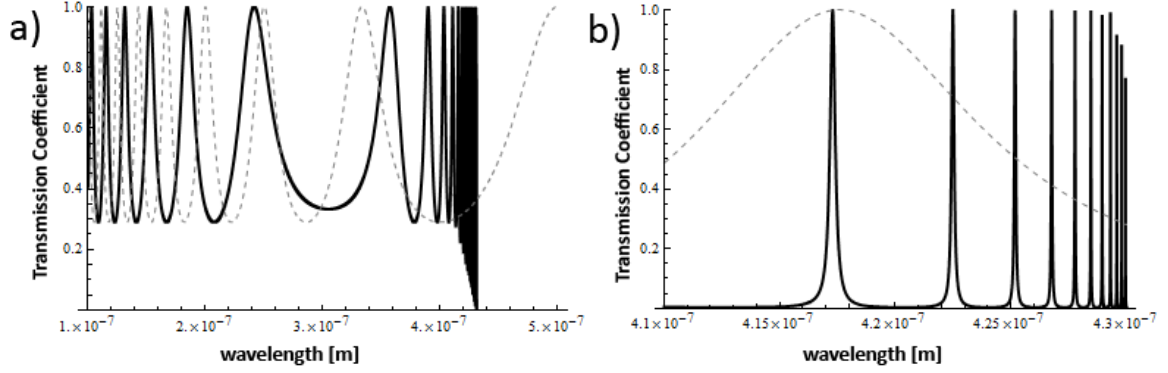


Figure 4.9: Comparing the interference pattern of a conventional etalon (dashed line) and a HPO etalon (solid line) with critical wavelength $\lambda_{crit} = 431nm$. An external reflector of reflectivity $R_I = 30\%$ is applied to both etalons which have a thickness of $0.5\mu m$. The wide band and narrow band responses are plotted in figures a) and b) respectively. It can be seen from a) that far from λ_{crit} the peak fwhm resolution of the HPO etalon approaches that of the conventional etalon.

the HPO etalon to be in vacuum and using equation (4.15) for the HPO refractive index. This yields:

$$I_T(\lambda, T, T_c, H, H_c, l, n_s^0) = I_{inc}(1 - R_I(\lambda))^2 \left(\frac{1 + R_I(\lambda)^2 - 2R_I(\lambda)^2 \cos \left(\frac{4\pi \left(1 - \frac{\lambda^2 \epsilon^2 \mu_0 n_s^0 \left(1 - \frac{T}{T_c^0 (1 - H/H_c)^{1/2}} \right)^4}{4\pi^2 m_e} \right)^{1/2} l \cos(0)}{\lambda} \right)}{\lambda} \right)^{-1} \quad (4.18)$$

where we have assumed normal incidence, i.e. $\theta = 0$. This equation then yields the response of a HPO etalon at normal incidence as a function of experimental and material parameters.

The responses for a conventional etalon and a HPO etalon have been plotted in figure 4.9. In both cases we assumed the surfaces of the cavity have been silvered with a material of reflection coefficient $R_I = 0.9$ across the entire waveband of interest. In order to illustrate how the etalon response varies away from the critical wavelength, the wide band transmission function of the HPO etalon has been plotted in figure 4.9.

As can be seen from figure 4.9, the high reflectivity of a HPO element near λ_{crit} has no detrimental effect on the etalon transmission pattern. This result may seem counter intuitive at first, since one would assume that, if $R \rightarrow 1$ no light enters the device and therefore no interference can occur. This

is, however, not correct. For any R arbitrarily close to unity there exists a wavelength at which all the incident light is transmitted. A lucid derivation of this fact and the etalon transmission function is given by Hecht [76]. As $R \rightarrow 1$ the spectral width w of the transmission peaks $w \rightarrow 0$.

4.3.2.1 Etalon Absorbtion

So far we considered hypothetical perfect devices where the coefficient of absorption $A_I = 0$ so that $R_I + T_I = 1$. For $A_I > 0$ we then have $R_I + T_I + A_I = 1$. For the case of ultrahigh resolving power dispersion prisms as outlined in section 4.3.1 absorbtion does not constitute a major problem. For $\lambda < \lambda_{crit}$ any non-zero A_I is introduced by the normal material parameters rather than any HPO specific effects. If the optical absorbtion of the material in the normal state is small than so is the superconducting state absorbtion for $\lambda < \lambda_{crit}$.

In the case of an etalon one might wonder whether the absorbtion introduced by the etalon material introduces an intrinsic limit for the fwhm resolution of the etalon. A derivation of the effect of absorbtion on etalon transmission is provided by Hecht [76] where it is shown that the peak separation is unaltered and the transmission peak height is reduced according to:

$$\frac{I_t}{I_{inc}} = \left[1 - \frac{A_I}{1 - R_I} \right]^2 \quad (4.19)$$

Thus, while absorbtion in the etalon reduces the fwhm resolution it does not create an absolute limit. The effects of absorbtion are identical for conventional etalons and HPO etalons operated at $\lambda < \lambda_{crit}$. As an example, for an etalon with reflectivity $R_I = 95\%$ and absorbbtivity $A_I = 1\%$ equation (4.19) yields $I_t/I_{inc} = 64\%$.

4.3.3 Optical Routers and Quantum Non-Demolition Routing

So far the applications described in sections 4.3.1 and 4.3.2 have exploited the diverging refractive index and dispersion which are the central features of HPO technology. This section will describe how also the ability to vary the refractive index at run time can be exploited and made into the central feature of a novel optical routing technology.

It is possible to alter the reflectivity of a thin film by altering its refractive index. In section 4.2.2 it has been shown that the refractive index of any HPO device can be manipulated by methods that manipulate the superconducting carrier density, such as changes in temperature or applied magnetic fields. By varying these parameters it is possible in principle to change the critical wavelength λ_{crit}

to any value between its minimum value and infinity. A thin HPO film that is transparent to optical light but reflective at the critical wavelength can then be used to either redirect light or let it pass unhindered.

The basic routing principle is illustrated in figure 4.10. A route from the client to the host is negotiated electronically, where upon all routers along the determined path set the reflectivity of their HPO elements as to direct the signal along the negotiated route. In this way, an uninterrupted optical path is created from the client to the host allowing for direct optical communication. Care must be taken in the routing of the signals, so that all HPO elements that are not meant to influence an incoming signal of wavelength λ_{signal} are set to critical wavelengths $\lambda_{crit} > \lambda_{signal}$ in order to prevent absorption in the inactive HPO elements.

This routing architecture essentially requires two separate physical network layers: The electronic network layer which negotiates the route and the optical layer on which the actual communication occurs. The current day internet could be employed as the electronic layer. Its facilities for the determination of possible routings, such as the Internet Control Message Protocol (ICMP) would make it ideally suitable for the task.

The most obvious advantage of such Direct Optical Link (DOL) routing is the increase in communication speeds. In conventional networks, routing of optical signals is achieved by converting the optical signal to an electronic signal, decoding its routing data, and re-emitting the signal onto the correct route. This conversion is slow, and the major bottleneck of modern optical communication networks. Thus HPO-DOL routing can potentially lead to significant increases in optical communication speeds.

Maybe the most significant advantage of this kind of routing technology is that it provides quantum non-demolition routing, i.e. it has the ability to route photons without altering their quantum mechanical wave functions. The exchange of photons in quantum mechanically entangled polarization states is one of the key ingredients of Quantum Key Distribution (QKD), a system that allows for the secure exchange of one time pad keys. As such HPO-DOL routing can provide QKD in switched networks. It is the authors opinion that the ability to deploy QKD in switched networks would increase the economic significance of QKD systems dramatically, moving them from niche military markets into the mainstream banking sector.

4.3.4 Universal Optical Logic Gates and Optical Logic Chips

All-optical computing components and logic gates are attractive for a number of reasons. In theory optical logic components may be faster and consume less power than electronic systems, while also

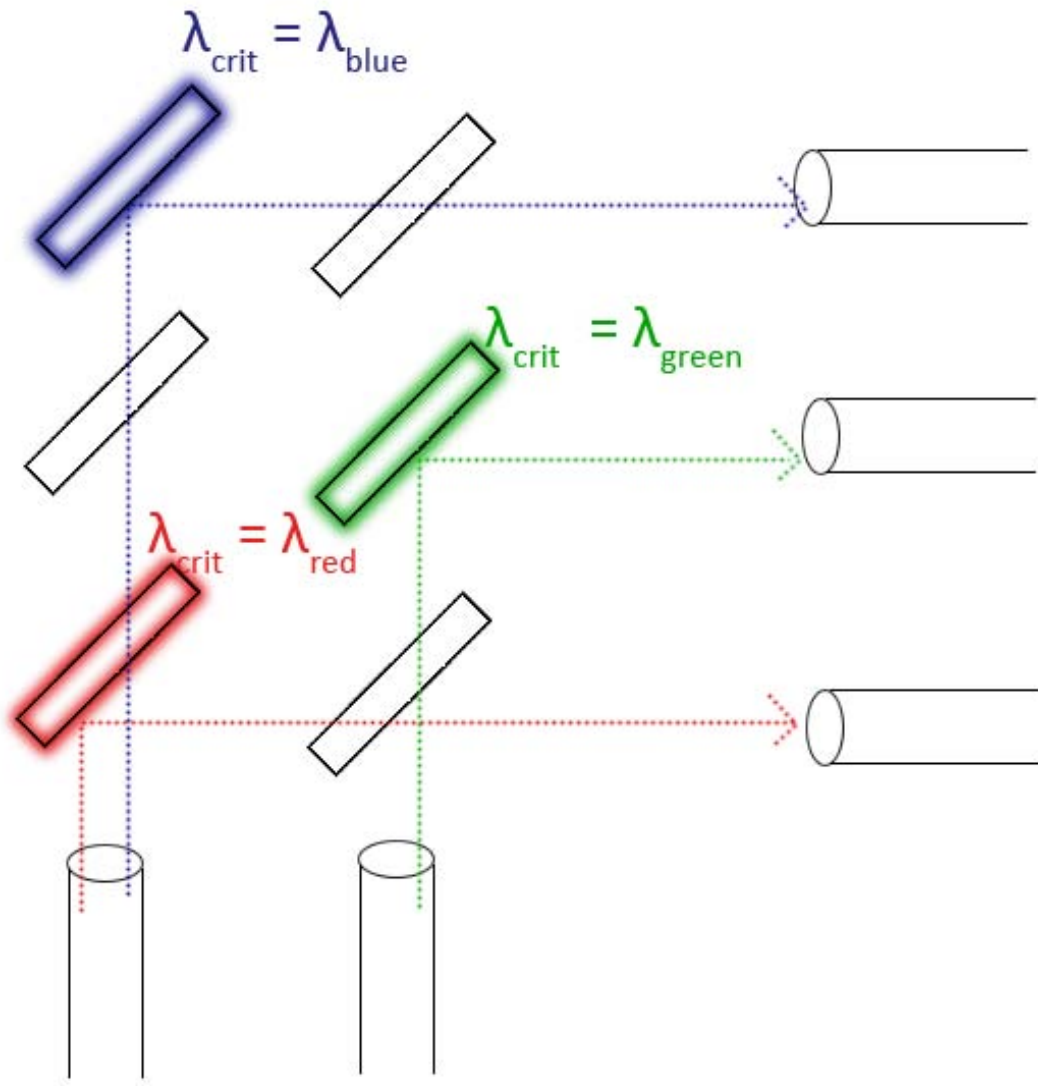


Figure 4.10: Illustration of the optical routing principle: Only the elements set to $\lambda_{crit} = \lambda_{signal}$ are reflective. All other elements allow the signal to pass unhindered.

allowing direct interfacing with quantum computing components.

In this section we outline how a hypothetical optical AND gate may be constructed using HPO technology. The design outlined here requires high thermal stability, of order $\pm 1\mu K$. As such it is intended as a demonstration of principle rather than detailed technical description of a practical device. It is presented here since it demonstrates a possible application for the extremely high non-linearity provided by HPO elements.

Consider a HPO etalon made from ITO with carrier density $3 \times 10^{21} \text{ cm}^{-3}$. The etalon has a critical temperature $T_c = 1.5K$, critical field $B_c = 101G$ and is driven at $T = 1.4K, B = 0G$. The surfaces of the etalon are silvered to a reflectivity of $R_I = 0.9$. We set the signal wavelength to be $\lambda_s \approx 877.021nm$ to coincide with the transmission peak in figure 4.11. Given the settings outlined in this paragraph the etalon transmission function has a maximum at the signal wavelength (figure 4.11). If a signal of power density $6mW/m^2$ is applied this increases the root mean square(rms) magnetic field in the etalon by $\approx 72\mu G$ and consequently reduces the carrier density. This is sufficient to reduce the etalon transmission at λ_s to below 1% (figure 4.11b). If a signal of power density $2 \times p = 12mW/m^2$ is applied the resulting total field shift of $\approx 144\mu G$ is sufficient to move a different transmission maximum onto the signal wavelength (figure 4.11c). Thus we have constructed an AND gate: A single signal beam of wavelength λ_s and power density p will be reflected while two signal beams of individual power density p (i.e. combined power density $2p$) and wavelength λ_s will be transmitted.

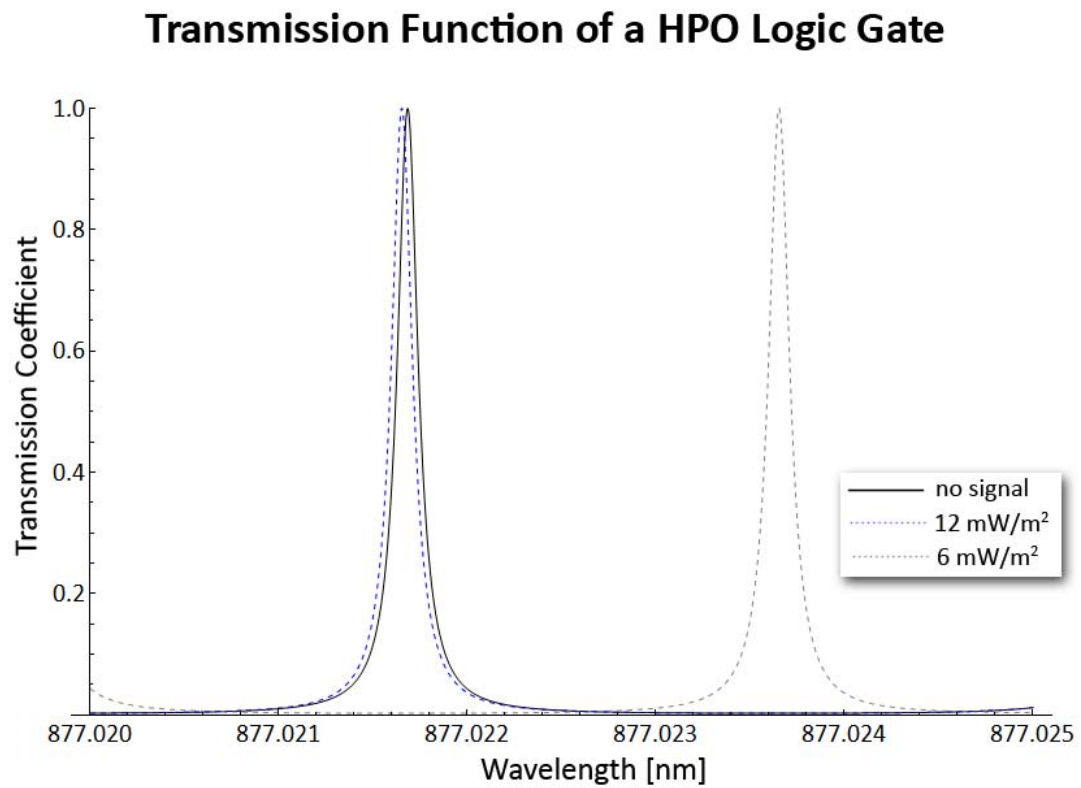


Figure 4.11: Transmission coefficient of a HPO etalon as a function of wavelength. This etalon is used as a logic gate. The transmission coefficient varies with applied signal strength and transmission functions are plotted for signal strengths of $6\text{mW}/\text{m}^2$ (grey dashed line), $12\text{mW}/\text{m}^2$ (blue dashed line) and "no signal" (black solid line).

Chapter 5

Massive Gauge Bosons in Quantum Coherent Matter

Up to this point a large proportion of this thesis has been concerned with the properties of massive photons as described by the Proca equations (3.12). The fact of this symmetry breaking has been accepted, without any attempt to truly understand its source.

The extent to which the physics developed in Chapters 3 and 4 relies on massive photons should be sufficient reason by itself to motivate an investigation of the exact mechanism which causes non-zero photonic mass. Furthermore, in order to be able to evaluate other mechanisms than low- T_c superconductivity (e.g. high- T_c superconductivity) as potential candidates for the creation of massive photons, a good understanding of the relevant processes is required.

Finally, an intriguing question is whether other traditionally massless gauge bosons can be assigned a mass by symmetry breaking mechanisms. It is well known [60] that the Z-boson acquires its mass by symmetry breaking, and we have made heavy use of the fact that it can be shown [60] that the γ -boson (i.e. photon) does so as well. In front of this background an obvious and extremely intriguing candidate is what, for consistency, might be referred to as the g-boson: The graviton.

This chapter will begin with a section discussing the U(1) symmetry, which is the symmetry giving rise to what is generally known as electromagnetic gauge invariance. The same section will then proceed to explain why U(1) symmetry is lost when a material undergoes sn-transition. This is generally, and incorrectly, known as gauge symmetry breaking. If one were to be mathematically precise it would be necessary to realize that a gauge symmetry is a degeneracy inherent to the description of a system and can never be broken. The correct mathematical statement is: *U(1) phase rotations are*

removed from the group of electromagnetic gauge symmetries. However, since the finer points of topology and gauge theories are of no interest to us for the purpose of the derivations that are to follow we shall refer to the process as gauge invariance breaking, which is consistent with most of the literature available on the topic.

This chapter will proceed to outline the Gravitoelectromagnetic (GEM) equations which govern gravity in nearly flat space times and outline the process by which the gauge boson of GEM gravity will acquire non-zero rest mass. This method is almost identical to the derivation of the photonic mass. While the differences of the two derivations will be pointed out at the end of the section, it is believed that they are sufficiently similar so as to not require repetition. A full derivation of the photonic mass for the relativistic and non-relativistic case can be found in [60]. At the end of this subsection a full and closed derivation of the rest mass of a spin-1 graviton will have been achieved from first principles.

To conclude, the consequences of a massive graviton for astrophysics and for some known experimental anomalies will be discussed, and topics for future research will be highlighted.

5.1 U(1) Phase Rotational Symmetry and Local Electromagnetic Gauge Invariance

This section will introduce the concept of local gauge invariances and the U(1) symmetry group. These concepts will then be used as a basis for approaching the problem of electromagnetic gauge symmetry breaking and its consequences.

A fundamental feature of Maxwellian electromagnetism is the arbitrariness of electromagnetic potentials. Adding the same constant voltage offset Δ to every point in an arbitrary physical setup does not change any observables. Only potential differences, not absolute potentials, are observable. This symmetry is the global gauge symmetry of electromagnetism.

However, relativity dictates that we also require a local symmetry. Since two arbitrary points A and B in the physical setup separated by any non-zero distance cannot communicate instantaneously it appears that any change in potential Δ_A at A would have to be independent of potential changes Δ_B at B . Thus, in order to make gauge invariance consistent with relativity we require the change in gauge to be an arbitrary function of time and space $\Delta(\vec{r}, t)$. Let us repeat the definition of the electric field E and magnetic field B in terms of the scalar potential ϕ and vector potential \vec{A} from section 3.5.

$$\vec{E} = -\frac{1}{c} \frac{\partial \vec{A}}{\partial t} - \nabla \phi \quad (5.1)$$

$$\vec{B} = \nabla \times \vec{A} \quad (5.2)$$

Considering Maxwell's equations and replacing \vec{E} and \vec{B} with the expressions from (5.1) and (5.2) it is indeed possible to find such a local gauge symmetry which can reconcile the arbitrariness of electromagnetic potentials with relativity, allowing any $\Delta(\vec{r}, t)$ which can be expressed as the derivative of an arbitrary well behaved function χ . Consider the transformations:

$$\vec{A} \rightarrow \vec{A}' + \nabla \chi(\vec{r}, t) \quad (5.3)$$

$$\phi \rightarrow \phi' + \frac{\partial \chi(\vec{r}, t)}{\partial t} \quad (5.4)$$

Using the above transformations and substituting them into Maxwell's equations we find that all physical observables remain unchanged. This is known as the electromagnetic $U(1)$ symmetry, sometimes referred to as electromagnetic phase rotation symmetry.

Mathematically, $U(n)$ denotes the *unitary group of degree n* , i.e. the group of $n \times n$ unitary matrices. Geometrically, multiplication with a $U(n)$ matrix rotates a point around the origin in a coordinate system of n complex dimensions, without changing the distance to the origin. Without going into the details of group or matrix theory, $U(1)$ is the group of all complex numbers of magnitude unity. Consider any point on the complex plain. This point can be described by its distance from the origin (the magnitude r of the number) and the direction from the origin in which it can be found (the phase ϕ). The effect of the above transformations (5.3)(5.4) is to multiply the complex wave function of a quantum mechanical particle by a member of the $U(1)$ group, rotating the number around the origin of the complex plane without changing its magnitude. This effectively amounts to changing the phase of a point in complex 1-dimensional space, which is why electromagnetic gauge invariance is referred to as phase rotational symmetry. Such diagrams visualizing complex numbers as points on a two dimensional plane are called Argand diagrams. Argand diagrams and $U(1)$ phase rotations are illustrated in figure 5.1, below.

Considering a quantum mechanical particle, the effect of the transformations (5.3) (5.4) have on the Schroedinger equation is that of introducing an exponential phase factor:

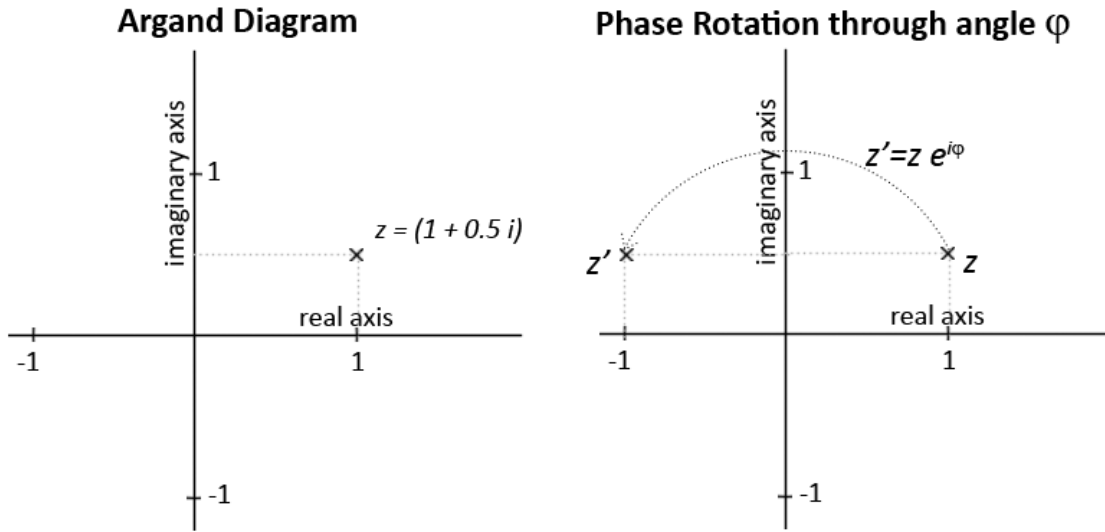


Figure 5.1: a) Argand diagram and b) Point on the complex plain undergoing U(1) rotation

$$\Psi(\vec{r}, t) \rightarrow \Psi_0(\vec{r}, t) \exp[iS(\vec{r}, t)] \quad (5.5)$$

The Hamiltonian of the system is unchanged under the transformation (5.5) since it depends on $\langle \Psi | \Psi \rangle = \langle \Psi_0 | \Psi_0 \rangle$. Since the Maxwell equations are also invariant under transformations (5.3)(5.4) no observable differences occur if a particle's wave function undergoes U(1) phase rotation.

The breaking of $U(1)$ symmetry in superconductors occurs due to the observability of the phase S . In a general quantum mechanical system the phase S and number of quanta N cannot be observed simultaneously. According to [4] the S and N can be fixed simultaneously inside a superconductor provided that N is large. Now the transformations (5.3) to (5.5) lead to observable changes in the physical system (for example in Ginzburg-Landau theory, which introduces an energy cost for gradients in \vec{A} [4]), removing $U(1)$ phase rotations from the group of electromagnetic gauge symmetries.

It is in fact possible to observe the electromagnetic U(1) symmetry breaking independently of superconductivity. All that is required are particles with correlated wave functions and a method to observe those wave functions. It is, for example, well known that the self-interference pattern of electrons projected through a double slit depends on the electromagnetic vector potential in the region in between the two slits, despite the fact that the electron never interacts with the resulting magnetic field [88]. This is known as the Aharonov-Bohm Effect according to Yakir Aharonov and David Joseph Bohm who demonstrated it in 1959.

5.1.1 The Relativistic Photon Field

At this point one central question seems to remain unanswered: What is the nature of the gauge potentials ϕ, \vec{A} ? Are they merely a mathematical convenience or do they have actual physical meaning, and how can manipulating their symmetries help us to deduce the properties of a photon?

The gauge transformations (5.3)(5.4) outlined above can be combined into a single four-vector transformation:

$$A^\mu \rightarrow A'^\mu = A^\mu - \partial^\mu \chi \quad (5.6)$$

where $A^\mu = (\phi, \vec{A})$. Using the identities (5.1)(5.2) to substitute A^μ into the vacuum ($J = 0$) Ampere-Maxwell law it is possible to arrive at the equation [89]:

$$\nabla^2 A^\mu = \frac{1}{c} \frac{d^2 A^\mu}{dt^2} \quad (5.7)$$

This is the wave equation for a massless quantum mechanical particle. The particle must also be non-self-interacting in order for the phase rotations to remain unobservable in normal matter. And this non-self-interacting gauge boson of zero rest mass is indeed well known: It is the photon. Thus the gauge invariant 4-vector potential A^μ is the quantum mechanical photon field and changes to the allowed gauge transformations will lead directly to changes in the mathematical form of the photon field.

5.2 Massive Gauge Bosons From Broken U(1) Symmetry

In this section we present a derivation of the mass of the graviton inside a superconductor. However, no part of this derivation is restricted in validity to a superconductor. Rather, the key ingredient is the presence of particles with coherent wave functions ("quantum coherent matter") so that the number of particles and their phase are both observable. As such the same derivation is valid for superconductors, superfluids and any other kind of quantum coherent matter. We start from the gravitomagnetic equations and use the breaking of U(1) phase rotational symmetry of particles with a macroscopic wave function. We arrive at a simple and complete analytical expression for the graviton mass in terms of fundamental constants, with the mass density of the superconductor the only free parameter entering the ratio of photon- to graviton mass. We conclude by comparing predictions of our graviton mass with existing experimental data concerning the Tate Cooper pair mass anomaly [30][90].

The mechanism employed here to allow photons to acquire a rest mass inside a superconductor is the Higgs mechanism and the broken symmetry required to drive the Higgs mechanism is that of electromagnetic gauge invariance. It has recently been conjectured [30] that inside a superconductor gravitons might acquire mass by a mechanism similar to photons and that this might aid the explanation of the Cooper pair mass anomaly reported by Tate et al.[90], who found by experiment that the ratio of two electron masses to the cooper pair mass $2m_e/m_c$ in their rotating superconductor disagreed with the available theory by about 9 parts in 10^5 . According to [30], the massive gravity frame-dragging field generated by a rotating superconductor would influence the magnetic field generated by the London moment. All calculations made to this effect are within the framework of the gravitoelectromagnetic (GEM) equations, which are an approximation to general relativity in nearly flat space times. They also closely resemble Maxwell's equations, and for this reason the conjecture of the massive graviton has been created, giving rise to the GEM-Proca equations [30]. However, no derivation of the graviton mass from first principles has been given to date.

In section 5.2.1, below, we introduce the standard GEM equations and vector potentials and use the gauge invariant derivative operator to derive the quantum mechanical mass current density inside a superconductor.

In section 5.2.2, we show from first principles that this leads to a graviton mass of magnitude $\approx 10^{-54}$ kg, giving rise to a gravitational Meissner effect, essentially shielding gravitomagnetic fields with a characteristic penetration length of $\lambda_g \approx 10^{11}$ m. The result from our theoretical calculation agrees exactly with the conjectures used by Tajmar et al. [30]. At the time of writing the author is not aware of any other complete derivation of the graviton mass inside a superconductor.

Following the conjecture by [30] we use the derived graviton mass and resulting gravitomagnetic London moment to attempt an explanation of the Tate Cooper pair mass anomaly in section 5.2.4. Our result is too small by one order of magnitude; we present a short list of possible causes and shortcomings in the current theory.

5.2.1 The Gravitoelectromagnetic Equations and Gravitoelectromagnetic Gauge Invariance

We begin by finding a framework for gravitational effects which can be used without recourse to tensors and the full general relativistic treatment. Considering test masses with non-relativistic velocities in a nearly flat spacetime we find that, to first order, gravity can be approximated by the gravitoelectromagnetic (GEM) 3-vector equations. In Heaviside- Lorentz units these equations are [91]:

$$\nabla \cdot \vec{g} = -4\pi G\rho \quad (5.8)$$

$$\nabla \cdot \vec{B}_g = 0 \quad (5.9)$$

$$\nabla \times \vec{g} = -\frac{1}{2c} \frac{\partial \vec{B}_g}{\partial t} \quad (5.10)$$

$$\nabla \times \frac{1}{2} \vec{B}_g = \frac{1}{c} \left(-4\pi G \vec{j}_m + \frac{\partial \vec{g}}{\partial t} \right) \quad (5.11)$$

where \vec{g} is the gravitoelectric field, \vec{B}_g is the gravitomagnetic or frame dragging field, \vec{j}_m is the mass current density and all the other symbols have their usual meanings. The factors of $\frac{1}{2}$ are remnants of the conversion from rank-2 tensors to vectors. On inspection these equations are of a form largely identical to that of the Maxwell's equations, and they transform in the same way.

The \vec{g} and \vec{B}_g fields can be defined by introducing the 4-vector potential $A^\mu = (V, \vec{A})$ such that:

$$\vec{B}_g = \nabla \times \vec{A} \quad (5.12)$$

$$\vec{g} = -\nabla V - \frac{\partial \vec{A}}{\partial t} \quad (5.13)$$

For a massless gauge field all observables must be unchanged under the gauge transformation [60]:

$$A^\mu \rightarrow A'^\mu = A^\mu - \partial^\mu \chi \quad (5.14)$$

where χ is an arbitrary well behaved function of time t and position \vec{r} .

In order to evaluate equation (5.11) we require an expression for the mass current density. We assume the mass current density consists of two parts, the Cooper pair mass current density and the ion lattice current density. The quantum mechanical mass current density of Cooper pairs can be written as:

$$\vec{j}_{m,c} = -\frac{i\hbar}{2} [\psi_c^* \nabla \psi_c - \psi_c \nabla \psi_c^*] \quad (5.15)$$

Since in a superconductor the phase of the macroscopic wave function becomes observable the above expression is not invariant under the transformation $\psi_c \rightarrow \psi'_c = e^{im\chi(\vec{r},t)}\psi_c$ [60]. In order to retain gauge invariance of the current density we have to replace all derivatives with the gauge-covariant derivative:

$$\partial \rightarrow D = \nabla \pm \frac{im}{\hbar} A \quad (5.16)$$

In this way we obtain the following expression for the gauge-invariant Cooper pair mass current density in a superconductor:

$$\vec{j}_{m,c} = -\frac{i\hbar}{2}[\psi_c^* \nabla \psi_c - \psi_c \nabla \psi_c^*] - \frac{m_c}{2} |\Psi|^2 A \quad (5.17)$$

By contrast with the electromagnetic case where the current density is given by the velocity difference between Cooper pairs and ion lattice, the GEM equations require the total mass current density. One may be tempted to just add the classical quantum mechanical mass current density for the ion lattice analogous to the electron current density in equation (5.15) since the ion lattice is not represented by a macroscopic wave function and the ion phase should be unobservable. This is incorrect. Since the substitution in equation (5.16) is essentially a local topological transformation it must apply to all derivatives. Also, if we did not use the covariant derivative in the case of the ion mass current density the Cooper pairs would be in a gravitational gauge different from the ions, violating the principle of equivalence. Thus the total mass current has to be written in the form:

$$\vec{j}_m = -\frac{i\hbar}{2}[\psi_c^* \nabla \psi_c - \psi_c \nabla \psi_c^*] - \frac{i\hbar}{2}[\psi_{ion}^* \nabla \psi_{ion} - \psi_{ion} \nabla \psi_{ion}^*] - \frac{m_c}{2} |\Psi|^2 A - \frac{m_{ion}}{2} |\Psi|^2 A \quad (5.18)$$

Actually the above equations are only strictly true in the zero-temperature limit, where all electrons are bound in Cooper pairs. Above zero temperature but below T_c some electrons will be in the normal state while others are superconducting. The fraction of electrons in the normal state is given by eq. (1.1). For the same reason that the ion lattice contributes to the graviton mass the normal state electrons will contribute as well. This leads directly to the question of why the photon mass in a superconductor as discussed in section 5.2.2 depends only on the density of superconducting electrons and not on the density of superconducting and normal electrons. The reason for this lies in the nature of the electromagnetic interactions: The normal state electrons have to be assumed to be stationary with respect to the ion lattice. In the electromagnetic case, charge currents are caused by electrons moving relative to the ion lattice, i.e. are caused only by superconducting electron pairs, while mass currents are due to the absolute movement of the entire local mass: ion lattice, Cooper pairs and normal state electrons.

5.2.2 Massive Spin-1 Gravitons by GEM Gauge Invariance Breaking

We will now manipulate the mass current and GEM field terms discussed in the previous section in order to show that the differential equation governing the vector potential $A_{GEM}^{\vec{}}$ takes the form appropriate to a massive spin-1 boson field as discussed by [60]. From now on all calculations will be kept in SI units in order to allow the use of intuitively accessible units and quantities when evaluating them.

Consider the fourth GEM equation (eq (5.11)) for the static case ($\frac{\partial}{\partial t} = 0$) in SI units:

$$\nabla \times \frac{1}{2} \vec{B}_g = \frac{1}{c^2} (-4\pi G \vec{j}_m) \quad (5.19)$$

Substituting from eqs.(5.12), (5.18) into eq.(5.19) we obtain in the Lorentz gauge ($\nabla \cdot \vec{A} = 0$):

$$\nabla^2 \vec{A} = -\frac{4\pi G}{c^2} i\hbar ([\psi_c^* \nabla \psi_c - \psi_c \nabla \psi_c^*] + [\psi_{ion}^* \nabla \psi_{ion} - \psi_{ion} \nabla \psi_{ion}^*]) - \frac{4\pi G(m_c |\psi_c|^2 + |\psi_{ion}|^2 m_{ion})}{c^2} \vec{A} \quad (5.20)$$

Assuming a monovalent material (i.e. one conduction electron per atom) of atomic mass $m \approx m_{ion} + 0.5m_c$ with the density of superconducting electrons constant everywhere in the superconductor and defining $\psi_{ion}^2 = 2\psi_c^2 = n$, equation (5.20) simplifies to:

$$\nabla^2 \vec{A} = -\frac{4\pi Gmn}{c^2} \vec{A} \quad (5.21)$$

which according to [60] has the form of a massive spin-1 vector field. Massive vector fields decay exponentially with distance. The exponential decay length of the field described by (5.21) is $\lambda_g = \left(\frac{4\pi Gmn}{c^2}\right)^{-1/2}$. We call λ_g the graviton penetration length. The mass of the massive spin-1 graviton can now be determined as:

$$m_g = \frac{\hbar}{\lambda_g c} \quad (5.22)$$

Using $mn = \rho$ where ρ is the local mass density, we can rewrite equation (5.22) as

$$m_g = \frac{2\hbar\sqrt{\pi G\rho}}{c^2} \quad (5.23)$$

Thus we have used the breaking of U(1) phase rotational symmetry in superconductors to show that gravitons have non-zero rest mass inside a superconductor. The procedure is almost entirely analogous to the derivation of the photon mass in superconductors [60]. A correct prediction of the graviton mass hinges on the realization that the ion mass contributes to the graviton mass. For the case of niobium (the material used in the original experiment by [90]) the predicted graviton mass is $m_g \approx 3.1 \times 10^{-54} \text{kg}$ and the characteristic penetration length $\lambda_g = 1.1 \times 10^{11} \text{m}$, assuming $\rho_{Nb} = 8570 \text{kgm}^{-3}$. There is no part about the above derivation specific to superconductivity. The symmetry breaking mechanism described above will occur in any kind of quantum coherent matter where the phase of the macroscopic wave function is observable, like for example superfluids.

We will now express the ratio of the graviton mass to the photon mass in terms of the parameters of the quantum coherent medium in order to gain insight into the ratio of the gravitational to the electromagnetic forces.

The photon rest mass m_γ is inversely proportional to the London penetration length λ_L which is given by [4] as $\lambda_L = \left(\frac{m_e}{e\rho_e\mu_0} \right)^{1/2}$ where m_e is the mass of the electron, ρ_e is the charge density and all other symbols have their usual meaning. Thus the ratio of graviton mass to photon mass is given by:

$$\frac{m_g}{m_\gamma} = \frac{\lambda_L}{\lambda_g} = \left(\frac{\mu_g m_e \rho_m}{\mu_0 e \rho_e} \right)^{1/2} \quad (5.24)$$

The massive gravitons predicted by this derivation are spin-1 gravitons, sometimes called graviphotons, allowing for the existence of gravitational dipole waves. General relativity only predicts spin-2 gravitons and quadrupole waves. This apparent problem is resolved since in the massless graviton case the spin-1 part of the graviton is not propagating as the spin-1 components of massless gravity satisfy elliptic constraint equations.

5.2.3 Derivation of the Photonic Mass

We shall outline briefly the working of the analogous derivation of the photonic mass. Similarly to the GEM case, we begin by considering the quantum mechanical charge current density of cooper pairs:

$$\vec{j}_c = -\frac{i\hbar e}{m} [\psi_c^* \nabla \psi_c - \psi_c \nabla \psi_c^*] \quad (5.25)$$

We now employ the electromagnetic gauge invariant derivative $\partial \rightarrow D = \nabla \pm \frac{im}{\hbar} \vec{A}$ to obtain the gauge invariant current density:

$$\vec{j}_c = -\frac{i\hbar e}{m} [\psi_c^* \nabla \psi_c - \psi_c \nabla \psi_c^*] - \frac{e^2}{m_e} |\psi|^2 \vec{A} \quad (5.26)$$

Using the steady state ($\partial/\partial t = 0$) of the Ampere-Maxwell law to obtain $\nabla^2 \vec{A}_{em} = \mu_0 \vec{j}_c$ we can rearrange eq.(5.26) to obtain:

$$\nabla^2 \vec{A}_{em} = -\frac{\mu_0 e n_{e,s}}{m_e} \vec{A}_{em} \quad (5.27)$$

which, analogously to equations (5.21)(5.22)(5.23) is the equation of a massive vector field. The decay constant in (5.27) turns out to be the inverse square of the London penetration depth $\frac{\mu_0 e n_{e,s}}{m_e} = \frac{1}{\lambda_L^2}$ (from eq.(4.12)). Only the superconducting electrons contribute to the photonic mass, since electric currents result only from the motion of electrons relative to the ion lattice and not, as in the case of mass currents, from the total motion of the system.

Thus we have shown that the breaking of electromagnetic gauge invariance indeed leads to a non-zero photon mass which is governed directly by the materials London penetration depth. Evaluating the mass directly, analogously to (5.22), yields $m_\gamma = \frac{\hbar}{\lambda_{Lc}}$ as was used throughout this thesis (and as introduced in eq.(3.11)).

5.2.4 Experimental Evidence for Massive Gravitons

As discussed in section 1.1.2.2, the two defining magnetic properties of a superconductor are the Meissner-Ochsenfeld effect (magnetic field exclusion) and the London moment. The London moment is the magnetic field generated by any superconductor set into rotation. Empirically, the field generated is given by equation (1.6).

Using a rotating ring of superconducting Nb, Tate et al.[90] measured the London moment with sufficient accuracy to determine the Cooper pair mass m_c . They found that their value of $(m_c/2m_e) = 1.000084$ was larger than the theoretically predicted value of 0.999992.

It was shown in[30] that a sufficiently strong GEM field could solve the anomaly if a GEM term analogous to the London moment is included in the full canonical momentum derivation of the normal magnetic London moment.

In order to solve the mass anomaly $\Delta m = m_{exp} - m_{theory}$ we require $\vec{B}_g = 2\vec{\omega}(\Delta m/m_c)$ [30].

We will now evaluate \vec{B}_g taking into account the graviton mass derived in section 5.2.2. Since we have shown in section 5.2.2 that gravitons have non-zero rest mass in superconductors we can replace

the GEM equations by a set of massive-GEM equations similar to the Proca equations for massive electromagnetism [30]. Taking the curl of the fourth massive-GEM equation and solving the resulting differential equation yields [92]:

$$\vec{B}_g = B_{0,g} \vec{e}^{-x/\lambda_g} - 2\omega\rho\mu_{0g}\lambda_g^2 \quad (5.28)$$

where $\mu_{0g} = \frac{4\pi G}{c^2}$ is the gravitational permeability of free space.

The first term of equation (5.28) is the Meissner term, the second term is the GEM London moment. We set the externally applied field $B_{0,g} = 0$ and evaluate the GEM London moment explicitly. Using the graviton penetration length in Nb, we find the ratio of the predicted massive-GEM London moment to the value required to solve the experimental anomaly to be:

$$\frac{\rho\mu_{0g}\lambda_g^2}{\frac{\Delta m}{m_c}} \approx 0.06 \quad (5.29)$$

The change in the London moment predicted by our theory is of the correct sign but approximately an order of magnitude too small in order to account for the experimental anomaly. This may be due to several reasons:

1. No thin film effects have been taken into account, despite the fact that the superconducting Nb used experimentally by [90] was of cross sectional area of order tens of nm.
2. The theory used was local and isotropic. For anisotropic materials either a non-local theory has to be used, or the scalar mass has to be replaced by a second rank tensor to account for anisotropies in the local mass density [4].
3. The Lagrangian derivations used by [30] consider the electromagnetic and GEM Lagrangians separately. In order to obtain a reliable prediction a systematic derivation of the Lagrangian of the system in the simultaneous presence of both electromagnetic and GEM fields is required.
4. The Tate Cooper pair mass anomaly has a different source, or the theory applied is incorrect and gravitational gauge invariance breaking does not occur inside superconductors.

5.2.5 Massive Gauge Bosons: Conclusions

It has been shown that the fact that the phase of the electronic or cooper pair wave functions ψ becomes observable leads to the breaking of U(1) phase rotational symmetry upon transition to the

superconducting state. This means that any gauge field interacting with the electrons loses U(1) phase rotational invariance. If the gauge field in question can be modeled by a 4-vector potential of the form $A^\mu = (A_t, \vec{A})$ it will acquire mass via the Higgs mechanism. Explicitly evaluating the symmetry breaking yields a photonic mass $m_\gamma = \frac{\hbar}{\lambda_L c}$ consistent with the work done in sections 3 and 4.

The same derivation that can be used to derive the photonic mass inside a superconductor can be applied to the GEM 3-vector equations describing gravity in nearly flat space times. This approach yields a way to derive the mass of a spin-1 graviton from first principles. The mass of the graviton is estimated as $m_g = \frac{2\hbar\sqrt{\pi G\rho}}{c^2} \approx 3 \times 10^{-54} kg$. This is the value conjectured by Martin Tajmar et al. [30]. While this agreement between conjecture and derived value is a remarkable result it is too small by about one order of magnitude to completely account for the cooper pair mass anomaly as outlined in section 5.2.4.

5.3 Quantised Gravity and the Consequences

Given the shortcomings of massive-GEM theory in explaining the Tate anomaly, it seems desirable to have alternative experimental verifications of massive-GEM theory. We will now show that the gravitomagnetic flux through a superconducting ring is quantised and that this results in gravitationally induced currents measurable in the laboratory.

In this way we will not only demonstrate the foundation for an experimental regime that may verify or disprove massive gravitational frame dragging, but also point to something far more fundamental. By writing the equations governing massive gravity in vector- rather than tensor-form we have managed to demonstrate that, in the right circumstances, gravity and gravitational effects may be quantised in a manner similar to electromagnetic effects. As such, we believe that gravitomagnetic effects may have a role to play in the search for mathematical and physical mechanisms which may eventually lead to a unified field theory.

5.3.1 Quantisation of Gravitational Flux

In a superconducting ring the amount of magnetic flux penetrating the inlying area is quantised to be $\phi = n\phi_0$ where ϕ_0 is the magnetic flux quantum and n is an integer [4]. As the external field changes a supercurrent is induced which keeps the magnetic flux through the centre constant. A similar effect should occur for gravitomagnetic flux, inducing a mass current of electrons which in turn results in a charge current large enough to be measurable in principle.

Consider a superconducting ring with mass current j_m small enough that the density of current carriers ψ remains unaltered. It is possible to rewrite the current equation (5.18) in terms of the gradient of the order parameter phase ∇S :

$$\vec{j}_m = \frac{\hbar}{2} |\psi|^2 \nabla S - \frac{m}{2} |\psi|^2 A_{GEM}^{\vec{}} \quad (5.30)$$

Since the order parameter $\psi(S)$ must be single valued the integral of ∇S along any closed curve C enclosing the hole in the ring must be $\oint_C \nabla S \cdot d\vec{l} = 2\pi n$ with $n \in \text{integer}$. Thus, integrating equation (5.30) we obtain:

$$\oint \vec{j}_m \cdot d\vec{l} = \pi n \hbar |\psi|^2 - \frac{m}{2} |\psi|^2 \int_{\Sigma} \vec{B}_g \cdot d\Sigma \quad (5.31)$$

where we have used Stokes' theorem to transform the integral of \vec{A} along \vec{l} into an integral of $\vec{B} = \nabla \times \vec{A}$ over the surface Σ spanning the closed curve C . Assuming that \vec{B} is constant over Σ and \vec{j}_m is constant along C we obtain:

$$\vec{j}_m = \frac{\pi n \hbar |\psi|^2}{C} - \frac{m}{2} |\psi|^2 \vec{B}_g \frac{\Sigma}{C} \quad (5.32)$$

Drawing the curve a long distance $d > \lambda_g$ from the hole the screening current is zero and by rearranging (5.32) with $\vec{j}_m = 0$ we obtain:

$$\frac{\hbar n}{m} = \vec{B}_g \Sigma \quad (5.33)$$

This can be re-written in terms of the total flux Φ_g penetrating the ring to obtain:

$$n_g \phi_{0,g} = \Phi_g \quad (5.34)$$

where $\phi_{0,g} = \frac{\hbar}{m}$ is the gravitomagnetic flux quantum and n_g is the gravitomagnetic quantum number. This is analogous to the electromagnetic flux quantum $\phi_{0,em} = \frac{2e}{\hbar}$ which quantizes the magnetic flux Φ_M through the hole. Quantisation arises because the integrated phase change along C always has to be $\Delta S = 2\pi n$ in order to maintain single-valuedness of the order parameter. Since S is just the phase of the electronic wave function both the gravitomagnetic flux Φ_g and the magnetic flux Φ_M influence S at the same time causing flux quantisation according to:

$$\oint_C \nabla S \cdot d\vec{l} = 2\pi n = \frac{2e}{\hbar} \oint_C \vec{A}_M \cdot d\vec{l} + \frac{m}{\hbar} \oint_C \vec{A}_{GEM} \cdot d\vec{l} \quad (5.35)$$

Again using Stokes' theorem to solve the integrals:

$$2\pi n = \frac{2e}{\hbar} \Phi_M + \frac{m}{\hbar} \Phi_g \quad (5.36)$$

An applied external magnetic field B_M induces a current in the ring which keeps the penetrating flux constant. It is well known that these currents are measurable experimentally. In the next section we show that the currents induced by earth's gravitomagnetic field are also measurable by experiment. Thus the phase of the order parameter provides a coupling between the electromagnetic and gravitational fields, the magnitude of which appears accessible in the laboratory.

5.3.2 Gravity Induced Currents in Multiply Connected Superconductors

Consider a ring of open area Σ with surface normal $\vec{\Sigma}$ normal to the gravitomagnetic field \vec{B}_g during the transition from the superconducting to the normal state. The gravitomagnetic flux penetrating Σ is zero, requiring $n_g = 0$. If the ring is rotated in order to align $\vec{\Sigma}$ with \vec{B}_g the gravitomagnetic flux through the ring is kept constant at zero by an induced supercurrent. From equation (5.32) we obtain:

$$\vec{J}_m = -\frac{m_c}{4} |\psi_c|^2 \vec{B}_g r \quad (5.37)$$

where we have assumed Σ to be the surface spanning the circular closed curve C of radius r . The subscripts "c" arise since we have assumed that the ion lattice is fixed immovably to the lab frame and the entire mass current is due to the movement of Cooper pairs.

The massless gravitomagnetic field of a point mass m moving with velocity \vec{v} at position \vec{r} relative to the observer can be calculated from:

$$\vec{B}_g = -\frac{\mu_0 m}{r^2} (\vec{v} \times \hat{r}) \quad (5.38)$$

Thus we can calculate the gravitomagnetic field generated by the rotation of the Earth from the integral:

$$B_{g,earth} = \mu_0 \int_{earth} \rho(\vec{r}) \frac{\vec{v} \times \hat{r}}{r^2} d\vec{r} \quad (5.39)$$

where $\rho(\vec{r})$ is the density of earth at position \vec{r} . Using conformal transformations and numerical integration this integral can be readily evaluated. Assuming the density of the Earth to be constant $\approx 5515\text{kg/m}^3$ we find the frame dragging field at the equator to be approximately $B_{g,eq} \approx -1.89 \times 10^{-7} \text{rad s}^{-1}$ horizontal. Since any experiment would usually be co-rotating with earth this effect is difficult to detect in a ground based laboratory. However, if the experiment is loaded onto an aeroplane the effect can be observed. Any frame of reference circling the earth within 24h will be subject to the frame dragging field discussed above. Loading the experiment onto an aeroplane yields a number of additional advantages as well. Instead of having to mechanically rotate the ring inside the cryostat, we can effectively tilt the entire laboratory by having the plane perform appropriate manoeuvres. Parabolic Flights, for example, would provide flying laboratories of sufficient manoeuvrability.

According to equation (5.37) this yields a total gravity induced current in the ring of:

$$I_{grav} = \frac{m_c}{4} |\psi_c|^2 B_{g,eq} A r \quad (5.40)$$

where $|\psi_c|^2$ is the density of Cooper pairs, A is the cross sectional area of the superconducting ring and r is the ring radius. For a superconducting ring of radius 10 cm made from 0.2mm diameter niobium wire we find $I_{grav} \approx -0.62nA$, a current which should be easily detectable in the laboratory and thus provide experimental evidence for the quantisation of gravitational flux.

5.4 Massive Gravity and Astrophysics - Neutron Star Cores and Gravitational Collapse

Any massive vector field decays exponentially with distance [60]. In the case of gravity inside a laboratory type superconductor the decay constant is too large for the effect to be observable ($\lambda_g \approx 10^{11}\text{m}$). However, since the decay constant is inversely proportional to the root of the local mass density the effect may become relevant in extremely high density systems. There is an ongoing discussion about the state of matter at the centre of neutron stars but generally researchers agree that some sort of quantum coherent condensate can be expected, whether it is a type-I superconductor, type-II superconductor, a neutron superfluid or a quark-matter colour superconductor [93] [94]. Using equation (5.23) and assuming a local mass density of $\approx 10^{14}\text{gcm}^{-3}$ we find the gravitational

penetration length to be of order $\approx 30\text{km}$, indicating that massive gravity may be a significant factor in neutron star physics, especially in the physics of gravitational collapse and in determining the limiting masses of neutron stars (a typical Neutron star radius is $10 - 20\text{ km}$). It may be possible to put constraints on possible core sizes and constitutions by considering only those types of core whose massive gravity is reconcilable with observation.

Chapter 6

Summary and Conclusions

After an introduction to the thesis in general and to the basics of superconductivity in particular in Chapter 1, Chapter 2 discusses the basic types of superconducting detectors. In the course of this discussion the problem of TES excess noise is encountered and an explanation of the excess noise phenomenon is sought. The existing models of Phase Slip Shot Noise (PSSN) and percolation noise are discussed and both found to be in reasonable agreement with experiment. However, when analysing the temperature region of validity it is found that the models of PSSN and percolation noise only strictly apply over the low-temperature and mid- to high-temperature parts of the sn-transition respectively. Neither of them can explain the persistence of white excess noise throughout the entirety of the sn-transition. As part of the investigation into the predictions of PSSN and percolation noise the existing model for the PSSN noise current is extended to include the magnetic field dependence of the noise in the presence of strong magnetic fields. In the case of percolation noise a new quantitative analytical model is created which describes the dependence of percolation noise on the device temperature and external magnetic field and the material parameters (critical temperature and field). At the time of writing and to the best of the author's knowledge this is the first quantitative analytical model of TES percolation noise. The resultant models are compared with the empirical excess noise equation provided by Takei et al. [7], and PSSN is found to be in extremely good agreement with the empirical expression. The Chapter concludes with speculating about the possibility of a combined noise model in which excess noise is generated by PSSN in the low temperature part of the sn-transition, followed by a smooth transition to percolation noise in the high temperature part of the transition. It is reported by Voss [47] that the excess noise power spectrum changes with bias current, indicating at least two different noise regimes and giving credibility to the concept of a combined noise theory. An important step towards solving the excess noise problem would be a dedicated experiment trying to detect the $i_n \propto A^{-1/2}$ dependence of the excess noise

current density i_n on the macroscopic device area A predicted by PSSN.

The the work presented in Chapter 2 creates a strong sense of the sensitivity of the sn-transition to even tiny electromagnetic disturbances, like the motion of an individual magnetic flux quantum (section 2.3.2). It is this sensitivity to quantum scale effects that prompts the digression into quantum electrodynamics from which the remaining Chapters are motivated.

In Chapter 3 the extreme sensitivity of the sn-transition to quantum mechanical effects leads to what turns out to be a fruitful digression into the field of QED and the physics of the quantum vacuum. The initial intention is to find a possible coupling between quantum mechanical vacuum fluctuations and the TES excess noise phenomenon. From the literature it is apparent that a coupling between the sn-transition and the QED vacuum indeed exists in modifications to the Casimir energy of a cavity with superconducting boundaries [10]. The conventional form of the equations governing the Casimir effect is found to be unsuitable and the corrections required for a system with superconducting boundaries are discussed. A complete mathematical model of the dielectric functions of the evacuated cavity volume and the cavity boundaries is presented for the case of the parallel plane geometry cavity with superconducting boundaries. The functions are of a form suitable for implementation with Lifshitz theory, and numerical evaluation of the effect shows that the corrections to the Casimir force predicted are of an order of magnitude reconcilable with observations. It is believed that the model of the superconductivity induced massive-em Casimir effect is an important contribution to the analysis of the data presented by Bimonte et al.[74].

An investigation of the type of electromagnetic equations suitable for tackling the problem of the Casimir energy of systems with superconducting boundaries forces us to consider a scenario in which Maxwellian electromagnetism is replaced by Proca electromagnetism. In Proca electromagnetism the photon rest mass is non-zero. Discussion of this massive electromagnetism leads us in Chapter 4 to investigate the properties of optical elements made from superconductors, giving rise to the idea of Heavy Photon Optics (HPO). It is shown how optical elements and devices based on the HPO technology can exploit the diverging refractive index and dispersion of photons near a critical wavelength λ_{crit} determined by the material parameters. It is found that λ_{crit} depends crucially on the density of superconducting electron pairs. The macroscopic optical parameters such as refractive index and dispersion of HPO elements are derived, along with their dependence on the superconducting material parameters. The type and availability of materials suitable for forming transmission-HPO devices are discussed. Following this investigation into the basic concepts of HPO devices the thin film reflectance/ etalon response characteristics are established. A number of promising technological applications based on high refractive index, ultrahigh dispersion, non-linear optical elements is discussed. For these potential applications a patent application has been filed (priority filing number GB0806470.1).

A closer look at the mechanisms responsible for the photon mass which is pivotal to HPO technology leads into the general field of gauge symmetries and vector bosons. It is found that the underlying principle by which photons acquire a non-zero rest mass is the Higgs mechanism applied to the breaking of U(1) phase rotational symmetry of the macroscopic electronic wave function in a superconductor. In Chapter 5 the same mechanism is applied to the gravitational field generated by the superconducting electrons. The mathematical model of the gravitational field used is the 3-vector based Gravitoelectromagnetism (GEM), which is valid in nearly flat space times and allows for a mathematical treatment of the problem without recourse to tensors or the full relativistic treatment. The gauge invariance breaking mechanism is used successfully to derive the mass of a hypothetical massive spin-1 graviton (conventional gravitons are spin-2). The mass of this graviton is of order $10^{-55}kg$ and in exact agreement with the graviton mass conjectured by Tajmar and de Matos [30] in their discussion of superconducting frame dragging effects. In principle this mechanism can be applied to create a non-zero vector boson rest mass for any gauge field generated by the particle for which phase rotational symmetry is broken, in this case the electron. Also, the mechanism is not restricted to superconductivity in any way but rather depends on the breaking of symmetry which occurs, for example, in any kind of quantum coherent matter such as superfluids or indeed any Bose-Einstein Condensate (BEC). The most significant consequences of massive spin-1 gravity are the existence of the gravitomagnetic flux quantum $\phi_{0,g}$ and the prediction of the gravitomagnetic London moment as discussed by Tajmar and de Matos [30]. The existence of $\phi_{0,g}$ yields a quantised gravitational effect which, significantly, depends on the sum of the gravitomagnetic flux quantum $\phi_{0,g}$ and the magnetic flux quantum ϕ_0 , thus yielding a direct dependence of an observable parameter (phase slip ΔS around a ring) on a combination of quantum mechanical and gravitational constants (number of flux quanta $\phi_{0,g}$ and ϕ_0 penetrating the ring). The gravitomagnetic London moment predicted might make the generation of gravitational frame dragging effects in the laboratory feasible [30] and efforts are underway to detect those effects experimentally [28]. The Chapter concludes with speculations about the implications of massive spin-1 gravity for neutron star astrophysics, based on the hypothesis that neutron stars may have a superconducting/quantum coherent core.

6.1 Closing Remarks

What becomes apparent from the work presented herein is that, while the phenomenon of superconductivity has been known for almost a century, a true understanding of the implications of a quantum coherent matter state is still incomplete, despite the fact that a good model describing the physics underlying the effect has been around for about 50 years in the form of BCS theory.

Particularly the interactions between the gravitomagnetic and electromagnetic flux quanta outlined in Chapter 5 indicate superconductor physics may make substantial contributions to modern fundamental physics, while the HPO technology developed in Chapter 4 demonstrates that unexpected but significant practical applications may be found along the way.

As such it is the author's believe that superconductivity has got a significant role to play in theoretical and experimental physics, not just as a means to an end in the field of superconducting detectors, but primarily as a testbed for advanced concepts like gauge theory and the Higgs mechanism. As a final conclusion, due to the diversity of the fields to which the results obtained are applicable, superconductor research, both theoretical and experimental, has important contributions to make to any comprehensive modern physics research programme.

Bibliography

- [1] Christian Enss. *Cryogenic Particle Detection*. Springer-Verlag GmbH, Heidelberg, Germany, 2005.
- [2] G. W. Fraser. On the nature of the superconducting-to-normal transition in transition edge sensors. *Nuclear Instruments and Methods in Physics Research A*, 523:234–245, 2003.
- [3] Wikimedia foundation. <http://www.wikimedia.org/>, Open Source.
- [4] D.R. Tilley and J. Tilley. *Superfluidity and superconductivity 3rd Ed.* IOP Publishing Ltd, Bristol, England, 1990.
- [5] Guy Brammertz. *Development of low critical temperature tunnel junctions for application as photon detectors in astronomy*. Print Partners Ipskamp, Enschede, The Netherlands, 2003.
- [6] Vladimir Polushkin. *Nuclear Electronics*. John Wiley and Sons Ltd., Chichester, England, 2004.
- [7] Y. Takeia, K. Tanaka, R. Fujimoto and, Y. Ishisaki, U. Morita, T. Morooka, T. Oshima, K. Futamoto, T. Hiroike, T. Koga, K. Mitsuda, N.Y. Yamasaki T. Ohashi, N. Iyomoto, T. Ichitsubo, K. Sato, T. Fujimori, K. Shinozaki, S. Nakayama, and K. Chinone. Performance of a bridge-type tes microcalorimeter, excess noise characteristics and dependence of sensitivity on current. *Nuclear Instruments and Methods in Physics Research A*, 523:134–146, 2004.
- [8] J. N. Ullom, W. B. Doriese, G. C. Hilton, J. A. Beall, S. Deiker, W. D. Duncan, L. Ferreira, K. D. Irwin, C. D. Reintsema, and L. R. Vale. Characterization and reduction of unexplained noise in superconducting transition-edge sensors. *Applied Physics Letters*, 84:4206–4208, 2004.
- [9] Zamanda yolculuk arastirmacilarina duyuru. <http://www.zamandayolculuk.com/>.
- [10] Giuseppe Bimonte, Enrico Calloni, Giampero Esposito, and Luigi Rosa. Casimir energy and the superconducting phase transition. *Journal of Physics A*, 39:6161–6171, 2006.
- [11] A. Luukanen, K.M. Kinnunen, A.K. Nuottajaervi, H.F.C. Hoevers, W.M. Bergmann Tiest, and J.P. Pekola. Fluctuation-limited noise in a superconducting transition-edge sensor. *Physical Review Letters*, 90, 2003.

- [12] Edward D. Palik. *Handbook of optical constants of solids*. Academic Press, Oxford, United Kingdom, 1985.
- [13] Cvi laser. <http://www.cvilaser.com>.
- [14] Georgia state university hyperphysics. hyperphysics.phy-astr.gsu.edu/Hbase/hph.html, Georgia State University, US.
- [15] W. Meissner and R. Ochsenfeld. *Naturwiss.*, 21, 1933.
- [16] H. Kamerlingh-Ones. *Leiden Comm.*, 122b, 124c, 1911.
- [17] V.L. Ginzburg and L.D. Landau. *Sov. Phys. JETP*, 20, 1950.
- [18] A.A. Abrikosov. *J. Phys Chem. Solids*, 2, 1957.
- [19] E. Maxwell. *Phys. Rev.*, 78, 1950.
- [20] C.A. Reynolds, B. Serin, W.H. Wright, and L.B. Nesbitt. *Phys. Rev.*, 78, 1950.
- [21] L.N. Cooper. *Phys. Rev.*, 104, 1956.
- [22] J. Bardeen, L.N. Cooper, and J.R. Schrieffer. *Phys. Rev.*, 108, 1957.
- [23] B.D. Josephson. *Phys. Lett.*, 1, 1962.
- [24] J. Clarke(Editor) and Alex I. Braginski(Editor). *The SQUID Handbook: Set*. John Wiley and Sons Ltd., Chichester, England, 2006.
- [25] Michel Cyrot and Davor Pavuna. *Elemental and High-Tc Superconductivity (Paperback)*. World Scientific Publishing Co Pte Ltd, 57 Shelton Street, London, WC2H 9HE, United Kingdom, 1990.
- [26] J. Bednorz and K. Mueller. Possible high-tc superconductivity in the ba-la-cu-o system. *Zeitschrift fuer Physik B-Condensed Matter*, 64, 1962.
- [27] M.K. Wu, J.R. Ashburn, C. Torng, P. Hor, R. Meng, L. Gao, Z. Huang, Y. Wang, and C. Chu. Possible high-tc superconductivity in the ba-la-cu-o system. *Physical Review Letters*, 58, 1987.
- [28] M. Tajmar, F. Plesecu, K. Marhold, and C.J. de Matos. Experimental detection of the gravitomagnetic london moment. *Physica C (UNDER REVIEW)*, submitted 2006.
- [29] J. C. Gallop. *SQUIDS, the Josephson Effects and Superconducting Electronics*. IOP Publishing ltd, Bristol, England, 1990.
- [30] C.J. de Matos and M. Tajmar. Gravitomagnetic london moment and the graviton mass inside a superconductor. *Physica C: Superconductivity*, 432:167–172, 2005.
- [31] E. A. Hecht. *Superconductivity*. Barnes and Noble, Inc., USA, 1969.

- [32] H. Froehlich. *Physics Review*, 79, 1950.
- [33] P. Verhoeve, D.D.E. Martin, R.A. Hijmering, J. Verveer, A. van Dordrecht, G. Sirbi, T. Oosterbroek, and A. Peacock. S-cam 3: optical astronomy with a stj-based imaging spectrophotometer. *Nuclear Instruments and Methods in Physics Research A*, 2006.
- [34] Z. Ahmed, D.S. Akerib, M.J. Attisha, C.N. Bailey, L. Baudis, D.A. Bauer, P.L. Brink, P.P. Brusov, R. Bunker, B. Cabrera, D.O. Caldwell, C.L. Chang, J. Cooley, M.B. Crisler, P. Cushman, M. Daal, F. DeJongh, R. Dixon, M.R. Dragowsky, L. Duong, R. Ferril, E. Figueroa-Feliciano, J. Filippini, R.J. Gaitskell, S.R. Golwala, D.R. Grant, R. Hennings-Yeomans, D. Holmgren, M.E. Huber, S. Kamat, S. Leclercq, R. Mahapatra, V. Mandic, P. Meunier, N. Mirabolfathi, H. Nelson, R.W. Ogburn, M. Pyle, X. Qiu, E. Ramberg, W. Rau, A. Reissetter, R.R. Ross, T. Saab, B. Sadoulet, J. Sander, R.W. Schnee, D.N. Seitz, B. Serfass, K.M. Sundqvist, J.-P.F. Thompson, G.Wang, S. Yellin, J. Yoo, and B.A. Young. Status of the cryogenic dark matter search experiment. *Journal of Low Temperature Physics*, 151, 2006.
- [35] H.F.C. Hoevers, M.P. Bruijn, B.P.F. Dirks, L. Gottardi, P.A.J. de Korte, J. van der Kuur, A.M. Popescu, M.L. Ridder, Y. Takei, and D.H.J. Takken. Comparative study of tiau-based tes microcalorimeters with different geometries. *Journal of Low temperature Physics*, 151:94–99, 2008.
- [36] The x-ray evolving universe spectrometer public website. <http://sci.esa.int/science-e/www/area/index.cfm?fareaid=103>, European Space Agency (ESA), 2006.
- [37] G.W. Frasesr, J.S. Heslop-Harrison, T. Schwarzacher, A.D. Holland, P. Verhoeve, and A. Peacock. Detection of multiple fluorescent labels using superconducting tunnel junction detectors. *Review of Scientific Instruments*, 74, 2003.
- [38] C. Enss, A. Fleischmann, K. Horst, J. Schoenefeld, J. Sollner, J. S. Adams, Y. H. Huang, Y. H. Kim, and G. M. Seidel. Metallic magnetic calorimeters for particle detection. *Journal of Low Temperature Physics*, 121:137–176, 2000.
- [39] D. McCammon. *Thermal Equilibrium Calorimeters - An Introduction*. In [1], 2005.
- [40] K. Irwin and G. Hilton. *Transition-Edge Sensors*. In [1], 2005.
- [41] M.B. Ketchen, D.D. Awschalom, W.J. Gallagher, A.W. Kleinsasser, R.L. Sandstrom, J.R. Rozen, and B. Bumble. Design, fabrication, and performance of integrated miniature squidsusceptometers. *IEEE Transactions on Magnetics*, 25:1212–1215, 1989.
- [42] A. Fleischmann, M. Linka, T. Daniyarova, H. Rotzinger, C. Enss, and G.M. Seidel. Metallic magnetic calorimeters (mmc): detectors for high-resolution x-ray spectroscopy. *Nuclear Instruments and Methods in Physics Research A*, 520:27–31, 2004.

- [43] Glenn F. Gnoll. *Radiation Detection and Measurement 3rd Edition*. John Wiley and Sons Ltd., Chichester, England, 2000.
- [44] Op amps for everyone. <http://focus.ti.com/lit/an/slod006b/slod006b.pdf>, Texas Instruments (TI), 2002.
- [45] D. Andrews, W. Bruksch, W. Ziegler, and E. Blanchard. *Rev. Sci. Instrum.*, 13:281, 1942.
- [46] M.A. Lindemana, M.B. Anderson, S.R. Bandler, N. Bilgria, J. Chervenak, S. Gwynne Crowder, S. Fallows, E. Figueroa-Feliciano, F. Finkbeinerb, N. Iyomoto, R. Kelley, C.A. Kilbourne, T. Lai, J. Man, D. McCammon, K.L. Nelms, F.S. Porter, L.E. Rocks, T. Saab, J. Sadleir, and G. Vidugiris. Percolation model of excess electrical noise in transition-edge sensors. *Nuclear Instruments and Methods in Physics Research A*, 559:715–717, 2006.
- [47] R. F. Voss, C. M. Knoedler, and P. M. Horn. Phase-slip shot noise at the two-dimensional superconducting transition: Evidence for vortices? *Physical Review Letters*, 45:1523–1526, 1980.
- [48] Onuttom Narayan. Driving force on an abrikosov vortex. *Journal of Physics A: Mathematical and General*, 36:372–377, 2003.
- [49] Gordon Lasher. Mixed state of type-i superconducting films in a perpendicular magnetic field. *Physical Review*, 154:345–348, 1966.
- [50] Petter Minnhagen. Kosterlitz-thouless transition for a two-dimensional superconductor: Magnetic-field dependence from a coulomb gas analogy. *Physical Review B*, 23:5745–5761, 1981.
- [51] Hans Fangohr, Simon J. Cox, and Peter A. J. de Groot. Vortex dynamics in two-dimensional systems at high driving forces. *Physical Review B*, 64, 2001.
- [52] Kyungsun Moon, Richard T. Scalettar, and Gergely T. Zimnyi. Dynamical phases of driven vortex systems. *Physical Review Letters*, 77:2778–2781, 1996.
- [53] Wolfram research. <http://mathworld.wolfram.com/PercolationThreshold.html>.
- [54] L. B. Kiss and P. Svedlindh. New noise exponents in random conductor-superconductor and conductor-insulator mixtures. *Physical Review Letters*, 71:2817–2820, 1993.
- [55] R. Fujimoto et al. Low temperature detectors 9. In F.S. Porter, D. McCammon, M. Galeazzi, and C. Stahle (Eds.), editors, *AIP Conference Proceedings*, 2002.
- [56] M.A. Lindeman, R.P. Brekosky, E. Figueroa-Feliciano, F.M. Finkbeiner, M. Li, C.K. Stahle, C.M. Stahle, and N. Tralshawala. Low temperature detectors 9. In M. Galeazzi C. Stahle (Eds.) 'F.S. Porter, D. McCammon, editor, *AIP Conference Proceedings*, 2002.
- [57] Y. B. Kim, C. F. Hempstead, and A. R. Strnad. Flux creep in hard superconductors. *Physical Review*, 131:2486–2496, 1963.

- [58] T. L. Hylton and M. R. Beasley. Flux-pinning mechanisms in thin films of $YBa_2Cu_3O_x$. *Physical Review B*, 41:669–671, 1990.
- [59] P. C. van Son, H. van Kempen, and P. Wyder. New method to study the proximity effect at the normal-metal - superconductor interface. *Physical Review Letters*, 59:2226–2228, 1987.
- [60] I.J.R. Aitchison and A.J.G. Hey. *Gauge Theories in Particle Physics*. Adam Hilger Ltd, Bristol, England, 1982.
- [61] M.E. Peskin and D.V. Schroeder. *An Introduction to Quantum Field Theory*. Westview, 1995.
- [62] Peter W. Milonni. *The Quantum Vacuum: An Introduction to Quantum Electrodynamics*. Academic Press, 1993.
- [63] B.H. Bransden and C.J. Joachain. *Quantum Mechanics 2nd Ed*. Pearson Education Ltd., Essex, England, 2000.
- [64] Hans A. Bethe. The electromagnetic shift of energy levels. *PHYSICAL REVIEW*, 72, 1947.
- [65] Willis E. Lamb and Robert C. Retherford. Fine structure of the hydrogen atom by a microwave method. *PHYSICAL REVIEW*, 72, 1947.
- [66] Stephen W. Hawking. Particle creation by black holes. *Communications in Mathematical Physics*, 43, 1975.
- [67] W. G. Unruh. Notes on black-hole evaporation. *Physical Review D*, 14, 1976.
- [68] Pisin Chen and Toshi Tajima. Testing unruh radiation with ultraintense lasers. *Physical Review Letters*, 83, 1999.
- [69] H. B. Casimir and D. Polder. The influence of retardation on the london-van der waals forces. *Physical Review*, 73, 1948.
- [70] M. Bordag, U. Mohideen, and V. M. Mostepanenko. New developments in the casimir effect. *Physics Reports*, 353, 2001.
- [71] R.E. Glover and M. Tinkham. Transmission of superconducting films at millimetre-microwave and far infrared frequencies. *Physics Review*, 108:844–845, 1957.
- [72] R.J. Soulen, J.H. Colwell, and W.E. Fogle. The superconductive critical magnetic field of beryllium. *Journal of low temperature physics*, 124:515–526, 2001.
- [73] Giuseppe Bimonte, Detlef Born, Enrico Calloni, Giampiero Esposito, Evgeni Ilichev, Luigi Rosa, Ornella Scaldaferrì, Francesco Tafuri, Ruggero Vaglio, and Uwe Huebner. The aladin2 experiment: status and perspectives. *Journal of Physics A*, 39:6153– 6159, 2006.

- [74] Giuseppe Bimonte, Detlef Born, Enrico Calloni, Giampiero Esposito, Uwe Huebner, Evgeni Ilichev, Luigi Rosa, and Francesco Tafuri and Ruggero Vaglio. Low noise cryogenic system for the measurement of the casimir energy in rigid cavities. *Journal of Physics A*, 41, 2008.
- [75] Liang-Cheng Tu, Jun Luo, and George T Gillies. The mass of the photon. *Rep. Prog. Phys.*, 68:77–130, 2005.
- [76] Eugene Hecht. *Optics*. Pearson Education, Inc., Addison Wesley, San Francisco, USA, 2002.
- [77] P. P. Edwards, A. Porch, M. O. Jones, D. V. Morgan, and R. M. Perks. Basic materials physics of transparent conducting oxides. *Dalton Trans.*, 559, 2004.
- [78] G. Barton and N. Dombey. Significance of electromagnetic potentials in quantum theory. *Physics Review*, 115:485–491, 1959.
- [79] D. Beaglehole and M. Wihl. Optical studies of the electronic structure of aluminium manganese and aluminium-copper alloys. *J. Phys. F: Metal Physics*, 2:43–54, 1971.
- [80] R. E. LaVilla and H. Mendlowitz. Optical properties of beryllium in the ultraviolet from electron energy absorbtion. *Applied Optics*, 4:955–960, 1965.
- [81] C.G. Granqvist and A. Hultaker. Transparent and conducting ito films: new developments and applications. *Thin Film Solids*, 411:1–5, 2002.
- [82] Taichiro Nishio, Satoru Okayasu, Jun ichi Suzuki, Nobuhito Kokubo, , and Kazuo Kadowaki. Effective penetration depth in thin superconducting films obtained by a squid microscope image. In *Core-to-Core Integrated Action Initiative*.
- [83] I.S. Grant and W.R. Phillips. *Electromagnetism*. John Riley and Sons Ltd, Chichester, West Sussex, PO19 1UD, England, 1990.
- [84] Natsuki Mori. Superconductivity in transparent In_2O_3 films. *Journal of Applied Physics*, 73:1327, 1992.
- [85] Tadatsugu Minami. Transparent and conductive multicomponent oxide films prepared by magnetron sputtering. *J. Vac. Sci. Technol. A*, 17:1765–1772, 1999.
- [86] Lata Gupta, Abhai Mansingh, and P.K. Srivasta. Band gap narrowing and the band structure of tin-doped indium oxide films. *Thin Solid Films, Electronics and Optics*, 176:33–44, 1989.
- [87] W. W. Sleator. The resolving power of a prism. *Am. J. Phys.*, 8:47–48, 1940.
- [88] Y Aharanov and D. Bohm. The casimir effect with finite-mass photons. *Annals of Physics*, 162:231–272, 1985.
- [89] Roger Barlow. Introducing gauge invariance. *European Journal of Physics*, 11, 1990.

- [90] J. Tate, B. Cabrera, S.B. Felch, and J.T. Anderson. Precise determination of cooper-pair mass. *Physical Review Letters*, 62:845–848, 1989.
- [91] Matteo Luca Ruggiero and Angelo Tartaglia. Gravitomagnetic effects. *Nuovo Cim.*, 117B:743–768, 2002.
- [92] M. Tajmar and C.J. de Matos. Local photon and graviton mass and its consequences. *International Journal of Modern Physics D (UNDER REVIEW)*, submitted 2006.
- [93] Mark Alford, Juergen Berges, and Krishna Rajagopal. Magnetic fields within color superconducting neutron star cores. *Nuclear Physics B*, 571:269–284, 2007.
- [94] Birk B.W. Buckley, Max A. Metlitski, and Ariel R. Zhitnitski. Neutron stars as type-i superconductors. *PHYSICAL REVIEW LETTERS*, 92:151102, 2004.